

**THE CRYSTAL CHEMISTRY OF APATITE FROM AN EXPERIMENTAL AND
NATURAL PERSPECTIVE**

by

© **ANDREW CANALI**

A Thesis submitted to the

School of Graduate Studies

in partial fulfillment of the requirements for the degree of

Master of Science

Department of Earth Sciences

Memorial University of Newfoundland

October, 2017

St. John's

Newfoundland and Labrador

ABSTRACT

Apatite has a relatively accommodating crystal structure that allows for the incorporation of geochemically important elements (e.g., high field strength elements [HFSE]: Hf, Th and U; and rare earth elements [REE]: lanthanides plus Y and Sc) that can be analyzed with modern microanalytical techniques, making it a useful tracer of petrogenesis, post crystallization alteration, and mineralization. Chapter 2, presents the results from an experimental investigation of REE-doped fluorapatites, which suggest that Si is the preferred charge balancing cation in apatite, whereas Na played a minor role in the charge balancing of the REE under the experimental conditions used. Varying the proportion of the REEs in the starting reagents produced REE distributions in the apatite crystals indicating that the melt composition plays a more important role in the incorporation of REEs in apatite than the crystal chemistry of apatite. However, the enrichment of LREE (e.g., La, Nd, Sm) in the synthetic apatite crystals also suggest a crystal-chemical structural control for the larger LREEs that share similar ionic radii with the Ca1 and Ca2 sites as compared to the ionically smaller HREE. Chapter 3, presents a comparative study of natural apatites including the major, minor, and trace element compositions of reference apatites from well-known geological localities, along with those of the case study apatites from the Gruvberget (northern Sweden) magnetite apatite (MtAp) deposit and related rocks. These specific reference apatite samples were chosen because they provide a range of compositions with distinguishing characteristics for each locality. This range allows for empirical discrimination, which is used to develop a framework for apatite from a given rock type, and/or to constrain the effects of post-crystallization alteration processes. The assemblage of actinolite + scapolite in the Gruvberget host rocks and ore suggests metasomatic alteration of the apatite post- and/or syn-mineralization. The Gruvberget apatites, relative to the reference

apatites in general, are: 1) relatively depleted in total REEs, especially LREEs; 2) enriched in Cl and OH compared to the other MtAp ore samples; 3) relatively enriched in Mn; and 4) depleted in REE charge balancing cations Na and Si. It is postulated that the primary composition of the Gruvberget apatites were overprinted via metasomatism by hydrothermal fluids composed of a sodium, calcium, and chlorine rich brine, by metamorphism, or by both.

TABLE OF CONTENTS

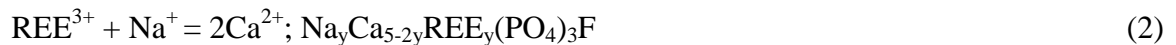
Abstract	i
Table of Contents	iii
Chapter 1: Introduction	1
1.1 Apatite in igneous systems.....	3
1.2 Objectives.....	5
1.3 Experimental methods for apatite syntheses	7
1.4 Sample preparation for Gruvberget apatite samples	8
1.5 Analytical methods.....	9
1.6 References	10
Chapter 2: Assessment of charge balancing between Na and Si in REE-doped synthetic fluorapatite: implications for melt composition and crystal-chemical controls on REE substitution in apatite	19
Abstract	19
2.1 Introduction	20
2.2 Experimental methods.....	22
2.3 Analytical methods.....	24
2.3.1 Sample preparation.....	24
2.3.2 Scanning electron microscopy	24
2.3.3 Bench-top cathodoluminescence.....	25

2.3.4 Electron probe microanalysis	25
2.3.5 Laser ablation inductively coupled plasma mass spectrometry	26
2.3.6 Powder X-ray diffraction	27
2.4 Results	28
2.4.1 Run-product homogeneity.....	28
2.4.2 Synthetic apatite crystal chemistry.....	30
2.4.3 Unit cell refinement of synthetic apatites	35
2.5 Discussion	36
2.5.1 Controls on apatite REE crystal chemistry	36
2.6 Conclusions.....	45
2.7 References	47
Chapter 2 Tables	53
Chapter 2 Figures	60
Chapter 3: Composition and crystal chemistry of apatite with a case study of apatite from the Gruvberget magnetite-apatite (MtAp)deposit, Norrbotten region, northern Sweden .	70
Abstract	70
3.1 Introduction.....	71
3.1.1 Geologic settings of the apatite samples used in this study	75
3.2 Analytical methods.....	80
3.2.1 Sample preparation.....	80

3.2.2 Scanning electron microscopy	81
3.2.3 Bench-top cathodoluminescence.....	81
3.2.4 Electron probe microanalysis.....	82
3.2.5 Laser ablation inductively coupled plasma mass spectrometry	83
3.3 Results.....	84
3.3.1 Part 1: Reference apatites.....	84
3.3.2 Part 2: Gruvberget apatites.....	92
3.4 Discussion	96
3.4.1 Reference apatites compared to the Gruvberget apatites	96
3.5 Conclusions.....	105
3.6 References	108
Chapter 3 Tables	123
Chapter 3 Figures	140
Chapter 4: Conclusions	159
Appendix.....	162
Appendix Tables	163
Appendix Figures	171

Chapter 1: Introduction

Apatite is a widely occurring accessory mineral that forms in many igneous, metamorphic, and sedimentary rocks. The general formula for apatite supergroup minerals is ${}^{\text{IX}}\text{M}_1{}_2{}^{\text{VII}}\text{M}_2{}_3({}^{\text{IV}}\text{TO}_4)_3\text{X}$ (e.g., M = Large ion lithophile elements [LILE]: Ca^{2+} , Sr^{2+} , Ba^{2+} ; Mg^{2+} , Mn^{2+} , Na^+ T = P^{5+} , As^{5+} , S^{5+} , V^{5+} , Si^{4+} ; X = F^- , Cl^- , OH^-), crystallizing in the hexagonal system, space group $\text{P6}_3/\text{m}$ (Elliot 2002; Pasero, 2010). Calcium phosphate apatite is the most common apatite that occurs in nature, with the formula $\text{Ca}_5(\text{PO}_4)_3\text{X}$, where F, Cl or OH occupy the X anion site to form the ternary system of fluorapatite (FAp), chlorapatite (CAp) and hydroxyapatite (HAp). The prevalent end-member in igneous systems is FAp, and its trace element composition is sensitive to changes in pressure (P) and temperature (T) conditions, oxygen fugacity ($f\text{O}_2$), and melt composition (M_x) (Boudreau et al., 1995; Piccoli and Candela, 2002; Hovis and Harlov, 2010). Substitution may occur at the ${}^{\text{IX}}\text{M}_1{}_2{}^{\text{VII}}\text{M}_2{}_3$ and ${}^{\text{IV}}\text{TO}_4$ sites (e.g., Na^+ or Sr^{2+} for Ca^{2+} and SiO_2 or AsO_4^{3-} for PO_4^{3-}) within the apatite structure, often as coupled substitutions (Rønsbo, 1989; Elliot, 2013). Substitution involving vacancies at the Ca site may also accommodate REEs in apatite (Fleet and Pan, 2002). In the following reactions the two coupled substitution mechanisms, and one substitution involving vacancies at the Ca site, are given as examples:



The accommodation of geochemically important elements in apatite such as high field strength elements (e.g., Hf, Th and U), the rare earth elements (e.g., the lanthanides, Sc, and Y) and As, Fe, Ba, Mn, and Mg, make it an important tracer of petrogenetic and post crystallization

alteration processes. This variability in apatite chemistry has led many researchers to investigate its behaviour in a range of geologic environments attempting to identify a chemical signature unique to different conditions (e.g., Harlov et al., 2002; Belousova et al., 2002; Jinjie et al., 2007; Bonyadi et al., 2011). One area of interest for detailed investigations into apatite chemistry are what are often referred to as iron-oxide apatite (IOA) deposits, or magnetite-apatite (MtAp) deposits (e.g., Kiruna in the Norrbotten region of northern Sweden) (Philpotts, 1967; Hitzman, 1992; Nyström and Henriquez, 1994; Frietsch and Perdahl, 1995; Jonsson et al., 2013; Westhues et al., 2016). Some world-renowned localities of this type include: the Adirondacks (e.g., Mineville) (Foose and McLelland, 1995; Valley et al., 2009; Valley et al., 2011); the Great Bear Magmatic Zone, Northwest Territories, Canada (Hitzman, 1992; Gandhi et al., 2000; Ootes et al., 2010); Olympic Dam, South Australia (Haynes et al., 1995; Partington and Williams, 2000; Belperio and Freeman, 2004); the southeastern Missouri metallogenic province (e.g., Pea Ridge and Pilot Knob) (Nuelle et al., 1992; Nold et al., 2013; Nold et al., 2014; Starkey and Seeger, 2016, for review); and El Laco, Chile (Nyström and Henriquez, 1994; Tornos et al., 2016; Velasco et al., 2016). Although apatite is typically low in modal abundance in most rocks that make up much of the crust and mantle, it is concentrated in these deposits within massive iron-oxide ore bodies; which may occur as discordant brecciated zones, or concordant tabular lenses in stratified successions (e.g., volcanic, and/or sedimentary rocks) (Piccoli and Candela, 2002; Hitzman, 1992; Williams et al., 2005). An example of the latter is the Kiirunavaara IOA deposit in Kiruna, Sweden, estimated to contain 2.6 billion tonnes at 60% Fe (Parak, 1975; Forsell et al., 1980; Hitzman, 1992; Westhues et al., 2016). The ore genesis of the Kiirunavaara deposit is still under debate (Geijer and Ödman, 1974; Parak, 1975; Frietsch, 1978; Wright, 1986; Jonsson et al., 2013; Westhues et al., 2016; Westhues et al., 2017). Apatite occurs in high volume in some

of these deposits, and studies into its chemistry may provide important details regarding mineral exploration, hydrothermal alteration, the nature of the P, F, and REE-bearing fluids, and ore forming processes (e.g., Roegge et al., 1974; Williams and Cesbron, 1977; Watson and Capobianco, 1981; Piccoli and Candela, 1994; Belousova et al., 2002; Dempster, 2003; Harlov, 2015; Mao et al., 2016).

In addition to the research done on natural samples, experimental approaches in assessing apatite chemistry have also been undertaken (e.g., Watson, 1979, 1980; Watson and Green, 1981; Green and Watson, 1982; Harrison and Watson, 1984; Wolf and London, 1994, 1995; Hovis and Harlov, 2010.). The general principle of these experiments is to replicate the conditions in which apatite forms in nature to better understand its crystal chemical behaviour in natural systems (e.g., Ghiorso and Sack, 1995; Cherniak, 2000; Klemme and Dalpé, 2003).

1.1 APATITE IN IGNEOUS SYSTEMS

Apatite is an important accessory mineral in igneous and metamorphic systems because it presumably records rock forming and post-crystallization processes (Harlov et al., 2002; Bonyadi et al., 2011; Harlov, 2015). Research into apatite has implications for thermochronology, U-Th-Pb geochronology, Nd-Sm, Lu-Hf radiogenic isotope geochemistry, redox conditions, volcano-stratigraphic correlation, magmatic processes and sources, weathering, metasomatic alteration by hydrothermal fluids, and ore deposit genesis (e.g., Roegge et al., 1974; Williams and Cesborn, 1977; Huff, 1983; Boudreau and McCallum, 1989, 1990; Samson et al., 1995; Tepper and Keuhner, 1999; Belousova et al., 2001, 2002; Chew et al., 2011; Miles et al., 2014; Harlov, 2015).

The crystal habit of apatite in igneous systems is likely dependent on the degree of undercooling. Equant crystals tend to form near equilibrium growth at low undercooling, and

acicular growth dominates at high undercooling (Piccoli and Candela, 2002). Much like other accessory minerals, apatite may exhibit compositional zoning—revealed by back-scattered electron (BSE) imaging or cathodoluminescence (CL) imaging—that is most apparent with respect to minor and trace elements (e.g., Mn, Mg, Sr, Ba, REE). The X-site elements (i.e., F, Cl and OH) tend not to show compositional zoning (Brenan, 1993a,b; Webster and Piccoli, 2015). The geochemical compilation in Piccoli and Candela (2002) shows that in felsic-intermediate ore producing and non-ore producing igneous rocks, FAp is the most common end member. Given that F, Cl, and OH play an important role in magmatic/ hydrothermal processes, variation in the halogen ratios of apatite may be used to constrain information about melt and/or aqueous phase (i.e., hydrothermal fluid) halogen composition, as well as timing of volatile saturation (Korzhinskiy 1981, Boudreau and McCallum, 1989; Zhu and Sverjensky 1991,1992; Harlov, 2015). However, it is crucial that apatite composition is considered in combination with detailed petrographic information; in order to trace the effects of initial and evolved melt composition, paragenesis, volatile exsolution, and subsequent subsolidus alteration (Piccoli and Candela, 2002).

Apatite solubility in silicate melts tends to increase with increasing temperature, along with decreasing SiO₂ content and degree of polymerization (Watson and Capobianco, 1981; Watson and Green, 1981; Green and Watson, 1982; London et al., 1999). Thus, apatite solubility is greater in mafic melts, which have lower SiO₂ contents and a lower degrees of polymerization. High-pressure and -temperature experiments done by Wolf and London (1994), using a range of peraluminous and metaluminous melt compositions, indicated that apatite solubility is generally greater in the latter. Those authors concluded that a linear relationship exists between the aluminum saturation index (ASI = molecular Al₂O₃/[Na₂O +K₂O + CaO]) and concentration of

P₂O₅ in the melt at elevated ASI—suggesting lower apatite saturation temperatures in peraluminous melts than in metaluminous systems. The unique solubility characteristics of apatite also allows for the determination of apatite crystallization temperatures in magmatic systems based on Nernst partition coefficients derived from the saturation behaviour, investigated by Harrison and Watson (1984) through high pressure dissolution experiments at a range of water contents and temperatures at 0.8 GPa pressure.

The inability to achieve apatite saturation is common in Ca-poor melts (i.e., low Ca activity), or in melts that have undergone early fractionation of other Ca-bearing minerals, such as plagioclase, augite, or titanite. In the case of augite, the melt may be saturated in other phosphate minerals (e.g., xenotime and monazite in peraluminous rocks) as the P/Ca ratio increases (Piccoli and Candela, 2002). At low bulk melt P content, local precipitation of apatite may occur on boundary layers around major minerals (Harrison and Watson, 1984). Fractionation also plays an important role in determining the LREE:HREE ratio in apatite, depending on the bulk melt REE composition at the time of apatite crystallization. Highly differentiated magmas that undergo plagioclase fractionation tend towards LREE enrichment in apatite, and depletion in the Eu content (i.e., negative Eu anomaly) due to the incorporation of Eu²⁺ in plagioclase. The sites occupied by Ca in apatite tend to accommodate LREEs rather than HREE (e.g., La/Er ratios are usually greater 1) because they have ionic radii similar to that of Ca.

1.2 OBJECTIVES

The current study is a two part investigation of synthetic and natural apatite samples to better understand the crystal chemistry of apatite according to: 1) experimental data from synthetic REE and Si or Na doped apatite; 2-A) apatite from well-known apatite localities, from a range of geologic environments, in the collection of Professor Hanchar (Mud Tank, Australia;

Durango, Mexico; Otter lake, Québec; Mineville, New York; Sludyanka, Siberia, Russia; and Kovdor from the Kola Peninsula, in northwestern Russia); and 2-B) a case study of apatites from ore and their respective host rocks of the Gruvberget MtAp deposit, Svappavaara, Sweden.

For the experimental component of this work, analyses of synthetic apatite (synthesized in the experimental geochemistry laboratory at Memorial University of Newfoundland) provide insights into the processes that control crystal chemistry, including: 1) efficiency of Si^{4+} or Na^+ at charge balancing REEs in apatite, based on the equations (1) and (2) above; and 2) melt composition and crystal chemical structural control on resulting apatite REE crystal chemistry.

The samples listed above in #2-A (hereafter, referred to as reference apatites) provide a survey of apatite chemistry, albeit limited in number of samples, to reveal any significant and unique chemical characteristics, including the potential uses of apatite for discerning petrogenetic and ore forming processes. For #2-B, natural apatite samples from Gruvberget, one of the major MtAp deposits in the Norrbotten region (one ore sample and hydrothermally altered host rock and cross cutting diabase dike), enable comparison between the reference material apatites (2-A above) to define any inter- and intra-sample variations in apatite chemistry and to determine if there is a unique chemical “fingerprint” for apatite that crystallize in MtAp deposits or their hydrothermally altered host rock and related rocks. Synthetic apatites doped with Si, Na, and REEs also provide a compositional analog to natural samples with insights into the controls of melt composition on apatite REE crystal chemistry. By altering the REE composition of the melt from which the apatite crystal grew to reflect conditions similar to those in nature, the synthetic apatites appear to share similar REE distributions to natural apatite compositions (e.g., REE- and Si-enriched Mineville apatite). This comparative survey of natural apatite chemistry reveals important insight into rock- and ore-forming processes, especially metasomatism via

hydrothermal fluids overprinting original apatite composition, related to different geologic environments.

1.3 EXPERIMENTAL METHODS FOR APATITE SYNTHESSES

Microcrystalline apatite was synthesized by combining calcium phosphate ($\text{Ca}_3[\text{PO}_4]_2$) and fluorite (CaF_2) powders in a 25 mL Pt crucible. The Pt crucibles were cleaned prior to use with concentrated HF and then concentrated HNO_3 , followed by deionized H_2O . The mixture was sintered in the “hot spot” of a Deltech MoSi_2 glass making (i.e., box) furnace at 950°C using a solid-state exchange reaction to produce microcrystalline fluorapatite following the method by Prener (1970) and Kreidler & Hummel (1970):



This microcrystalline fluorapatite in turn was then added to more fluorite at a ratio of 45:55 wt.%, respectively. The starting materials were mechanically mixed in an agate mortar and pestle, under ethanol, and then transferred to the 25 mL platinum crucible. The Pt crucible was covered with a tight-fitting Pt lid and placed in the “hot spot” of the same Deltech furnace, preheated to 1375°C for 15 hours and then cooled to 1220°C at $3^\circ\text{C}/\text{hr}$ to produce mm to cm sized single crystals of fluorapatite. Using a type S control thermocouple, the temperature in the hot spot was measured to within $\pm 5^\circ\text{C}$. The apatite was cooled slowly to return the mixture to a solid phase consisting of crystalline apatite embedded in the residual fluorite flux. After cooling to room temperature the crystals were extracted from the residual flux (if any remained) by placing the crucible in a 20% (by volume) boiling solution of $\text{Al}(\text{NO}_3)_3 \cdot 9\text{H}_2\text{O}$ in a 500 mL Pyrex beaker on a hotplate, followed by rinsing in distilled H_2O . The $\text{Al}(\text{NO}_3)_3 \cdot 9\text{H}_2\text{O}$ treatment was done for as short a time as possible to avoid any dissolution, or chemical alteration of the apatite crystals.

The synthesis of the doped fluorapatites followed the aforementioned procedure, with the dopants added as multiples of their abundances in nature (e.g., 1x [100s of ppm], 10x [1000s of ppm] and 100x [10,000s of ppm]) directly to the undoped mixture prior to fusion. The composition of natural apatite, which cover a range of compositions from Roeder et al. (1987) was used as a target composition for the synthetic apatite REE contents. In order to reproduce REE abundances in the synthetic apatites as close as possible to natural compositions, elements from both LREE (La, Nd, and Sm) and HREE (Dy, Y, and Er) were added with either Na, or Si, in equal molar proportions. Syntheses were also done at variable LREE:HREE ratios: LREE > HREE, LREE = HREE and LREE < HREE to see if the abundance of LREE relative to HREE in the starting materials controlled the incorporation of the REE in the apatite.

Evacuated silica tube syntheses were done to limit Na volatility during synthesis. These syntheses consisted of a 10% by mass aliquot of the microcrystalline apatite + dopants mixture in a 2.5 cm length of Pt tubing. The Pt tubing was sealed at both ends and placed in a ~15 cm section of fused silica tubing. This section of silica tubing was then attached to a vacuum line, evacuated for ~1 hr, and later sealed with an oxy-acetylene torch. The resulting silica ampoule was then subject to the same run conditions as those in the 25 mL Pt crucible.

1.4 SAMPLE PREPARATION FOR GRUVBERGET APATITE SAMPLES

Sample preparation was done using standard techniques in the facilities at the Department of Earth Science at Memorial University of Newfoundland. Preparation began with nearly 10 kg of rock samples which were processed using a jaw crusher and disk mill, followed by sieving to a grain size range of 63 μm to 500 μm . The remaining fraction was split using a sample splitter into workable aliquots of several hundred grams, and rinsed in distilled water to remove any adhering dust. After drying, removal of magnetite was done using a hand magnet. This was

followed by density separation via heavy liquids (and bromoform [density 2.85 g/cm³ and Methylene Iodide [density 3.3 g/cm₃]). Apatite grains were then handpicked from the final separate, mounted in 2.5 cm epoxy rounds, and polished to expose the crystal centers for analysis.

1.5 ANALYTICAL METHODS

The following outlines the analyses that were done at the Memorial University of Newfoundland Microanalytical Facility of the Bruneau Innovation Centre (MAF-IIC) and in the Department of Earth Sciences.

X-ray diffraction (XRD) was used to determine the crystallographic properties of apatites for each synthesis. Cathodoluminescence (CL) and back-scattered electron (BSE) imaging was done using a scanning electron microscope (SEM) to reveal any internal chemical zoning in the natural apatite grains; which were later used to guide where to do the in situ analyses on the apatite grains. A bench-top optical microscope based system was also used to acquire CL images of synthetic and natural apatite grains.

Major and minor elements in apatite were measured using an electron probe micro-analyzer (EPMA), and trace elements using laser ablation inductively coupled plasma mass spectrometry (LA-ICPMS).

1.6 REFERENCES

- Belousova, E., Walters, S., Griffin, W., & O'Reilly, S. (2001). Trace-element signatures of apatites in granitoids from the Mt Isa Inlier, northwestern Queensland. *Australian Journal of Earth Sciences*, 48, 603-619.
- Belousova, E. A., Griffin, W. L., O'Reilly, S. Y., & Fisher, N. I. (2002). Apatite as an indicator mineral for mineral exploration: Trace-element compositions and their relationship to host rock type. *Journal of Geochemical Exploration*, 76, 45-69.
doi:[http://dx.doi.org/10.1016/S0375-6742\(02\)00204-2](http://dx.doi.org/10.1016/S0375-6742(02)00204-2)
- Belperio, A., & Freeman, H. (2004). Common geological characteristics of Prominent Hill and Olympic Dam-implications for iron oxide copper-gold exploration models. *AusIMM Bulletin*, 1990, 67-70.
- Bonyadi, Z., Davidson, G. J., Mehrabi, B., Meffre, S., & Ghazban, F. (2011). Significance of apatite REE depletion and monazite inclusions in the brecciated Se-Chahun iron oxide-apatite deposit, Bafq District, Iran: Insights from paragenesis and geochemistry. *Chemical Geology*, 281, 253-269. doi:<http://dx.doi.org/10.1016/j.chemgeo.2010.12.013>
- Boudreau, A., & McCallum, I. (1989). Investigations of the Stillwater Complex: Part V. apatites as indicators of evolving fluid composition. *Contributions to Mineralogy and Petrology*, 102, 138-153.
- Boudreau, A., & McCallum, I. (1990). Low temperature alteration of REE-rich chlorapatite from the Stillwater Complex, Montana. *American Mineralogist*, 75, 687-693.
- Boudreau, A. E., Love, C., & Prendergast, M. D. (1995). Halogen geochemistry of the Great Dyke, Zimbabwe. *Contributions to Mineralogy and Petrology*, 122, 289-300.
doi:10.1007/s004100050128.

- Brenan, J.M. (1993). Kinetics of fluorine, chlorine and hydroxyl exchange in fluorapatite. *Chemical Geology*, 110, 195-210.
- Brenan, J. M. (1993). Partitioning of fluorine and chlorine between apatite and aqueous fluids at high pressure and temperature: Implications for the F and Cl content of high P-T fluids. *Earth and Planetary Science Letters*, 117, 251-263. doi:[http://dx.doi.org/10.1016/0012-821X\(93\)90131-R](http://dx.doi.org/10.1016/0012-821X(93)90131-R)
- Cherniak, D. J. (2000). Rare earth element diffusion in apatite. *Geochimica et Cosmochimica Acta*, 64, 3871-3885. doi:[http://dx.doi.org/10.1016/S0016-7037\(00\)00467-1](http://dx.doi.org/10.1016/S0016-7037(00)00467-1)
- Chew, D. M., Sylvester, P. J., & Tubrett, M. N. (2011). U–Pb and Th–Pb dating of apatite by LA-ICPMS. *Chemical Geology*, 280, 200-216. doi:<http://dx.doi.org/10.1016/j.chemgeo.2010.11.010>
- Dempster, T., Jolivet, M., Tubrett, M., & Braithwaite, C. (2003). Magmatic zoning in apatite: A monitor of porosity and permeability change in granites. *Contributions to Mineralogy and Petrology*, 145, 568-577.
- Elliott, J. C. (2013). *Structure and chemistry of the apatites and other calcium orthophosphates*. (pp. 1-404). Amsterdam: Elsevier.
- Elliott, J., Wilson, R., & Dowker, S. (2002). Apatite structures. *Advances in X-Ray Analysis*, 45, 172-181.
- Foose, M. P., & McLelland, J. M. (1995). Proterozoic low-Ti iron-oxide deposits in New York and New Jersey: Relation to Fe-oxide (Cu–U–Au–rare earth element) deposits and tectonic implications. *Geology*, 22, 665-668.
- Forsell, P., Godin, L., & Frietsch, R. (1980). Geology of the Kiruna area. Paper presented at the *26th International Geological Congress, Guidebook*, Paris. pp. 143-150.

- Frietsch, R. (1978). On the magmatic origin of iron ores of the Kiruna type. *Economic Geology*, 73, 478-485.
- Frietsch, R., & Perdahl, J. (1995). Rare earth elements in apatite and magnetite in Kiruna-type iron ores and some other iron ore types. *Ore Geology Reviews*, 9, 489-510.
- Gandhi, S. S., Carrière, J. J., & Prasad, N. (2000). *Implications of a preliminary fluid-inclusion study of giant quartz veins of the southern Great Bear Magmatic Zone, Northwest Territories* Natural Resources Canada, Geological Survey of Canada, Current Research 2000-C1:13.
- Geijer, P., & Ödman, O. H. R. (1974). *The emplacement of the Kiruna iron ores and related deposits*(No. 700). Sveriges geologiska undersökning. 1-48
- Ghiorso, M. S., & Sack, R. O. (1995). Chemical mass transfer in magmatic processes IV. A revised and internally consistent thermodynamic model for the interpolation and extrapolation of liquid-solid equilibria in magmatic systems at elevated temperatures and pressures. *Contributions to Mineralogy and Petrology*, 119, 197-212.
- Green, T., & Watson, E.B. (1982). Crystallization of apatite in natural magmas under high pressure, hydrous conditions, with particular reference to 'orogenic' rock series. *Contributions to Mineralogy and Petrology*, 79, 96-105.
- Harlov, D. E. (2015). Apatite: A fingerprint for metasomatic processes. *Elements*, 11, 171-176.
- Harlov, D. E., Andersson, U. B., Förster, H., Nyström, J. O., Dulski, P., & Broman, C. (2002). Apatite–monazite relations in the Kiirunavaara magnetite–apatite ore, Northern Sweden. *Chemical Geology*, 191, 47-72.

- Harrison, T. M., & Watson, E. B. (1984). The behavior of apatite during crustal anatexis: Equilibrium and kinetic considerations. *Geochimica et Cosmochimica Acta*, 48, 1467-1477.
- Haynes, D. W., Cross, K. C., Bills, R. T., & Reed, M. H. (1995). Olympic Dam ore genesis; a fluid-mixing model. *Economic Geology*, 90, 281-307.
- Hitzman, M. W., Oreskes, N., & Einaudi, M. T. (1992). Geological characteristics and tectonic setting of Proterozoic iron oxide (Cu-U-Au-REE) deposits. *Precambrian Research*, 58, 241-287. doi:[http://dx.doi.org/10.1016/0301-9268\(92\)90121-4](http://dx.doi.org/10.1016/0301-9268(92)90121-4)
- Hovis, G. L., & Harlov, D. E. (2010). Solution calorimetric investigation of fluor-chlorapatite crystalline solutions. *American Mineralogist*, 95, 946-952.
- Huff, W. D. (1983). Correlation of middle Ordovician K-bentonites based on chemical fingerprinting. *The Journal of Geology*, 91, 657-669.
- Jinjie, Y., Qi, Z., Jingwen, M., & Shenghao, Y. (2007). Geochemistry of apatite from the Apatite-rich iron deposits in the Ningwu Region, East Central China. *Acta Geologica Sinica (English Edition)*, 81, 637-648.
- Jonsson, E., Troll, V. R., Högdahl, K., Harris, C., Weis, F., Nilsson, K. P., et al. (2013). Magmatic origin of giant 'Kiruna-type' apatite-iron-oxide ores in central Sweden. *Scientific Reports*, 3, 1644, doi:10.1038/srep01644.
- Klemme, S., & Dalpé, C. (2003). Trace-element partitioning between apatite and carbonatite melt. *American Mineralogist*, 88, 639-646.
- Korzhinskiy, M. (1981). Apatite solid solutions as indicators of the fugacity of HCl and HF in hydrothermal fluids. *Geochemistry International*, 3, 45-60.

- Kreidler, E. R., & Hummel, F. (1970). The crystal chemistry of apatite: Structure fields of fluor- and chlorapatite. *American Mineralogist*, 55, 170-184.
- London, D., Wolf, M. B., Morgan, G. B., & Garrido, M. G. (1999). Experimental silicate–phosphate equilibria in peraluminous granitic magmas, with a case study of the Albuquerque Batholith at Tres Arroyos, Badajoz, Spain. *Journal of Petrology*, 40, 215-240.
- Mao, M., Rukhlov, A. S., Rowins, S. M., Spence, J., & Coogan, L. A. (2016). Apatite trace element compositions: A robust new tool for mineral exploration. *Economic Geology*, 111, 1187-1222.
- Miles, A., Graham, C., Hawkesworth, C., Gillespie, M., Hinton, R., & Bromiley, G. (2014). Apatite: A new redox proxy for silicic magmas? *Geochimica et Cosmochimica Acta*, 132, 101-119.
- Nold, J. L., Davidson, P., & Dudley, M. A. (2013). The Pilot Knob magnetite deposit in the Proterozoic St. Francois Mountains terrane, Southeast Missouri, USA: A magmatic and hydrothermal replacement iron deposit. *Ore Geology Reviews*, 53, 446-469.
- Nold, J. L., Dudley, M. A., & Davidson, P. (2014). The Southeast Missouri (USA) Proterozoic iron metallogenic province—Types of deposits and genetic relationships to magnetite–apatite and iron oxide–copper–gold deposits. *Ore Geology Reviews*, 57, 154-171.
- Nuelle, L. M., Desborough, G. A., Hatch, J. R., & Leventhal, J. S. (1992). *Geology and mineral paragenesis of the Pea Ridge iron ore mine, Washington County, Missouri—origin of the rare-earth-element-and gold-bearing breccia pipes* U.S. Geological Survey Bulletin 1989, A1–A11

- Nyström, J. O., & Henriquez, F. (1994). Magmatic features of iron ores of the Kiruna type in Chile and Sweden; ore textures and magnetite geochemistry. *Economic Geology*, 89, 820-839.
- Ootes, L., Goff, S., Jackson, V. A., Gleeson, S. A., Creaser, R. A., Samson, I. M., et al. (2010). Timing and thermochemical constraints on multi-element mineralisation at the Nori/RA Cu–Mo–U prospect, Great Bear Magmatic Zone, Northwest Territories, Canada. *Mineralium Deposita*, 45, 549-566.
- Parak, T. (1975). Kiruna iron ores are not "intrusive-magmatic ores of the Kiruna type". *Economic Geology*, 70, 1242-1258.
- Parak, T. (1985). Phosphorus in different types of ore, sulfides in the iron deposits, and the type and origin of ores at Kiruna. *Economic Geology*, 80, 646-665.
- Partington, G. A., & Williams, P. J. (2000). Proterozoic lode gold and (iron)-copper-gold deposits; a comparison of Australian and global examples. *Reviews in Economic Geology*, 13, 69-101.
- Pasero, M., Kampf, A. R., Ferraris, C., Pekov, I. V., Rakovan, J., & White, T. J. (2010). Nomenclature of the apatite supergroup minerals. *European Journal of Mineralogy*, 22, 163-179.
- Philpotts, A. (1967). Origin of certain iron-titanium oxide and apatite rocks. *Economic Geology*, 62, 303-315.
- Piccoli, P. M., & Candela, P. A. (2002). Apatite in igneous systems. *Reviews in Mineralogy and Geochemistry*, 48, 255-292. doi:10.2138/rmg.2002.48.6

- Piccoli, P., & Candela, P. (1994). Apatite in felsic rocks; a model for the estimation of initial halogen concentrations in the Bishop Tuff (Long Valley) and Tuolumne Intrusive Suite (Sierra Nevada Batholith) magmas. *American Journal of Science*, 294, 92-135.
- Roegge, J., Logsdon, M., Young, H., Barr, H., Borcsik, M., & Holland, H. (1974). Halogens in apatites from the Providencia Area, Mexico. *Economic Geology*, 69, 229-240.
- Rønso, J. (1989). Coupled substitutions involving REEs and Na and Si in apatites in alkaline rocks from the Ilimaussaq Intrusion, south Greenland, and the petrological implications. *American Mineralogist*, 74, 896-901.
- Samson, S. D., Matthews, S., Mitchell, C. E., & Goldman, D. (1995). Tephrochronology of highly altered ash beds: The use of trace element and strontium isotope geochemistry of apatite phenocrysts to correlate K-bentonites. *Geochimica et Cosmochimica Acta*, 59, 2527-2536.
- Starkey, M., & Seeger, C. (2016). Mining and exploration history of the southeast Missouri Iron Metallogenic Province. *Economic Geology*, 111, 1815-1823.
- Tepper, J. H., & Kuehner, S. M. (1999). Complex zoning in apatite from the Idaho batholith: A record of magma mixing and intracrystalline trace element diffusion. *American Mineralogist*, 84, 581-595.
- Tornos, F., Velasco, F., & Hanchar, J. M. (2016). Iron-rich melts, magmatic magnetite, and superheated hydrothermal systems: The El Laco deposit, Chile. *Geology*, 44, 427-430, <http://dx.doi: 10.1130/G37705.1>.
- Velasco, F., Tornos, F., & Hanchar, J. M. (2016). Immiscible iron-and silica-rich melts and magnetite geochemistry at the El Laco volcano (Northern Chile): Evidence for a magmatic origin for the magnetite deposits. *Ore Geology Reviews*, 79, 346-366.

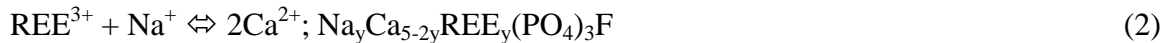
- Watson, E. B. (1979). Apatite saturation in basic to intermediate magmas. *Geophysical Research Letters*, 6, 937-940.
- Watson, E. B. (1980). Apatite and phosphorus in mantle source regions: An experimental study of apatite/melt equilibria at pressures to 25 kbar. *Earth and Planetary Science Letters*, 51, 322-335.
- Watson, E. B., & Capobianco, C. (1981). Phosphorus and the rare earth elements in felsic magmas: An assessment of the role of apatite. *Geochimica et Cosmochimica Acta*, 45, 2349-2358.
- Watson, E. B., & Green, T. H. (1981). Apatite/liquid partition coefficients for the rare earth elements and strontium. *Earth and Planetary Science Letters*, 56, 405-421.
- Westhues, A., Hanchar, J. M., Whitehouse, M. J., & Martinsson, O. (2016). New constraints on the timing of host-rock emplacement, hydrothermal alteration, and iron oxide-apatite mineralization in the Kiruna district, Norrbotten, Sweden. *Economic Geology*, 111, 1595-1618, <http://dx.doi.org/10.2113/econgeo.111.7.1595>.
- Westhues, A., Hanchar, J. M., LeMessurier, M. J., & Whitehouse, M. J. (2017). Evidence for hydrothermal alteration and source regions for the Kiruna iron oxide-apatite ore (northern Sweden) from zircon Hf and O isotopes. *Geology*, 45, 571-574, <http://dx.doi.org/10.1130/G38894.1>.
- Williams, S. A., & Cesbron, F. P. (1977). Rutile and apatite: Useful prospecting guides for porphyry copper deposits. *Mineralogical Magazine*, 41, 288-292.
- Wolf, M. B., & London, D. (1994). Apatite dissolution into peraluminous haplogranitic melts: An experimental study of solubilities and mechanisms. *Geochimica et Cosmochimica Acta*, 58, 4127-4145.

- Wolf, M. B., & London, D. (1995). Incongruent dissolution of REE- and Sr-rich apatite in peraluminous granitic liquids: Differential apatite, monazite, and xenotime solubilities during anatexis. *American Mineralogist*, 80, 765-775.
- Wright, S. F. (1986). On the magmatic origin of iron ores of the Kiruna type; an additional discussion. *Economic Geology*, 81, 192-194.
- Zhu, C., & Sverjensky, D. A. (1991). Partitioning of F-Cl-OH between minerals and hydrothermal fluids. *Geochimica et Cosmochimica Acta*, 55, 1837-1858.
- Zhu, C., & Sverjensky, D. A. (1992). F-Cl-OH partitioning between biotite and apatite. *Geochimica et Cosmochimica Acta*, 56, 3435-3467.

Chapter 2: Assessment of charge balancing between Na and Si in REE-doped synthetic fluorapatite: implications for melt composition and crystal-chemical controls on REE substitution in apatite

ABSTRACT

Apatite is a common accessory mineral in most igneous rocks, and substitutions within the apatite structure allow for the incorporation significant geochemical tracer elements (e.g., rare earth elements [REE; the lanthanides, Y, and Sc], As, Fe, Ba, Mn, and Mg) that reflect the geologic conditions (e.g., temperature, pressure, oxygen fugacity, composition) in which the apatite crystallized. Substitutions at cation sites, for example, can yield several weight percent REE substituted for Ca. This occurs as a coupled substitution with other cations in the fluorapatite structure ($\text{Ca}_5[\text{PO}_4]_3\text{F}$) to charge balance the substituting REE^{3+} , as follows in two possible reactions:



To better understand the incorporation of REE in apatite, a suite of REE-doped (REE in this study means a subset including the trivalent La, Nd, Sm, Dy, Er, and Y) fluorapatites were synthesized in the presence of Si or Na to assess the effectiveness of the substitution mechanisms above. The results of this investigation suggest that Si is the preferred charge balancing cation, for the experimental conditions used, whereas Na played a less significant role in the charge balancing of the REEs. Varying the proportion of the REEs in the starting reagents produced REE distributions in the apatite crystals indicating that the melt composition plays a more important role in the incorporation of REEs in apatite than the crystal chemistry of apatite. However, the enrichment of LREE (e.g., La, Nd, Sm) in the synthetic apatite crystals also suggests a crystal-chemical structural control for the larger LREEs that share similar ionic radii

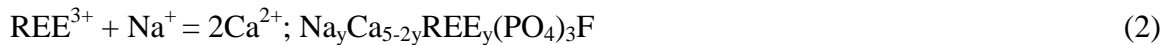
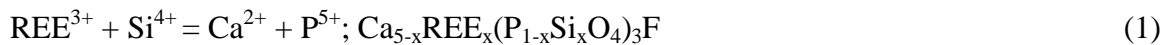
with the host Ca1 and Ca2 cations, as compared to the ionically smaller HREE (e.g., Dy, Er, Y). A comparison to natural apatites from different geological settings reveal similar REE distributions; suggesting that the partitioning behaviour of the REE in these experiments may reflect those of natural melts.

2.1 INTRODUCTION

The amount of a rare earth element (REE are defined as the lanthanides plus Y and Sc) incorporated into the crystal structure of a mineral varies with the compatibility between the host cation in its structural site (i.e., the ionic radius and charge) and the REE entering the structure. The difference in the behaviour between REEs are a result of the decrease in REE ionic radius, the so-called lanthanide contraction (Cotton et al., 1988), in which, as the atomic number increases, the ionic radii decrease from La to Lu (e.g., 1.216 Å for La to 1.032 Å for Lu in IX-fold coordination with oxygen; Shannon, 1976) (Pan et al., 2000). This leads to a preferential incorporation of either light REE (LREE: Sc, La, Ce, Pr, Nd, Sm, Eu, and Gd) or heavy REE (HREE: Y, Tb, Dy, Ho, Er, Tm, Yb, and Lu) progressing from larger to smaller Ca structural sites in Ca-bearing minerals, respectively (e.g., LREE in the larger 1.180 Å Ca site in IX-fold coordination in apatite and HREE in the smaller 1.120 Å Ca site *in* VIII-fold coordination in garnet) (Fleet and Pan, 1995). The accommodation of a REE in a crystal structure normally adheres to Goldschmidt's rules of substitution as follows: 1) a REE ion of the same size and charge as the host ion will enter readily; 2) if two REE ions have the same charge, the smaller ion will enter more readily; and 3) if two REE ions are of the same radius, the ion with the higher charge will enter more readily (Goldschmidt, 1926). Bonding effects may also influence substitution, coupled with ionic properties, where substitution is favored with increasing bond strength (Fleet and Pan, 1995). Crystal field stabilization energy (CFSE) effects are not

significant in REE crystal chemistry because the CFSE of a $4f$ orbital in a weak octahedral field, due to the $4f$ valence electrons not being in the outermost shell, is small ($\Delta_o \approx 1\text{kJ/mol}$) and may be ignored (e.g., Morss, 1976; Molloy, 2010). This is unlike the d-block elements (e.g., Ti, V, Cr) that exhibit a site preference that can be explained with crystal field theory (Burns, 1975).

Apatite is a common accessory mineral in igneous, metamorphic, and sedimentary rocks. It belongs to a much broader group termed the apatite supergroup minerals with the general formula ${}^{\text{IX}}\text{M}_1{}^{\text{VII}}\text{M}_2{}^{\text{IV}}\text{TO}_4)_3\text{X}$ ($Z=2$), which crystallize in the hexagonal crystal system with a space group of $\text{P6}_3/m$ (Pasero et al., 2010). Apatite typically occurs as $\text{Ca}_5(\text{PO}_4)_3(\text{F,Cl,OH})$ in nature as part of a ternary system consisting of fluorapatite (FAp), chlorapatite (CAp), and hydroxyapatite (HAp), respectively (Elliot, 2013). The M sites are occupied by Ca with Ca1 (IX-fold coordination) lying on a three-fold screw axis and having a multiplicity of 4, and Ca2 (VII-fold coordination) lying on a six-fold screw axis and having a multiplicity of 6 (Elliot, 2002; Hughes et al., 1991; Pasero, 2010). Substitutions at the M and T sites in apatite (i.e., ${}^{\text{IX}}\text{Ca}1^{2+}$, ${}^{\text{VII}}\text{Ca}2^{2+}$, ${}^{\text{IV}}\text{P}^{5+}$) are common, typically through coupled substitution (Figure 2.1) (Hughes et al., 1991; Elliot, 2002; Hughes and Rakovan 2015). Substitution involving vacancies at the M sites may also accommodate REEs in apatite (Fleet and Pan, 2002). Two examples of coupled substitutions involving REE (summarized by Rønsbo, 1989; Fleet and Pan 1995), and one example involving vacancies at the Ca site, may be expressed as follows:



Substitutions (1) and (2) have been supported by compositional data from natural REE-bearing apatites (e.g., Roeder et al. 1987; Rønsbo 1989; Comodi et al. 1999), and the substitution

in (3) has been noted as playing a minor role in REE accommodation in synthetic $\square\text{CaREE}_8(\text{SiO}_4)_6\text{F}_2$ and $\square_2\text{REE}_8(\text{SiO}_4)_6\square_2$ (Grisafe and Hummel, 1970; Fleet and Pan, 2002). Recent X-ray structural refinements reveal REE prefer the Ca2 site in FAp and site-occupancy ratios (REE-Ca2/REE-Ca1) decrease systematically with increasing atomic number of 4f lanthanides (Hughes et al., 1991; Fleet and Pan 1994; Fleet and Pan 1995; Fleet and Pan, 1997; Elliot, 2013). These substitutions are strongly influenced by changes in pressure (P), temperature (T), oxygen fugacity ($f\text{O}_2$) and the composition and structure (M_x) of the melt in which the apatite crystallized (e.g., Boudreau, 1995; Piccoli and Candela, 2002; Hovis and Harlov, 2010).

To better understand the incorporation and charge balancing of REEs in apatite, this study presents results for a suite of REE-doped (REE in this project consist of La, Nd, Sm, Dy, Er, and Y) fluorapatites synthesized (at fixed P and T) with either Si or Na added for charge balancing. The purpose of this investigation was to assess the following: 1) the effectiveness of the substitution mechanisms (1) and (2) above; and 2) the influence of melt composition versus crystal structure on the resulting apatite crystal chemistry.

2.2 EXPERIMENTAL METHODS

Microcrystalline apatite was synthesized by combining calcium phosphate ($\text{Ca}_3[\text{PO}_4]_2$) and fluorite (CaF_2), at a 3:1 molar ratio, in a 25 mL Pt crucible. The Pt crucibles were cleaned prior to use with concentrated HF and then concentrated HNO_3 , followed by deionized H_2O . The powder mixture was sintered in the “hot spot” of a Deltech MoSi_2 glass making (i.e., box) furnace at 950°C using a solid-state exchange reaction to produce microcrystalline fluorapatite following the method by Prener (1970) and Kreidler & Hummel (1970):



Using a type S control thermocouple, the temperature in the hot spot was measured to within ± 5 °C. After sintering for an hour, the crucible was removed from the furnace and left to cool in air.

The microcrystalline fluorapatite was then added to more fluorite at a ratio of 45:55 wt.%, respectively, and transferred back into the same 25 mL Pt crucible and into the hotspot of the box furnace at 950°C. The furnace was then set for a 3-step program: (i) a temperature ramp up to 1375°C at 250°C/hr; (ii) a dwell at 1375°C for 15 hrs; and (iii) a temperature ramp down to 1220°C at 3°C/hr to produce millimeter to centimeter sized apatite crystals. After the program was completed (~ 68 hr run time), the crucible was then removed and left to cool at room temperature. Apatite crystals embedded in the CaF₂ flux were removed manually, and any remaining flux was dissolved by repeated boiling in a 20% Al(NO₃)₃• 9H₂O_(aq), followed by a rinse with distilled H₂O. The Al(NO₃)₃ 9H₂O treatment was done for as short a time as possible to avoid any dissolution of the remaining apatite crystals.

The synthesis of the doped fluorapatites followed the aforementioned procedure, with the dopants added as multiples of their abundances in nature (e.g., 1x [100s of ppm], 10x [1000s of ppm] and 100x [10,000s ppm]) directly to the undoped mixture prior to synthesis (Table 2.1). The trace element composition of natural apatite (Roeder et al. 1987) was used as the baseline for REE contents. In order to resolve the shape of the REE distribution profile, elements from both LREE (La, Nd and Sm) and HREE (Dy, Er and Y) groups were added with either Na or Si in equal molar proportions. Yttrium was selected due to its similar ionic radius relative to Ho and Er. Syntheses were also done at variable LREE:HREE ratios in the starting flux mixture: LREE > HREE, LREE = HREE and LREE < HREE.

Evacuated silica tube syntheses were also done to limit potential Na volatility during fusion. These syntheses consisted of a 10% (i.e., 10% of the amount normally put in the Pt

crucible in the glass making furnace) by mass aliquot of the microcrystalline apatite + dopants mixture in a 2.5 cm length of Pt tubing. The Pt tubing was sealed at both ends and placed in a ~15 cm section of fused silica tubing. This section of silica tubing was then attached to a vacuum line, evacuated for ~1 hr, and later sealed with an oxy-acetylene torch. The resulting silica ampoule was then subject to the same run conditions as those in the 25 mL Pt crucible.

All starting materials were mixed in an agate mortar and pestle under ethanol and dried under a heat lamp, and subsequent analysis via powder X-ray diffraction was used to confirm the structure and composition of each apatite synthesis and the starting materials (microcrystalline apatite, calcium phosphate, and fluorite) (Figure A.1 to Figure A.10).

2.3 ANALYTICAL METHODS

2.3.1 Sample preparation

Five to ten euhedral apatite grains from each synthesis were picked and placed onto double sided tape, parallel to the *c*-axis when possible, then epoxy was poured over the grains in the form of a 25mm round Teflon mount. Once the epoxy polymerized, the mounts were gently ground using silicon carbide sand paper (P600 to P2000 grit) until the centers of the apatite grains were exposed. The mounts were then polished first with 3 μm diamond film, and finally with 1 μm alumina powder. The epoxy mounts were also trimmed on the back side to a thickness of 6 mm, and subsequently polished as described above, in order to be transparent for optical microscopy and to fit into the laser ablation sample cell. All grinding and polishing was done using water as a lubricant, and the mounts were thoroughly ultrasonicated between each step.

2.3.2 Scanning electron microscopy

Back-scattered electron (BSE) imaging was done using a JEOL JSM-7100F scanning electron microscope (SEM) with a field-emission source at Memorial University of

Newfoundland. Epoxy mounts containing apatite grains were coated with a ~20 nm (~200 Å) evaporated carbon film to prevent charge build up during imaging and analysis. An accelerating voltage of 15 kV was used during imaging and energy dispersive spectroscopy (EDS) analyses because it is a sufficient energy to produce characteristic X-ray emissions for all of the elements in question.

2.3.3 Bench-top cathodoluminescence

A bench-top optical microscope based system was used to acquire cathodoluminescence (CL) images on apatite grains in epoxy mounts at Memorial University of Newfoundland. The system consists of an Olympus BX50 binocular polarizing microscope, and a cold cathode electron gun that is focused on samples in a stainless steel chamber under relatively low vacuum (10 - 50 mTorr) (PATCO ELM-3). A KAPPA DX-30C Peltier cooled digital camera affixed to the microscope was used to capture the CL images, and each CL image was accompanied by an image of the same location on each sample in cross-polarized light. The CL images were all acquired using the same RGB settings in order to make the images comparable

2.3.4 Electron probe microanalysis

Apatite grains were analyzed for their major and minor element compositions at Memorial University of Newfoundland, using a JEOL JXA-8230 SuperProbe electron probe microanalyzer (EPMA) equipped with five tuneable wavelength-dispersive X-ray spectrometers (WDS). All mounts containing synthetic apatite grains were coated with a ~20 nm (~200 Å) evaporated carbon film to prevent charge build up during imaging and microanalysis. The analysis locations for the EPMA were precisely marked on back-scattered electron (BSE) and/or cathodoluminescence (CL) photomicrographs. Samples underwent initial wavelength scans and energy dispersive spectroscopy (EDS) to ensure that the proper elements were selected and

measured, to identify appropriate peak and background positions, and to identify interferences. Two traverses of five points each were done on each apatite grain, along and perpendicular to the c-axis, as guided by the BSE and/or CL images. Apatite grains were analyzed for F, Na, Si, P, and Ca (Table A.4). Analytical conditions were set as follows: an accelerating voltage of 15 kV; a Faraday cup current of 20 nA; and a defocused beam diameter of 10 μm . Count times were optimized to each element as follows: 120 s on peak and 60 s on background for Ca, P and Si; and 40 s on peak and 20 s on background for F and Na. The following natural mineral standards, provided by Astimex Standards Ltd., were used: ablite (Strickland Quarry, Haddam, CT, USA) for Na and Si; and apatite (Wilberforce, ON, Canada) for Ca and P. Fluorine was calibrated on a piece of natural topaz from Topaz Mountain, Utah (e.g., Henderson, 2011).

2.3.5 Laser ablation inductively coupled plasma mass spectrometry

Trace element concentrations of the apatites were determined using LA-ICPMS at the Mineral Analyses Facility – Bruneau Innovation Centre (MAF-IIC) at Memorial University of Newfoundland. The analyses were done using a Thermo-Finnigan ELEMENT XR, a high-resolution double focusing magnetic sector inductively coupled plasma mass spectrometer (HR-ICP-MS) coupled to a GEOLAS 193 nm Excimer laser ablation system. The ablated material was transported to the ICP-MS using He gas with a flow rate of 1.25 l/min, with additional Ar make-up gas added after the ablation cell and prior to introduction into the ICP-MS. A laser spot size of 40-70 μm , depending on the crystal analyzed, was used with an energy density of approximately 3 J/cm^2 , and a laser repetition rate of 8-10 Hz. Time-resolved intensity data were acquired by peak-jumping in a combination of pulse-counting and analog modes, depending on signal strength, with one point measured per peak.

The Ca concentrations determined by the EPMA on the synthetic apatite were used as internal standard to normalize counts to concentrations for the trace element LA-ICPMS analyses (i.e., ^{44}Ca). For primary calibration, the ~500 ppm National Institute of Standards in Technology (NIST) 610 glass was used (Pearce et al., 1997). Additional reference materials (i.e., secondary standards) were analyzed to assess the accuracy and precision of the LA-ICP-MS analyses. These included NIST 612 (~50 ppm) and the USGS reference basalt sample BCR-2G glass (Pearce et al., 1997), two fragments of apatite from Sludyanka, Russia; hereafter referred to as “MUN Sludyanka” (Dempster et al., 2003), and “JMH Sludyanka” (Figure A.1; Table A.1). The data acquisition methodology used an analytical sequence of two analyses of the NIST 610 glasses, one analysis of the NIST 612 or BCR-2G glass, one analysis of the external reference materials, followed by 14 analyses of the synthetic apatites, closing the sequence with a repetition of the external reference materials, followed by two analyses of the NIST 610 series glass.

The LA-ICPMS data were reduced using Iolite software (Paton, 2011). Iolite allows for selection of representative signal intervals, background subtraction, and internal standard correction for ablation yield differences, instrument sensitivity drift, mass bias and mass fractionation, during the analytical session, and does calculations converting count rates into concentrations by reference to the internal standard used (i.e., Ca from the EPMA).

2.3.6 Powder X-ray diffraction

All starting materials and synthetic apatites were analyzed by powder X-ray diffraction (XRD) using a Rigaku Ultima IV X-ray diffractometer at Memorial University of Newfoundland. Apatite crystals were handpicked to reduce interference with other phases (i.e., residual flux materials), and the aliquots were then ground into a powder using an agate mortar

and pestle under ethanol. The XRD used an incident X-ray beam using Bragg-Brentano geometry with CuK_α radiation (at 1.5406 Å) operated at 40 kV and 44 mA over a 2θ range of 5° to 70° at $0.015^\circ 2\theta$ per step in fixed time (FT) mode at a 2 second dwell time per step. All powders were run in triplicate, and averaged, manually unpacking and repacking the samples between each analysis, to reduce any bias in the measurement resulting from preferred orientation of the microcrystalline powders. Data processing was done using MDI JADE V9 (<http://www.materialsdata.com/>), which allows for plotting the diffraction patterns from each powder XRD analysis. The International Center for Diffraction Data (ICDD) database was used to identify the phases present and to index the apatite peaks for refinement of the unit cell parameters.

Unit cell parameters were calculated using UnitCell software, according to the method described by Holland and Redfern (1997), via regression analysis of powder diffraction data. To ensure the appropriate {hkl} reflection positions were chosen from the diffraction patterns, the multipeak fit v1.4 macro in IgorPro version 6 (www.wavemetrics.com) was used to fit the individual XRD peaks and deconvolve the $\text{K}_{\alpha 1}$ and $\text{K}_{\alpha 2}$ peaks. A Pseudo-Voigt function was used for fitting the peak positions for the $\text{K}_{\alpha 1}$ peaks which in turn were subsequently used for the unit cell refinements. To remain consistent, forty reflections in the range 5° - $70^\circ 2\theta$ were indexed by reference to the PDF#00-015-0876 ICDD (Natl. Bur. Stand. [U.S.] Monogr. 25, v3 p22 [1964]) card for synthetic FAp.

2.4 RESULTS

2.4.1 Run-product homogeneity

Homogeneity of the doped FAp grains was assessed qualitatively via BSE and CL, and quantitatively through EPMA and LA-ICPMS analyses to reveal any compositional zoning and

chemical variations within the crystals. The BSE images displayed no significant variation in BSE intensity throughout the grains (Figure 2.2-A and D), but overall grain brightness increased with increasing REE content (i.e., greater proportion of higher atomic number elements replacing Ca). Cathodoluminescence imaging, however, revealed weak sector and growth zoning with respect to REE (Figure 2.3- 1x REE + Si). Much like BSE, the CL activation was influenced by REE content in the apatite, seen as a progression from dark blue through to bright orange-red (Figure 2.3) as the dopant level increased. The bright orange and dull red luminescence (~600 to 645 nm) of the apatite grains is most likely a result CL activation by Sm^{3+} and Nd^{3+} , respectively, which intensifies with increasing REE content (Kempe and Götze, 2002).

Syntheses done with Na and Si doped at 100x natural concentrations produced a third REE-oxide component, which formed either as a separate crystalline phase (Figure 2.2- B and E), or as blebby (10 to 100 μm) inclusions (Figure 2.2- C and F) in the FAp grains. The REE-oxide crystals produced in syntheses 214 (Figure 2.2- B and E) and 217 (Figure 2.2- C and F) may in fact be two different forms of the same phase; either forming as standalone purple (in transmitted light microscopy) spheres in the residual flux (i.e., 214), or as blebby inclusions in the apatite (i.e., 217). This REE-oxide phase, in the latter, suggests REE saturation resulting in the crystallization of a primary REE_2O_3 phase (Table 2.1- synthesis 217) prior to the apatite crystallization (based on inclusions of the REE_2O_3 in the synthetic apatite crystals). Individual LA-ICPMS analyses yielded stable time resolved signals during ablation allowing for integration of nearly the entire ablation signal (Figure 2.4). Rare micro-inclusions of a slightly REE-enriched phase sometimes produced a peak of less than 2 seconds duration with elevated REE counts during ablation; however, these peaks were easily avoidable during the data reduction. The resulting trace element contents reveal little to no significant intra-grain variation in REE

content, suggesting homogeneous synthesized apatites (Figure 2.5). There is, however, some inter-grain variation between selected apatite grains for each respective synthesis (e.g., Table 2.2- synthesis 213: grain 1 and grain 2). That may be due to the surface area of the crystal that was analyzed. It was very difficult to polish each crystal to precisely expose the crystal center.

2.4.2 Synthetic apatite crystal chemistry

The, Ca, P, Si, and F values are reported from EPMA measurements, and all REE values are reported from LA-ICPMS measurements (Table 2.3). As an exception, the composition of the REE-oxide phases are reported entirely from the EPMA measurements (Table 2.3) due to their high concentrations of REEs. Note that the EPMA F measurements of the apatites are occasionally in excess of the stoichiometric value of 3.77 wt.%. This is likely a result of the apatite crystals in the mount not oriented perfectly parallel to *c*-axis, and increasing apparent F concentrations with time under the electron beam (e.g., Stormer, 1993; Henderson, 2011), or that the crystals incorporated an excess of F.

2.4.2.1 Set #1 syntheses: Effects of varying overall dopant level

The first set of experiments were done to assess the effect of systematically increasing the REE concentration in the flux on the resulting apatite crystal chemistry, via incremental doping at 1, 10, and 100 times the REE content reported for natural apatite (Roeder et al., 1987). This was done using Si (Set 1a: syntheses 212, 213 and 214) and Na (Set 1b: syntheses 215, 216 and 217) to determine which was more effective at charge balancing REEs in apatite. As was expected, the resulting REE concentrations in each synthesis were proportional to the amount of dopant added; however, the REE concentrations varied significantly between the syntheses charge balanced with Si and those charge balanced with Na, respectively (Figure 2.6- A and B).

Note that elemental REE concentrations are reported here, since there is no Oddo-Harkins effect, and in turn no need to normalize to chondritic values to smooth the data.

Regarding the trace element chemistry of FAp synthesized with Si, the total REE content (Σ REE) increases from an average of 100 ppm to 1800 ppm from 1x to 10x (syntheses 212 to 213), and to 32,000 ppm for the 100x (synthesis 214). This represents a 15-fold increase between each increment and a net 250-fold increase from 1x to 100x. The Si content of the FAp also increased with increasing REE content to charge balance the increase in REEs, from below 500 ppm at 1x to over 8,000 ppm Si at 100x. The incremental increase in REE content is evidenced by the stepwise increase in REE distributions, proportional to respective dopant level (Figure 2.6- A).

Syntheses charge balanced with Na, however, displayed a less noticeable increase in Σ REE content, from 100 ppm to over 1000 ppm from 1x to 10x (syntheses 215 to 216), then to 5000-6000 ppm from 10x to 100x (syntheses 216 to 217). This represents a 10-fold and 5-fold increase, respectively, with a net 75-fold increase in Σ REE from 1x to 100x. The REE distributions for the Na-doped syntheses display a lesser increase in Σ REE content with increasing dopant quantity compared to the Si-doped syntheses (Figure 2.6- B), with the 100x Na-doped apatite containing five times less REE than the equivalent Si-doped apatite.

Collecting reliable measurements of Na in apatite came with two main challenges: 1) the high background levels and poor ionization efficiency made measurements via LA-ICPMS unsuitable (Shepherd and Chenery, 1995); and 2) the low levels of Na in the apatite grains were below detection limits (28 ppm for most measurements; Table A.4) for EPMA under the conditions used. As a result, the only Na values measured via EPMA were those doped at 100x natural content (synthesis 217), with an average Na concentration of 170 ppm. Although, this

one measurement of Na is still two orders of magnitude less than the Si content of the Si-doped apatites synthesized at the same REE dopant level (i.e., 100x).

2.4.2.2 Set # 2 syntheses: Effects of varying dopant LREE : HREE ratio

The goal of this set of syntheses was to evaluate the influence of variable proportions of LREE and HREE in the melt on the crystal chemistry of the synthesized apatites. To accomplish this, a suite of three syntheses were done at 20x natural concentrations with Si, and REE, added, in molar proportions, as LREE > HREE (synthesis 227), LREE = HREE (synthesis 235) and LREE < HREE (synthesis 236). 20x natural concentrations were used for these three syntheses in order to: 1) ensure that enough of the LREE and HREE were incorporated in the apatite crystals to be analyzed by the EPMA and LA-ICPMS with minimal uncertainties; and 2) to add more data to Figure 2.6, Figure 2.7, and Figure 2.8, with concentrations greater than 10x natural concentrations but not so high as to induce REE saturation and cause REE-oxides to precipitate (i.e., 100x). The resulting REE concentrations for each synthesis reflect the melt LREE:HREE ratios (Figure 2.6- C), with opposing REE distributions between synthesis 227 and 236. However, 227 shows a strong LREE enrichment, whereas 236 yields a more subtle HREE enrichment. The difference between these profiles is due to the compatibility of the LREE in the larger Ca sites in the apatite structure, relative to the smaller HREE (Fleet and Pan, 1995). This is demonstrated by the much greater La:Er ratio of ~30 in apatite from synthesis 227 (LREE > HREE), compared to a ratio of ~0.5 for synthesis 236 (LREE < HREE). Represented graphically in Figure 2.6-C as a steep decline and a shallow incline, respectively. Apatite from synthesis 235 (LREE = HREE) exhibits a REE curve with a similar shape to those mentioned in the previous section. This was expected since the synthesis was done with Si and equal proportions of LREE

and HREE; hence, it falls in between the 10x and 100x syntheses when comparing Figure 2.6 A and C.

These experiments are also an excellent example of Goldschmidt's first and second rules, because all REE are within 1 to 10% of the ionic radii of the host Ca1 and Ca2 cations residing in the M sites of the crystal structure (i.e., from La to Er), and all REE are in a 3+ oxidation state during synthesis, so preferential accommodation is given to the ion with the more compatible ionic radius (i.e., La preferred over Er in the apatite structure). Despite the differences in the REE concentrations between the two syntheses, both 227 and 236 yield a Σ REE content between 1000 ppm to 1500 ppm. These concentrations are similar to those of the equally doped synthesis, 213, at 10x with Si. The \sim 1000 ppm Σ REE content of the syntheses done with uneven proportions of LREE and HREE is tripled in the apatite from the LREE = HREE synthesis, synthesis 235, at over 5000 ppm. Neither of the apatites from the LREE > HREE or LREE < HREE syntheses yield individual REE concentrations in excess of the apatite from the LREE = HREE synthesis (Figure 2.6-C), resembling an upper limit for individual REE incorporation in apatite despite being in different proportions in the starting materials.

2.4.2.3 Set # 3 syntheses: Assessment of Na and Si volatility

To assess potential volatilization of Na and Si from the melt in the unconfined Pt crucible during fusion at high temperature, syntheses 288_2 and 289_2, doped at 20x nature with Si and Na, respectively, were done in Pt tubing in an evacuated silica tube assembly as described above. These syntheses were done to determine the extent of Na volatility during the apatite synthesis.

It was assumed that the volatility of Na during synthesis explains the lower concentration of REE that were incorporated in the REE + Na apatites than in the REE + Si apatites. The Si-doped synthesis (288_2) produced apatite with a homogenous Σ REE and SiO₂ content of 15,800

ppm and 0.8 wt. %, respectively (Figure 2.6-D). These REE and Si contents exceed those of the equivalent synthesis done in the Pt crucible at 20x REE with Si (Synthesis 235) (Table 2.2; Figure 2.6-C). The Na-doped evacuated silica tube synthesis (289_2) did yield a slight increase in the Na content of 100 ppm Na, compared to the previous syntheses that contained Na contents below the EPMA detection limits (Table A.4). The apatite Na₂O content of 0.01 wt.% at 20x in the evacuated silica tube is similar to that of the Pt crucible apatite growth REE + Na in synthesis 217, doped at 100x nature; therefore, considering the difference in dopant levels, the evacuated silica tube synthesis did yield a relative increase in Na content in apatite. Unfortunately, the 289_2 apatite also contains anomalously high Si, in excess of 1 wt.%, despite the fact that the synthesis was run with no Si in the starting mixture. The low content of Si in other Na-doped apatites—grown from similar starting mixtures as 289_2—suggests no significant Si contamination in the starting reagents. Hence, this is likely a result of addition of Si in vapor phase to the melt during fusion via the surrounding silica tube. Furthermore, the apatite from synthesis 289_2 exhibits extreme inter-grain heterogeneity, with the two grains selected for analysis varying considerably in Si and ΣREE content (Table 2.2- synthesis 289_2: grain 1 and grain 2).

The resulting ΣREE concentrations of the apatites grown from evacuated silica tubes differ from those grown in the Pt crucible. This indicates a shift in the REE incorporation when confined to the evacuated silica tube assembly. Instead of the typical systematic decrease from LREE to HREE content seen in the apatites from the Pt crucible growths, apatite from synthesis 289_2 exhibits a sinusoidal enrichment, with lower concentrations at La and Er (Figure 2.6-D). Despite the compositional heterogeneities between the REE + Na evacuated silica tube syntheses, the shape of the REE curve remains consistent between each apatite grain.

2.4.3 Unit cell refinement of synthetic apatites

In order to assess the structural properties of the synthetic apatites in this study, unit cell constants were determined from powder X-ray diffraction (XRD) data (Table 2.4). The purpose of the unit cell refinements was to identify changes in the unit cell parameters (i.e., a -axis, c -axis and unit cell volume) with increasing dopant content of synthetic apatite, related to the REE and Si or REE and Na substitution. The preferential substitution of LREE over HREE in natural apatite yields an increase in the unit cell volume (Hughes et al., 1991). This relationship is due to the ionic radius, R^{3+} , of a substituting LREE being greater than that of the host R^{2+} of Ca^{2+} at 1.180 Å and 1.06 Å, respectively (ionic radii from Shannon, 1976; Fleet and Pan, 1995).

The synthetic apatite unit cell parameters in this study vary significantly with respect to the REE and Si contents (Figure 2.7- A; Table 2.4). The unit cell volume increased from $522.81 \pm 0.03 \text{ \AA}^3$ for the undoped apatite (synthesis 211) to $526.41 \pm 0.04 \text{ \AA}^3$ for the 100x REE + Si doped apatite (synthesis 214) (Table 2.4). This increase in cell volume is the result of a mutual increase in the lengths of the a - and c -axes of the apatite crystal structure from syntheses 211 and 214 (Table 2.4). There is a systematic increase in cell volume with increasing Si content (Figure 2.7- B), reflecting the effect of the larger Si substituting for P in the apatite structure and the increase in REEs substituting for Ca. The Na-doped apatites, however, display a less pronounced increase in unit cell volume, remaining near the same size as the undoped apatite at 1x and 10x, with a jump to $524.26 \pm 0.03 \text{ \AA}^3$ at 100x. This is related to a lower accommodation of REEs due to the limited amount of Na that incorporated in the apatite structure to charge balance the REEs.

Perhaps the most significant variation in unit cell volumes can be observed in the apatites doped at different LREE:HREE with Si at 20x, exhibiting a systematic increase in cell volume from LREE < HREE ($523.99 \pm 0.03 \text{ \AA}^3$), to LREE = HREE ($524.51 \pm 0.03 \text{ \AA}^3$) and LREE > HREE

($524.59 \pm 0.03 \text{ \AA}^3$). This increase is proportional to the concentration of LREE relative to HREE; hence, showing a strong correlation with the La:Er ratio in Figure 2.7- C.

2.5 DISCUSSION

2.5.1 Controls on apatite REE crystal chemistry

The variability in apatite composition among the syntheses in this study yields important insights into the crystal-chemical and melt composition controls on cation substitution. The composition of a mineral growing in a melt are controlled by: 1) the composition and structure of the liquid (Watson, 1976); or 2) a crystal-chemical structural control (Ryerson, 1978). In the present case, the apatite chemistry may be controlled by either the apatite crystal structure, the composition and structure of the melt in which it grew, or both. More recent investigations regarding apatite/melt partitioning, such as the work done by Prowatke and Klemme (2006) summarize this concept. However, they also state the influence of crystal structure on the OHAp-melt partition coefficients is negligible in their experiments given the low concentrations of Na, Si, and REE trace element concentrations. Conversely, the current study reveals potential structural controls on REE substitution at high concentrations of Na, Si, and REE.

2.5.1.1 Charge balancing REE in apatite

The crystal chemistry of the synthetic apatite grains from each group of syntheses (i.e., set 1 to 3) reveals a relationship between REE substitution in apatite with increasing REE and Si content of the melt. Firstly, there is a systematic increase in REE content in the synthetic apatite as the REE content of the melt increases. Secondly, the syntheses with Si have a greater ΣREE content compared to those with Na as the substituent balancing the replacement of Ca^{2+} by REE^{3+} . This suggests that Si was more effective at charge balancing REEs in apatite using the

experimental conditions presented here, assuming that the Na did not volatilize and remained in the system for the duration of the synthesis.

There are examples of Na remaining in a silicate melt during high-T fusion, such as the example of haplo-andesite (i.e., Fe free) Na-bearing glass syntheses (Míková et al., 2009). These anhydrous glasses were fused three times for two hours each at 1450°C, over 100°C higher than these apatite syntheses, and the Na contents were very close (within 10% r.s.d., of the 3.5% Na₂O) to the nominal starting composition (Míková et al., 2009).

That study, as well as a single-crystal diffraction X-Ray refinement study on synthetic REE and Na substituted FAp (e.g., Mayer, 1974, 1983), however, bear little relevance to the current study given the low Na content of the apatites presented here and the experimental conditions used. The study done by Fleet and Pan (1995) on synthetic Na-doped FAp report concentrations of Na exceeding 1 wt.%; however, these experiments were run in a cold seal hydrothermal apparatus heated to ~900°C at pressures of ~0.15 GPa. These conditions are far different from those presented here, at higher temperature and at atmospheric pressure (~0.1 MPa).

The lack of using relatively high-pressure equipment in the present study may have limited the ability of the synthetic apatite incorporate Na into its structure. Also, the un-geologic (i.e., very different from a silicate melt) composition and structure of the fluorite flux that was used may also have influenced the ability for the synthetic apatites to incorporate Na into their structure. The presence of Na (several thousand parts per million; e.g., Roeder et al., 1987; Rønsbo, 1989; Comodi et al., 1999) in natural apatites suggests that something in the synthesis method may be limiting Na incorporation. Given that the rock types from Rønsbo (1989) are derived from peralkaline melts, they resemble the closest geological analogue to the fluorite melt

used to synthesize the apatites in present study. Rønsbo (1989), reports apatite compositions from a sodalite foyaite and a peralkaline pegmatite with Na₂O concentrations between 0.7 wt.% to 3.1 wt.% for Na-bearing, REE-enriched apatite. However, the same study also reports Na₂O concentrations of 0.15 wt.% for Na-poor, REE-enriched apatite from the sodalite foyaite. The lesser Na content of the Na-poor, REE-enriched apatite is associated with a higher SiO₂ concentration. The experiments presented in the current study are similar to the latter, except they lack an associated Si-enrichment because there was no Si in the Na-doped starting reagents. This suggests that differences in the partitioning behaviour of Na in apatite between the natural and synthetic melt composition, although unconstrained, may be limiting Na uptake by the synthetic apatites. In addition to the composition and structure of the flux that was used, the experimental conditions (i.e., P, T and fO_2) in which the apatites were synthesized, or simply the incompatibility of Na to fit into the apatite structure, or the volatility of Na during synthesis, or a combination of those factors, could have contributed to precluding Na from effectively being able to charge balance the REEs in these experiments. The role of Na in charge balancing REE substitution in the synthetic apatite is at present poorly understood and requires further investigation.

However, since the main objective in the present study was to compare the charge-balancing efficiency of Si and Na for charge balancing REEs under identical experimental conditions this comparison is still valid.

The inhibition of Na incorporation in the synthetic Fap in the present study may also be due to the fact that Na⁺ and REE³⁺ both compete for a Ca1 and Ca2 structural site in equation (2) and possibly the site preference for Na in apatite may be more compatible than for the REE. Published unit cell refinements reveal a systematic decrease in the site occupancy ratio (REE-

Ca2 / REE-Ca1) in apatite with increasing atomic number of 4f lanthanides (Fleet and Pan, 1994, 1995, 1997). The later work done by Fleet and Pan (1997) regarding the site preference of REE in binary-REE (LREE + HREE) doped FAp shows a discrepancy between single-REE doped FAp as a result of non-ideal mixing of LREE and HREE. Although still exhibiting a monotonic decrease, the resulting site occupancy ratios for binary-REE doped FAp are smaller than the single-REE doped FAp. Since the apatites presented here are multi-REE doped, from La to Er, it is difficult to assess which site is preferred by the REEs, and given the nature of the coupled substitution with Na it complicates which site is available to the entering cation since both Na and REEs may substitute at the Ca1 and Ca2 sites. Further, the larger 1.12 Å and 1.24 Å ionic radii of Na⁺ in VII-fold and IX-fold, respectively, are not well suited to either the 1.06 Å VII-fold Ca2 site or the 1.18 Å IX-fold Ca1 site.

The Si⁴⁺ for P⁵⁺ and REE³⁺ for Ca²⁺ exchange in equation (1) above describes a substitution mechanism for the entering REE and Si. There is, however, a discrepancy in the Si:REE ratio for these apatites, which ideally should be 1:1, according to equation (1). This may be a result of accommodation of REE involving vacancies at the Ca site, via the substitution mechanism presented in equation (3). The incorporation of REE in apatite involving vacancies at the Ca site has been reported by Grisafe and Hummel (1970) for synthetic □CaREE₈(SiO₄)₆F₂. Although the synthetic apatites presented in the present study do not represent end-member compositions, vacancies at the Ca site may still play a role in accommodating REEs.

Unit cell parameters suggest that the substitution of the larger 0.26 Å Si⁴⁺ ion for the smaller resident 0.17 Å P⁵⁺ in IV-fold coordination ion induces a compounded increase in cell volume with progressive LREE coupled substitution (Table 2.4) (ionic radii from Shannon, 1976). This is seen in natural apatite in the case of britholite ([RE₃Ca₂][(SiO₄)₃](OH,F)]

(Oberti et al., 2001). The substitution of a LREE for Ca and Si for P extends the unit cell edges (i.e., a and c axes) and yields an increase in cell volume from 526.03 \AA^3 for natural end-member fluorapatite (Hughes et al., 1991) to 562.25 \AA^3 for britholite (Oberti et al., 2001). Compared to the data presented in this study, the unit cell volume for synthesis 214 is close to the volume for natural fluorapatite from Hughes et al. (1991), which is also similar to the cell parameters reported by Fleet (1995) for synthetic Nd- and Gd-FAp, at 527.71 \AA^3 and 525.36 \AA^3 , respectively.

The trace concentrations of Si in the Na doped apatites suggest a Si impurity in the starting reagents. The increase in Si content in the Na-doped apatites, from 150 ppm at 1x to 500 ppm at 100x, most likely represents progressive scavenging of the small amount of Si present in the starting reagents. This minor Si component may play a significant role in limiting Na incorporation, and inducing REE incorporation through coupled substitution with Si. To address the question of which starting material contained Si, a separate mount was made with portions of the starting material powders used to synthesize the apatites, and subsequently analyzed for Si using the JEOL JXA-8230 Superprobe EPMA (Table A.2). High resolution WDS scans were done prior to the quantitative analyses, on both sides of the Si $K\alpha$ peak, on all materials. The detection limit for wavelength scans is not as low as proper quantitative WDS measurements; however, this technique revealed a Si peak in the calcium phosphate ($\text{Ca}_3[\text{PO}_4]_2$) starting material (Figure A.12). Subsequent quantitative analyses confirmed the presence of Si in the calcium phosphate. The detection limit for Si for the conditions used for the analyses was ~ 20 ppm, which was well below the measured concentrations of 400 ± 20 ppm Si in the calcium phosphate. Hence, this contamination explains the presence of Si in the REE + Na- doped experiments.

The presence of the excess REE₂O₃ phase produced in the syntheses doped at 100x (214 and 217) also provides physical evidence that suggests Si⁴⁺ is more effective than Na⁺ at charge balancing REEs in apatite. Both syntheses done at 100x with Si (214) and Na (217) produced a REE₂O₃ precipitate from the flux during the apatite syntheses. However, only the syntheses charge balanced with Na (217) produced the REE₂O₃ phase as inclusions within the residual flux and in the apatite crystals (e.g., Figure 2.2- C). In synthesis 214, there are also 200-500 μm euhedral purple REE₂O₃ spheres mixed in with the apatite crystals (these were separated from the apatite using methylene iodide in a 100 mL separatory funnel). By inspection these constitute a smaller proportion of REE-oxide than the REE₂O₃ inclusions in the apatite crystals and residual flux of synthesis 217. This is consistent with the EPMA data showing that in the presence of Si the apatite from synthesis 214 were able to accommodate a greater concentration of REE than in synthesis 217. In turn, the greater remaining concentration of REE in the melt for synthesis 217 allowed for more REE-oxide to precipitate.

LA-MC-ICPMS data for the REE₂O₃ spheres reveal that they are isotopically homogenous with respect to Sm and Nd (JM Hanchar and CM Fisher, 2013 unpub. data). They are also compositionally HREE-enriched (Table 2.3), in contrast to the coexisting LREE-enriched apatite, suggesting precipitation post-apatite crystallization from a LREE depleted melt. The HREE-enriched composition seems reasonable given that apatite preferentially incorporates more LREE into its structure. In the case of synthesis 214, the apatite consumed its maximum amount of REEs, leaving behind a relatively LREE depleted melt from which the REE-oxides would later precipitate.

2.5.1.2 Effect of melt composition vs. crystal structure

The syntheses at REE dopant levels 20x those found in nature with Si and variable LREE:HREE ratios tested the effects of melt composition versus structural controls on apatite crystal chemistry. In theory, if the crystal structure wholly controlled the REE incorporation, the resulting REE profile would match that of the syntheses doped in equal proportions; whereas, complete melt control would yield apatite with same REE profile as the bulk composition. The results show that neither the crystal structure or melt composition wholly control apatite REE crystal chemistry.

The REE profiles in Figure 2.6-C illustrate the tendency for apatite to preferentially incorporate LREEs due to the similarity in ionic radii to that of the host Ca1 and Ca2 cations. This yields a heightened LREE enrichment relative to HREE and a suppressed HREE enrichment relative to LREE. Hence, the La : Er ratios of 35 and 0.5 for syntheses with LREE > HREE and LREE < HREE, respectively. Although each apatite composition mimics the melt composition from which it grew, the apatite structure introduces a crystal chemical control on the resulting REE profile. Further, synthesis 235, done at a 1:1 LREE:HREE ratio, suggests a maximum site occupancy in apatite at a given melt composition for individual REEs which neither synthesis at variable LREE:HREE ratios surpasses (Figure 2.6- C).

2.5.1.3 Comparison to natural apatite data

As mentioned above, the crystal chemistry of apatite is strongly influenced by the melt composition in which it formed making apatite an excellent proxy for tracing the geochemical conditions at time of crystallization, provided that crystal structure control are taken into account (Piccoli and Candela, 2002; Pan and Fleet, 2002). This is revealed here by the relationship

between the REE profiles for some natural apatites and selected synthetic apatite samples (Figure 2.8).

The natural apatite samples chosen for this comparison are from Mineville, New York (magnetite-apatite [MtAp] ore) (Roeder et al., 1987; Foose and McLelland, 1995; Valley et al., 2009; 2010); Sludyanka, Siberia, Russia (Skarn) (Gillen and Rundqvist, 1997); and Mud Tank, Australia (Carbonatite) (Currie et al., 1992). There are similarities between the natural samples and the syntheses in the present study in which LREE are equal to, and in excess, of the HREE (Figure 2.8). However, none of the natural samples corresponded to the synthetic apatite grains, in which HREE are in excess of LREE. As discussed above, the preferential incorporation of LREE in apatite explains the similarity between natural and synthetic apatites. Natural apatite in which the HREEs are enriched relative to LREEs, suggests a fluid or melt depleted in LREEs through precipitation of a separate LREE-enriched phase (e.g., monazite; $[\text{LREE,Th,Ca}][\text{P,Si}]\text{O}_4$) prior to crystallization of apatite. There are cases in which apatite concentrates HREEs, however, such as the apatite from the Sogwe Hill Carbonatite, Malawi (Broom-Fendley et al., 2017). Although, the HREE are usually concentrated in other HREE-bearing phases, such as xenotime ($[\text{HREE,Zr,U}][\text{P,Si}]\text{O}_4$) in carbonatites (e.g., HREE-enriched xenotime from The Lofdal Carbonatite Complex, Namibia; Wall et al., 2008). Depletion of LREE in apatite may also occur through metasomatism via hydrothermal fluids, where the LREE are stripped out of apatite and re-deposited as other REE-rich phases in complexes with F or Cl (Harlov, 2015). The composition of post-alteration apatite should in turn be relatively enriched in HREE. Such is the case in apatite from the MtAp deposits at Kiirunavaara, Northern Sweden, with monazite forming as inclusions and along grain boundaries in apatite as result of mobilized LREEs via Cl-rich fluids during metasomatism (e.g., Harlov et al., 2002).

The geologic environments from which the natural apatites were sampled represent a robust, albeit limited, suite for comparison between the synthetic apatites in this study, with deeper insights into the importance of charge balancing. Firstly, the Mud Tank apatite yields a clear LREE enrichment with respect to HREE, similar to the LREE > HREE synthesis, which is expected from apatite sourcing a highly differentiated (LREE enriched) carbonatitic melt (Currie, et al., 1992). Secondly, the Mineville apatite has exceptionally high REE content (the greatest REE content ever reported at the time of publication) (Roeder et al., 1987), plotting above all other samples on Figure 2.8. The concentration of REE in the Mineville samples is close to the predicted value from the present experiment suite if a starting composition was prepared with 500x natural levels of REE. They also contain over 2 wt.% SiO₂ (Roeder et al., 1987; Chapter 3 of the present study), making them an excellent analogue to the experiments of this study charge in which REE substitution was charge balanced with Si.

It is important to note, however, there are several other factors influencing REE crystal chemistry of the natural apatite samples since they crystallized from far more complicated systems (e.g., at variable P, T and M_x), which have experienced convoluted magmatic evolution and post-crystallization alteration processes, compared to the synthetic apatites presented here. For example, the effects of metasomatism caused by the infiltration of hydrothermal fluids on REE crystal chemistry is not considered in the synthetic apatites presented here; however, the influence of subsolidus reactions may greatly alter apatite REE composition (e.g., Mineville apatite; Foose and McLelland, 1995).

The work conducted by Rønsbo (1989) on Na, Si and REE enriched apatites from late Precambrian syenites and a peralkaline pegmatite from the Ilímaussaq Intrusion, South Greenland, laid the framework for mechanisms (1) and (2) above. Rønsbo presents a 1:1 inverse

relationship (i.e., slope of -1) between Si + REE and P + Ca atoms per formula unit (apfu) through substitution by equation (1), and a relationship exactly half that (i.e., slope of -1/2) through substitution by equation (2). Figure 2.9 shows the molar sum of REE + Si against that of Ca + P for both the present synthetic apatites and the Mineville apatite. Figure 2.9 confirms that the substitution mechanism expressed in equation (1) operates in both the present synthetic apatites and the Mineville samples and confirms the former represent valid analogues of the latter.

2.6 CONCLUSIONS

The sensitivity of apatite composition to changing environments in which it crystallizes makes it an excellent proxy for determining the environmental conditions at the time of crystallization. This study demonstrates that the REE crystal chemistry of apatite varies greatly with the availability and effectiveness of charge balancing cations. The strong correlation between Si and REE content of the apatites synthesized in the presence of Si suggests that charge balancing REEs in apatite with Si via equation (1) is the more effective coupled substitution mechanism for the experimental conditions used. Lesser Na contents in REE and Na-doped apatites indicate an inhibition to the incorporation of Na; therefore, coupled substitution via equation (2) is an ineffective mechanism for charge balancing REEs at the experimental conditions presented here. The inhibition for the incorporation of Na in the synthetic apatite may be due to the un-geological melt composition, the experimental conditions (i.e., P, T and fO_2) in which the apatites were synthesized, or simply the incompatibility of Na to fit into the apatite structure, or the volatility of Na during synthesis, or a combination of those factors. The role of Na in charge balancing REE substitution in the synthetic apatite is at present poorly understood and requires further investigation..

Rare earth element contents of the starting melt composition are reflected in the synthetic apatite REE composition. However, the large Ca1 and Ca2 sites in apatite imposes a crystal chemical structural control preferentially concentrating LREEs. This suggests the resulting crystal chemistry of apatite is controlled by both melt composition and structure and the selectivity of apatite crystal chemistry.

Unit cell refinements reflect the influence of progressive substitution of Si for P in apatite, and REE for Ca as an increase in unit cell volume proportional to Si and REE content of the synthetic apatite. Further, apatite unit cell refinements demonstrate the effect of the monotonic decrease in REE ionic radius as an increase in apatite unit cell volume proportional to the LREE:HREE content ratio in apatite (i.e., more LREEs yield a larger cell volume).

Comparison between synthetic apatites to natural apatites from selected apatite localities supports the substitution mechanism in equation (1).

2.7 REFERENCES

- Anders, E., & Grevesse, N. (1989). Abundances of the elements: Meteoritic and solar. *Geochimica et Cosmochimica Acta*, 53, 197-214.
- Boudreau, A., Love, C., & Prendergast, M. (1995). Halogen geochemistry of the Great Dyke, Zimbabwe. *Contributions to Mineralogy and Petrology*, 122, 289-300.
- Burns, R. G. (1975). Crystal field effects in chromium and its partitioning in the mantle. *Geochimica et Cosmochimica Acta*, 39, 857-864.
- Comodi, P., Liu, Y., Stoppa, F., & Woolley, A. (1999). A multi-method analysis of Si-, S- and REE-rich apatite from a new find of kalsilite-bearing leucitite (Abruzzi, Italy). *Mineralogical Magazine*, 63, 661-661.
- Cotton, F. A., Wilkinson, G., Murillo, C. A., Bochmann, M., & Grimes, R. (1988). *Advanced inorganic chemistry*. Wiley: New York. 1-1376.
- Currie, K., Knutson, J., & Temby, P. (1992). The Mud Tank carbonatite complex, central Australia—an example of metasomatism at mid-crustal levels. *Contributions to Mineralogy and Petrology*, 109, 326-339.
- Dempster, T., Jolivet, M., Tubrett, M., & Braithwaite, C. (2003). Magmatic zoning in apatite: a monitor of porosity and permeability change in granites. *Contributions to Mineralogy and Petrology*, 145, 568-577.
- Elliott, J. C. (2013). Structure and chemistry of the apatites and other calcium orthophosphates. Amsterdam: Elsevier. 1-404
- Elliott, J., Wilson, R., & Dowker, S. (2002). Apatite structures. *Advances in X-Ray Analysis*, 45, 172-181.

- Fleet, M. E., & Pan, Y. (1994). Site preference of Nd in fluorapatite [Ca₁₀(PO₄)₆F₂]. *Journal of Solid State Chemistry*, 112, 78-81.
- Fleet, M. E., & Pan, Y. (1995). Site preference of rare earth elements in fluorapatite. *American Mineralogist*, 80, 329-335.
- Fleet, M. E., & Pan, Y. (1997). Site preference of rare earth elements in fluorapatite: Binary (LREE HREE)-substituted crystals. *American Mineralogist*, 82, 870-877.
- Foose, M. P., & McLelland, J. M. (1995). Proterozoic low-Ti iron-oxide deposits in New York and New Jersey: Relation to Fe-oxide (Cu–U–Au–rare earth element) deposits and tectonic implications. *Geology*, 23, 665-668.
- Gillen, C., & Rundqvist, D. (1997). Precambrian ore deposits of the East European and Siberian cratons. Amsterdam: Elsevier.1-457
- Goldschmidt, V. M. (1926). Die gesetze der krystallochemie. *Naturwissenschaften*, 14, 477-485.
- Grisafe, D., & Hummel, F. (1970). Crystal chemistry and color in apatites containing cobalt, nickel, and rare-earth ions. *American Mineralogist*, 55, 1131-1145.
- Harlov, D. E. (2015). Apatite: A fingerprint for metasomatic processes. *Elements*, 11, 171-176.
- Harlov, D. E., Andersson, U. B., Förster, H., Nyström, J. O., Dulski, P., & Broman, C. (2002). Apatite–monazite relations in the Kiirunavaara magnetite–apatite ore, northern Sweden. *Chemical Geology*, 191, 47-72.
- Henderson, C. (2011). Protocols and pitfalls of electron microprobe analysis of apatite. Unpublished MSc, The University of Michigan.
- Holland, T., & Redfern, S. (1997). Unit cell refinement from powder diffraction data: the use of regression diagnostics. *Mineralogical Magazine*, 61, 65-77.

- Hovis, G. L., & Harlov, D. E. (2010). Solution calorimetric investigation of fluor-chlorapatite crystalline solutions. *American Mineralogist*, 95, 946-952.
- Hughes, J. M., Maryellen, M., & Mariano, A. N. (1991). Rare-earth-element ordering and structural variations in natural rare-earth bearing apatites. *American Mineralogist*, 76, 1165-1173.
- Hughes, J. M., & Rakovan, J. F. (2015). Structurally robust, chemically diverse: apatite and apatite supergroup minerals. *Elements*, 11, 165-170.
- Kempe, U., & Götze, J. (2002). Cathodoluminescence (CL) behaviour and crystal chemistry of apatite from rare-metal deposits. *Mineralogical Magazine*, 66, 151-172.
- Kreidler, E. R., & Hummel, F. (1970). The crystal chemistry of apatite: structure fields of fluor- and chlorapatite. *American Mineralogist*, 55, 170-184.
- Linnen, R., Samson, I., Williams-Jones, A., & Chakhmouradian, A. (2014). Geochemistry of the rare-earth element, Nb, Ta, Hf, and Zr deposits. In H. Holland, K. Karl Turekian & S. Scott (Eds.), *Geochemistry of Mineral Deposits* (Second ed., pp. 543-568). Elsevier-Pergamon, Oxford: Elsevier Ltd.
- Mayer, I., & Cohen, S. (1983). The crystal structure of $\text{Ca}_6\text{Eu}_2\text{Na}_2(\text{PO}_4)_6\text{F}_2$. *Journal of Solid State Chemistry*, 48, 17-20.
- Mayer, I., Roth, R., & Brown, W. (1974). Rare earth substituted fluoride-phosphate apatites. *Journal of Solid State Chemistry*, 11, 33-37.
- Míková, J., Košler, J., Longenrich, H. P., Wiedenbeck, M., & Hanchar, J. M. (2009). Fractionation of alkali elements during laser ablation ICP-MS analysis of silicate geological samples. *Journal of Analytical Atomic Spectrometry*, 24, 1244-1252, doi: 10.1039/b900276f.

- Molloy, K. (2013). 9 - Octahedral Complexes. *Group Theory for Chemists (Second Edition)* (pp. 97-108) Woodhead Publishing. doi:<https://doi.org/10.1533/9780857092410.3.97>
- Morss, L. R. (1976). Thermochemical properties of yttrium, lanthanum, and the lanthanide elements and ions. *Chemical Reviews*, 76, 827-841.
- Oberti, R., Ottolini, L., Della Ventura, G., & Parodi, G. C. (2001). On the symmetry and crystal chemistry of britholite: New structural and microanalytical data. *American Mineralogist*, 86, 1066-1075.
- Pan, L., Huang, X., Li, J., Wu, Y., & Zheng, N. (2000). Novel Single-and Double-Layer and Three-Dimensional Structures of Rare-Earth Metal Coordination Polymers: The Effect of Lanthanide Contraction and Acidity Control in Crystal Structure Formation. *Angewandte Chemie*, 112, 537-540.
- Pan, Y., & Fleet, M. E. (2002). Compositions of the apatite-group minerals: substitution mechanisms and controlling factors. *Reviews in Mineralogy and Geochemistry*, 48, 13-49.
- Pasero, M., Kampf, A. R., Ferraris, C., Pekov, I. V., Rakovan, J., & White, T. J. (2010). Nomenclature of the apatite supergroup minerals. *European Journal of Mineralogy*, 22, 163-179.
- Paton, C., Hellstrom, J., Paul, B., Woodhead, J., & Hergt, J. (2011). Iolite: Freeware for the visualisation and processing of mass spectrometric data. *Journal of Analytical Atomic Spectrometry*, 26, 2508-2518.
- Pearce, N. J., Perkins, W. T., Westgate, J. A., Gorton, M. P., Jackson, S. E., Neal, C. R., et al. (1997). A compilation of new and published major and trace element data for NIST SRM

- 610 and NIST SRM 612 glass reference materials. *Geostandards Newsletter*, 21, 115-144.
- Piccoli, P. M., & Candela, P. A. (2002). Apatite in igneous systems. *Reviews in Mineralogy and Geochemistry*, 48, 255-292.
- Prener, J. (1967). The Growth and Crystallographic Properties of Calcium Fluor- and Chlorapatite Crystals. *Journal of the Electrochemical Society*, 114, 77-83.
- Prowatke, S., & Klemme, S. (2006). Trace element partitioning between apatite and silicate melts. *Geochimica et Cosmochimica Acta*, 70, 4513-4527.
- Roeder, P. L., MacArthur, D., Ma, X., Palmer, G. R., & Mariano, A. N. (1987). Cathodoluminescence and microprobe study of rare-earth elements in apatite. *American Mineralogist*, 72, 801-811.
- Rønso, J. (1989). Coupled substitutions involving REEs and Na and Si in apatites in alkaline rocks from the Ilimaussaq intrusion, South Greenland, and the petrological implications. *American Mineralogist*, 74, 896-901.
- Ryerson, F., & Hess, P. (1978). Implications of liquid-liquid distribution coefficients to mineral-liquid partitioning. *Geochimica et Cosmochimica Acta*, 42, 921-932.
- Shannon, R. T. (1976). Revised effective ionic radii and systematic studies of interatomic distances in halides and chalcogenides. *Acta Crystallographica Section A: Crystal Physics, Diffraction, Theoretical and General Crystallography*, 32, 751-767.
- Stormer, J., Pierson, M. L., & Tacker, R. C. (1993). Variation of F and Cl X-ray intensity due to anisotropic diffusion in apatite. *American Mineralogist*, 78, 641-648.
- Valley, P. M., Hanchar, J. M., & Whitehouse, M. J. (2009). Direct dating of Fe oxide-(Cu-Au) mineralization by U/Pb zircon geochronology. *Geology*, 37, 223-226.

- Valley, P. M. (2010). *Fluid Alteration and Magnetite-Apatite Mineralization of the Lyon Mountain Granite: Adirondack Mountains, New York State*. (Doctoral dissertation, Memorial University of Newfoundland)
- Wall, F., Niku-Paavola, V. N., Storey, C., Müller, A., & Jeffries, T. (2008). Xenotime-(Y) from carbonatite dykes at Lofdal, Namibia: unusually low LREE: HREE ratio in carbonatite, and the first dating of xenotime overgrowths on zircon. *The Canadian Mineralogist*, 46, 861-877.
- Watson, E. B. (1976). Two-liquid partition coefficients: experimental data and geochemical implications. *Contributions to Mineralogy and Petrology*, 56, 119-134.

CHAPTER 2 TABLES

Table 2.1. Summary of syntheses and rationale.

Set	Synthesis number	Experiment Type	Phases Present				Rationale
			<i>Apatite</i>	<i>CaF₂ flux</i>	<i>REE₂O₃ + Apatite</i>	<i>REE₂O₃ + CaF₂ flux</i>	
0	211	Undoped apatite	x	x		x	To develop and perfect the method
1a	212	REE + Si at 1x	x	x			Investigating the effects of overall REE concentration in the flux and the efficiency of Na and Si charge balancing REE
	213	REE + Si at 10x	x	x			
	214	REE + Si at 100x	x	x	x	x	
1b	215	REE + Na at 1x	x	x			Investigating the effects of relative proportions of dopant in the flux on crystal chemistry
	216	REE + Na at 10x	x	x			
	217	REE + Na at 100x	x	x			
2	227	REE + Si at 20x : LREE > HREE	x	x			Syntheses run in evacuated silica tube to investigate potential Si and Na volatility
	288_1	REE + Si at 20x : LREE = HREE	x	x			
	236	REE + Si at 20x : LREE < HREE	x	x			
3	288_2	REE + Si at 20x : LREE = HREE	x	x			Syntheses run in evacuated silica tube to investigate potential Si and Na volatility
	289_2	REE + Na at 20x : LREE = HREE	x	x			

Table 2.2 Major and trace element composition of synthetic apatites.

Synthesis #	211		212		213		214		215									
Grain #	1	(err)	1	(err)	2	(err)	1	(err)	2	(err)	1	(err)	2	(err)				
EPMA																		
n	10		10		10		10		10		10		10					
Major Elements (wt%)																		
F	3.79	(0.07)	3.94	(0.08)	3.86	(0.06)	3.78	(0.06)	3.83	(0.05)	3.69	(0.06)	3.70	(0.07)	4.41	(0.21)	3.88	(0.07)
Na ₂ O	bdl		bdl	-	bdl	-	bdl	-										
SiO ₂	bdl		0.04	(0.00)	0.03	(0.00)	0.23	(0.02)	0.20	(0.04)	1.72	(0.06)	1.79	(0.16)	bdl	-	bdl	(0.00)
P ₂ O ₅	42.38	(0.07)	42.36	(0.11)	42.38	(0.09)	42.24	(0.08)	42.24	(0.13)	39.69	(0.06)	39.55	(0.33)	42.40	(0.07)	42.48	(0.06)
CaO	55.19	(0.25)	55.20	(0.05)	55.16	(0.05)	55.19	(0.05)	55.21	(0.05)	53.06	(0.06)	52.69	(0.35)	55.92	(0.11)	55.24	(0.07)
O=F	-1.59	(0.03)	-1.66	(0.03)	-1.62	(0.02)	-1.59	(0.02)	-1.61	(0.02)	-1.55	(0.03)	-1.56	(0.03)	-1.86	(0.09)	-1.63	(0.03)
Total	99.77	(0.27)	99.89	(0.15)	99.81	(0.12)	99.84	(0.11)	99.86	(0.16)	96.61	(0.13)	96.17	(0.51)	100.88	(0.27)	99.97	(0.12)
LA-ICPMS																		
n	3		3		3		3		3		3		3		3		3	
Trace Elements (ppm)																		
Y	bdl		12.04		9.01		240		184.5		2351		2612		10.08		7.027	
La	bdl		26.98		23.06		517.7		439.7		11990		11990		24.86		21.77	
Nd	bdl		27.13		22.49		441.7		358.4		7549		7759		24.04		20.39	
Sm	bdl		25.92		20.60		398		318.7		5871		6151		21.8		17.88	
Dy	bdl		15.29		11.52		259.1		198.8		2247		2510		11.98		8.463	
Er	bdl		8.597		6.13		177.9		130.7		1183		1370		7.613		4.783	
ΣREE	bdl		116		92.81		2034		1631		31190		32390		100.4		80.31	

Note: "bdl" = below detection limit; "-" = not reported; "err" = 1σ s.d.

Table 2.2. Cont'd.

Synthesis #	216		217		227		235									
Grain #	1	(err)	2	(err)	1	(err)	2	(err)	1	(err)	2	(err)				
EPMA																
n	10		10		10		10		5		5					
Major Elements (wt%)																
F	3.91	(0.07)	3.83	(0.05)	4.64	(0.12)	4.63	(0.04)	3.83	(0.06)	3.84	(0.05)	3.86	(0.12)	3.81	(0.10)
Na ₂ O	bdl	-	bdl	-	0.02	(0.01)	0.01	(0.01)	bdl	-	bdl	-	bdl	-	bdl	-
SiO ₂	0.02	(0.01)	0.02	(0.01)	0.04	(0.01)	0.02	(0.01)	0.10	(0.01)	0.08	(0.01)	0.40	(0.02)	0.47	(0.03)
P ₂ O ₅	42.51	(0.08)	42.52	(0.08)	42.19	(0.19)	42.21	(0.12)	42.20	(0.09)	42.11	(0.11)	41.45	(0.32)	41.43	(0.61)
CaO	55.32	(0.09)	55.35	(0.06)	55.32	(0.08)	55.97	(0.59)	55.09	(0.10)	54.97	(0.09)	55.23	(0.10)	55.19	(0.12)
O=F	-1.65	(0.03)	-1.61	(0.02)	-1.95	(0.05)	-1.95	(0.02)	-1.61	(0.02)	-1.62	(0.02)	-1.63	(0.05)	-1.61	(0.04)
Total	100.12	(0.15)	100.11	(0.12)	100.25	(0.25)	100.89	(0.60)	99.61	(0.15)	99.38	(0.16)	99.32	(0.36)	99.29	(0.63)
LA-ICPMS																
n	3		3		5		3		3		3		5		5	
Trace Elements (ppm)																
Y	112.4		82.63		342.2		271.8		37.22		30.98		438.5		603.4	
La	286.6		242.8		2365		2173		860		681.8		1299		1540	
Nd	249.8		206.5		1617		1431		322.8		253.1		869		1051	
Sm	228.9		183		1166		988.2		142.1		113.8		796.2		1020	
Dy	126.2		95.1		377.5		303.5		42.58		35.12		449.5		621.6	
Er	85.63		61.87		196.7		154.3		24.81		21.21		304.4		402.4	
ΣREE	1090		871.9		6064		5322		1430		1136		4157		5238	

Note: "bdl" = below detection limit; "-" = not reported; "err" = 1σ s.d.

Table 2.2. Cont'd.

Synthesis #	236		288_2		289_2							
Grain #	1	(err)	2	(err)	1	(err)	2	(err)				
EPMA												
n	10		10		10		10					
Major Elements (wt%)												
F	3.74	(0.06)	3.72	(0.05)	4.10	(0.04)	4.14	(0.03)	4.02	(0.07)	4.85	(0.17)
Na ₂ O	bdl	-	bdl	-	0.00	(0.00)	0.00	(0.01)	0.01	(0.00)	0.01	(0.01)
SiO ₂	0.28	(0.05)	0.24	(0.04)	0.79	(0.04)	0.81	(0.03)	1.06	(0.45)	1.56	(0.30)
P ₂ O ₅	42.11	(0.14)	42.06	(0.14)	40.67	(0.15)	40.64	(0.11)	40.23	(0.79)	39.59	(0.54)
CaO	55.22	(0.04)	55.23	(0.08)	55.84	(0.27)	55.48	(0.10)	55.05	(1.01)	54.03	(0.41)
O=F	-1.58	(0.02)	-1.57	(0.02)	-1.73	(0.02)	-1.74	(0.01)	-1.69	(0.03)	-2.04	(0.07)
Total	99.77	(0.17)	99.68	(0.17)	99.68	(0.31)	99.32	(0.16)	98.69	(1.36)	98.00	(0.76)
LA-ICPMS												
n	5		5		3		3		5		5	
Trace Elements (ppm)												
Y	455.2		400.2		2123		2081		2796		5213	
La	136.6		130.4		2066		2066		2839		5164	
Nd	102.8		95.6		2982		2922		3941		6574	
Sm	192.8		172.8		3345		3297		4427		5684	
Dy	233.6		200.5		2925		2931		3815		3826	
Er	331.1		274.7		2458		2482		3222		3815	
ΣREE	1452		1274		15900		15780		21040		30280	

Note: "bdl" = below detection limit; "-" = not reported; "err" = 1σ s.d.

Table 2.3 Composition of REE-oxide phases.

Synthesis #	214 err	217 err
EPMA		
n	10	5
Major Elements (wt%)		
F	0.23 (0.02)	0.21 (0.12)
P₂O₅	0.06 (0.01)	0.91 (1.82)
CaO	0.93 (0.05)	1.77 (2.27)
Y₂O₃	26.03 (0.14)	19.72 (1.36)
La₂O₃	1.21 (0.11)	1.20 (0.35)
Nd₂O₃	6.82 (0.49)	6.41 (0.70)
Sm₂O₃	12.78 (0.69)	13.15 (1.44)
Dy₂O₃	24.13 (0.34)	27.18 (3.34)
Er₂O₃	27.83 (1.04)	28.60 (1.98)
Total	100.02 (1.39)	99.14 (5.29)

Table 2.4 Synthetic apatite unit cell parameters.

Synthesis Number	Cell		
	<i>a</i> -axis (Å) σ	<i>c</i> -axis (Å) σ	Volume (Å ³) σ
211	9.3658 (2)	6.8808 (3)	522.81 (3)
212	9.3720 (2)	6.8863 (3)	523.82 (3)
213	9.3754 (2)	6.8883 (3)	524.35 (3)
214	9.3872 (2)	6.8976 (3)	526.41 (4)
215	9.3721 (2)	6.8863 (3)	523.83 (3)
216	9.3721 (2)	6.8864 (3)	523.84 (3)
217	9.3748 (2)	6.8880 (3)	524.26 (3)
227	9.3766 (2)	6.8897 (3)	524.59 (3)
235	9.3757 (2)	6.8900 (3)	524.51 (3)
236	9.3729 (2)	6.8873 (3)	523.99 (3)

Note: numbers in parentheses denote 1 standard deviation of least significant digit.

CHAPTER 2 FIGURES

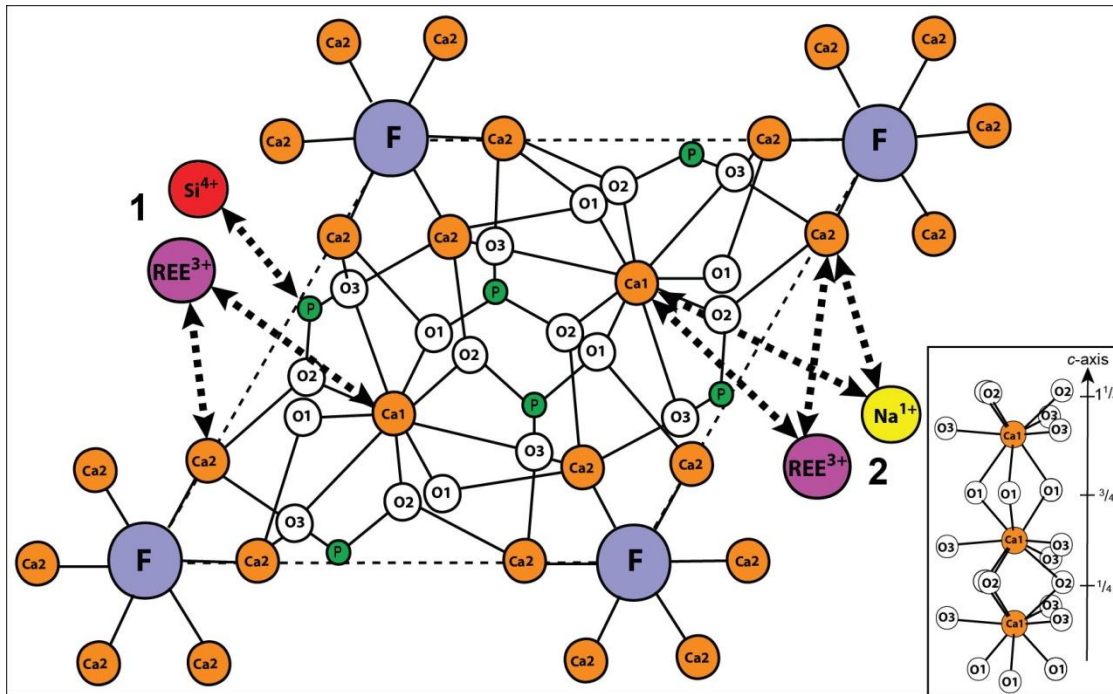


Figure 2.1 Schematic cross section through the apatite structure projected down the c -axis. Note the two substitutions, 1 and 2, showing the coupled substitutions with Si and Na, of equations 1 and 2, respectively. The oxygen coordination of columnar Ca1 ions of the apatite structure is also represented here (bottom right), with horizontal mirror planes at $1/4$, $3/4$, $1\ 1/4$, etc. Modified from Fleet and Pan (1995) and Elliot et al. (2002).

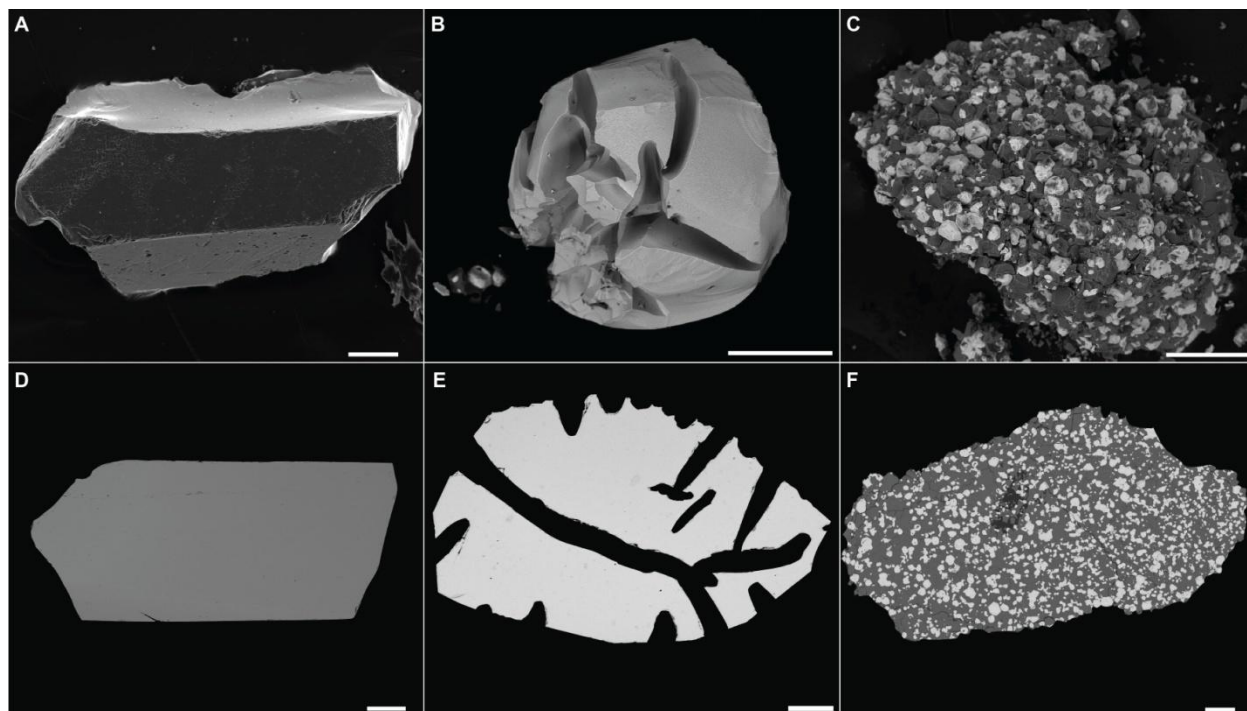


Figure 2.2 Representative back-scattered electron images of materials produced from different syntheses. The top row of images, from left to right (**A** to **C**), show the morphology of a single apatite crystal (Synthesis 211), a single REE-oxide grain (Synthesis 214), and REE-oxide blebs suspended in apatite (Synthesis 217). The lower row of images (**D** to **E**) show the same phases imaged in a polished epoxy mount. Scale bars are 100 μm . The black tunnels in **E** are the epoxy filled chasms seen on the surface of the REE-oxide grain **B**.



Figure 2.3 CL intensity of synthetic apatite grains with respect to increasing REE content. The syntheses shown here are, from left to right, reveal a notable increase in CL intensity of incrementally Si doped syntheses (212, 213 and 214) with respect to the undoped apatite (211: furthest left). Note the increase in orange-red luminescence due to activation of Sm^{3+}

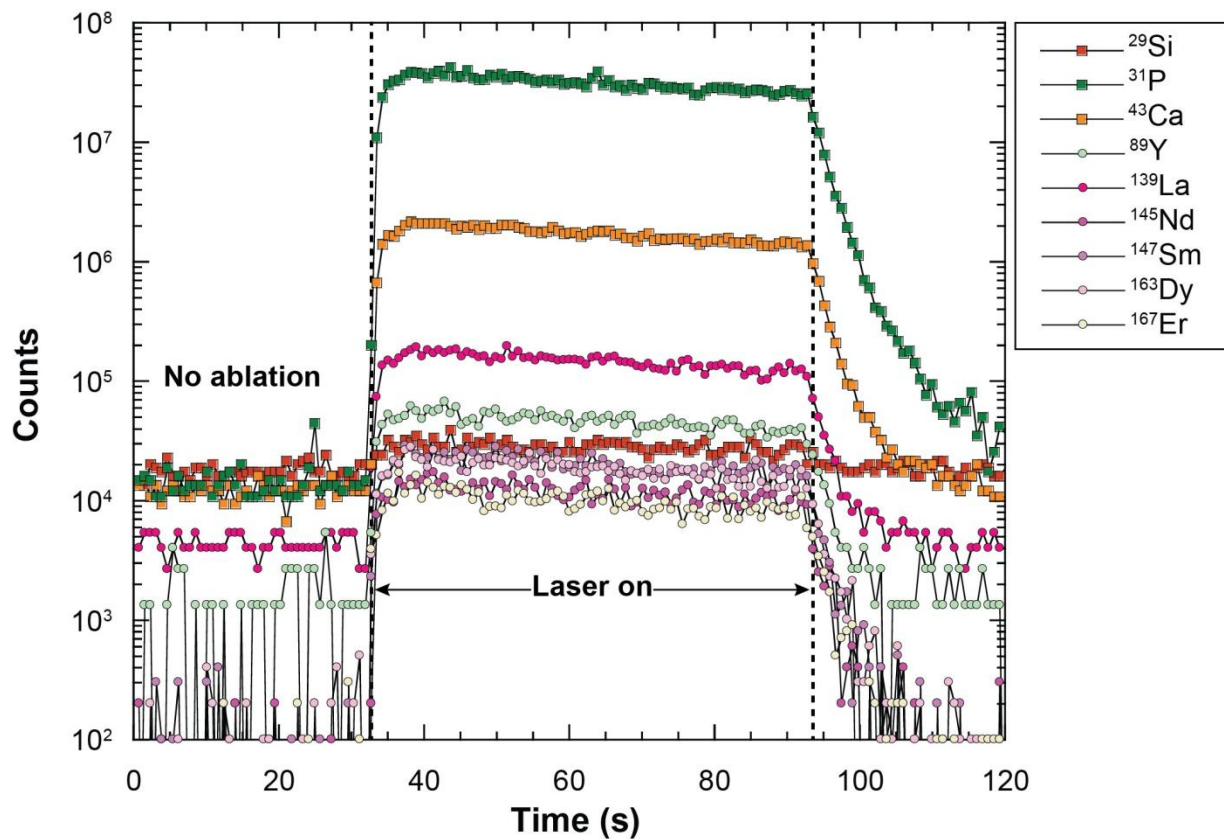


Figure 2.4 Typical time-resolved spectra (TRS) from LA-ICPMS analyses on synthetic apatite grains. The REE and Si TRS shown here are from a 49 μm spot analysis on apatite grain 1 from synthesis 214. Note the log y-axis.

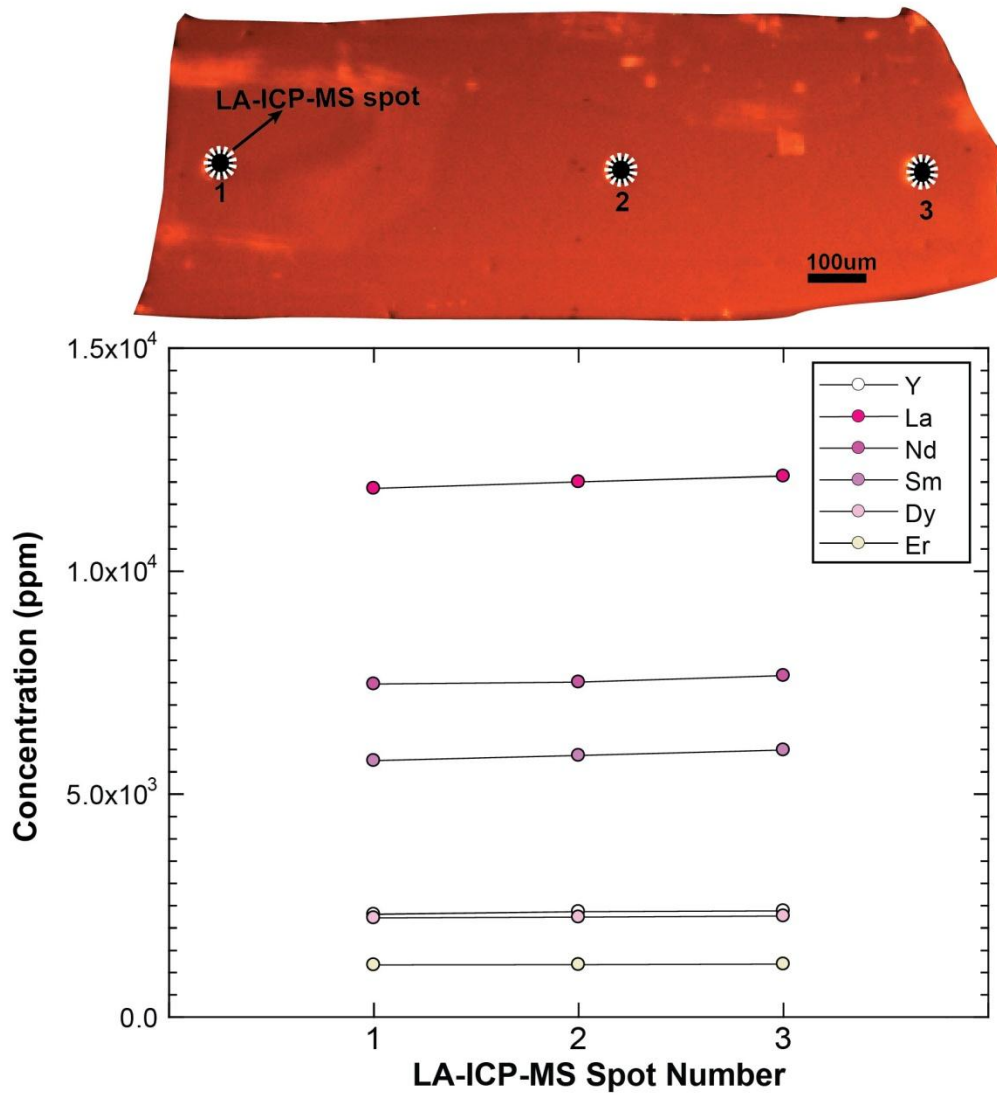


Figure 2.5 REE content in synthetic apatite from LA-ICP-MS measurements made parallel to the *c*-axis according to the annotated BT-CL image above the plot. Note the consistent trace element concentrations and overall grain homogeneity.

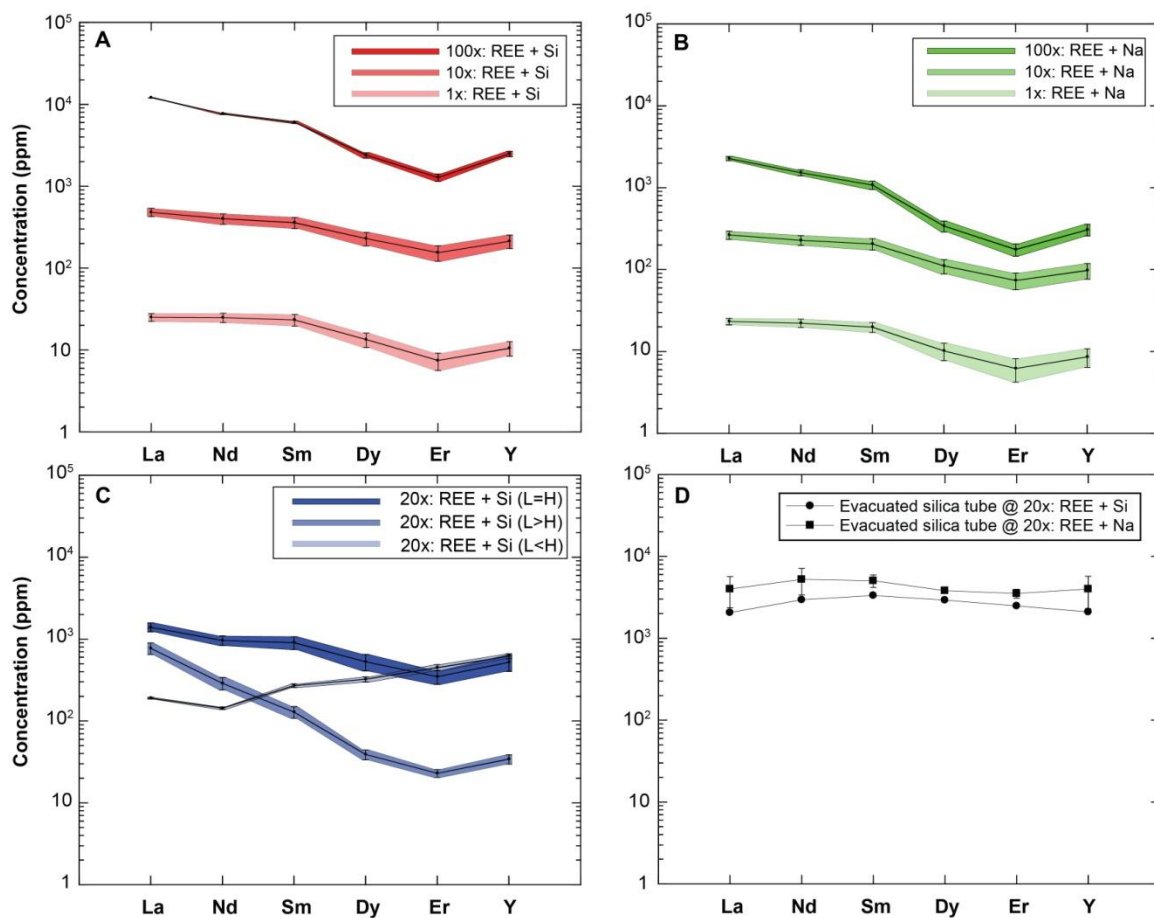


Figure 2.6 Rare earth element spider diagrams showing REE content of all synthetic apatite grains. Concentrations plotted are raw, non-normalized, REE values. Note the influence of increasing dopant level (**A** and **B**), varying the respective proportions of LREE to HREE (**C**), and syntheses run in evacuated silica tubes (**D**) on resulting REE crystal chemistry.

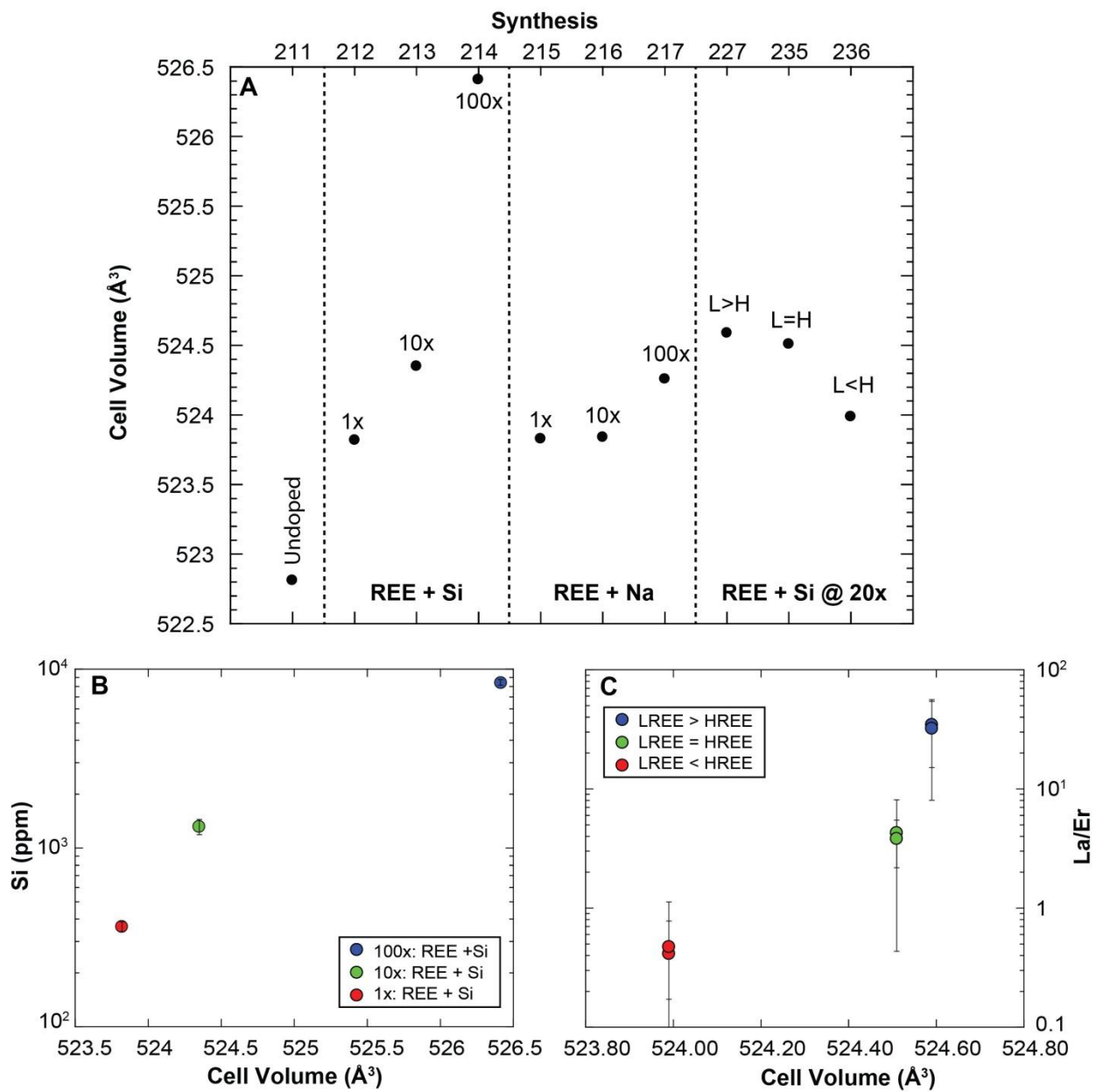


Figure 2.7 A shows the respective cell volume for each synthesis determined from XRD cell refinements. Note the positive correlation between Si and cell volume in B and La/Er ratios with cell volumes in C; see text for discussion.

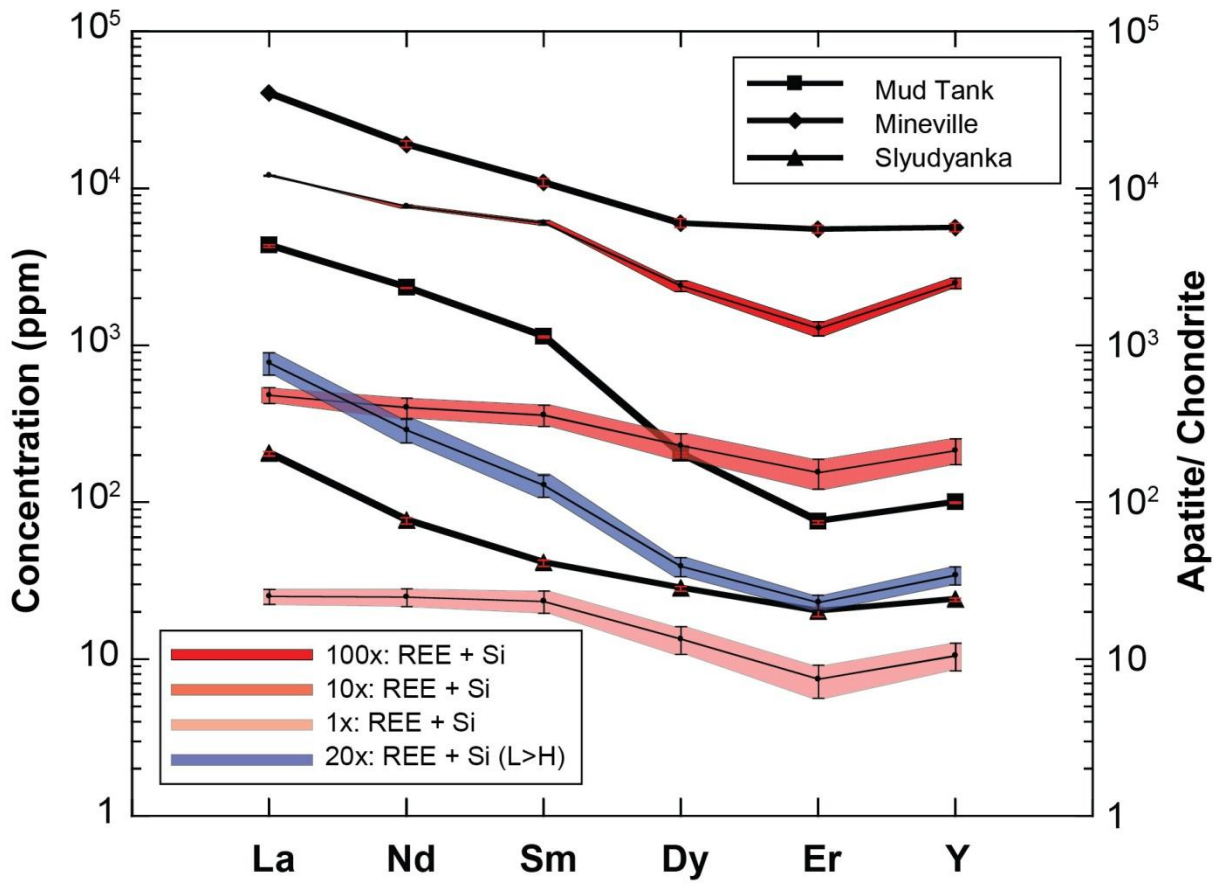


Figure 2.8 Rare earth element spider diagrams showing selected synthetic and natural apatite samples. Note that all natural apatites REE values are chondrite normalized to Anders and Grevesse (1989) and are represented on the y-axis to the right.

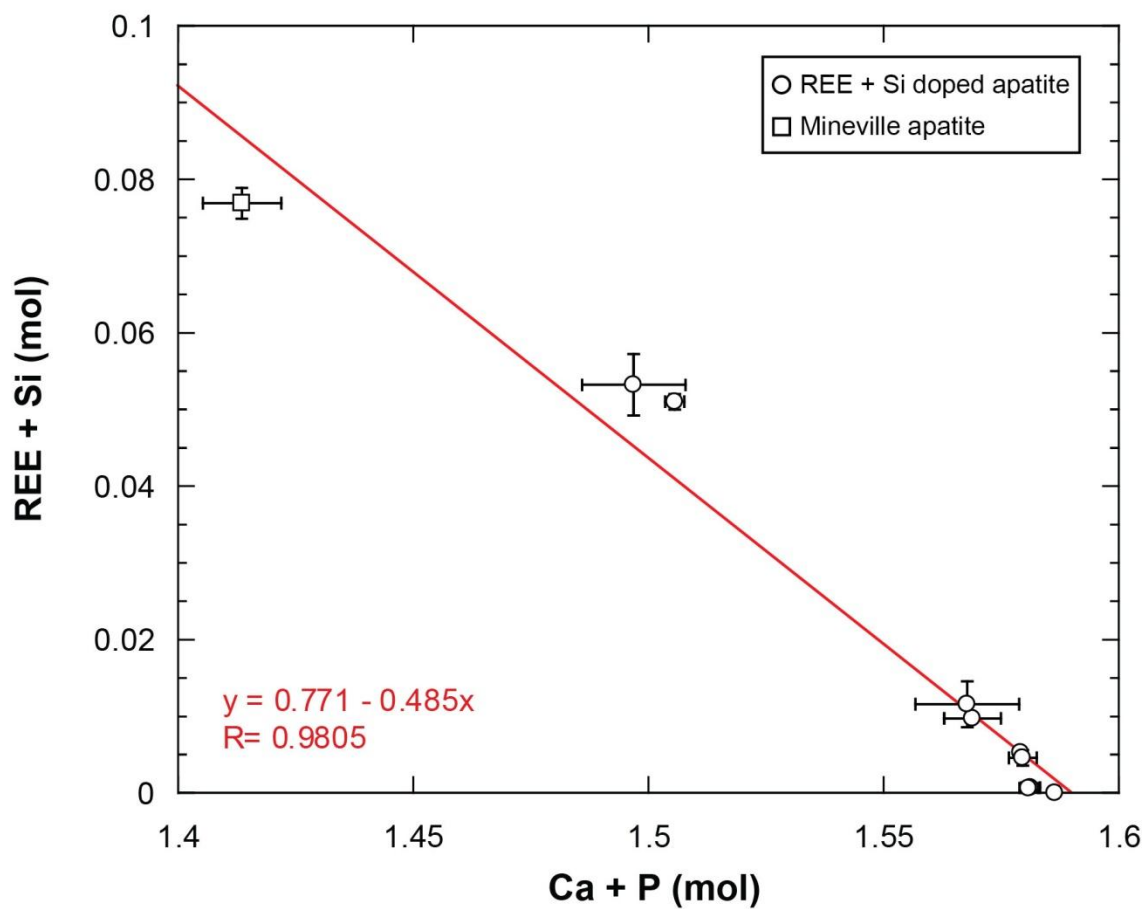


Figure 2.9 Plot of mol REE + Si versus mol Ca + P for all REE + Si doped synthetic apatites (circles) and natural apatite from Mineville (square). Note the positive correlation as result of REE accommodation through the coupled substitution in equation (1) that are consistent with the natural apatite from Mineville.

Chapter 3: Composition and crystal chemistry of apatite with a case study of apatite from the Gruvberget magnetite-apatite (MtAp) deposit, Norrbotten region, northern Sweden

ABSTRACT

Apatite has a relatively accommodating crystal structure that allows for the incorporation of geochemically significant elements (e.g., high field strength elements [HFSE]: Hf, Th and U; and rare earth elements [REE]: lanthanides, Y, and Sc) that can be analyzed with modern micro-analytical techniques, making it a useful tracer of petrogenesis, post crystallization alteration, and mineralization. Major, minor, and trace element compositions of reference apatites from well-known geological localities are presented here, along with those of the case study apatites from the Gruvberget (northern Sweden) magnetite apatite (MtAp) deposit and related rocks. Apatite of the Gruvberget MtAp deposit was sampled from the footwall biotite schist, the MtAp ore, and a metadiabase dyke that crosscuts the ore and host rocks. The reference apatites, for comparison, are from two carbonatites (Mud Tank, Australia; Kola Kovdor, Russia), MtAp ore (Durango, Mexico; Mineville, New York, USA), skarns (Sludyanka, Russia; Otter Lake, Québec, Canada) and an alkaline suite (Kola Kovdor, Russia). The assemblage of actinolite + scapolite in the host biotite schist and the metadiabase dyke suggests metasomatic alteration by hydrothermal fluids of the apatite post- and/or syn-mineralization. The Gruvberget apatites, compared to the reference apatites, are: 1) depleted in total REEs, especially LREEs; 2) depleted in REE charge balancing cations Na and Si; 3) enriched in Cl and OH; and 4) enriched in Mn. It is postulated that the primary composition of the Gruvberget apatites were overprinted via metasomatism by hydrothermal fluids composed of a sodium, calcium, and chlorine rich brine, by metamorphism, or by both processes. The chlorine enrichment in the Gruvberget apatite is thought to be

metasomatic. The LREE depletion may be a result of leaching during metasomatic alteration rather than regional metamorphism, however both events could be related.

3.1 INTRODUCTION

The general formula for apatite supergroup minerals is ${}^{\text{IX}}\text{M1}_2{}^{\text{VII}}\text{M2}_3({}^{\text{IV}}\text{TO}_4)_3\text{X}$ (roman numeral superscripts denote the coordination number for the respective site), which crystallize in the hexagonal system with a space group of $\text{P6}_3/m$ (Elliot, 1994; Pasero, 2010). The ${}^{\text{IX}}\text{M1}$ and ${}^{\text{VII}}\text{M2}$ sites are occupied by large cations (e.g., Large ion lithophile elements [LILE]: Ca^{2+} , Sr^{2+} , Ba^{2+} ; Mg^{2+} , Mn^{2+} , and Na^+) (Pan and Fleet, 2002), and the ${}^{\text{IV}}\text{T}$ site is occupied by small, highly charged, cations (e.g., P^{5+} , As^{5+} , S^{5+} , V^{5+} and Si^{4+}) (Pan and Fleet, 2002; Piccoli and Candela, 2002). Calcium phosphate apatite, expressed as $\text{Ca}_5(\text{PO}_4)_3\text{X}$, is the most common composition. The X site is occupied by F^- , Cl^- and/or OH^- producing a ternary solid solution with end-members of fluorapatite (FAp), chlorapatite (CAp) and hydroxyapatite (HAp). Fluorapatite ($\text{Ca}_5[\text{PO}_4]_3\text{F}$) is the most abundant composition in most igneous systems, and its minor and trace element composition varies with changes in pressure (P), temperature (T), oxygen fugacity ($f\text{O}_2$) and melt composition (M_x) (Boudreau and Prendergast, 1995; Piccoli and Candela, 2002; Hovis and Harlov, 2010).

Substitution of geochemically interesting elements (e.g., high field strength elements [HFSE]: Hf, Th and U; and rare earth elements [REE]: lanthanides, Y, and Sc) in apatite make it a useful tracer of petrogenesis, metasomatism, and economic mineralization (e.g., Roegge et al., 1974; Williams and Cesbron, 1977; Huff, 1983; Boudreau and McCallum, 1989; Tepper and Keuhner, 1999; Belousova et al., 2001, 2002; Piccoli and Candela, 2002; Chew et al., 2011; Miles et al., 2014; Harlov, 2015). These elements may enter the apatite structure through either: 1) direct substitution (e.g., Sr^{2+} for Ca^{2+} , or As^{5+} for P^{5+}); or 2) coupled substitutions (Rønnsbo,

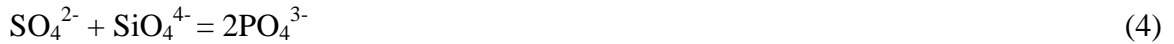
1989; Elliot,1994; Fleet and Pan 1995; Pan and Fleet, 2002). Substitution involving vacancies at the Ca sites (i.e., ^{IX}Ca1 and ^{VII}Ca2) may also accommodate REEs (Fleet and Pan, 2002). Substitution for Ca²⁺ may result in several weight percent of Sr²⁺, Ba²⁺, Mg²⁺, Mn²⁺, Fe²⁺ and Pb²⁺ in some natural apatite (Rakovan and Hughes, 2000; Pan and Fleet, 2002). Coupled substitutions, such as those involving a REE³⁺ and a charge balancing cation (e.g., Si⁴⁺ or Na⁺) can yield significant concentrations of REE in apatite, and in one example up to 27 wt.% REE₂O₃ (Zirner et al., 2015) (Fleet and Pan, 1995; Klemme and Dalpé, 2003; Prowatke and Klemme, 2006). Coupled substitutions take place by the following mechanisms:



In substitutions (1) and (2) the REE prefer the ^{VII}Ca2 site (Fleet and Pan, 1995). Data for synthetic apatite (Chapter 2 of this thesis) suggest that equation (1) is the preferred pathway for REE³⁺ charge balancing in the experimental conditions used in that study, making Si⁴⁺ a significant constituent in REE-enriched apatite. Likewise, charge balancing via equation (2) makes Na⁺ the most common monovalent cation in apatite; far exceeding reported trace concentrations of the larger K⁺, Li⁺ and Rb⁺ (e.g., Young et al., 1969). Equation (3) represents REE substitution involving a vacancy (denoted by the box in Equation 3) at the Ca site, and was assumed to play a role in charge balancing REE in synthetic britholite (Grisafe and Hummel, 1970).

The PO₄³⁻ group in apatite may be replaced directly with VO₄³⁻ and AsO₄³⁻, or by SiO₄⁴⁻ and SO₄²⁻ through coupled substitution(Hughes and Drexler, 1991; Peng et al., 1997, Comodi et

al., 1999; Persiel et al., 2000). Two proposed coupled substitutions involving the latter oxide groups are (Rouse and Dunn, 1982; Peng et al., 1997):



This variability in apatite chemistry has led many researchers to investigate its behaviour in a range of geologic environments to identify a chemical signature unique to different conditions in which it formed (e.g., Harlov et al., 2002a; Belousova et al., 2002; Jinjie et al., 2007; Bonyadi et al., 2011; Ziner et al., 2015; Mao et al., 2016). Studies typically implement a survey approach by sampling apatite from different geologic settings, and statistically constrain various apatite compositions to discriminate representative populations related to a given geologic environment or process (e.g., Belousova et al., 2002; Piccoli and Candela, 2002; Chu et al., 2009; Mao et al., 2016).

One area of particular interest for detailed investigations into apatite chemistry are the Kiruna Type iron-oxide apatite (IOA) deposits (referred hereafter as magnetite-apatite [MtAp] deposits) (e.g., Kiruna in the Norrbotten region of northern Sweden) (Philpotts, 1967; Hitzman, 1992; Nyström and Henriquez, 1994; Frietsch and Perdahl, 1995; Jonsson et al., 2013; Westhues et al., 2016; Westhues et al., 2017). Some world-renowned deposit localities of this type include: the Adirondacks (e.g., Mineville) (Foose and McLelland, 1995; Valley et al., 2009; Valley et al., 2011); the Great Bear Magmatic Zone, Northwest Territories, Canada (Hitzman, 1992; Gandhi et al., 2000; Ootes et al., 2010); Olympic Dam, South Australia (Haynes et al., 1995; Partington and Williams, 2000; Belperio and Freeman, 2004); the southeastern Missouri metallogenic province (e.g., Pea Ridge and Pilot Knob) (Nuelle et al., 1992; Nold et al., 2013; Nold et al., 2014; Starkey and Seeger, 2016, for review); and El Laco, Chile (Nyström and Henriquez, 1994; Tornos et al.,

2016; Velasco et al., 2016). The MtAp deposits above are mainly Proterozoic in age; deposits also occur in the Cambrian (e.g., Bafq District, Iran; Heinz-Günter et al., 2011) to the Paleogene (e.g., Durango, Mexico; McDowell and Keizer, 1977) and the Holocene (e.g., El Laco, Chile; Nyström and Henriquez, 1994; Tornos et al., 2016; Velasco et al., 2016). These deposits are a current focus of research activity due to the widespread debate over their ore-forming processes and metasomatic alteration (e.g., Kirunavaara MtAp deposit: Geijer and Ödman, 1974; Parak, 1975; Frietsch, 1978; Wright, 1986; Jonnson et al., 2013; Westhues et al., 2016; Tornos et al., 2016; Velasco et al., 2016; Westhues et al., 2017). Though apatite is typically low in modal abundance in most crustal and mantle rocks, these deposits tend to concentrate apatite within iron-oxide ore bodies; which may occur as discordant brecciated zones, or concordant tabular lenses in stratified successions (e.g., volcanic, and/or sedimentary rocks) (Roeder et al., 1987; Piccoli and Candela, 2002; Hitzman, 1992; Williams et al., 2005; Tornos et al., 2016; Velasco et al., 2016). Since apatite is ubiquitous in these deposits, and occurs in such high volume, studies into its chemistry may provide important details regarding petrogenesis, ore forming processes, and metasomatic alteration (e.g., Roegge et al., 1974; Williams and Cesborn, 1977; Belousova et al., 2002).

The first part of this study is an assessment of the chemistry of apatite from several well-known apatite localities (Table 3.1). The apatite samples of this study are from: Mud Tank, Australia; Durango, Mexico; Otter lake, Quebec; Mineville, New York; Sludyanka, Siberia, Russia; and Kovdor from the Kola Peninsula, in northwestern Russia. These samples provide a survey of apatite compositions from well known geologic environments. These specific apatite samples were chosen because they provide a range of compositions with distinguishing characteristics for each locality. This range allows for an empirical discrimination, which is used

to develop a framework for apatite from a given rock type, and/or to constrain the effects of post-crystallization alteration processes.

The second part of this study is an investigation of the chemistry of apatite from the Gruvberget MtAp deposit southeast of Kiruna in the Norrbotten region of northern Sweden. This deposit was selected for this study because the apatite from the ore body, and spatially related rocks, had not previously been investigated for its minor or trace element geochemistry unlike the Kiruna deposits. The Gruvberget apatites are compared to the reference apatites to determine any compositional differences that set them apart. This comparative portion of the study helps unravel the geological history of the Gruvberget apatites by relating them to areas in which the geology is well-constrained and the apatite compositions have previously been studied.

3.1.1 Geologic settings of the apatite samples used in this study

See Table 3.1 for a summary of the apatites studied.

3.1.1.1 Mud Tank, Australia

The Mud Tank carbonatite complex intruded into a portion of the ~1860 Ma (Claoué-Long et al., 2008) Strangways Metamorphic Complex (SMC) at ~732 Ma (Gulson and Black, 1978) in the Northern Territory of Australia. Apatite is a major accessory phase in the carbonatite; which resides in a northeast-trending mylonite zone, with carbonate-rich dykes cross-cutting other units, associated with sub-vertical apatite- and magnetite-rich layers (Currie et al., 1992). The lens-like form and tectonic foliation resembles other metamorphosed and deformed carbonatites (e.g., Perry River, Canada; Höy and Pell, 1980), yet the abundance and form of inclusions (e.g., xenoliths) make it unique compared to other sub-circular metasomatised carbonatites or vein-type complexes (Heinrich, 1966; Currie, 1976; LeBas 1987). This apatite sample is referred to as Mud Tank in this thesis.

3.1.1.2 Durango, Mexico

Durango apatite occurs as a major ore-forming mineral in the Tertiary MtAp deposits of the Cerro de Mercado deposit near the city of Durango, Mexico (Young, 1969). The majority of the volcano consists of Tertiary (32.1 Ma to 28.3 Ma; McDowell and Keizer, 1977) intermediate to felsic composition volcanic rocks. Apatite from this deposit is thought to have been derived metasomatically from post-emplacement hydrothermal fluids (Barton and Johnson, 1996), and occurs in cavities as large gemmy fluorapatite crystals several mm to several cm in length (Piccoli and Candela, 2002). Durango apatite has been widely used as an analytical standard for EPMA due to compositional homogeneity (Roeder et al., 1987; Rösbo, 1989; Sha and Campbell, 1999; Miles et al., 2014), for (U-Th)/He thermochronology (Flowers et al., 2007, Peppe and Reiner, 2007), and as a Sm-Nd standard (Fisher et al., 2011). Fluorapatite occurs intimately with martite (pseudomorphic replacement of magnetite by hematite) occurrences throughout the ore body, commonly in fissures and cavities in the host volcanic rock (Young et al., 1969). These apatite samples are referred to in this thesis as Durango ($\perp c$) and Durango ($\parallel c$), for crystals that were prepared perpendicular and parallel to their *c*-crystallographic axis, respectively.

3.1.1.3 Otter Lake, Québec, Canada.

The Otter Lake area in Québec, Canada, is located in a highly-eroded portion of the Precambrian Grenville Orogen between the Central Metasedimentary Belt and the Central Gneiss Belt (Barford, 2003). It consists of gneisses, metabasites, and carbonate skarns, that are the result of high-grade metamorphism throughout the area (Kretz, 1993). The apatite is hosted in the Ca-pyroxene-scapolite-titanite-fluorite skarn that occurs in marble throughout the area, and

varies from red-brown to green (Trzcienski et al., 1974; Kretz, 1993). This apatite sample is referred to as Otter Lake in this thesis.

3.1.1.4 Mineville, New York, USA

The MtAp ore deposits at Mineville in Essex County, New York, are hosted in highly K and Na metasomatised post-Grenville igneous intrusive rocks (McLelland et al., 2001; Valley et al., 2009; Valley et al., 2011). The two main ore bodies in the area are the Old Bed and Harmony Bed, associated with two different altered gabbroic units near the bottom and top of an igneous succession, respectively (McKeown and Klemic, 1954; Valley et al., 2009; Valley et al., 2010; Valley et al., 2011). The fluorapatite of the Old Bed has been noted for its high REE (~10% REE-oxides), Th and U contents (Roeder et al., 1987). This apatite sample is referred to as Mineville in this thesis and is from the Old Bed locality.

3.1.1.5 Sludyanka, Siberia, Russia

The Sludyanka Group make up the crystalline rocks of the Upper Archean portion of Western Khamar-Daban, Siberia, and is host to several industrial skarn-type mineral deposits (Gillen and Rundqvist, 1997; Kovach et al., 2013). The rocks of the Sludyanka Group consist of mainly carbonate rocks and metamorphic quartz-diopside rocks, that split the area into calcic and magnesian units. Fluorapatite is common to all of the crystalline rocks of the Obruchev assemblage of the Sludyanka Group, in some cases forming 5-20 cm thick apatite-rich lenses (Gillen and Rundqvist, 1997; Shkol'nik et al., 2016). These apatite samples are referred to as MUN Sludyanka (Dempster et al., 2003), and JMH Sludyanka (obtained by J.M. Hancher in St. Petersburg, Russia, from a mineral dealer who had collected the sample at the Sludyanka locality) in this thesis.

3.1.1.6 Kovdor, Kola Peninsula, Russia

The Paleozoic Kola alkaline province is located in the eastern portion of the Kola Peninsula, Russia, and is one of the world's largest alkaline-carbonatite provinces (Epshteyn and Danil'chenko, 1988; Zaitsez and Bell, 1995). Kovdor, is a ca. 370 - 280 Ma (Kramm et al., 1993; Bayanova et al., 1997) alkaline massif in the north-eastern part of the Baltic Shield, which contains a variety of magmatic and metasomatic rocks; ranging from ultrabasites to carbonatites (Zaitsez and Bell, 1995). The two fluorapatite samples in this study were collected from both the carbonatite and alkaline rocks at Kovdor. These samples are referred to as Kola Kovdor-C (for the carbonatite) and Kola Kovdor-A (for the alkaline rock) in this thesis.

3.1.1.7 Gruvberget, Kiruna, Sweden

The Proterozoic MtAp deposits of Kiruna in the Norrbotten region, northern Sweden, are hosted in a suite of felsic to intermediate composition volcanic rocks encompassed in the Fennoscandian Shield. The Fennoscandian Shield is composed of four NW-SE trending orogenic belts, spanning an active period from ~2.0 Ga to ~0.9 Ga, consisting of the following from oldest to youngest (~northeast to southwest): Kola-Karelian Orogen; Svecofennian Orogen; Gothian Orogen; and Sveco-Norwegian Orogen (Plant et al., 2003).

Gruvberget is a 10 Mt MtAp deposit with 53 % Fe (LKAB, 2010) located ~40 km southeast of Kiruna. The surrounding area, referred to as Svappavaara, is host to several other ore deposits (e.g., Tansari, Leveäniemi, Mertainen: MtAp; Kiilavaara and Alpha: skarn type iron ore; Pahtohavare: epigenetic Au-Cu), and has been mined for iron and copper since 1654 (Frietsch, 1980). The Svappavaara area is comprised mainly of supracrustal (greenstone and Porphyry Group volcanic rocks ± sedimentary rocks) and intrusive rocks (e.g., Lina granite) (Figure 3.1). The greenstone throughout the area consist of mafic volcanic tuffites that have

experienced up to amphibolite facies metamorphism, and are composed of tremolite-actinolite, albite, and biotite (Ojala and Juhani, 2007).

The ca. 1.8 Ga (Billström & Martinsson, 2000, Edfelt & Martinsson, 2005) Gruvberget MtAp deposit is a ~1300 m long x 6-65 m wide tabular ore body striking roughly N-S and dipping 50-75° E, located ~3 km to the west of Svappavaara village. The northern ore body consists mainly of magnetite (\pm hematite) with a gangue assemblage of apatite, calcite, and minor actinolite. Progressing southward, there is a transition into hematite ore (i.e., oxidized magnetite ore) containing apatite, calcite, scapolite and anhydrite (Ojala and Juhani, 2007). Fragment-bearing ore zones (~400m x 20m) are common near the hanging wall of hematite ore. These fragmented portions consist of angular to subangular clasts of hematite and sericite schist suspended in a matrix of hematite and chlorite (\pm quartz \pm calcite), considered to be a tectonic crush-zone along the margin between ore and wall rock (Frietsch, 1980).

Three hand samples from Gruvberget were collected in July, 2011, by geologists at Luossavaara Kiirunavaara Aktiebolag (LKAB) and shipped to Professor Hanchar. These included samples from outcrops of the footwall biotite schist host rock adjacent to the ore (GRV-11-01), the MtAp ore (GRV-11-02), and a crosscutting, late, metadiabase dyke (GRV-11-04) (Figure 3.2). Transmitted light microscopy, cathodoluminescence, and back-scattered electron imaging (coupled with energy dispersive spectroscopy [EDS]) were used to locate apatite in thin sections and determine its spatial and temporal relationships to other minerals (Figure 3.3). The footwall biotite schist, contains late primary euhedral to subhedral ~0.5 mm apatite grains coexisting with biotite and magnetite (Figure 3.2-1); seen in Figure 3.3-1c forming preferentially along foliation (i.e., left to right). The MtAp ore sample, consists of massive magnetite and hematite with centimetre wide veins of calcite and apatite (Figure 3.2-2). The apatite in the

MtAp ore occur as euhedral to subhedral 0.5 to 1 mm crystals that form in enclaves intimately associated with calcite \pm actinolite (Figure 3.3-2a-d). The third sample was collected from a dyke that crosscuts both the ore and host rocks (Figure 3.2-3). The dyke was likely a diabase prior to amphibolite facies metamorphism and/or metasomatism, based on relict pyroxene altered to scapolite with interstitial actinolite and titaniferous magnetite \pm apatite (Figure 3.3-3c). The mineral assemblage of this sample is an example of the pervasive sodic-calcic alteration throughout the area. Apatite occurs as anhedral \sim 0.2 mm grains, intergrown with the actinolite and iron-oxide in interstitial with scapolite (Figure 3.3-3c). Whole-rock geochemistry discriminant plots, based on major elements and immobile/ incompatible element composition, yield mafic alkalic compositions for the biotite schist and metadiabase dyke (Figure 3.4-A and B). See Table 3.2 for whole-rock compositions for the three Gruvberget rock samples.

3.2 ANALYTICAL METHODS

3.2.1 Sample preparation

Sample preparation for the Gruvberget apatite samples was done using standard techniques in the facilities at the Department of Earth Science at Memorial University of Newfoundland (MUN). Preparation began with approximately 10 kg of rock samples which were crushed in a jaw crusher to pea-sized particles, and then processed in a disk mill to intermediate sand-size particles. The material from the disk mill was split using a sample splitter into aliquots of several hundred grams. One quarter of the material was archived for future use, and the remainder was sieved to a grain size in which the majority of the material was retained on a 63 μ m sieve passed through from a 500 μ m sieve. In most igneous rocks the accessory minerals are usually between 63 μ m to 500 μ m in size and are separated as individual mineral grains and not aggregates of other minerals, or as broken grains. The material was then rinsed in water to

remove any dust. Next, the removal of magnetite was done using a hand magnet. This was followed by density separation using heavy liquids (e.g., bromoform; IUPAC name Tribromomethane, [density 2.85 g/cm³] and Methylene Iodide; IUPAC name Diiodomethane [MI] [density 3.3 g.cm³]). Apatite grains were then handpicked from the final separate under a binocular microscope, mounted in epoxy, and polished for analysis.

The reference apatite samples came from Dr. Hanchar's collection and had previously been mounted in epoxy, polished, and ready for microanalysis (Mud Tank, Otter Lake, etc.).

3.2.2 Scanning electron microscopy

Back-scattered electron (BSE) imaging was done using a JEOL JSM-7100F scanning electron microscope (SEM) with a field-emission source at Memorial University of Newfoundland. Epoxy mounts containing apatite grains and thin sections were coated with a ~20 nm (~200 Å) evaporated carbon film to prevent charge build up during imaging and analysis. An accelerating voltage of 15 kV was used during imaging and energy dispersive spectroscopy (EDS) analyses because it is a sufficient energy to produce characteristic X-ray emissions for all of the elements in question.

3.2.3 Bench-top cathodoluminescence

A bench-top optical microscope based system was used to acquire cathodoluminescence (CL) images on apatite grains in epoxy mounts and thin sections at Memorial University of Newfoundland. The system consists of an Olympus BX50 binocular polarizing microscope, and a cold cathode electron gun that is focused on samples in a stainless-steel chamber under relatively low vacuum (10 - 50 mTorr [1.33×10^{-6} MPa - 6.66×10^{-6} MPa]) (PATCO ELM-3). A KAPPA DX-30C Peltier cooled (to -30°C) digital camera affixed to the microscope was used to

capture the CL images, and each CL image was accompanied by an image of the same location in cross-polarized light.

3.2.4 Electron probe microanalysis

Three polished epoxy mounts containing selected apatite grains were coated with a 20 nm (200 Å) evaporated carbon film to prevent charge build up during imaging and microanalysis in the electron probe micro-analyzer (EPMA). The areas analyzed by EPMA were precisely marked on back-scattered electron (BSE) and/or cathodoluminescence (CL) photomicrographs. Apatite grains were analyzed for their major and minor element compositions at MUN using a JEOL JXA-8230 Superprobe EPMA equipped with five tuneable wavelength-dispersive X-ray spectrometers (WDS). Samples underwent initial wavelength scans, and energy dispersive spectroscopy (EDS), to determine which elements would be analyzed, and to identify appropriate background positions and potential interferences. Five analyses were done on each of the nine reference apatite samples, whereas three analyses were done each of the sixty Gruvberget apatites.

The apatite grains were analyzed by EPMA for F, P, Ca as major elements, and Na, Mg, Si, S, Cl, Mn, Fe, As, Sr and Y as minor elements (See Table A.5 for EPMA analytical conditions). Analyses were done using an accelerating voltage of 15 kV, a Faraday cup current of 20 nA, and a defocused beam diameter of 20 µm to minimize damage to the crystals. Count times were optimized to each element as follows: 20 s on peak and 10 s on each background for F, Na, P, Cl, and Ca; 40 s on peak and 20 s on each background Mg, Si, S, Mn, Fe, As, Sr and Y. Synthetic stoichiometric undoped fluorapatite and chlor-fluorapatite grown in the experimental geochemistry laboratory at Memorial University was used to calibrate Ca and F, and Cl, respectively. The other standards that were used, provided by Astimex Standards Ltd., were:

apatite (Wilberforce, ON, Canada) for P; albite (Strickland Quarry, Haddam, Connecticut, USA) for Na and Si; sphalerite (synthetic, CERAC Inc. USA) for S; celestite (Madagascar) for Sr; tugtupite (Greenland) for Cl; rhodinite (locality unknown) for Mn; diopside (Wakefield, Quebec, Canada) for Mg; arsenopyrite (Yaogangxian Mine, Hunan Province, China) for Fe and As; synthetic $Y\text{P}_5\text{O}_{14}$ (synthesized by Ellis Rare Earth Phosphates Ltd.) for Y. Lastly, the OH content in the apatite was calculated using the method proposed by Ketcham (2015).

3.2.5 Laser ablation inductively coupled plasma mass spectrometry

Trace element concentrations in apatite were determined using LA-ICPMS. It was not possible to measure Fe, Na, and S via LA-ICPMS because the high background levels for Fe and the poor ionization efficiency of Na and S make it difficult to produce accurate measurements (San Blas et al., 2015). The 25 mm diameter polished epoxy mounts containing apatite previously analyzed by EPMA were analyzed at the Mineral Analyses Facility – Bruneau Innovation Centre (MAF-IIC) at MUN. The analyses were done using a Thermo-Finnigan ELEMENT XR, a high-resolution double focusing magnetic sector single collector inductively coupled plasma mass spectrometer (HR-ICPMS) coupled to a GEOLAS 193 nm Excimer laser ablation system. The ablated material was transported to the ICP-MS using He gas with a flow rate of 1.25 l/min, with additional Ar make-up gas added after the ablation cell prior to introduction into the ICP-MS. A laser spot size of 40 μm was used with an energy density of 3 J/cm^2 and a laser repetition rate of 8-10 Hz. Time-resolved intensity data were acquired by peak-jumping in a combination of pulse-counting and analog modes, depending on signal strength, with one point measured per peak. Elements in high abundance were analyzed in analog mode to avoid tripping the detector, whereas those in low abundance (i.e., less than 0.1%) were analyzed using pulse-counting mode.

The Ca concentrations determined by the EPMA on the natural apatite samples were used as the internal standard to normalize counts to concentrations for the trace element LA-ICPMS analyses (i.e., ^{44}Ca) (Figure 3.5). For primary calibration, National Institute of Standards in Technology (NIST) 610 glass was used (Pearce et al., 1997). Secondary standards were analyzed to assess the accuracy and precision of the LA-ICP-MS analyses. These included NIST 612 and BCR-2G glass (Pearce et al., 1997), two fragments of apatite from Sludyanka, Russia; as noted above, “MUN Sludyanka” (Dempster et al., 2003), and “JMH Sludyanka” (Figure A.2; Table A.1). The data acquisition sequence consisted of two analyses of the NIST 610 glasses, one analysis of the NIST 612 or BCR-2G glass, one analysis of the external reference materials, followed by 14 analyses of the natural apatites, closing the sequence with a repetition of the secondary standards, followed by two analyses of the NIST 610 series glass.

The LA-ICPMS data were reduced using Iolite software (Paton, 2011). Iolite allows for selection of representative signal intervals, background subtraction, and internal standard correction for ablation yield differences, instrument sensitivity drift, mass bias and mass fractionation, during the analytical session, and does calculations converting count rates into concentrations by reference to the internal standard used (i.e., Ca from the EPMA).

3.3 RESULTS

In order to develop an understanding of both sets of apatite samples, the chemistry of the reference and Gruvberget apatites are presented separately. The datasets are compared in the discussion.

3.3.1 Part 1: Reference apatites

The chemical homogeneity of the reference apatite samples was first assessed qualitatively by doing BSE and CL imaging of each grain to assess internal zoning, and the

presence of mineral inclusions. The only grain that displayed noticeable growth zoning in the BSE images was the Durango apatite, in which the core is slightly darker than the rim, seen as weak growth zoning (Figure 3.5). Other apatite grains are homogenous in BSE, appearing either dark- or light-grey. Some grains, however, such as those from Mineville contain fractures infilled with blebs of BSE dark phases (quartz and feldspar verified by EDS) with inclusions of a BSE bright phase (magnetite). Imaging via CL reveals opposite trends to those seen in BSE imaging, as is usually the case, because regions that are bright in BSE are dark in CL, and vice versa in most minerals (Hanchar and Miller, 1993). Cathodoluminescence images from the bench-top CL (BT-CL) instrument reveal apatite luminescence ranging from blue/lilac to violet (Figure 3.6), attributed to activation of variable amounts of Nd^{3+} , Sm^{3+} , Eu^{3+} and Dy^{3+} ions (Figure 3.6-A, B and E), and in some cases a pale to deep yellow-green activation due to activation of Mn^{2+} which is the usual CL activator in igneous low REE apatite (Roeder et al., 1987; Kempe and Götze, 2002; Bouzari et al., 2016).

Table 3.3 presents data for the major, minor, and trace element composition of the reference apatites. The major cation sites of the reference apatites vary between 52-55 wt.% CaO and 39-42 wt.% P_2O_5 , which is consistent with most igneous apatites (Liu and Comodi, 1993; Piccoli and Candela, 2002). There are some low concentrations, however, including the Mineville MtAp ore sample at 50 wt.% CaO, and the Kola Kovdor-C sample at 39.06 wt.% P_2O_5 . The majority of the samples have high F contents, typically in excess of 3.0 wt.%, classifying them as fluorapatite (Pasero, 2010). Both apatite samples from carbonatites have lower average F values, at 2.39 ± 0.07 wt.% F for the Mud Tank apatite and 0.93 ± 0.03 wt.% F for the Kola Kovdor-C apatite. The Mud Tank and Kola Kovdor-C apatites are, in fact, hydroxyl-

fluorapatites given the negligible Cl content (e.g., 0.03 and 0.01 wt.% Cl), and 1.16 wt.% OH and 2.29 wt.% OH, respectively.

In order to evaluate any crystallographic effects on F concentration (i.e., mobility during electron bombardment), one apatite crystal from the Durango ore was sawed into separate pieces with a diamond sectioning saw and mounted parallel and perpendicular to the *c*-crystallographic axis. The grain mounted parallel to the *c*-axis yielded consistently lower F concentrations ($F = 3.44 \pm 0.03$ wt.% for), whereas the grain mounted perpendicular to the *c*-axis yielded higher concentrations of F, often in excess of the stoichiometric 3.77 wt.% F (e.g., $F = 3.91 \pm 0.03$ wt.%).

The minor element contents vary significantly between apatite samples. The data show a range of Na₂O content between 0.10 wt.% to 0.20 wt.%, and SrO content varies from 250 ppm to 3.5 wt.%. The 3.5 wt.% SrO is associated with the apatite from Kola Kovdor-A and the Mud Tank apatite has the next highest SrO content at 0.44 wt.%. The average SrO content is 0.18 wt.%, excluding the alkaline sample. SiO₂ is in concentrations greater than most other minor elements, ranging from 0.2 wt.% for the Durango ($\perp c$) sample to 2.1 wt.% for the Mineville apatite (Table 3.3). The Mud Tank and Kola Kovdor-A apatite, however, contains no measurable SiO₂ with the EPMA (Table A.4). The Na₂O contents range from 0.08 wt.% for the Otter Lake skarn and Kola Kovdor-C apatite to 0.21 wt.% for the Mineville ore and Sludyanka skarn, with an average of 0.16 wt.% between apatite samples. Lastly, SO₃ contents vary between 0.02 to 1.04 wt.%, and FeO is in the lowest concentration of 0.03 wt.% on average. Intra-grain variation is negligible for most minor elements that are above EPMA detection limits. The percent relative standard deviation ($\% \text{RSD} = (s/\bar{x}) * 100$), calculated from the observed spread in the data, range from 0.2 % to 2 % for major elements, to between 8 % to 40 % for minor elements (Table 3.3).

The following introduces some of the key variations of selected trace element concentrations between apatite samples (Table 3.3).

Magnesium concentrations range between 50 to 200 ppm; the highest and lowest Mg values are associated with the Kola Kovdor-A and C samples and the Durango MtAp ore, respectively. Although, this relationship varies; for instance, when comparing the Durango ore and the carbonatite at Mud Tank the opposite relationship is seen, with the latter having a greater Mg content.

Vanadium contents range from 1 ppm up to 160 ppm. The carbonatite hosted apatite from Kola Kovdor has a V content of 160 ppm. Conversely, the other carbonatite apatite from Mud Tank yields a lower V content of 2 ppm.

Chromium values are generally below 10 ppm for most samples; averaging 5 ppm among all samples. The apatites with highest Cr content are the Otter Lake and the Kola Kovdor-C samples at 6 ppm. Other apatites samples have between 1 to 3 ppm Cr, and Cr contents of the Mineville and Durnago apatite are below LA-ICPMS detection limits (Table 3.3; Table A-3).

Manganese contents vary between 70 to 200 ppm (Table 3.3). The first group, from 70 to 100 ppm comprises the three skarn samples, the Durango ore, and the Kola Kovdor-C sample. The second group that reaches 200 ppm Mn consists of the Kola Kovdor-A, the Mud Tank and the Mineville ore samples. The Mud Tank carbonatite represents the highest Mn content at 245 ppm; yet the other Kola Kovdor-C carbonatite apatite have a Mn content of 68 ppm.

Cobalt concentrations vary between 8 to 40 ppm, with the highest concentration in the Mineville apatites. The Otter Lake and Sludyanka skarn apatites tend to have the lowest Co content, below detection limits (Table A.3) and at 8 ppm (Table 3.3), respectively.

Copper and *zinc* are mostly below LA-ICPMS detection limits of 0.79 ppm and 1.38 ppm, respectively (Table A.3); hence they are in the lowest concentration of all of the trace elements that were measured. Only the Mineville and Mud tank apatites yield Cu contents greater than 1 ppm (Table 3.3), and nearly all Zn concentrations are below the detection limit. These elements are expected to be in low concentration in apatite, because neither has suitable ionic properties (e.g., neither Cu or Zn exist in IX or VII fold coordination in a 2+ oxidation state) to substitute for Ca in igneous apatites (Shannon, 1976).

Arsenic concentrations vary from 9 ppm in the Kola Kovdor-A and Mud Tank samples, to 3,888 ppm in the Mineville ore apatite. Given that AsO_4^{3-} may substitute directly for PO_4^{3-} , apatites crystallizing from an As rich liquid can accommodate high concentrations of As (Hughes and Drexler, 1991); however, for As to effectively substitute for P^{5+} , the As needs to be in an oxidizing environment and be pentavalent because trivalent As is less compatible in the apatite structure. The apatite from the Durango ore has the next highest As content, compared to the Mineville apatite, ranging from 740 to 1085 ppm for Durango ($\perp c$) and Durango ($\parallel c$), respectively. It is important to note that As contents reported here represent ^{75}As measured by LA-ICPMS, which has been reported in several other studies (Xie et al., 2007; Dussubieux and Williams, 2009; Choi et al., 2014). However, this isotope of As has known isobaric interferences, such as $^{40}\text{Ar}^{35}\text{Cl}^+$ (Evans and Giorgio, 1993; May and Wiedmeyer, 1998) that may cause problems for high Cl materials that are analyzed for As.

In order to assess the accuracy of these LA-ICPMS As measurements, three high As apatite crystals, two from Mineville and one from Durango, were measured for As using the EPMA and LA-ICPMS and the results compared (Figure 3.7). These selected reference apatites were chosen due to their high As contents; which allowed for a more reliable interpretation

relative the other reference and Gruvberget apatites at lower As contents and, in turn, higher errors. The data used for the Mineville apatite sample in Figure 3.7 are unpublished LA-ICPMS and EPMA data (JM Hanchar, pers. comm.), respectively, on apatite samples from the Old Bed ore at Mineville, New York.

The average EPMA and LA-ICPMS As contents for these samples were used because they are representative values for each respective technique over a large enough range to draw a reliable comparison between them. The difference in average As content measured by both techniques for the Durango and Old Bed Ore apatite are 25% and 6% difference, whereas the Mineville ore apatite of this study yields only a 5% difference. Further, nearly all three data points, with the exception of the Durango ore apatite, agree within error with respect to the 1:1 line on Figure 3.7. These variations are quite small given the inherent variation in As contents between the techniques coupled with intra-gain heterogeneities; hence, this comparison reveals that As concentrations reported from LA-ICPMS are accurate relative to the EPMA.

Strontium values range from 300 ppm to 2.6 wt.%. The high Sr concentrations of 2.6 wt.% correspond to the Kola Kovdor-A sample. The Mud Tank and Kola Kovdor-C carbonatites as well as the Otter Lake and Sludyanka skarns range from 3,100-3,700 ppm down to 1,200 ppm, respectively. The apatite from Mineville and Durango ore yield the lowest Sr values from 300 to 500 ppm. Though discussed earlier as a minor element measured via EPMA, Sr is also presented here to demonstrate consistency and accuracy between the two analytical techniques. The high Sr contents of the apatites in this study may allow for measurement of Rb-Sr isotopes in apatite, which may be used as a radiometric dating technique or as a correlation tool between lithologies (Samson et al., 1995; Carey et al., 2009).

Barium concentrations form three groups: one is between 1 to 4 ppm; another from 20 to 40 ppm; and one sample at 350 ppm (Table 3.3). The lower Ba values belong to the Sludyanka, Otter lake, Durnago, and Mineville apatites, the second intermediate group represents the Mud Tank and Kola-Kovdor-C samples, and the highest Ba contents belong to the apatite from the Kola Kovdor-A sample.

Rare earth elements (the lanthanides La to Lu and Y and Sc [but Sc was not measured in this study]) in all of the apatite crystals analyzed show a general LREE enrichment (Figure 3.8-A). The degree of enrichment is revealed by the $(Ce/Yb)_{cn}$ ratio (Belousova et al., 2002; Dempster, 2003), which ranges from 7 to 380 for all the samples, depending on the type of host rock. Apatite from skarns tend to have the lowest LREE enrichment whereas, the carbonatite samples show the greatest enrichment (Figure 3.8-A). The $(Ce/Yb)_{cn}$ ratios for the Mud Tank and Kola Kovdor-C carbonatites and the Kola Kovdor-A alkaline samples range from 100 to 380, respectively, and the lowest ratios are seen in the Sludyanka and Otter Lake skarns and Durango and Mineville MtAp ore samples, ranging from 10 to 40. This reflects a greater LREE enrichment in apatite from highly differentiated, carbonatitic and alkaline melts in which the apatite crystallized (Loubet et al., 1972; Verplanck et al., 2014). The total REE content (ΣREE) of the apatites analyzed, varies from 1.0 to 2.0 wt. %; with a low and high values at 200 ppm (Sludyanka, Skarn) and 5.6 wt.% (Mineville). The range between 1.0 to 2.0% ΣREE includes the Mud Tank carbonatite, Durango ore, Kola Kovdor-A and only one skarn (Otter Lake) hosted apatite sample. The high REE content of the Mineville apatite has been known for decades now, and shows the ability of apatite to accommodate high concentrations of trace elements without significantly compromising the apatite crystal structure (e.g., McKeown and Klemic 1954; Roeder et al. 1987).

Apatite samples display variable Eu anomalies (e.g., $\text{Eu}/\text{Eu}^* = [2^*\text{Eu}]_{\text{cn}} / [\text{Gd}+\text{Sm}]_{\text{cn}}$), in which Eu/Eu^* values range from 0.3 to nearly 1. The lowest Eu/Eu^* values, represented graphically by a deeper Eu trough (Figure 3.8-A), correspond to the MtAp and skarn apatites at 0.3 and 0.7, respectively. Conversely, the apatites from the Mud Tank and Kola Kovdor-C carbonatitic and Kola Kovdor-A alkaline rocks show little to no Eu anomaly, with an average Eu/Eu^* of nearly 1.0. The variation in Eu anomalies between the apatites appears to be proportional to the degree of fractionation, given that Eu^{2+} may be incorporated into feldspars during fractional crystallization of silicate melts (Weill and Drake, 1973; Bau, 1991). Strontium in apatite has been proposed as a reliable tracer of whole rock Sr (Piccoli and Candela, 2002; Belousova et al., 2002; Pan et al., 2016), and in Figure 3.9 Eu anomalies and apatite Sr content show a positive correlation.

Lead, Thorium, and Uranium contents tend to exhibit a covariation with total REE content, which suggests the apatites crystallized from a source mutually enriched in REE and HFSE. Lead (i.e., radiogenic and non-radiogenic Pb) contents cluster to form two groups: one ranging from 1 ppm to 10 ppm and another from 30 ppm to 100 ppm. The higher Pb values are generally associated with enrichment in other HFSEs (Table 3.3). Much like Pb, the Th content also appears to be proportional to REE content, with the highest Th concentrations seen in the most REE enriched samples (e.g., Mineville ore and Kovdor Carbonatite). There is, however, noticeable variation in Th content within the sample groups. Apatite from the Kola Kovdor-C and Mud Tank carbonatites yield both high and low Th values, from 1,600 ppm to 27 ppm, respectively; whereas, Sludyanka and Otter Lake skarn samples vary from 125 ppm to 400 ppm, respectively. Thorium is high in the Mineville ore apatite at 1,200 ppm relative to the lower 240 to 180 ppm Th in the apatite from the Durango ore. The concentration of Th is lowest in the Kola

Kovdor-A alkaline sample, at 14 ppm. Uranium concentrations vary from 2 ppm up to 180 ppm for the Kola Kovdor-A apatite and the Mineville ore sample, respectively. In general, the Mineville ore and Sludyanka skarn apatites have the highest U content, from 180 ppm to 60 ppm. Remaining apatite U values decrease in content from the Kola Kovdor-C at 30 ppm, the Durango ore at 10 ppm, the Mud Tank carbonatite at 6 ppm, down to the Kola Kovdor-A apatite at 1.6 ppm.

3.3.2 Part 2: Gruvberget apatites

The population of Gruvberget apatite samples comprises 60 apatite grains consisting of 20 grains per each of the three samples.

The Gruvberget apatites were imaged using BSE and CL to assess grain homogeneity and reveal any visible compositional zoning or inclusions of other minerals. The BSE imaging revealed little to no compositional zoning within grains from all three samples. In general, all grains appeared a homogenous grey to light grey at the same brightness and contrast settings in BSE (Figure 3.5); with the apatites from the ore and dyke yielding both light grey and grey grains, and the biotite schist containing only grey grains. CL imaging revealed slight grain heterogeneities, such as weak sectoral and concentric zoning. The yellow-green luminescence seen in the bench-top CL images of the MtAp ore apatite (Figure 3.3-2b and 2d) is likely attributed to Mn²⁺ activation (Kempe and Götze, 2002).

See Table 3.4 for major and trace element compositions of the three Gruvberget apatite samples. Despite the samples being from very different host rocks, they share similarities in their composition. This is due to the weak minor element enrichment. As a result, some elements may be grouped together and described collectively, with exceptions noted. The major cation structural elements, Ca and P, are nearly stoichiometric with concentrations of 55.1 to 55.9 wt.%

CaO and 41.8 to 42.5 wt.% P₂O₅ for all three apatite samples. However, the halogen site is dominated by F, with lesser amounts of Cl and OH. The fluorine content decreases systematically from 3.0 wt.% for the biotite schist to 2.5 wt.% for the MtAp ore, and 2.2 wt.% for the metadiabase dyke. The decrease in the F content is balanced by an increase in Cl content from 0.4 wt.% to 0.6 wt.%. The calculated apatite OH contents in apatite range from a mean of 0.4 wt.% (biotite schist), through 0.8 wt.% (MtAp), to 1.0 wt.% (metadiabase). The nominal OH and Cl content appears to be characteristic of the Gruvberget apatites, particularly the Cl contents which separate them from the reference apatites. Average concentrations (over all Gruvberget samples) for minor elements measured by EPMA, in decreasing content, range from 300 ppm S, 200 ppm Si, 150 ppm Na and 150 ppm Fe. Sulfur is in the highest concentration, and it also displays the most variation between the three Gruvberget samples, increasing from the biotite schist at 160 ppm, to the MtAp ore at 240 ppm, up to the metadiabase dyke at 280 ppm.

Like the minor element composition, the trace element chemistry of the Gruvberget apatite samples shows little variation (Table 3.4-Trace Elements), and individual element contents rarely exceeding 1000 ppm. Despite the low concentrations, there is enough variation in the trace element chemistry of the apatites to distinguish intra- and inter-sample trends.

Magnesium contents are greatest in the biotite schist apatite, ranging an order of magnitude from 67 ppm to 715 ppm, at an average of 150 ± 150 ppm Mg. Concentrations of Mg for the MtAp ore and metadiabase dyke average 80 ppm.

Vanadium increases from an average of 1.5 ppm in the biotite schist to 20 ppm in the metadiabase dyke, and 40 ppm in the MtAp ore. Vanadium content is most variable in the biotite schist and the least in the MtAp ore with RSDs at 60% and 30%, respectively. The metadiabase dyke apatite is in between these with an RSD of 40%. The higher V content of the MtAp ore

apatite is reasonable given that apatite typically forms in veins in the MtAp ore in the Gruvberget ore, which is most enriched in V (Table 3.2; Figure 3.2- MtAp ore).

Chromium is another transition metal in low concentrations, ranging from 5 to 20 ppm. Chromium contents are greatest in the MtAp ore and diabase dyke apatites at an average of 6 ppm. The Cr contents of the biotite schist apatite average 5 ppm.

Manganese concentrations range between 250 to 600 ppm over the three groups of Gruvberget apatites, forming discrete clusters in Mn content within and between samples. Firstly, the biotite schist exhibits two distinct clusters in Mn content at 300 ppm and 600 ppm, whereas the MtAp ore and metadiabase dyke apatites form single fields in Mn content at 300ppm and 400ppm, respectively (Table 3.4; Figure 3.10-B). These fields are well-resolved when shown with respect to Sr in Figure 3.10-B, since the Sr homogeneity in apatite acts as a basis to reveal variations in Mn content.

Cobalt, copper, and zinc are in the lowest concentrations in apatites from all sample sets. Most measurements are below detection limit, with sparse concentrations of 0.5 ppm to 3 ppm.

Arsenic contents range from the metadiabase dyke at 270 ppm, to the MpAp ore at 260 ppm, and the biotite schist at 40 ppm; with an RSD of 15% for the prior, to 25% for the latter two samples.

Strontium is present in similar concentrations to Mn and decreases from 440 ppm to 250 ppm down to 215 ppm, from the biotite schist to the MtAp ore to the metadiabase dyke, respectively. The low RSDs of 5-10% make Sr the trace element with the most consistent concentrations in the Gruvberget apatites (Table 3.4; Figure 3.10-A and B).

Barium is known to form a complete solid solution with Ca in ClAp (Akhavan-Niaki, 1961); however, the Gruvberget apatites in all three samples yield Ba contents that are mostly below detection limits and, when detected, rarely exceed 1 ppm.

The REE (*La to Lu* and *Y*) chemistry of all apatites is consistent, with subtle variations unique to each sample set. Chondrite normalized REE profiles for the Gruvberget apatites in Figure 3.8 (B, C and D) reveal overlap in La to Lu content between samples, and the spread in REE content decreases from the MtAp ore, the biotite schist and metadiabase dyke. The biotite schist and MtAp ore apatite yield an average Σ REE content of 0.15 wt.%, and the metadiabase dyke apatite has 0.10 wt.% Σ REE (Figure 3.10-C). Although, some MtAp apatite grains have up to 0.5 wt.% Σ REE content (Figure 3.10-C)

Note that the chondrite normalized whole-rock REE contents for the biotite schist, the MtAp ore, and metadiabase dyke (unpub. data from A. Westhues and JM Hanchar, pers. comm.) are also shown on Figure 3.8 (B,C and D) as the black dotted line. All three samples exhibit negative Eu anomalies and a LREE enrichment. However, the biotite schist and metadiabase dyke also display a slight negative Y anomaly. The MtAp ore sample shows the most apparent LREE enrichment in Figure 3.8-C.

The Gruvberget apatite REE distributions exhibit both LREE and HREE enrichment as revealed by the $(\text{Ce}/\text{Yb})_{\text{cn}}$ values in excess of and below one, respectively (Figure 3.10-C). When considering LREE enrichment with respect to total REE content in Figure 3.10-C, there appears to be a moderate correlation; with the exception of some outliers from the MtAp ore apatite that show excess REE enrichment. The latter REE enriched apatites, at 0.5 wt.% total REE, maintain $(\text{Ce}/\text{Yb})_{\text{cn}}$ ratios of 10 as REE content increases (Figure 3.8-C; Figure 3.10-C).

There magnitude of europium anomalies ranges from an average of 0.6 for the biotite schist apatite, to an average of 0.4 for the MtAp ore and the metadiabase dyke (Figure 3.10-D). This variation is more clearly seen in Figure 3.8 as a smaller negative Eu anomaly for the biotite schist (Figure 3.8-B) compared to the MtAp ore (Figure 3.8-C), and the metadiabase dyke (Figure 3.8-D).

Lead, thorium, and uranium are present in low quantities in all of the Gruvberget apatites. Uranium and thorium are in greater concentration than lead, with an average of 4 ppm U and 2 to 6 ppm Th, compared to 0.5 to 1 ppm Pb. The concentrations of Pb, U and Th vary between samples. The increasing concentration of these elements covary with REE content (Figure 3.11).

3.4 DISCUSSION

3.4.1 Reference apatites compared to the Gruvberget apatites

Discerning differences in apatite chemistry is key in revealing potential implications for ore and rock forming processes; assuming that apatite is an effective tracer of geochemical processes (e.g., Tepper and Keuhner, 1999; Belousova et al., 2001, 2002; Piccoli and Candela, 2002; Chew et al., 2011; Miles et al., 2014; Harlov, 2015). In an attempt to better understand differences in apatite chemistry between the apatite analyses of the nine reference samples and the three Gruvberget samples, discrimination diagrams from other studies were used to display the data (from Belousova et al., 2002; Piccoli and Candela, 2002) (Figure 3.10 and Figure 3.12). The environments in which the reference apatite samples crystallized are generally well constrained; which in turn provide compositional constraints from a larger geologic perspective, discussed with respect to the detailed case study for the Gruvberget apatite samples.

Figure 3.10 (A to D) presents four empirical discrimination plots for apatite chemistry from different rock types described in Belousova et al. (2002). It is important to note that not all

of the apatites in the present study, from the known rock types, plot in their respective compositional fields, revealing the lack of suitability in using empirical diagrams such as these. In particular, the apatite from all skarn samples, the alkaline complex, and the exceptionally REE-enriched Mineville apatites, plot outside of the discriminant fields in Figure 3.10. In the case of the skarn samples, it is reasonable that they do not plot in any regime given the unconstrained influences of metasomatism on primary apatite chemistry. However, the Mineville ore apatites, and other particularly REE-enriched apatites, are important to consider given that they represent compositional end members for trace element enrichment. The Mineville apatite, for example, plot outside of the compositional regimes for iron ore, as well as the whole graph area in Figure 3.10-B, C and D due to the 5.5 wt.% REE and 0.8 wt.% Y. Therefore, the discriminant diagrams in Figure 3.10 work only for specific cases, and may misrepresent apatites with anomalous trace element compositions from a known deposit type.

Figure 3.10-A shows variation in Sr content with respect to Y content. Substitution of Sr for Ca is common in apatite and has been supported by both experimental and natural data (Efimov et al. 1962; Hughes et al. 1991; Khattech and Jemal 1997; Rakovan and Hughes 2000; Fleet and Pan, 2002). The Durango ore apatites plot closest to the biotite schist apatite samples from Gruvberget, and both plot in the granitoid and iron ore field. The MtAp ore and metadiabase dyke plot further left into the granitoid field, at a lower Y concentration.

The three Gruvberget apatite samples exhibit a relative Mn enrichment compared to the reference apatites, as can be seen in a plot of Fe-Mn-Ce (Figure 3.12-A) with a spread in Gruvberget data points towards the Mn apex. The amount of enrichment towards the Mn apex is seen as a step-like progression towards the Mn apex from the biotite schist, to the MtAp ore, to the metadiabase coinciding with a systematic decrease in Fe content, respectively. Likewise,

each Gruvberget sample exhibits a Mn enrichment in Figure 3.12-C, seen plotting along the Ca-Mn line, compared to the reference apatites that plot along the Ca-Na line. Once again, the biotite schist exhibits the greatest Mn and Fe enrichment, followed by the MtAp ore, and metadiabase. This variation likely reflects the availability of large radius cations substituting for Ca with changes to the environment in which the apatite crystallized. Projecting the Gruvberget and reference apatite data in Fe-Mn-Ca ternary space (Figure 3.12-B) yields the closest similarity between the two populations. This represents direct multi-cation substitution of Fe^{2+} and Mn^{2+} for Ca^{2+} . The Mn enrichment, coupled with an increased Fe content, directs the trend of the Gruvberget apatites perpendicular to the Mn-Fe line in Figure 3.12-B. However, all apatites are generally low in Fe (typically less than 0.1 wt.%), as a result of iron-rich minerals precipitating (e.g., magnetite) prior to apatite crystallization (Johannes and Holtz 1996). In the case of the massive MtAp deposit at Gruvberget, Mineville, and Durango, it is reasonable to assume the ore bodies act as a major sink for Fe; hence, limiting Fe uptake by apatite. This is evidenced by petrographic relationships, where magnetite forms intimately within apatite crystals in the Gruvberget host rocks (e.g., biotite schist: Figure 3.3-1c)—suggesting Fe sequestration in magnetite that forms along grain boundaries and as inclusions in apatite. The accommodation of Fe may also be a function of $f\text{O}_2$, where a reducing environment would be favoured to incorporate Fe^{2+} instead of Fe^{3+} to maintain charge balance via direct substitution for Ca^{2+} (Hughes et al., 1993).

Although the Gruvberget MtAp ore apatites are depleted in LREEs relative to the Durango MtAp ore apatite, the Y contents are within the same range from 400 ppm to 800 ppm (Figure 3.10-A). The biotite schist apatite from Gruvberget also plots directly atop the Durango MtAp ore samples in Figure 3.10-A. As seen in Figure 3.8 and Figure 3.10-C, all three

Gruvberget samples are depleted in LREEs compared to the reference apatites, reflected by the $(\text{Ce}/\text{Yb})_{\text{cn}}$ values for the reference apatites which range from 10 to 300 (moderate to steep LREE enrichment), whereas the Gruvberget apatites range from 0.1 to 10 (shallow to moderate LREE enrichment). This LREE depletion, however, is variable for all Gruvberget samples as revealed by a greater spread in the La to Sm contents compared to Gd to Lu when considering all REE patterns from La to Lu (Figure 3.8-B, C and D; Figure 3.10-C). The greatest spread in LREE values is associated with the MtAp ore apatite (Figure 3.8-C), and the spread tightens from the biotite schist to the metadiabase dyke (Figure 3.8-B and D). The apatite LREE and HREE concentrations may be a primary (magmatic) or secondary (hydrothermal, or ore mineralization) signature, controlled by either melt REE composition, or that of a metasomatic fluid (Boudreau and McCallum, 1990; Harlov and Förster, 2002; Piccoli and Candela, 2002; Harlov, 2015). According to Frietsch and Perdahl (1995), the clearly magmatic associated apatites of the Kiruna MtAp deposits may yield a LREE-depletion from: 1) more mafic host rocks; or 2) through mobilization of LREEs via Cl-rich hydrothermal fluids (Taylor and Fryer, 1983). The findings of Taylor and Fryer (1983) reflect alteration of granitoid rocks, and it is assumed that these processes yield similar implications regarding the more mafic host rocks at Gruvberget. Both of these factors 1) and 2) may be responsible for the REE composition of the three Gruvberget apatite samples, given that the rocks are generally more mafic than host rocks of the Kiruna deposits (Frietsch and Perdahl, 1995; Bergman et al., 2007) and have likely experienced protracted metasomatism by Cl-rich hydrothermal fluids (Harlov et al., 2002).

As mentioned above, the three Gruvberget apatite samples are characteristically enriched in Cl and OH relative to most of the reference apatites (Figure 3.12-E). According to Zhu and Sverjensky (1991), apatite F, Cl and OH contents are controlled by 3 factors: 1) the melt and/ or

fluid composition; 2) the presence of other F- and Cl-bearing minerals (e.g., biotite and scapolite); and 3) the P-T conditions. The Gruvberget apatites are enriched in Cl and OH relative to the reference apatites in Figure 3.12-E. Later hydrothermal alteration of apatite via metasomatism by Cl-rich fluids could also explain the enrichment in OH, Cl of the three Gruvberget apatite samples (Frietsch and Perdahl, 1995; Harlov and Förster, 2002). However, the complex magmatic-hydrothermal evolution of these systems and lack of constraints on P and T make it difficult to constrain the role of hydrothermal alteration. Given that Gruvberget MtAp ore apatite lacks other REE phosphates inclusions (e.g., monazite), which are common alteration products during metasomatism (Harlov et al., 2002a; Harlov et al., 2002b), it limits the interpretation as to what extent the rocks interacted with Cl-rich hydrothermal fluids. The absence of a separate REE phosphate mineral (e.g., monazite or xenotime), however, may be explained by the presence of Na in NaCl brines, discouraging the growth of monazite inclusions and rim grains via Na retention in the apatite structure to maintain charge balance through equation 2 above (Harlov, 2015). This case is likely, given the pervasive sodic alteration (i.e., scapolitization) of the rocks at Gruvberget (e.g., Figure 3.3-3b and 3c). It is also possible that the original apatite composition did not contain enough REEs to precipitate a separate REE phosphate; therefore, the resulting hydrothermal fluid composition, subsequent to apatite alteration, was undersaturated in REEs.

The reference apatites are enriched in Na and Si compared to the Gruvberget apatites due to their higher REE content (see equations 1 and 2). This is seen clearly in Figure 3.12 -C and D. The apatites from Gruvberget plot inside the ternary between Na_{02} and Na_{10} in Figure 3.12-C and, the highest Si concentrations reach the lowest Si content of the Durango apatite in Figure 3.12-D. The coupled substitution of REE and Na (equation 2 above) is expressed by the reference

apatites plotting along the Ca and Na line, and direct substitution of Mn^{2+} for Ca^{2+} is represented along the Ca-Mn line. Substitution of Mn is common in apatite, with reported Mn contents reaching 1.37 atoms per formula unit in natural fluorapatite (Fleet and Pan, 2002). Like Fe, Mn is also sensitive to redox conditions and may exist as Mn^{2+} and Mn^{3+} in reducing and oxidizing environments, respectively (Miles et al., 2014). This sensitivity of Mn oxidation state makes it an excellent redox proxy for silicic magmas; evidenced by a strong correlation with $f\text{O}_2$ (cf., Fig. 9 of Miles et al., 2014). Given that all three Gruvberget apatites are depleted in REE, they tend to plot closer to the apexes involving directly substituting cations (Mn in Figure 3.12-C), or stoichiometric elements (P in Figure 3.12-D), as opposed to the cations involved in coupled substitution with REE (Na in Figure 3.12-C). This is evidenced in S-Si-P ternary space (Figure 3.12-D), with the reference apatite plotting towards the Si apex and the Gruvberget apatites closer to the P apex—controlled by substitution of Si and REE^{3+} via equation 1. Although, the mutual enrichment in Si and S in Figure 3.12-D for all three Gruvberget apatites may also reflect coupled substitution of SiO_4^{4-} and SO_4^{2-} for PO_4^{3-} via equation (3).

3.4.1.1 Controls on apatite chemistry

To summarize the previous discussion, compared to reference apatites, the Gruvberget apatites are: 1) depleted in REEs, especially LREEs; 2) depleted in REE charge balancing cations Na and Si; 3) enriched in Cl and OH; and 4) enriched in Mn. The following explains in more detail the differences between the three Gruvberget apatite samples themselves with respect to the general comparisons made in points 1) through 4). For 1), the metadiabase apatite is most depleted in REE, whereas the apatite from the biotite schist and MtAp ore have greater REE contents (Figure 3.10-C). Based on the $(\text{Ce}/\text{Yb})_{\text{cn}}$ values shown in Figure 3.10-C, all apatite samples overlap from 0.1 to 10, with the MtAp ore apatite slightly enriched in LREE relative to

the biotite schist and metadiabase dyke. This seems reasonable given that the magmatic apatite of the diabase dyke would have primarily had a mantle-signature, meaning that the LREE composition would have initially been less enriched relative to the MtAp ore (cf. dolerite and iron ore in Fig. 1 of Belousova et al., 2002). For 2), the metadiabase apatite has greater OH and Cl contents relative to the biotite schist and MtAp ore (Figure 3.12-E). However, the biotite schist exhibits the greatest spread in Cl and OH content (Figure 3.12-E). Like the LREE composition, the greater Cl content of the metadiabase dyke may be explained by a mantle-derived melt; whereby apatite may have crystallized earlier from an undifferentiated melt prior to volatile exsolution at a higher bulk melt Cl content (Piccoli and Candela, 2002). For 3), the Mn contents of each apatite sample form distinct single clusters for the MtAp ore and metadiabase, and two independent clusters for the biotite schist in Figure 3.10-B. The higher cluster for the biotite schist has the greatest Mn content relative to the metadiabase dyke and MtAp ore, while the other lower cluster in Mn content for the biotite schist groups with both of the latter samples (Figure 3.12-B and C). The distinct groupings in Mn content likely reflect local changes to redox conditions of the melt and/or metasomatic fluid, with Mn accommodation in apatite increasing under reducing conditions due to the compatibility of Mn^{2+} through direct substitution (Miles, 2014). For 4), the REE charge balancing cations, Na and Si, display significant overlap between all three samples (Figure 3.12-C and D). The Na contents, however, form a tighter cluster of points in Figure 3.12-C compared to Si in Figure 3.12-D. The significance of the tighter cluster of Na content relative to Si is consistent with a sodic hydrothermal fluid that may have buffered the Na content of the apatite to retain REE charge balance (Harlov, 2015). These chemical indicators suggest that alteration may be the controlling factor for the composition of the Gruvberget apatite samples, and the current chemical footprint hides most, but not all, of the

preceding history each apatite grain has experienced since primary crystallization. In the case of the apatite from the biotite schist and the metadiabase dyke at Gruvberget, the primarily magmatic compositions have been overprinted by metamorphism, and then later by metasomatism, but they still retain relict signatures that offer insight into the geological environments in which they originally crystallized. The MtAp ore apatite, however, presents a geological quandary since it shares a similar composition to the other two samples, but the origin of its composition is unknown due to the uncertainties in ore genesis (i.e., it was either originally magmatic with a metasomatic overprint, or it has an entirely metasomatic origin).

Similar apatite compositions characteristic of metasomatism have been reported in apatite from other deposits, such as the Ødegårdens Verk in Norway (Liefertink, 1994; Engvik et al., 2009; Harlov et al., 2002b; Harlov, 2015), as well as other aforementioned Kirunavaara MtAp deposits (Harlov et al., 2002a). These similarities further supports possible metasomatic alteration that has overprinted the primary compositional signatures for each of the three Gruvberget samples; for example, all three Gruvberget apatite samples share an overprinted halogen site composition and significant REE depletion. Further, the Ødegårdens Verk, similar to Gruvberget, contains apatite coexisting with Cl-endmember scapolite (marialite: $\text{Na}_4\text{Al}_3\text{Si}_9\text{O}_{24}\text{Cl}$). Although the apatite at the Ødegårdens Verk is hosted in a metagabbro which is not a direct geological analogue to the host rocks at Gruvberget, it does offer insight into the processes that may overprint apatite halogen compositions through alteration by hydrothermal fluids. Other examples include metasomatism of fluorapatite to chlorapatite documented in mafic-ultramafic complexes of the Ural Mountains, Russia (Krause et al., 2013) due to alteration via CaCl_2 -enriched brines derived from alteration of plagioclase by NaCl brines.

In Figure 3.12-E, the halogens occupying the X site in apatite are represented as mole fractions as XHAp, XCAp and XFAp. At the bottom right apex of Figure 3.12-C the Gruvberget biotite schist apatite clusters near the Durango ore apatite. Although, the Gruvberget apatites trend away from XFAp apex, with the data points for the metasdiabase dyke and MtAp ore apatite extending further towards the XHAp-XCAp line. The MtAp ore apatite theoretically should plot near the Durango ore apatite given that they are both derived from iron ore hosted in hydrothermally altered rocks; however, the MtAp ore data points plot away from the Durango ore apatite due to enrichment in OH and Cl. This may suggest a contrast in hydrothermal fluid compositions between the samples, or a difference in original apatite composition for the Gruvberget MtAp ore sample that was either more susceptible to metasomatism, or had primarily been enriched in OH and Cl.

The Gruvberget apatites also diverge from the Mud Tank and Kola Kovdor-C carbonatite apatites and the Sludyanka skarn apatites which lie along the XHAp-XFAp line. This divergence is expected since those reference apatites formed in vastly different geological settings than the rocks from which the Gruvberget apatites were derived and have experienced variable degrees of alteration. The spread in the biotite schist apatite Cl content in Figure 3.12-C may reflect local changes in hydrothermal alteration of apatite, or could be related to original apatite composition. By plotting Cl against Mn for the three Gruvberget apatite samples, two discrete populations for biotite schist are resolved; with one cluster at 0.25 wt.% Cl and 350 ppm Mn, and another at 0.65 wt.% Cl and 650 ppm Mn (Figure 3.13). The other Gruvberget samples in Figure 3.13 cluster at 300 ppm Mn and 0.25 wt.% Cl for the MtAp ore apatite, and span from 400 to 500 ppm Mn and 0.5 wt.% to 0.6 wt.% Cl for the metadiabase apatite. As expected, the Cl- and Mn-enriched Gruvberget apatites plot away from the reference apatites that are relatively depleted in these

elements. The two Durango MtAp ore samples, however, do share a Cl enrichment close to that of the Gruvberget MtAp ore apatite at ~ 0.4 wt. % Cl, but lack an associated Mn enrichment. The variation in the Cl content of the apatite from the biotite schist may be explained by minor local changes to the hydrothermal (potentially metamorphic derived) fluid composition, and the presence of other Cl-bearing minerals buffering the Cl content in apatite (Zhu and Sverjnsky, 1991). This seems reasonable given that the apatite in biotite schist sample occurs as intergrowths within biotite along foliation (Figure 3.3-1c), so the magmatic apatite was likely metamorphosed and later locally overprinted by a hydrothermal fluid during metasomatism. The covariance between Cl and Mn in Figure 3.13 for the biotite schist may imply local changes to hydrothermal fluid composition and redox conditions, assuming that Mn is a reliable tracer of fO_2 (Miles, 2014). The presence of scapolite and actinolite in the metadiabase dyke that crosscuts the ore and host rocks suggests metasomatic alteration post- and/or syn-mineralization by a sodic-calcic brine.

3.5 CONCLUSIONS

This study presents the chemistry of apatites from different geological environments (i.e., reference apatites), as well as apatite from the Gruvberget MtAp deposit in Northern Sweden. The reference samples consist of apatites hosted in carbonatites, MtAp ores, skarns and an alkaline suite. The Gruvberget apatites were sampled from the footwall biotite schist that is adjacent to the iron ore body, a portion of the MtAp ore, and a metadiabase that crosscuts both the MtAp ore and host rocks. Analyses using EPMA and LA-ICPMS were used to determine major, minor, and trace element compositions of apatite, respectively. The crystal chemistry of the reference and Gruvberget apatites were compared in order to provide insights into geological environments and/or processes associated with a given apatite composition.

Observations from apatite compositions on empirical discrimination diagrams reveal insights into the effects of rock-forming and post-crystallization metasomatic alteration on apatite chemistry. Given that the geological settings associated with the reference apatites are relatively well constrained, plotting their compositions on these empirical discrimination diagrams (e.g., Figure 3.10) tested the reliability of properly representing the data in the respective environment in which they crystallized. The diagrams in Figure 3.10 misrepresent the apatite source region of apatites that are highly enriched in elements normally presented as traces. Other apatite samples, however, from the carbonatites, and the Durango and Gruvberget MtAp ore do plot in the respective compositional fields in Figure 3.10. Further discrimination of the apatites was using ternary plots involving elements that commonly substitute in the apatite structure (e.g., Mn and Fe; Figure 3.12).

The three Gruvberget samples with respect to the reference apatites are: 1) depleted in REEs, especially LREEs; 2) depleted in REE charge balancing cations Na and Si; 3) enriched in Cl and OH; and 4) enriched in Mn.

These points may be further explained based on differences between the three Gruvberget samples as follows: 1) the metadiabase dyke being most depleted in REEs is indicative of a primary mantle-signature; 2) the greater Cl content of the metadiabase dyke relative to the biotite schist and MtAp ore suggests a mantle-derived melt; 3) the distinct groupings in Mn content likely reflect local changes to redox conditions of the melt and/or metasomatic fluid; and 4) the significance of the tighter cluster of Na content is consistent with a sodic hydrothermal fluid that may have buffered the Na content of the apatite to retain REE charge balance. The halogen composition of apatite was used as a proxy for degree of hydrothermal alteration, given that metasomatism of apatite allows for overprinting of primary halogen site composition (e.g.,

fluorapatite altered to chlorapatite). The pervasive alteration assemblage of actinolite and scapolite in the biotite schist host rock and metadiabase dyke that cross cuts the ore and host rocks suggests metasomatism via a sodic-calcic hydrothermal fluids post- and/or syn-mineralization. Moreover, the Cl-enriched and LREE-depleted nature of the apatites suggests that the hydrothermal fluid was a Cl-brine that imparted a higher Cl content and removed LREEs during the metasomatic reaction. Covariation in the Mn and Cl content of apatite from the biotite schist footwall in Figure 3.13 may also represent a case of local variations in the composition and redox conditions of the same sodic-calcic Cl-brine, and buffering of Cl by the presence of other Cl-bearing minerals. In the case of the apatite from the biotite schist and the metadiabase dyke at Gruvberget, the primarily magmatic compositions have been overprinted by metamorphism, and then later by metasomatism, but they still retain relict signatures that offer insight into the geological environments in which they originally crystallized. The MtAp ore apatite, however, presents a geological quandary since it shares a similar composition to the other two samples, but the origin of its composition is unknown due to the uncertainties in ore genesis (i.e., it was either originally magmatic with a metasomatic overprint, or it has an entirely metasomatic origin). This study demonstrates how sensitive apatite composition is to post-crystallization alteration, but the retention of primary signatures in apatite also exhibits how chemically robust this mineral is and its usefulness when attempting to unravel the complex evolution of rock- and ore-forming processes.

3.6 REFERENCES

- Akhav, AN. (1961). Contribution a letude des substitutions dans les apatites. Paper presented at the *Annales de Chimie France*, 6, pp. 51-79.
- Anders, E., & Grevesse, N. (1989). Abundances of the elements: Meteoritic and solar. *Geochimica et Cosmochimica Acta*, 53, 197-214.
- Barfod, G. H., Otero, O., & Albarède, F. (2003). Phosphate Lu–Hf geochronology. *Chemical Geology*, 200, 241-253.
- Barton, M. D., & Johnson, D. A. (1996). Evaporitic-source model for igneous-related Fe oxide–(REE-Cu-Au-U) mineralization. *Geology*, 24, 259-262.
- Bau, M. (1991). Rare-earth element mobility during hydrothermal and metamorphic fluid-rock interaction and the significance of the oxidation state of europium. *Chemical Geology*, 93, 219-230.
- Bayanova, T., Kirnarskij, Y. M., & Levkovich, N. (1997). U-Pb dating of baddeleyite from Kovdor massif. *Doklady Akademii Nauk-Rossijskaya Akademiya Nauk*, 356, 509-511.
- Belousova, E., Walters, S., Griffin, W., & O'Reilly, S. (2001). Trace-element signatures of apatites in granitoids from the Mt Isa Inlier, northwestern Queensland. *Australian Journal of Earth Sciences*, 48, 603-619.
- Belousova, E. A., Griffin, W. L., O'Reilly, S. Y., & Fisher, N. I. (2002). Apatite as an indicator mineral for mineral exploration: trace-element compositions and their relationship to host rock type. *Journal of Geochemical Exploration*, 76, 45-69.
doi:[http://dx.doi.org/10.1016/S0375-6742\(02\)00204-2](http://dx.doi.org/10.1016/S0375-6742(02)00204-2)

- Bergman, S., Weihed, P., Martinsson, O., & Eilu, P. (2007). Geological and tectonic evolution of the northern part of the Fennoscandian Shield (Field trip guidebook No. Guide 54) Geological Survey of Finland.
- Billström, K., & Martinsson, O. (2000). Links between epigenetic Cu-Au mineralizations and magmatism/deformation in the Norrbotten county, Sweden. Paper presented at the *Abstract volume and Field trip Guidebook, 2nd annual GEODE-Fennoscandian shield field workshop on Palaeoproterozoic and Archean greenstone belts and VMS districts in the Fennoscandian Shield, 28.*
- Black, L., & Gulson, B. (1978). The age of the Mud Tank carbonatite, Strangways Range, Northern Territory. *BMR Journal of Australian Geology and Geophysics*, 3, 227-232.
- Bonyadi, Z., Davidson, G. J., Mehrabi, B., Meffre, S., & Ghazban, F. (2011). Significance of apatite REE depletion and monazite inclusions in the brecciated Se–Chahun iron oxide–apatite deposit, Bafq district, Iran: insights from paragenesis and geochemistry. *Chemical Geology*, 281, 253-269.
- Boudreau, A., Love, C., & Prendergast, M. (1995). Halogen geochemistry of the Great Dyke, Zimbabwe. *Contributions to Mineralogy and Petrology*, 122, 289-300.
- Boudreau, A., & McCallum, I. (1990). Low temperature alteration of REE-rich chlorapatite from the Stillwater Complex, Montana. *American Mineralogist*, 75, 687-693.
- Bouzari, F., Hart, C. J., Bissig, T., & Barker, S. (2016). Hydrothermal alteration revealed by apatite luminescence and chemistry: a potential indicator mineral for exploring covered porphyry copper deposits. *Economic Geology*, 111, 1397-1410.

- Carey, A., Samson, S. D., & Sell, B. (2009). Utility and limitations of apatite phenocryst chemistry for continent-scale correlation of Ordovician K-bentonites. *The Journal of Geology*, 117, 1-14.
- Caughlin, B. (2010). Developments in analytical technology. *Geochemistry: Exploration, Environment, Analysis*, 10, 137-141.
- Chew, D. M., Sylvester, P. J., & Tubrett, M. N. (2011). U–Pb and Th–Pb dating of apatite by LA-ICPMS. *Chemical Geology*, 280, 200-216.
doi:<http://dx.doi.org/10.1016/j.chemgeo.2010.11.010>
- Choi, S. H., Kim, J. S., Lee, J. Y., Jeon, J. S., Kim, J. W., Russo, R. E., et al. (2014). Analysis of arsenic in rice grains using ICP-MS and fs LA-ICP-MS. *Journal of Analytical Atomic Spectrometry*, 29, 1233-1237.
- Chu, M., Wang, K., Griffin, W. L., Chung, S., O'Reilly, S. Y., Pearson, N. J., et al. (2009). Apatite composition: tracing petrogenetic processes in Transhimalayan granitoids. *Journal of Petrology*, 50, 1829-1855.
- Comodi, P., Liu, Y., Stoppa, F., & Woolley, A. (1999). A multi-method analysis of Si-, S- and REE-rich apatite from a new find of kalsilite-bearing leucitite (Abruzzi, Italy). *Mineralogical Magazine*, 63, 661-661.
- Currie, K. L. (1976). *The alkaline rocks of Canada*. Ottawa: Department of Energy, Mines, and Resources Canada. 1 -128
- Currie, K., Knutson, J., & Temby, P. (1992). The Mud Tank carbonatite complex, central Australia—an example of metasomatism at mid-crustal levels. *Contributions to Mineralogy and Petrology*, 109, 326-339.

- Dempster, T., Jolivet, M., Tubrett, M., & Braithwaite, C. (2003). Magmatic zoning in apatite: a monitor of porosity and permeability change in granites. *Contributions to Mineralogy and Petrology*, 145, 568-577.
- Dussubieux, L., & Williams, P. (2009). Elemental analysis of Peruvian copper-based artifacts using LA-ICP-MS. *Archaeometallurgy in Europe 2007*, 489-497.
- Edfelt, Å., & Martinsson, O. (2005). Box 8-3: Fennoscandian Shield–Iron-Oxide–Copper–Gold deposits. *Geodynamics and Ore Deposit Evolution in Europe*, 27, 328.
- Efimov, A., Kravchenko, S., & Vasilieva, Z. (1962). Strontium apatite—a new mineral. *Doklady Akademii Nauk SSSR*, 142, 439.
- Elliott, J. (1994). Structure and Chemistry of the Apatites and Other Calcium Orthophosphates—Studies in Inorganic Chemistry. Elsevier (1st ed.). Amsterdam, London, New York, Tokyo: Elsevier Science. 1-404.
- Evans, E. H., & Giglio, J. J. (1993). Interferences in inductively coupled plasma mass spectrometry. A review. *Journal of Analytical Atomic Spectrometry*, 8, 1-18.
- Fisher, C. M., McFarlane, C. R., Hanchar, J. M., Schmitz, M. D., Sylvester, P. J., Lam, R., et al. (2011). Sm–Nd isotope systematics by laser ablation-multicollector-inductively coupled plasma mass spectrometry: Methods and potential natural and synthetic reference materials. *Chemical Geology*, 284, 1-20.
- Fleet, M. E., & Pan, Y. (1995). Site preference of rare earth elements in fluorapatite. *American Mineralogist*, 80, 329-335.
- Flowers, R. M., Ketcham, R. A., Shuster, D. L., & Farley, K. A. (2009). Apatite (U–Th)/He thermochronometry using a radiation damage accumulation and annealing model. *Geochimica et Cosmochimica Acta*, 73, 2347-2365.

- Foose, M. P., & McLelland, J. M. (1995). Proterozoic low-Ti iron-oxide deposits in New York and New Jersey: Relation to Fe-oxide (Cu–U–Au–rare earth element) deposits and tectonic implications. *Geology*, 23, 665-668.
- Frietsch, R. (1978). On the magmatic origin of iron ores of the Kiruna type. *Economic Geology*, 73, 478-485.
- Frietsch, R. (1980). Precambrian ores of the northern part of Norrbotten county, northern Sweden. *Guide to excursions 078 A C, part 1 (Sweden)* (pp. 35)
- Frietsch, R., & Perdahl, J. (1995). Rare earth elements in apatite and magnetite in Kiruna-type iron ores and some other iron ore types. *Ore Geology Reviews*, 9, 489-510.
- Gillen, C., & Rundqvist, D. (1997). Precambrian ore deposits of the East European and Siberian cratons. *Developments in Economic Geology, Vol. 30* (pp. 1-457). Amsterdam: Elsevier.
- Grisafe, D., & Hummel, F. (1970). Crystal chemistry and color in apatites containing cobalt, nickel, and rare-earth ions. *American Mineralogist*, 55, 1131-&.
- Hanchar, J.M., & Miller, C. (1993). Zircon zonation patterns as revealed by cathodoluminescence and backscattered electron images: implications for interpretation of complex crustal histories. *Chemical Geology*, 110, 1-13.
- Harlov, D. E. (2015). Apatite: a fingerprint for metasomatic processes. *Elements*, 11, 171-176.
- Harlov, D. E., Andersson, U. B., Förster, H., Nyström, J. O., Dulski, P., & Broman, C. (2002a). Apatite–monazite relations in the Kiirunavaara magnetite–apatite ore, northern Sweden. *Chemical Geology*, 191, 47-72.
- Harlov, D. E., & Förster, H. (2002). High-grade fluid metasomatism on both a local and a regional scale: the Seward peninsula, Alaska, and the Val Strona di Omegna, Ivrea–

- Verbano Zone, Northern Italy. Part I: petrography and silicate mineral chemistry. *Journal of Petrology*, 43, 769-799.
- Harlov, D. E., Förster, H., & Nijland, T. G. (2002b). Fluid-induced nucleation of (Y REE)-phosphate minerals within apatite: Nature and experiment. Part I. Chlorapatite. *American Mineralogist*, 87, 245-261.
- Haynes, D. W., Cross, K. C., Bills, R. T., & Reed, M. H. (1995). Olympic Dam ore genesis: a fluid-mixing model. *Economic Geology*, 90, 281-307.
- Heinrich, E. W. (1966). *The geology of carbonatites*. New York: Rand McNally.
- Henderson, C. (2011). Protocols and pitfalls of electron microprobe analysis of apatite. Unpublished MSc, The University of Michigan.
- Hitzman, M. W., Oreskes, N., & Einaudi, M. T. (1992). Geological characteristics and tectonic setting of proterozoic iron oxide (Cu-U-Au-REE) deposits. *Precambrian Research*, 58, 241-287. doi:[http://dx.doi.org/10.1016/0301-9268\(92\)90121-4](http://dx.doi.org/10.1016/0301-9268(92)90121-4)
- Hovis, G. L., & Harlov, D. E. (2010). Solution calorimetric investigation of fluor-chlorapatite crystalline solutions. *American Mineralogist*, 95, 946-952.
- Höy, T., & Pell, J. (1985). Carbonatites and associated alkalic rocks, Perry River and Mount Grace Areas, Shuswap Complex, Southeastern British Columbia (821N7, 13). *Geological Fieldwork*, 1986-1981.
- Huff, W. D. (1983). Correlation of Middle Ordovician K-bentonites based on chemical fingerprinting. *The Journal of Geology*, 657-669.
- Hughes, J., & Drexler, J. (1991). Cation substitution in the apatite tetrahedral site-crystal-structures of type hydroxyllestadite and type fermorite. *Neues Jahrbuch Fur Mineralogie-Monatshefte*, 327-336.

- Hughes, J., Fransolet, A., & Schreyer, W. (1993). The atomic arrangement of iron-bearing apatite. *Neues Jahrbuch Für Mineralogie Monatshefte*, 504-510.
- Hughes, J. M., Cameron, M., & Crowley, K. D. (1991). Ordering of divalent cations in the apatite structure: crystal structure refinements of natural Mn-and Sr-bearing apatite. *American Mineralogist*, 76, 1857-1862.
- Jinjie, Y., Qi, Z., Jingwen, M., & Shenghao, Y. (2007). Geochemistry of Apatite from the Apatite-rich Iron Deposits in the Ningwu Region, East Central China. *Acta Geologica Sinica (English Edition)*, 81, 637-648.
- Johannes, W., & Holtz, F. (2012). *Petrogenesis and experimental petrology of granitic rocks* (Vol. 22). Springer Science & Business Media. XIII-335.
- Jonsson, E., Troll, V. R., Högdahl, K., Harris, C., Weis, F., Nilsson, K. P., et al. (2013). Magmatic origin of giant 'Kiruna-type' apatite-iron-oxide ores in Central Sweden. *Scientific Reports*, 3
- Kempe, U., & Götze, J. (2002). Cathodoluminescence (CL) behaviour and crystal chemistry of apatite from rare-metal deposits. *Mineralogical Magazine*, 66, 151-172.
- Ketcham, R. A. (2015). Technical Note: Calculation of stoichiometry from EMP data for apatite and other phases with mixing on monovalent anion sites. *American Mineralogist*, 100, 1620-1623.
- Khattech, I., & Jemal, M. (1997). Thermochemistry of phosphate products. Part II: Standard enthalpies of formation and mixing of calcium and strontium fluorapatites. *Thermochimica Acta*, 298, 23-30.
- Klemme, S., & Dalpé, C. (2003). Trace-element partitioning between apatite and carbonatite melt. *American Mineralogist*, 88, 639-646.

- Kovach, V., Salnikova, E., Wang, K., Jahn, B., Chiu, H., Reznitskiy, L., et al. (2013). Zircon ages and Hf isotopic constraints on sources of clastic metasediments of the Slyudyansky high-grade complex, southeastern Siberia: Implication for continental growth and evolution of the Central Asian Orogenic Belt. *Journal of Asian Earth Sciences*, 62, 18-36.
- Kramm, U., Kogarko, L., Kononova, V., & Vartiainen, H. (1993). The Kola Alkaline Province of the CIS and Finland: Precise Rb-Sr ages define 380–360 Ma age range for all magmatism. *Lithos*, 30, 33-44.
- Krause, J., Harlov, D. E., Pushkarev, E. V., & Brüggemann, G. E. (2013). Apatite and clinopyroxene as tracers for metasomatic processes in nepheline clinopyroxenites of Uralian-Alaskan-type complexes in the Ural Mountains, Russian Federation. *Geochimica et Cosmochimica Acta*, 121, 503-521.
- Kretz, R. (1993). A garnet population in Yellowknife schist, Canada. *Journal of Metamorphic Geology*, 11, 101-120.
- Laznicka, P. (2013). *Empirical metallogeny: depositional environments, lithologic associations and metallic ores*. Elsevier. 1-760.
- Le Bas, M. (1987). Nephelinites and carbonatites. *Geological Society, London, Special Publications*, 30, 53-83.
- Lieftink, D. (1994). The behavior of rare earth elements in high temperature Cl-bearing aqueous fluids: results from the Ødegårdens Verk natural laboratory. *The Canadian Mineralogist*, 32, 149-158
- Liu, Y., & Comodi, P. (1993). Some aspects of the crystal-chemistry of apatites. *Mineralogical Magazine*, 57, 709-720.

- Mao, M., Rukhlov, A. S., Rowins, S. M., Spence, J., & Coogan, L. A. (2016). Apatite Trace Element Compositions: A Robust New Tool for Mineral Exploration. *Economic Geology*, 111, 1187-1222.
- May, T. W., & Wiedmeyer, R. H. (1998). A table of polyatomic interferences in ICP-MS. *Atomic Spectroscopy-Norwalk Connecticut-*, 19, 150-155.
- McKeown, F. A., & Klemic, H. (1954). *Rare-earth-bearing apatite at Mineville, Essex County, New York* US Department of the Interior, Geological Survey.
- Miles, A., Graham, C., Hawkesworth, C., Gillespie, M., Hinton, R., & Bromiley, G. (2014). Apatite: A new redox proxy for silicic magmas? *Geochimica et Cosmochimica Acta*, 132, 101-119.
- Nold, J. L., Dudley, M. A., & Davidson, P. (2014). The Southeast Missouri (USA) Proterozoic iron metallogenic province—Types of deposits and genetic relationships to magnetite–apatite and iron oxide–copper–gold deposits. *Ore Geology Reviews*, 57, 154-171.
- Nystroem, J. O., & Henriquez, F. (1994). Magmatic features of iron ores of the Kiruna type in Chile and Sweden: ore textures and magnetite geochemistry. *Economic Geology*, 89, 820-839.
- Ojala, V. J. (2007). *Metallogeny and tectonic evolution of the Northern Fennoscandian Shield: field trip guidebook* (Vol. 54). Geological survey of Finland.
- Pan, L., Hu, R., Wang, X., Bi, X., Zhu, J., & Li, C. (2016). Apatite trace element and halogen compositions as petrogenetic-metallogenic indicators: Examples from four granite plutons in the Sanjiang region, SW China. *Lithos*, 254, 118-130.

- Pan, Y., & Fleet, M. E. (2002). Compositions of the apatite-group minerals: substitution mechanisms and controlling factors. *Reviews in Mineralogy and Geochemistry*, 48, 13-49.
- Parak, T. (1975). Kiruna iron ores are not "intrusive-magmatic ores of the Kiruna type". *Economic Geology*, 70, 1242-1258.
- Pasero, M., Kampf, A. R., Ferraris, C., Pekov, I. V., Rakovan, J., & White, T. J. (2010). Nomenclature of the apatite supergroup minerals. *European Journal of Mineralogy*, 22, 163-179.
- Paton, C., Hellstrom, J., Paul, B., Woodhead, J., & Hergt, J. (2011). Iolite: Freeware for the visualisation and processing of mass spectrometric data. *Journal of Analytical Atomic Spectrometry*, 26, 2508-2518.
- Pearce, N. J., Perkins, W. T., Westgate, J. A., Gorton, M. P., Jackson, S. E., Neal, C. R., et al. (1997). A compilation of new and published major and trace element data for NIST SRM 610 and NIST SRM 612 glass reference materials. *Geostandards Newsletter*, 21, 115-144.
- Peng, G., Luhr, J. F., & McGee, J. J. (1997). Factors controlling sulfur concentrations in volcanic apatite. *American Mineralogist*, 82, 1210-1224.
- Peppe, D. J., & Reiners, P. W. (2007). Conodont (U-Th)/He thermochronology: initial results, potential, and problems. *Earth and Planetary Science Letters*, 258, 569-580.
- Perseil, E., Blanc, P., & Ohnenstetter, D. (2000). As-bearing fluorapatite in manganese deposits from St. Marcel-Praborna, Val d'Aosta, Italy. *The Canadian Mineralogist*, 38, 101-117.

- Philpotts, A. (1967). Origin of certain iron-titanium oxide and apatite rocks. *Economic Geology*, 62, 303-315.
- Piccoli, P. M., & Candela, P. A. (2002). Apatite in igneous systems. *Reviews in Mineralogy and Geochemistry*, 48, 255-292.
- Plant, J., Whittaker, A., Demetriades, A., De Vivo, B., & Lexa, J. (2003). The geological and tectonic framework of Europe. *Geochemical Atlas of Europe. Part, 1*
- Prowatke, S., & Klemme, S. (2006). Trace element partitioning between apatite and silicate melts. *Geochimica et Cosmochimica Acta*, 70, 4513-4527.
- Pyle, J. M., Spear, F. S., & Wark, D. A. (2002). Electron microprobe analysis of REE in apatite, monazite and xenotime: protocols and pitfalls. *Reviews in Mineralogy and Geochemistry*, 48, 337-362.
- Rakovan, J. F., & Hughes, J. M. (2000). Strontium in the apatite structure: strontian fluorapatite and belovite-(Ce). *The Canadian Mineralogist*, 38, 839-845.
- Roeder, P. L., MacArthur, D., Ma, X., Palmer, G. R., & Mariano, A. N. (1987). Cathodoluminescence and microprobe study of rare-earth elements in apatite. *American Mineralogist*, 72, 801-811.
- Roegge, J., Logsdon, M., Young, H., Barr, H., Borcsik, M., & Holland, H. (1974). Halogens in apatites from the Providencia area, Mexico. *Economic Geology*, 69, 229-240.
- Rønsbo, J. (1989). Coupled substitutions involving REEs and Na and Si in apatites in alkaline rocks from the Ilimaussaq intrusion, South Greenland, and the petrological implications. *American Mineralogist*, 74, 896-901.
- Rouse, R. C., & Dunn, P. J. (1982). A contribution to the crystal chemistry of ellestadite and the silicate sulfate apatites. *American Mineralogist*, 67, 90-96.

- Samson, S. D., Matthews, S., Mitchell, C. E., & Goldman, D. (1995). Tephrochronology of highly altered ash beds: the use of trace element and strontium isotope geochemistry of apatite phenocrysts to correlate K-bentonites. *Geochimica et Cosmochimica Acta*, 59, 2527-2536.
- San Blas, O. G., Gayón, J. M. M., & Alonso, J. I. G. (2015). Evaluation of multi-collector inductively coupled plasma mass spectrometry (MC-ICP-MS) for sulfur metabolic studies using ³⁴S-labeled yeast. *Journal of Analytical Atomic Spectrometry*, 30, 1764-1773.
- Sha, L., & Chappell, B. W. (1999). Apatite chemical composition, determined by electron microprobe and laser-ablation inductively coupled plasma mass spectrometry, as a probe into granite petrogenesis. *Geochimica et Cosmochimica Acta*, 63, 3861-3881.
- Shannon, R. t. (1976). Revised effective ionic radii and systematic studies of interatomic distances in halides and chalcogenides. *Acta Crystallographica Section A: Crystal Physics, Diffraction, Theoretical and General Crystallography*, 32, 751-767.
- Shkol'nik, S., Stanevich, A., Reznitskii, L., & Savelieva, V. (2016). New data about structure and time of formation of the Khamar-Daban terrane: U-Pb LA-ICP-MS zircon ages. *Stratigraphy and Geological Correlation*, 24, 19.
- Storner, J., Pierson, M. L., & Tacker, R. C. (1993). Variation of F and Cl X-ray intensity due to anisotropic diffusion in apatite. *American Mineralogist*, 78, 641-648.
- Stosch, H., Romer, R. L., Daliran, F., & Rhede, D. (2011). Uranium–lead ages of apatite from iron oxide ores of the Bafq District, East-Central Iran. *Mineralium Deposita*, 46, 9-21.
- Taylor, R., & Fryer, B. (1983). Rare earth element lithochemistry of granitoid mineral deposits. *CIM (can.Inst.Min.Metall.) Bull*, 76, 74-84.

- Tepper, J. H., & Kuehner, S. M. (1999). Complex zoning in apatite from the Idaho batholith: A record of magma mixing and intracrystalline trace element diffusion. *American Mineralogist*, 84, 581-595.
- Trzcinski, W. E., Perrault Jr., G., & Herbert, P. (1974). A note on apatite from Huddersfield township, Quebec. *Canadian Mineralogist*, 12, 289-292.
- Valley, P. M., Fisher, C. M., Hanchar, J. M., Lam, R., & Tubrett, M. (2010). Hafnium isotopes in zircon: A tracer of fluid-rock interaction during magnetite–apatite (“Kiruna-type”) mineralization. *Chemical Geology*, 275, 208-220.
- Valley, P. M., Hanchar, J. M., & Whitehouse, M. J. (2009). Direct dating of Fe oxide-(Cu-Au) mineralization by U/Pb zircon geochronology. *Geology*, 37, 223-226.
- Valley, P. M., Hanchar, J. M., & Whitehouse, M. J. (2011). New insights on the evolution of the Lyon Mountain Granite and associated Kiruna-type magnetite-apatite deposits, Adirondack Mountains, New York State. *Geosphere*, 7, 357-389.
- Weill, D. F., & Drake, M. J. (1973). Europium anomaly in plagioclase feldspar: experimental results and semiquantitative model. *Science (New York, N.Y.)*, 180, 1059-1060. doi:180/4090/1059 [pii].
- Westhues, A., Hanchar, J. M., Whitehouse, M. J., & Martinsson, O. (2016). New constraints on the timing of host-rock emplacement, hydrothermal alteration, and iron oxide-apatite mineralization in the Kiruna district, Norrbotten, Sweden. *Economic Geology*, 111, 1595-1618.
- Westhues, A., Hanchar, J. M., LeMessurier, M. J., & Whitehouse, M. J. (2017). Evidence for hydrothermal alteration and source regions for the Kiruna iron oxide–apatite ore (northern Sweden) from zircon Hf and O isotopes. *Geology*, 45, 571-574.

- Williams, S. A., & Cesbron, F. P. (1977). Rutile and apatite: useful prospecting guides for porphyry copper deposits. *Mineralogical Magazine*, 41, 288-292.
- Xie, H., Tang, Y., Li, Y., & Li, L. (2007). Determination of trace multi-elements in coal fly ash by inductively coupled plasma mass spectrometry. *Journal of Central South University of Technology*, 14, 68-72.
- Young, E., Myers, A., Munson, E. L., & Conklin, N. M. (1969). Mineralogy and geochemistry of fluorapatite from Cerro de Mercado, Durango, Mexico. *US Geological Survey Professional Paper*, 650, D84-D93.
- Zaitsev, A., & Bell, K. (1995). Sr and Nd isotope data of apatite, calcite and dolomite as indicators of source, and the relationships of phosphorites and carbonatites from the Kovdor massif, Kola peninsula, Russia. *Contributions to Mineralogy and Petrology*, 121, 324-335.
- Zhu, C., & Sverjensky, D. A. (1991). Partitioning of F-Cl-OH between minerals and hydrothermal fluids. *Geochimica Et Cosmochimica Acta*, 55, 1837-1858.
- Zirner, A. L., Marks, M. A., Wenzel, T., Jacob, D. E., & Markl, G. (2015). Rare Earth Elements in apatite as a monitor of magmatic and metasomatic processes: the Ilímaussaq complex, South Greenland. *Lithos*, 228, 12-22.

CHAPTER 3 TABLES

Table 3.1 Summary of reference apatites used in this study.

Sample locality	Host rock type	Tectonic setting	Age (Ma)	References
Mud Tank, Australia	Carbonatite	Continental-rift	ca. 732	Currie, 1976; Gulson and Black, 1978; Currie et al., 1992; Claoué-Long et al., 2008
Durango, Mexico	Intermediate-felsic volcanic rocks	Continental-arc	ca. 32 - 28	Young et al., 1960; McDowell and Keizer, 1977; Barton and Johnson, 1996
Otter Lake, Quebec, Canada	Skarn	Collisional mountain belt	ca. 1300 - 1000	Trzcinski, 1974; Kretz, 1993 Barford, 2003
Mineville, New York, USA	K- and Na-metasomatised igneous intrusive rocks	Collisional mountain belt	ca. 1150	McKeown and Klemic, 1954; McLelland et al., 2001; Valley et al., 2009; Valley et al., 2010; Vallet et al., 2011
Sludyanka, Siberia, Russia	Skarn	Collisional mountain belt	ca. 2500 - 3900	Gillen and Rundqvist, 1997; Kovach et al., 2013; Shkol'nik et al., 2016
Kola Kovdor-A,C, Russia	Alkaline/Carbonatite suite	Continental-rift	ca. 370-380	Epshteyn and Danil'chenko, 1988; Kramm et al., 1993; Zaitsez and Bell, 1995; Bayanova et al., 1997
Gruvberget, northern Sweden	Intermediate-mafic volcanic rocks	Collisional mountain belt	ca. 1800	Frietsch, 1980; Billström & Martinsson, 2000; Edfelt & Martinsson, 2005; Ojala and Juhani, 2007; Plant et al., 2003

Table 3.2 Composition of Gruvberget rock and ore samples.

Sample	GRV_11_01	GRV_11_02	GRV_11_04
Rock type	Biotite schist	MtAp ore	Metadiabase
Major Elements (wt %)			
SiO ₂	41.37	1.59	42.76
TiO ₂	0.674	0.131	0.943
Al ₂ O ₃	10.91	0.28	16.61
Fe ₂ O _{3(tot)}	26.94	86.84	16.36
MnO	0.095	0.321	0.099
MgO	10.53	0.92	0.94
CaO	1.04	6.83	9.54
Na ₂ O	1.59	0.03	5.87
K ₂ O	4.98	0.005	0.67
P ₂ O ₅	0.19	2.47	0.37
LOI	1.82	0.48	4.91
Total	100.14	99.89	99.07
Trace elements (ppm)			
V	342	648	219
Cr	120	10	10
Co	90	102	76
Cu	10	10	20
Zn	15	15	15
Ga	18	11	13
Ge	2	0.5	0.5
As	2.5	14	2.5
Sr	50	24	284
Y	7.36	28.03	13.68
Ba	918	4	135
La	20.31	50.70	40.94
Ce	40.60	126.85	85.83
Pr	4.74	17.13	9.89
Nd	19.12	70.29	35.69
Sm	3.55	11.94	5.15
Eu	0.61	1.62	0.80
Gd	2.58	9.93	4.03
Tb	0.38	1.23	0.56
Dy	1.84	6.15	2.88
Ho	0.39	1.22	0.60
Er	1.41	3.30	2.15
Tm	0.22	0.43	0.33
Yb	1.50	2.24	2.10
Lu	0.21	0.33	0.30
Pb	10	2.5	2.5
Th	5.76	7.95	4.92
U	11.10	2.50	1.60

Table 3.3 Major, minor, and trace element concentrations of reference apatites.

Location	Mud Tank	Kola Kovdor-C	MUN Sludyanka	JMH Sludyanka	Otter Lake	Mineville	Durango (L c)	Durango (c)	Kola Kovdor-A
Rock Type	Carbonatite	Carbonatite	Skarn	Skarn	Skarn	IOA ore	IOA ore	IOA ore	Alkaline rock
N	5	5	5	5	5	5	5	5	5
Major Elements (wt%)									
CaO	54.55 (0.08)	53.92 (0.08)	55.12 (0.11)	55.30 (0.09)	54.00 (0.04)	50.53 (0.24)	54.56 (0.07)	54.66 (0.10)	52.40 (0.07)
SrO	0.44 (0.03)	0.36 (0.02)	0.14 (0.03)	0.15 (0.02)	0.25 (0.02)	0.03 (0.02)	0.04 (0.01)	0.05 (0.02)	3.49 (0.08)
Na₂O	0.16 (0.02)	0.08 (0.01)	0.20 (0.02)	0.21 (0.03)	0.08 (0.02)	0.21 (0.02)	0.20 (0.02)	0.18 (0.02)	0.11 (0.02)
Y₂O₃	0.03 (0.01)	0.03 (0.01)	bdl	0.03 (0.01)	0.16 (0.01)	1.16 (0.06)	0.05 (0.02)	0.11 (0.01)	0.04 (0.02)
MnO	0.05 (0.01)	0.02 (0.00)	0.03 (0.00)	0.03 (0.00)	0.02 (0.02)	0.04 (0.01)	0.03 (0.02)	0.02 (0.01)	0.03 (0.01)
MgO	0.01 (0.01)	bdl	bdl	0.04 (0.01)	bdl	bdl	0.02 (0.01)	0.02 (0.01)	0.01 (0.00)
FeO	0.05 (0.02)	0.02 (0.00)	bdl	0.02 (0.01)	0.01 (0.01)	0.06 (0.01)	0.04 (0.01)	0.02 (0.01)	0.02 (0.01)
P₂O₅	41.43 (0.29)	39.06 (0.43)	40.66 (0.12)	40.42 (0.16)	38.42 (0.20)	36.37 (0.52)	41.11 (0.18)	41.17 (0.24)	40.89 (0.16)
SiO₂	bdl	1.20 (0.16)	0.33 (0.02)	0.45 (0.05)	0.91 (0.02)	2.06 (0.11)	0.23 (0.02)	0.35 (0.01)	bdl
As₂O₅	bdl	bdl	0.12 (0.05)	bdl	0.09 (0.01)	0.63 (0.03)	0.17 (0.03)	0.19 (0.05)	bdl
SO₃	0.02 (0.00)	0.14 (0.04)	0.80 (0.03)	1.04 (0.05)	0.46 (0.04)	0.12 (0.02)	0.35 (0.02)	0.27 (0.01)	bdl
F⁻	2.39 (0.07)	0.93 (0.03)	3.07 (0.02)	3.46 (0.05)	4.23 (0.19)	3.69 (0.09)	3.91 (0.03)	3.44 (0.03)	4.01 (0.20)
Cl⁻	0.03 (0.00)	0.02 (0.01)	0.14 (0.01)	0.11 (0.00)	0.03 (0.01)	0.20 (0.03)	0.44 (0.01)	0.40 (0.02)	bdl
OH⁻	1.16	2.59	0.49	0.23				0.11	
Total	100.33 (0.31)	98.37 (0.47)	101.11 (0.18)	101.48 (0.21)	98.67 (0.28)	95.10 (0.59)	101.15 (0.20)	100.98 (0.27)	101.01 (0.28)
O=F,Cl	-1.02 (0.03)	-0.40 (0.01)	-1.33 (0.01)	-1.48 (0.02)	-1.79 (0.08)	-1.60 (0.04)	-1.74 (0.01)	-1.54 (0.01)	-1.69 (0.08)
Total*	99.31 (0.31)	97.97 (0.47)	99.78 (0.18)	100.00 (0.21)	96.88 (0.30)	93.50 (0.59)	99.41 (0.20)	99.44 (0.27)	99.32 (0.29)
X(FAp)	0.64 0.02	0.25 0.01	0.82 0.01	0.92 0.01	1.12 0.05	0.98 0.02	1.04 0.01	0.91 0.01	1.07 0.05
X(CAp)	0.00 0.00	0.00 0.00	0.02 0.00	0.02 0.00	0.00 0.00	0.03 0.00	0.06 0.00	0.06 0.00	0.00
X(HAp)	0.34	0.76	0.14	0.07				0.03	

Note: "bdl" = below detection limit; "err" = 1 σ s.d.; † = OH calculation based on Ketcham, 2015; * = Total accounting for equivalent of oxygen for halogens

Table 3.3. Cont'd.

Location	Mud Tank	Kola Kovdor-C	MUN Sludyanka	JMH Sludyanka	Otter Lake	Mineville	Durango (L c)	Durango (I c)	Kola Kovdor-A
Rock Type	Carbonatite	Carbonatite	Skarn	Skarn	Skarn	IOA ore	IOA ore	IOA ore	Alkaline rock
N	3	3	3	3	3	3	3	3	3
Trace Elements (ppm)									
Mg	134.5	50.7	171.3	118.3	58.3	56.7	190.2	154.3	53.9
Si	232	7240	2296	2430	4893	10520	1405	2089	1147
V	1.47	157.2	20.8	28.3	14.5	0.825	29.4	39.2	62.5
Cr	3	6.13	3.19	4.85	6.17	bdl	bdl	3.7	bdl
Mn	250.8	70.6	95.9	95.9	105.7	211.2	95.2	99.4	176.9
Co	33.4	bdl	20.2	8.63	bdl	38.6	10.7	7.63	bdl
Cu	1.64	bdl	bdl	bdl	bdl	1.73	bdl	bdl	bdl
Zn	bdl	bdl	bdl	bdl	bdl	bdl	bdl	bdl	bdl
As	8.81	26.8	14	18	110.8	3888	736.3	1085	9.26
Sr	3699	3153	1259	1271	1949	297.7	461.4	494.8	25930
Y	154.6	221.9	25	37.3	1255	8783	410.7	779.3	302.5
Zr	0.32	140.4	10.2	2.79	0.754	3.64	0.529	0.496	0.739
Ba	39	18.7	2.17	2.99	0.953	1.44	1.18	1.11	374.7
La	997.3	3707	36.5	48	2887	9517	3239	4000	2330
Ce	2164	7523	72.6	89.9	7437	19390	3915	4836	3497
Pr	255.5	821.7	7.87	9.39	941.3	2169	304.9	394.7	331.4
Nd	1042	3073	29.3	34.8	3722	8680	975	1356	1188
Sm	164.5	388.7	4.51	6.07	530	1609	120.5	188.3	164.7
Eu	45.6	91.3	1.23	1.65	93.7	163.1	14.8	16.3	46.8
Gd	114	222.3	6.05	6.76	359	1620	103.6	170.9	129.3
Tb	11.6	20.3	0.697	1.03	41.3	237.4	12.5	22.4	14.5
Dy	49	78.1	4.49	6.85	214.5	1460	67.4	128	69.6
Ho	6.78	10.2	0.767	1.38	40.7	316.6	13.3	26	11.2
Er	11.8	15.6	2.17	3.14	104.7	872.7	34	67.7	22.4
Tm	1.05	1.27	bdl	0.487	13.7	116.5	4.23	8.33	2.16
Yb	4.34	6.03	1.49	2.59	84.7	720.2	24.1	47.4	8.84
Lu	0.428	0.473	0.222	0.357	10.8	88.7	3.11	5.55	0.85
Pb	3.51	54.8	8.15	9.13	34.8	96.5	0.567	0.737	bdl
Th	27.9	1626	124.1	120.9	414.9	1109	184.7	247.8	15.2
U	5.7	31.2	65.3	56.3	76.8	178.3	9.8	12.7	1.8

Table 3.4. Major, minor, and trace element composition of Gruvberget apatites.

Rock Type	Biotite schist (GRV-11-01)									
Grain #	7 err	8 err	11 err	14 err	16 err	17 err	19 err	21 err	24 err	26 err
N	3	3	3	3	3	3	3	3	3	3
Major Elements (wt.%)										
CaO	55.97 (0.09)	55.83 (0.18)	55.67 (0.15)	55.61 (0.12)	55.66 (0.14)	55.69 (0.04)	55.69 (0.06)	55.59 (0.12)	55.50 (0.04)	55.43 (0.05)
SrO	0.05 (0.03)	0.03 (0.02)	0.05 (0.01)	0.06 (0.02)	0.03 (0.01)	0.06 (0.01)	0.03 (0.02)	0.06 (0.00)	0.03 (0.03)	0.04 (0.04)
Na₂O	0.03 (0.00)	0.04 (0.02)	0.04 (0.01)	0.05 (0.02)	0.05 (0.01)	0.04 (0.01)	0.05 (0.02)	0.05 (0.01)	0.04 (0.02)	0.07 (0.02)
Y₂O₃	0.06 (0.01)	0.09 (0.01)	0.09 (0.01)	0.06 (0.02)	0.09 (0.02)	0.08 (0.02)	0.10 (0.02)	0.08 (0.01)	0.07 (0.01)	0.06 (0.01)
MnO	0.05 (0.03)	0.04 (0.01)	0.11 (0.02)	0.09 (0.02)	0.07 (0.01)	0.05 (0.03)	0.06 (0.02)	0.06 (0.01)	0.09 (0.01)	0.09 (0.02)
MgO	bdl	0.00 (0.00)	0.01 (0.01)	bdl	bdl	0.01 (0.01)	0.00 (0.01)	0.00 (0.01)	0.01 (0.01)	0.01 (0.00)
FeO	0.03 (0.01)	0.01 (0.01)	0.04 (0.00)	0.03 (0.02)	0.02 (0.02)	0.02 (0.01)	0.02 (0.00)	0.01 (0.01)	0.02 (0.01)	0.04 (0.00)
P₂O₅	42.47 (0.26)	42.20 (0.31)	42.32 (0.06)	42.28 (0.26)	42.16 (0.20)	42.14 (0.37)	42.09 (0.18)	42.39 (0.04)	42.22 (0.21)	42.09 (0.11)
SiO₂	0.03 (0.00)	0.04 (0.01)	0.03 (0.01)	0.03 (0.01)	0.04 (0.03)	0.04 (0.01)	0.04 (0.01)	0.03 (0.01)	0.02 (0.01)	0.04 (0.02)
As₂O₅	0.02 (0.03)	0.09 (0.10)	0.02 (0.04)	0.03 (0.04)	0.03 (0.05)	0.03 (0.05)	bdl	0.09 (0.08)	0.02 (0.04)	0.04 (0.08)
SO₃	0.05 (0.01)	0.06 (0.02)	0.04 (0.01)	0.04 (0.01)	0.05 (0.01)	0.07 (0.01)	0.05 (0.02)	0.06 (0.01)	0.03 (0.01)	0.06 (0.01)
F⁻	3.34 (0.06)	3.59 (0.16)	2.73 (0.02)	2.83 (0.08)	3.50 (0.06)	3.46 (0.09)	3.15 (0.10)	3.22 (0.05)	2.98 (0.07)	2.74 (0.13)
Cl⁻	0.17 (0.01)	0.18 (0.06)	0.61 (0.04)	0.69 (0.04)	0.23 (0.03)	0.16 (0.04)	0.30 (0.02)	0.24 (0.03)	0.49 (0.08)	0.64 (0.06)
OH	0.32	0.08	0.63	0.51	0.13	0.20	0.40	0.38	0.46	0.60
Total	102.59 (0.28)	102.28 (0.41)	102.38 (0.17)	102.30 (0.31)	102.06 (0.26)	102.03 (0.39)	101.99 (0.22)	102.26 (0.17)	101.99 (0.24)	101.96 (0.21)
O=F,Cl	-1.44 (0.02)	-1.55 (0.07)	-1.29 (0.01)	-1.35 (0.03)	-1.53 (0.03)	-1.49 (0.04)	-1.39 (0.04)	-1.41 (0.02)	-1.37 (0.03)	-1.30 (0.06)
Total*	101.14 (0.29)	100.73 (0.42)	101.09 (0.17)	100.95 (0.31)	100.53 (0.26)	100.54 (0.39)	100.60 (0.22)	100.85 (0.17)	100.63 (0.24)	100.66 (0.22)
X(FAp)	0.89 (0.02)	0.95 (0.04)	0.72 (0.01)	0.75 (0.02)	0.93 (0.02)	0.92 (0.02)	0.84 (0.03)	0.86 (0.01)	0.79 (0.02)	0.73 (0.03)
X(CAp)	0.02 (0.00)	0.03 (0.01)	0.09 (0.01)	0.10 (0.01)	0.03 (0.00)	0.02 (0.01)	0.04 (0.00)	0.03 (0.00)	0.07 (0.01)	0.09 (0.01)
X(HAp)	0.09	0.02	0.19	0.15	0.04	0.06	0.12	0.11	0.14	0.18

Note: "bdl" = below detection limit; "err" = 1σ s.d.; † = OH calculation based on Ketcham (2015); * = Total accounting for equivalent of oxygen for halogens

Table 3.4. Cont'd.

Rock Type Biotite schist (GRV-11-01)										
Grain #	31 err	34 err	35 err	36 err	37 err	39 err	48 err	51 err	52 err	54 err
N	3	3	3	3	3	3	3	3	3	3
Major Elements (wt.%)										
CaO	55.49 (0.21)	55.54 (0.07)	55.52 (0.12)	55.25 (0.16)	55.36 (0.19)	55.27 (0.16)	55.28 (0.21)	55.50 (0.10)	55.54 (0.10)	55.22 (0.13)
SrO	0.05 (0.03)	0.04 (0.01)	0.05 (0.02)	0.03 (0.03)	0.07 (0.02)	0.04 (0.01)	0.06 (0.02)	0.04 (0.03)	0.05 (0.01)	0.04 (0.03)
Na₂O	0.06 (0.00)	0.04 (0.02)	0.05 (0.01)	0.06 (0.01)	0.04 (0.00)	0.05 (0.01)	0.06 (0.03)	0.03 (0.01)	0.04 (0.03)	0.04 (0.01)
Y₂O₃	0.07 (0.02)	0.09 (0.02)	0.08 (0.04)	0.08 (0.02)	0.06 (0.02)	0.06 (0.01)	0.06 (0.01)	0.05 (0.02)	0.08 (0.03)	0.05 (0.01)
MnO	0.07 (0.03)	0.05 (0.03)	0.04 (0.04)	0.09 (0.02)	0.09 (0.01)	0.11 (0.03)	0.10 (0.01)	0.05 (0.02)	0.06 (0.02)	0.09 (0.01)
MgO	0.00 (0.01)	0.01 (0.01)	bdl	0.01 (0.00)	0.01 (0.01)	0.01 (0.00)	0.01 (0.00)	bdl	0.01 (0.01)	0.03 (0.04)
FeO	0.03 (0.01)	0.03 (0.00)	0.02 (0.02)	0.05 (0.00)	0.05 (0.04)	0.04 (0.01)	0.03 (0.01)	0.01 (0.01)	0.02 (0.00)	0.05 (0.04)
P₂O₅	42.00 (0.22)	42.35 (0.11)	42.19 (0.18)	42.00 (0.14)	41.87 (0.13)	41.97 (0.22)	41.74 (0.14)	41.83 (0.26)	41.96 (0.46)	42.17 (0.06)
SiO₂	0.03 (0.03)	0.04 (0.01)	0.02 (0.03)	0.02 (0.02)	0.03 (0.01)	0.03 (0.02)	0.03 (0.01)	0.03 (0.02)	0.02 (0.03)	0.05 (0.09)
As₂O₅	0.06 (0.06)	0.06 (0.10)	0.02 (0.03)	0.04 (0.07)	bdl	0.06 (0.06)	bdl	bdl	0.12 (0.10)	0.07 (0.11)
SO₃	0.05 (0.04)	0.05 (0.01)	0.04 (0.01)	0.04 (0.02)	0.03 (0.01)	0.04 (0.02)	0.04 (0.02)	0.03 (0.02)	0.04 (0.02)	0.02 (0.00)
F⁻	3.14 (0.15)	3.58 (0.20)	3.23 (0.09)	2.65 (0.01)	2.51 (0.01)	2.72 (0.09)	2.69 (0.09)	3.17 (0.15)	3.23 (0.07)	3.10 (0.22)
Cl⁻	0.28 (0.03)	0.21 (0.04)	0.21 (0.03)	0.67 (0.02)	0.74 (0.02)	0.59 (0.03)	0.65 (0.06)	0.24 (0.04)	0.23 (0.01)	0.45 (0.07)
OH[†]	0.41	0.08	0.38	0.66	0.74	0.63	0.62	0.39	0.36	0.37
Total	101.74 (0.35)	102.17 (0.27)	101.84 (0.25)	101.64 (0.23)	101.60 (0.24)	101.62 (0.30)	101.35 (0.28)	101.38 (0.33)	101.75 (0.49)	101.73 (0.31)
O=F,Cl	-1.39 (0.06)	-1.55 (0.09)	-1.41 (0.04)	-1.27 (0.01)	-1.22 (0.01)	-1.28 (0.04)	-1.28 (0.04)	-1.39 (0.06)	-1.41 (0.03)	-1.40 (0.09)
Total*	100.36 (0.36)	100.62 (0.28)	100.43 (0.25)	100.38 (0.23)	100.37 (0.24)	100.34 (0.30)	100.07 (0.28)	99.99 (0.33)	100.34 (0.49)	100.32 (0.32)
X(FAp)	0.83 (0.04)	0.95 (0.05)	0.86 (0.02)	0.70 (0.00)	0.67 (0.00)	0.72 (0.02)	0.72 (0.02)	0.84 (0.04)	0.86 (0.02)	0.82 (0.06)
X(CAp)	0.04 (0.00)	0.03 (0.01)	0.03 (0.00)	0.10 (0.00)	0.11 (0.00)	0.09 (0.00)	0.10 (0.01)	0.04 (0.01)	0.03 (0.00)	0.07 (0.01)
X(HAp)	0.12	0.02	0.11	0.19	0.22	0.18	0.18	0.12	0.11 (0.02)	0.11

Table 3.4. Cont'd.

Rock Type Biotite schist (GRV-11-01)																				
Grain #	7		8		11		14		16		17		19		21		24		26	
Spot #	1	2	1	2	1	2	1	2	1	2	1	2	1	2	1	2	1	2	1	2
Trace Elements (ppm)																				
Mg	350	79	91.5	66.8	101	114	81.4	109	88.7	78.6	608	70.6	79.3	78	76.7	79.7	239	715	102	111
Si	671	321	538	374	319	373	220	371	426	570	4260	272	463	403	388	479	496	985	375	395
V	1.85	0.43	1.59	4.58	0.90	0.92	2.12	1.05	1.37	1.44	2.80	0.83	1.19	1.50	1.27	1.34	1.53	3.53	0.88	1.04
Cr	6.5	4.54	5.6	4.9	2.86	4.2	3.2	4.04	3.45	3.3	145	6.31	5.54	1.8	3.61	6.1	5.49	4.54	4.7	5.39
Mn	375	348	364	300	647	665	588	653	338	339	358	315	360	340	334	339	613	638	642	647
Co	3.9	2.8	bdl	2.7	bdl	bdl	bdl	2.24	bdl	bdl	18.2	bdl	bdl	2.81	bdl	2.77	bdl	3	bdl	bdl
Cu	1.6	bdl	bdl	2.62	bdl	bdl	bdl	bdl	bdl	bdl	12.7	0.89	bdl	bdl	bdl	bdl	bdl	1.31	0.86	bdl
Zn	bdl	bdl	bdl	bdl	bdl	bdl	bdl	bdl	0.52	bdl	bdl									
As	42.9	38.5	43.7	52.9	31.2	29.1	39.2	22.5	36.5	40.2	35.7	61.3	38.3	42.5	40.9	36.1	30.3	27.1	25.3	30
Sr	382	382	403	440	458	480	453	442	414	432	429	434	428	441	438	422	457	455	463	463
Y	496	342	755	586	501	536	405	559	644	768	306	424	644	759	602	680	521	496	598	598
Zr	bdl	bdl	bdl	bdl	bdl	bdl	bdl	bdl	bdl	bdl	bdl									
Ba	3.7	bdl	1.08	0.72	bdl	bdl	bdl	bdl	1.69	bdl	14	3.81	bdl	bdl	bdl	bdl	bdl	bdl	0.7	0.59
La	85.4	39.3	153	7.05	34.2	58.5	13.8	55.6	30.1	16.7	33.1	24.9	43.1	38.3	39.7	82.9	24.9	28.8	92.8	172
Ce	327	148	619	32.2	150	229	68.4	225	140	79.5	88.5	87.8	197	168	182	339	106	115	311	543
Pr	55.6	27.4	105	6.93	31.7	45.6	16.4	45.2	29.6	18.4	16.2	16	39.8	34.2	36.5	60.7	22	24.1	54.3	85.1
Nd	313	173	580	56.8	238	316	137	313	217	145	87	101	271	241	239	358	173	182	352	481
Sm	85.9	50.6	142	33.6	89.3	104	61.4	111	76.3	66.6	33.7	33.6	88.7	84	79	94.1	74.8	75.7	109	129
Eu	19.5	12.2	23.9	12.1	18	20.2	13.9	22.9	16.7	17.5	7.6	12.8	18.8	19.6	15.6	18.7	17.5	17	23.2	25.9
Gd	97.7	62.7	146	72	111	121	86.8	128	102	110	36.6	53	112	119	100	115	105	103	130	134
Tb	13.9	9.13	21.5	12.9	15.8	16.5	11.9	17.4	16.3	18.8	4.76	8.6	17.2	19.6	14.9	17.6	15	14.5	18	18.1
Dy	81.6	54.5	132	89.6	89.5	94.9	68.9	101	105	128	41.9	60.4	109	128	100	112	89.3	85	104	105
Ho	17.8	12	27.5	20.3	18.3	19.5	14.5	20.4	22.8	28.2	8.1	14.3	23.4	27.9	21	24.8	18.6	18.3	21.4	21
Er	50	32	73.7	59.1	48.8	52.3	38.1	55	65.6	79.9	24.7	41.8	66.2	78	60.7	66.3	51.3	50	56.6	57.1
Tm	6.7	4.58	10.2	8.1	6.63	7.2	5.1	7.26	9.29	11.3	3.08	5.81	9.06	11.1	8.03	9.33	7.05	6.58	7.52	7.72
Yb	45.1	29.7	65.5	52.4	42.6	46	32.6	46.9	59	75.5	20.7	39	59.6	72.3	53.7	59.2	44.1	41.8	50.1	48.2
Lu	6.77	4.67	9.7	7.46	6.43	6.91	4.95	7.2	8.76	11	4.74	6.3	8.65	10.7	7.7	8.9	6.76	6.08	7.56	7.84
Pb	0.521	0.12	0.597	0.544	0.251	0.273	0.084	0.393	0.227	0.344	0.73	0.129	0.266	0.454	0.18	0.341	0.232	0.282	0.491	0.589
Th	2.85	0.529	3.94	3.36	0.723	1.09	0.118	2.02	1.25	2.86	2.52	0.43	1.2	2.96	0.98	2.13	1.13	5.54	2.76	3.86
U	5.77	1.72	7.96	5.43	2.84	3.99	0.805	7.83	4	6.61	1.03	1.76	3.79	6.81	3.08	5.21	2.78	2.82	7.54	8.43

Table 3.4. Cont'd.

Rock Type Biotite schist (GRV-11-01)																				
Grain #	31		34		35		36		37		39		48		51		52		54	
Spot #	1	2	1	2	1	2	1	2	1	2	1	2	1	2	1	2	1	2	1	2
Trace Elements (ppm)																				
Mg	105	73.2	80.3	553	76.7	78.7	146	212	111	87.5	97.3	108	116	95.6	74.4	76.7	73.6	118	234	88.4
Si	304	470	430	1040	493	279	441	422	340	239	267	262	281	361	357	378	348	501	440	263
V	0.65	1.49	1.32	3.93	1.45	0.48	1.29	0.97	0.94	6.60	0.80	0.90	0.74	1.04	1.20	1.46	1.30	1.75	1.03	0.96
Cr	5.22	6	5.62	4	5.1	4.85	4.2	2.85	4.2	5.3	4.8	4.6	3.8	4.78	4.28	6.3	5.2	4.6	4.7	6.5
Mn	392	323	342	321	346	346	640	625	668	616	645	670	675	652	342	322	311	312	557	569
Co	bdl	bdl	bdl	bdl	bdl	bdl	bdl	bdl	bdl	2.49	bdl	3.5	2.64	bdl						
Cu	bdl	bdl	bdl	1.27	bdl	bdl	bdl	bdl	bdl	bdl	bdl	bdl	bdl	bdl	bdl	bdl	bdl	bdl	bdl	bdl
Zn	bdl	bdl	bdl	bdl	bdl	bdl	bdl	bdl	bdl	bdl	bdl	bdl	bdl	bdl	bdl	bdl	bdl	bdl	bdl	bdl
As	61.4	41.4	44	41.8	37	56.8	31	28.7	25.1	56.6	31.9	31.7	27.7	31.6	45.6	55.7	44.1	37.6	26.6	32.2
Sr	413	435	422	443	431	426	460	478	454	460	465	468	482	459	444	446	425	434	443	437
Y	536	753	559	648	720	490	594	526	569	478	519	526	554	517	633	475	457	704	427	397
Zr	bdl	bdl	bdl	bdl	bdl	bdl	bdl	bdl	bdl	1.7	bdl	bdl	bdl	bdl	bdl	bdl	bdl	bdl	bdl	bdl
Ba	0.93	bdl	bdl	1.53	bdl	0.6	1.07	bdl	bdl	bdl	0.52	bdl	bdl	bdl	bdl	bdl	bdl	bdl	bdl	0.78
La	162	29.3	30.1	10.3	37.2	30.7	170	240	53.7	19.3	30.2	41.5	173	bdl	19.4	4.6	9.25	14	17.3	15.9
Ce	569	138	147	40.3	170	136	559	766	211	89.6	128	167	565	131	91.6	23.1	44.3	70.5	76.3	73.2
Pr	88.7	29.2	31.2	10	35.3	27.3	88.8	118	41.2	20.4	27.9	34.1	91	29.6	20	5.14	9.83	15.9	17	16.8
Nd	477	213	224	87.3	244	190	511	620	296	166	211	239	522	233	152	47	83	124	135	130
Sm	103	80.4	76	45.9	81.7	60.3	137	143	109	75.2	85.8	90.8	136	93.7	63.8	29.6	38.5	56.3	62.6	60.2
Eu	17.7	18.1	16.1	12.3	18.8	14	26	25.4	23.1	16.7	19.6	19.9	25.2	19.9	15.8	9.35	9.6	15	14.5	13.8
Gd	107	114	96.1	85.5	111	83	137	131	126	96.4	108	111	130	111	95.8	61.2	68.7	105	85.6	81.8
Tb	15.3	19.5	15	15.1	18.3	12.7	18.6	17.3	18	14.1	15.4	15.7	17.8	16	16	11.1	11.2	17.5	12.4	12.1
Dy	91.6	123	94.4	104	121	80.7	106	95.6	99.5	82.9	90.8	91.7	99.5	92.5	105	75.5	72.5	117	73.6	69.8
Ho	19	26.7	20.3	22.9	26.4	17.3	21.4	19	20.8	16.9	18.9	19.1	20.1	19	22.8	17	16.5	25.8	15.1	14.8
Er	51.6	74.1	54.3	65.9	72	48.4	57.3	50.9	55.9	46.2	51.7	50.8	52.6	49.5	61.8	47.8	44.4	72.6	40.2	39
Tm	6.87	10.3	7.5	8.9	10.1	6.61	7.71	6.87	7.44	6.08	6.82	7.04	6.97	6.61	8.87	6.59	6	9.56	5.25	5.19
Yb	45.2	66.6	47.5	56	65.6	41.7	50.1	43.6	46.9	39.4	43.6	41.9	46	42	56.6	43.9	39.4	65.1	33.4	32.2
Lu	6.57	9.69	7.11	8.32	9.97	6.47	7.59	6.58	7.19	5.86	6.47	6.64	6.89	6.35	8.22	6.3	5.59	9.11	5.26	4.68
Pb	0.189	0.419	0.65	0.326	0.255	0.153	0.674	0.316	0.392	0.14	0.231	0.288	0.26	0.201	0.189	0.136	0.186	0.454	0.172	0.161
Th	0.84	2.76	0.68	2.82	2.05	0.60	4.00	1.44	2.14	0.33	0.76	1.06	1.10	0.87	1.26	0.53	0.76	2.57	0.54	0.36
U	2.09	6.36	2.29	4.21	5.37	2.33	9.61	5.62	6.06	1.56	2.65	4.13	5.25	3.04	3.81	1.64	2.41	6.07	1.53	1.01

Table 3.4. Cont'd.

Rock Type Magentite-apatite ore (GRV-11-02)										
Grain #	4 err	5 err	11 err	13 err	14 err	15 err	16 err	21 err	26 err	31 err
N	3	3	3	3	3	3	3	3	3	3
Major Elements (wt.%)										
CaO	55.47 (0.14)	55.46 (0.13)	55.46 (0.12)	55.49 (0.07)	55.66 (0.07)	55.10 (0.20)	55.45 (0.15)	55.36 (0.05)	55.55 (0.08)	55.60 (0.18)
SrO	0.02 (0.02)	0.04 (0.01)	0.03 (0.03)	0.03 (0.00)	0.01 (0.01)	0.02 (0.01)	0.03 (0.02)	0.01 (0.03)	0.03 (0.01)	0.01 (0.02)
Na₂O	0.02 (0.01)	0.03 (0.01)	0.03 (0.00)	0.03 (0.01)	0.01 (0.01)	0.04 (0.01)	0.02 (0.01)	0.04 (0.00)	0.02 (0.00)	0.02 (0.02)
Y₂O₃	0.05 (0.00)	0.03 (0.02)	0.03 (0.01)	0.05 (0.02)	0.03 (0.03)	0.07 (0.03)	0.05 (0.02)	0.04 (0.01)	0.05 (0.03)	0.03 (0.02)
MnO	0.05 (0.02)	0.03 (0.00)	0.04 (0.01)	0.03 (0.02)	0.06 (0.01)	0.04 (0.00)	0.04 (0.01)	0.05 (0.03)	0.04 (0.01)	0.05 (0.02)
MgO	0.00 (0.01)	bdl	0.00 (0.01)	0.00 (0.00)	bdl	0.00 (0.00)	0.00 (0.01)	bdl	0.00 (0.01)	0.00 (0.00)
FeO	bdl	0.00 (0.01)	0.01 (0.02)	0.01 (0.01)	0.00 (0.01)	0.01 (0.01)	0.01 (0.01)	0.01 (0.01)	0.01 (0.01)	0.00 (0.01)
P₂O₅	41.84 (0.32)	41.51 (0.23)	42.09 (0.38)	41.86 (0.07)	41.59 (0.25)	41.85 (0.15)	42.01 (0.09)	41.74 (0.25)	41.90 (0.34)	42.05 (0.44)
SiO₂	0.03 (0.01)	0.05 (0.01)	0.08 (0.06)	0.04 (0.02)	0.02 (0.02)	0.18 (0.02)	0.10 (0.02)	0.11 (0.02)	0.08 (0.08)	0.03 (0.00)
As₂O₅	0.07 (0.06)	bdl	0.05 (0.08)	0.03 (0.06)	0.09 (0.03)	bdl	0.03 (0.05)	0.06 (0.05)	0.06 (0.05)	0.04 (0.04)
SO₃	0.03 (0.01)	0.05 (0.02)	0.07 (0.03)	0.05 (0.00)	0.02 (0.02)	0.04 (0.01)	0.08 (0.04)	0.09 (0.01)	0.05 (0.02)	0.05 (0.02)
F⁻	2.59 (0.02)	2.63 (0.05)	2.56 (0.04)	2.62 (0.02)	2.62 (0.04)	2.26 (0.02)	2.64 (0.02)	2.61 (0.05)	2.56 (0.00)	2.59 (0.01)
Cl⁻	0.38 (0.02)	0.34 (0.02)	0.37 (0.02)	0.39 (0.02)	0.37 (0.03)	0.61 (0.02)	0.36 (0.04)	0.40 (0.01)	0.38 (0.02)	0.36 (0.02)
OH^{-†}	0.84	0.82	0.88	0.82	0.82	1.03	0.82	0.82	0.88	0.87
Total	101.40 (0.36)	100.99 (0.27)	101.72 (0.41)	101.45 (0.12)	101.30 (0.28)	101.23 (0.26)	101.64 (0.20)	101.31 (0.27)	101.61 (0.36)	101.71 (0.48)
O=F,Cl	-1.18 (0.01)	-1.18 (0.02)	-1.16 (0.02)	-1.19 (0.01)	-1.19 (0.02)	-1.09 (0.01)	-1.19 (0.01)	-1.19 (0.02)	-1.16 (0.00)	-1.17 (0.01)
Total*	100.23 (0.36)	99.81 (0.27)	100.56 (0.41)	100.26 (0.12)	100.12 (0.28)	100.15 (0.26)	100.45 (0.20)	100.12 (0.27)	100.45 (0.36)	100.54 (0.48)
X(FAp)	0.69 (0.01)	0.70 (0.01)	0.68 (0.01)	0.69 (0.01)	0.69 (0.01)	0.60 (0.01)	0.70 (0.01)	0.69 (0.01)	0.68 (0.00)	0.69 (0.00)
X(CAp)	0.06 (0.00)	0.05 (0.00)	0.05 (0.00)	0.06 (0.00)	0.05 (0.00)	0.09 (0.00)	0.05 (0.01)	0.06 (0.00)	0.06 (0.00)	0.05 (0.00)
X(HAp)	0.25	0.24	0.26	0.24	0.24	0.30	0.24	0.24	0.26	0.26

Table 3.4. Cont'd.

Rock Type Magentite-apatite ore (GRV-11-02)										
Grain #	32 err	34 err	35 err	42 err	44 err	46 err	47 err	53 err	54 err	56 err
N	3	3	3	3	3	3	3	3	3	3
Major Elements (wt.%)										
CaO	55.53 (0.06)	55.03 (0.16)	55.47 (0.03)	55.52 (0.02)	55.42 (0.01)	55.43 (0.05)	55.52 (0.08)	55.59 (0.03)	55.50 (0.12)	55.47 (0.20)
SrO	0.06 (0.03)	0.02 (0.02)	0.03 (0.02)	0.02 (0.03)	0.04 (0.03)	0.02 (0.03)	0.02 (0.02)	0.04 (0.01)	0.01 (0.02)	0.04 (0.01)
Na₂O	0.03 (0.02)	0.05 (0.02)	0.02 (0.01)	0.02 (0.01)	0.03 (0.01)	0.00 (0.01)	0.02 (0.00)	0.02 (0.01)	0.02 (0.00)	0.01 (0.01)
Y₂O₃	0.05 (0.01)	0.13 (0.01)	0.03 (0.03)	0.02 (0.02)	0.03 (0.01)	0.03 (0.02)	0.03 (0.01)	0.05 (0.01)	0.02 (0.00)	0.05 (0.02)
MnO	0.04 (0.01)	0.04 (0.01)	0.04 (0.01)	0.04 (0.02)	0.04 (0.03)	0.04 (0.02)	0.03 (0.01)	0.04 (0.01)	0.03 (0.00)	0.05 (0.02)
MgO	bdl	0.04 (0.06)	0.00 (0.00)	0.01 (0.01)	bdl	bdl	bdl	bdl	0.00 (0.00)	bdl
FeO	bdl	bdl	bdl	0.00 (0.01)	0.02 (0.01)	0.00 (0.01)	0.01 (0.01)	0.01 (0.01)	bdl	0.01 (0.02)
P₂O₅	41.98 (0.11)	41.39 (0.17)	41.97 (0.20)	42.12 (0.19)	42.14 (0.16)	42.08 (0.17)	42.20 (0.21)	42.10 (0.10)	42.24 (0.11)	42.31 (0.12)
SiO₂	0.05 (0.01)	0.28 (0.10)	0.04 (0.02)	0.03 (0.01)	0.08 (0.01)	0.04 (0.02)	0.05 (0.03)	0.06 (0.01)	0.05 (0.03)	0.06 (0.04)
As₂O₅	0.04 (0.08)	0.09 (0.10)	0.07 (0.06)	0.03 (0.05)	bdl	0.03 (0.05)	0.06 (0.07)	0.13 (0.02)	0.05 (0.05)	0.03 (0.05)
SO₃	0.06 (0.03)	0.07 (0.02)	0.05 (0.01)	0.04 (0.01)	0.08 (0.01)	0.05 (0.02)	0.05 (0.01)	0.05 (0.02)	0.05 (0.01)	0.04 (0.01)
F⁻	2.63 (0.01)	2.17 (0.06)	2.67 (0.05)	2.58 (0.07)	2.57 (0.03)	2.61 (0.02)	2.85 (0.00)	2.66 (0.04)	2.58 (0.04)	2.71 (0.07)
Cl⁻	0.36 (0.01)	0.68 (0.02)	0.32 (0.03)	0.34 (0.03)	0.37 (0.01)	0.37 (0.01)	0.35 (0.02)	0.35 (0.02)	0.38 (0.01)	0.37 (0.02)
OH⁻	0.82	1.06	0.80	0.88	0.88	0.84	0.64	0.81	0.87	0.76
Total	101.64 (0.15)	101.04 (0.29)	101.51 (0.22)	101.66 (0.22)	101.69 (0.18)	101.55 (0.19)	101.83 (0.24)	101.91 (0.12)	101.81 (0.18)	101.91 (0.26)
O=F,Cl	-1.19 (0.01)	-1.07 (0.02)	-1.20 (0.02)	-1.16 (0.03)	-1.17 (0.01)	-1.18 (0.01)	-1.28 (0.00)	-1.20 (0.02)	-1.17 (0.02)	-1.23 (0.03)
Total*	100.45 (0.16)	99.98 (0.29)	100.31 (0.23)	100.49 (0.22)	100.53 (0.18)	100.37 (0.19)	100.55 (0.24)	100.71 (0.12)	100.64 (0.18)	100.68 (0.26)
X(FAp)	0.70 (0.00)	0.58 (0.02)	0.71 (0.01)	0.69 (0.02)	0.68 (0.01)	0.69 (0.01)	0.76 (0.00)	0.71 (0.01)	0.69 (0.01)	0.72 (0.02)
X(CAp)	0.05 (0.00)	0.10 (0.00)	0.05 (0.00)	0.05 (0.00)	0.05 (0.00)	0.05 (0.00)	0.05 (0.00)	0.05 (0.00)	0.06 (0.00)	0.06 (0.00)
X(HAp)	0.24	0.31	0.24	0.26	0.26	0.25	0.19	0.24	0.26	0.22

Table 3.4. Cont'd.

Rock Type	Magnetite-apatite ore (GRV-11-02)																			
Grain #	4		5		11		13		14		15		16		21		26		31	
Spot #	1	2	1	2	1	2	1	2	1	2	1	2	1	2	1	2	1	2	1	2
Trace Elements (ppm)																				
Mg	63.2	69.7	68	70.3	69.7	68.8	72.5	71.7	64	69.3	96.1	95.6	71.8	71.4	76.5	76.7	68.7	74.8	72.6	270
Si	283	362	613	511	778	540	747	603	326	298	991	1330	759	717	820	772	420	401	610	1230
V	20.3	26.7	64.2	52.7	54.6	59.2	31.8	35.7	31.7	32.2	63.7	64.7	47.5	53.7	48.8	46	24.3	27.4	40.2	31.9
Cr	6.2	4.7	7.3	5	8	5	7.2	6	5.3	7.1	5.9	4.7	5.2	6.2	8.6	5.5	5.9	5.46	19.2	10
Mn	285	287	311	314	307	314	292	297	269	276	275	271	290	286	300	292	272	283	285	304
Co	bdl	bdl	bdl	bdl	bdl	bdl	bdl	bdl	bdl	bdl	bdl	bdl	bdl	bdl	bdl	bdl	bdl	bdl	bdl	bdl
Cu	bdl	bdl	bdl	bdl	bdl	bdl	bdl	bdl	bdl	bdl	bdl	0.69	bdl	bdl	bdl	bdl	0.58	bdl	bdl	2.26
Zn	bdl	bdl	bdl	bdl	bdl	bdl	bdl	bdl	bdl	bdl	bdl	bdl	bdl	bdl	bdl	bdl	bdl	bdl	bdl	bdl
As	157	215	354	314	339	331	282	255	223	236	281	240	268	351	291	269	166	221	256	247
Sr	218	250	284	271	263	273	253	267	208	213	213	214	251	256	265	277	243	263	241	260
Y	159	211	273	255	268	291	352	249	167	185	534	749	357	263	348	266	205	183	239	178
Zr	bdl	bdl	bdl	bdl	bdl	bdl	bdl	bdl	bdl	bdl	bdl	0.102	bdl	bdl	bdl	bdl	bdl	bdl	bdl	bdl
Ba	bdl	bdl	0.79	bdl	bdl	bdl	bdl	bdl	bdl	bdl	bdl	bdl	bdl	bdl	bdl	bdl	bdl	bdl	bdl	bdl
La	3.7	8.02	30.3	20.1	39.9	43.7	145	71	1.66	1.76	317	429	68.7	74.1	142	144	19.6	37.5	43.4	30.7
Ce	21.3	46.3	142	105	192	193	574	341	12	13.6	1380	1900	322	332	594	573	118	221	211	171
Pr	5.38	11.3	28	21.6	35.9	37.7	95.4	63.7	3.61	3.96	231	308	58.4	58.3	97.9	91.6	25.6	45.1	36.8	36.5
Nd	41.8	83.4	192	157	222	239	541	367	31	36.2	1110	1500	358	338	519	466	172	268	218	213
Sm	20.4	39.7	65	55.5	67.9	74.5	124	90	20.3	22.3	228	299	97.1	81.9	122	104	54.5	68.3	64.4	61.9
Eu	3.92	6.97	9.1	8.05	9.75	10.3	17	12	3.32	4.2	29.6	40.4	13.7	11.7	16.4	13.5	7.85	9.95	10	8.79
Gd	34.2	52.4	71.8	67.1	72.9	83.5	113	79.2	33.2	38.6	177	241	101	79	113	88.7	55.5	64.6	66.2	56.6
Tb	5.39	7.36	9.96	9.09	9.79	11.3	14.5	10.3	5.4	6.08	22.2	30.1	13.5	10.2	14.1	11	7.64	7.55	9.22	7.26
Dy	31	41.8	55.1	49.5	53.2	61.8	77.4	51.7	32.3	34.6	113	153	71.7	50.9	73.7	56.1	39.8	38.6	50.7	37
Ho	5.96	8.06	10.5	9.59	10.2	11.1	14.9	10	6.35	7.09	20.9	28.4	13.5	10	13.9	10.5	7.73	7.23	9.44	7.25
Er	14.5	19.3	25.1	22.9	24.8	27.2	33.5	22	15.7	16.5	47.5	67.1	32.2	23.3	32.7	23.8	18.4	15.6	21.1	15.3
Tm	1.52	2.12	2.75	2.56	2.74	2.97	3.57	2.41	1.84	1.95	5.51	7.83	3.45	2.48	3.43	2.59	2.07	1.74	2.2	1.67
Yb	8.5	10.8	14.1	13.2	14.3	14.9	19.2	12.3	8.98	9.38	29.4	41.5	17.6	14.1	18.8	13.6	10.3	8.55	11.5	9.3
Lu	0.94	1.33	1.8	1.67	1.72	1.79	2.3	1.64	1.15	1.2	3.68	5.07	2.17	1.53	2.33	1.56	1.27	0.998	1.63	1.08
Pb	0.075	0.108	1.06	0.688	2.03	1.28	1.2	1.04	0.036	0.058	1.3	2.58	1.74	3.33	2.31	2.01	0.901	0.264	1.02	0.455
Th	0.339	0.215	6.9	4.36	11.7	8.38	7.99	6.32	0.114	0.117	8.31	18.3	11.4	19.7	12.9	11.4	5.13	1.29	6.23	2.08
U	0.942	2.89	4.62	3.58	6.12	4.97	4.67	6.39	1.06	1.24	3.33	7.5	7.64	8.29	6.94	8.28	4.06	5.2	5.75	4.87

Table 3.4. Cont'd.

Rock Type Magentite-apatite ore (GRV-11-02)																				
Grain #	32		34		35		42		44		46		47		53		54		56	
Spot #	1	2	1	2	1	2	1	2	1	2	1	2	1	2	1	2	1	2	1	2
Trace Elements (ppm)																				
Mg	81.2	79.4	94.7	117	75.5	94.8	80.3	76.5	67.3	67.4	78.9	78.6	78	77.2	174	75	82.4	83.1	80	75.4
Si	415	894	1250	1360	380	316	372	389	712	676	508	550	323	415	512	268	317	319	577	560
V	30.8	56.8	51.1	54.8	43.6	59.7	45.5	35.5	44.5	50.6	36	44.6	32.4	34.1	60.1	40.8	22.9	26.6	42.1	41.4
Cr	8.5	9	3.93	5.47	5.06	6.11	7	5.3	4.82	5.86	4.58	3.9	6.25	4.5	8	5.3	4.5	5.9	5.75	3.4
Mn	299	295	278	277	297	276	290	296	272	270	303	289	303	301	291	295	281	304	303	298
Co	bdl	5.1	bdl	2.36	bdl	bdl	bdl	2.8	bdl	bdl	bdl	bdl	bdl	1.6	bdl	bdl	bdl	bdl	bdl	bdl
Cu	bdl	bdl	bdl	bdl	bdl	0.57	bdl	bdl	bdl	bdl	bdl	bdl	bdl	bdl	bdl	bdl	bdl	bdl	bdl	bdl
Zn	bdl	bdl	bdl	bdl	bdl	bdl	bdl	bdl	bdl	bdl	bdl	bdl	bdl	bdl	bdl	bdl	bdl	bdl	bdl	bdl
As	240	261	224	244	300	358	291	306	251	331	265	297	253	275	297	256	208	231	271	272
Sr	259	253	221	223	285	273	224	275	235	242	265	282	283	268	238	243	260	266	273	248
Y	232	466	823	934	231	163	223	174	335	248	218	262	169	200	225	174	133	137	248	357
Zr	bdl	bdl	0.115	0.094	bdl	bdl	bdl	bdl	bdl	bdl	bdl	bdl	bdl	bdl	bdl	bdl	bdl	bdl	bdl	0.054
Ba	bdl	bdl	bdl	bdl	bdl	0.55	bdl	bdl	bdl	bdl	bdl	bdl	bdl	bdl	bdl	bdl	bdl	bdl	0.39	bdl
La	27.4	223	390	280	26.3	4.69	8.45	3.79	64.5	69.8	74.3	42.7	16.3	31.5	7.31	4.53	16.6	9.23	91.4	45.7
Ce	155	894	1780	1490	130	29.8	50.3	28.4	302	313	350	217	108	186	54.4	36.4	125	86.2	419	244
Pr	33.2	143	286	273	24.7	7.08	11.7	7.54	54.8	54.9	59.9	41.8	23.6	36.9	12.9	9.19	27.2	20.8	67.7	47.3
Nd	206	716	1410	1400	153	52.5	87.7	61.3	336	318	317	255	143	211	96.1	68.5	162	134	343	262
Sm	65.9	170	304	334	50.2	27.1	42.4	34	91.1	77.2	79.4	77.6	45.7	59.1	44.3	33	46.9	43.9	82.5	84.5
Eu	8.97	24.1	38.5	44.4	7.57	4.46	6.75	5.36	12.9	11	10.9	11.1	6.84	8.41	7.43	5.64	6.79	6.63	11.9	13.5
Gd	69.1	155	242	275	58.7	39.8	57.5	46.5	95	74.6	72.3	72.1	46.6	57.4	56.8	44	45.1	43.8	74.8	92.1
Tb	8.81	19.5	31	35.7	8.4	5.87	8.51	6.84	12.7	9.66	8.95	10	6.11	7.54	8.21	6.33	5.53	5.62	9.65	12.6
Dy	46.8	102	167	191	45.7	33.8	46.9	36.4	67.3	47.9	46.4	51.1	33.2	38.8	44	33.6	28.9	28.6	50.6	67.7
Ho	8.74	20	31	36.4	9.02	6.74	8.84	6.83	12.6	9.45	8.8	10.2	6.2	7.43	8.75	6.68	5.55	5.37	9.5	13.7
Er	20.1	43.8	73.4	85.1	20.7	16.1	20.5	16.1	30.2	21.9	19.6	22.5	14.3	17.4	19.6	15.2	11.7	12.7	21.6	31.3
Tm	2.32	4.84	8.76	10.2	2.3	1.71	2.15	1.71	3.23	2.34	2.23	2.48	1.61	1.96	2.35	1.67	1.28	1.37	2.41	3.48
Yb	12.8	25.2	50.8	57.5	12.8	8.96	12	8.91	16.5	13.3	11.8	13	7.99	9.89	11.9	8.75	6.95	6.82	12.8	18.1
Lu	1.64	2.93	6.2	7.04	1.44	1.09	1.44	1.06	2.04	1.45	1.39	1.53	1.02	1.2	1.44	1.11	0.824	0.788	1.47	2.22
Pb	0.189	1.85	3.28	3.41	0.698	0.156	0.578	0.108	1.64	3.14	1.33	1.37	0.214	0.338	0.567	0.171	0.38	0.258	1.78	1.03
Th	0.94	10.2	19.9	20.1	4.24	0.793	2.78	0.425	10.7	18.6	7.29	7.41	0.86	1.7	2.69	0.573	1.2	0.783	9.2	5.68
U	5.5	6.18	7.36	7.19	3.77	1.68	2.45	1.35	7.17	7.81	6.48	6.38	3.42	4.74	1.94	1.3	3.95	3.21	7.16	3.98

Table 3.4. Cont'd.

Rock Type	Metadiabase dyke (GRV-11-04)									
Grain #	9 err	10 err	15 err	16 err	17 err	22 err	25 err	27 err	28 err	29 err
N	3	3	3	3	3	3	3	3	3	3
Major Elements (wt.%)										
CaO	55.35 (0.07)	55.26 (0.05)	55.25 (0.10)	55.32 (0.07)	55.22 (0.09)	55.17 (0.16)	55.35 (0.20)	55.33 (0.06)	55.33 (0.09)	55.37 (0.18)
SrO	0.01 (0.03)	0.04 (0.01)	bdl	0.02 (0.03)	0.04 (0.02)	0.01 (0.02)	0.01 (0.02)	0.01 (0.02)	0.02 (0.03)	0.02 (0.02)
Na ₂ O	0.04 (0.02)	0.03 (0.01)	0.03 (0.01)	0.03 (0.01)	0.02 (0.01)	0.04 (0.01)	0.02 (0.01)	0.03 (0.00)	0.02 (0.02)	0.02 (0.02)
Y ₂ O ₃	0.03 (0.04)	0.05 (0.02)	0.04 (0.01)	0.02 (0.02)	0.09 (0.04)	0.07 (0.02)	0.02 (0.02)	0.04 (0.02)	0.04 (0.00)	0.04 (0.02)
MnO	0.06 (0.00)	0.07 (0.02)	0.07 (0.01)	0.07 (0.01)	0.09 (0.01)	0.07 (0.01)	0.08 (0.02)	0.06 (0.02)	0.08 (0.01)	0.03 (0.03)
MgO	0.01 (0.01)	0.01 (0.02)	bdl	bdl	0.01 (0.01)	0.00 (0.00)	bdl	bdl	0.00 (0.01)	bdl
FeO	0.01 (0.01)	bdl	0.01 (0.01)	bdl	0.01 (0.01)	0.01 (0.02)	bdl	0.01 (0.01)	0.01 (0.01)	0.00 (0.01)
P ₂ O ₅	42.03 (0.13)	41.92 (0.12)	41.99 (0.16)	42.13 (0.16)	41.75 (0.11)	41.68 (0.22)	41.88 (0.04)	41.96 (0.23)	42.15 (0.10)	41.88 (0.22)
SiO ₂	0.08 (0.04)	0.08 (0.03)	0.08 (0.01)	0.07 (0.02)	0.16 (0.11)	0.10 (0.04)	0.05 (0.02)	0.06 (0.00)	0.05 (0.02)	0.04 (0.00)
As ₂ O ₅	0.04 (0.07)	bdl	bdl	0.03 (0.05)	0.02 (0.03)	bdl	0.07 (0.07)	0.05 (0.05)	0.09 (0.08)	0.05 (0.04)
SO ₃	0.07 (0.04)	0.07 (0.01)	0.06 (0.02)	0.07 (0.04)	0.08 (0.03)	0.08 (0.01)	0.05 (0.01)	0.06 (0.01)	0.06 (0.01)	0.05 (0.01)
F	2.32 (0.06)	2.34 (0.01)	2.34 (0.02)	2.32 (0.05)	2.33 (0.01)	2.29 (0.04)	2.35 (0.05)	2.53 (0.03)	2.24 (0.02)	2.38 (0.04)
Cl	0.59 (0.03)	0.60 (0.01)	0.50 (0.01)	0.57 (0.01)	0.57 (0.01)	0.60 (0.03)	0.59 (0.01)	0.60 (0.00)	0.60 (0.01)	0.57 (0.03)
OH [†]	0.99	0.96	1.01	1.00	0.98	1.00	0.96	0.80	1.06	0.94
Total	101.64 (0.20)	101.42 (0.14)	101.37 (0.20)	101.66 (0.20)	101.36 (0.19)	101.11 (0.28)	101.43 (0.22)	101.53 (0.25)	101.75 (0.17)	101.39 (0.29)
O=F,Cl	-1.11 (0.02)	-1.12 (0.01)	-1.10 (0.01)	-1.10 (0.02)	-1.11 (0.01)	-1.10 (0.02)	-1.12 (0.02)	-1.20 (0.01)	-1.08 (0.01)	-1.13 (0.02)
Total*	100.53 (0.20)	100.30 (0.14)	100.27 (0.20)	100.56 (0.20)	100.25 (0.19)	100.01 (0.28)	100.31 (0.23)	100.33 (0.25)	100.67 (0.17)	100.26 (0.29)
X(Fap)	0.62 (0.01)	0.62 (0.00)	0.62 (0.01)	0.62 (0.01)	0.62 (0.00)	0.61 (0.01)	0.62 (0.01)	0.67 (0.01)	0.59 (0.00)	0.63 (0.01)
X(CAp)	0.09 (0.00)	0.09 (0.00)	0.07 (0.00)	0.08 (0.00)	0.08 (0.00)	0.09 (0.00)	0.09 (0.00)	0.09 (0.00)	0.09 (0.00)	0.08 (0.00)
X(HAp)	0.29	0.28	0.30	0.30	0.29	0.29	0.28	0.24	0.31	0.28

Table 3.4. Cont'd.

Rock Type	Metadiabase dyke (GRV-11-04)									
Grain #	34 err	36 err	37 err	40 err	41 err	42 err	45 err	49 err	55 err	58 err
N	3	3	3	3	3	3	3	3	3	3
Major Elements (wt.%)										
CaO	55.49 (0.01)	55.11 (0.23)	55.29 (0.12)	55.17 (0.02)	55.37 (0.03)	55.28 (0.07)	55.48 (0.16)	55.13 (0.03)	55.41 (0.06)	55.40 (0.18)
SrO	0.02 (0.03)	0.04 (0.02)	0.02 (0.02)	0.02 (0.02)	0.01 (0.01)	0.03 (0.03)	0.03 (0.03)	0.03 (0.01)	0.01 (0.01)	0.01 (0.01)
Na₂O	0.02 (0.01)	0.03 (0.01)	0.03 (0.01)	0.03 (0.01)	0.03 (0.00)	0.01 (0.02)	0.02 (0.01)	0.04 (0.01)	0.02 (0.01)	0.03 (0.00)
Y₂O₃	0.06 (0.01)	0.06 (0.01)	0.06 (0.04)	0.06 (0.02)	0.03 (0.03)	0.04 (0.02)	0.02 (0.00)	0.07 (0.03)	0.04 (0.01)	0.04 (0.01)
MnO	0.06 (0.01)	0.06 (0.02)	0.06 (0.02)	0.06 (0.03)	0.05 (0.01)	0.08 (0.02)	0.06 (0.03)	0.07 (0.01)	0.06 (0.03)	0.07 (0.01)
MgO	bdl	bdl	bdl	bdl	0.00 (0.00)	bdl	0.00 (0.01)	0.00 (0.00)	0.00 (0.00)	bdl
FeO	bdl	0.01 (0.01)	0.01 (0.01)	0.01 (0.01)	0.00 (0.01)	0.01 (0.01)	0.00 (0.01)	0.01 (0.02)	bdl	bdl
P₂O₅	42.04 (0.17)	41.77 (0.29)	41.94 (0.06)	41.81 (0.24)	42.13 (0.04)	42.01 (0.18)	42.14 (0.17)	41.82 (0.14)	41.97 (0.18)	41.72 (0.09)
SiO₂	0.08 (0.02)	0.14 (0.02)	0.11 (0.07)	0.09 (0.05)	0.07 (0.03)	0.07 (0.00)	0.04 (0.03)	0.12 (0.03)	0.05 (0.03)	0.07 (0.01)
As₂O₅	0.05 (0.04)	0.11 (0.02)	bdl	0.12 (0.11)	0.05 (0.09)	bdl	0.09 (0.08)	0.11 (0.10)	0.03 (0.05)	0.05 (0.09)
SO₃	0.06 (0.01)	0.10 (0.01)	0.09 (0.02)	0.08 (0.02)	0.06 (0.03)	0.06 (0.01)	0.05 (0.02)	0.10 (0.02)	0.06 (0.01)	0.08 (0.02)
F	2.35 (0.06)	2.27 (0.03)	2.26 (0.04)	2.38 (0.02)	2.34 (0.03)	2.48 (0.02)	2.32 (0.02)	2.31 (0.05)	2.49 (0.05)	2.52 (0.04)
Cl	0.60 (0.01)	0.58 (0.02)	0.61 (0.01)	0.60 (0.02)	0.52 (0.06)	0.59 (0.02)	0.58 (0.02)	0.60 (0.01)	0.59 (0.02)	0.56 (0.07)
OH	0.96	1.03	1.03	0.93	1.00	0.84	1.00	0.99	0.84	0.82
Total	101.79 (0.19)	101.33 (0.37)	101.52 (0.17)	101.34 (0.27)	101.67 (0.14)	101.50 (0.20)	101.84 (0.26)	101.39 (0.19)	101.58 (0.21)	101.36 (0.24)
O=F,Cl	-1.13 (0.03)	-1.09 (0.01)	-1.09 (0.02)	-1.13 (0.01)	-1.10 (0.02)	-1.18 (0.01)	-1.10 (0.01)	-1.11 (0.02)	-1.18 (0.02)	-1.19 (0.02)
Total*	100.67 (0.20)	100.24 (0.37)	100.43 (0.17)	100.20 (0.27)	100.57 (0.14)	100.32 (0.20)	100.73 (0.26)	100.28 (0.19)	100.39 (0.21)	100.17 (0.24)
X(Fap)	0.62 (0.00)	0.60 (0.00)	0.60 (0.01)	0.63 (0.01)	0.62 (0.01)	0.66 (0.00)	0.61 (0.01)	0.61 (0.01)	0.66 (0.00)	0.67 (0.00)
X(CAp)	0.09 (0.01)	0.08 (0.00)	0.09 (0.01)	0.09 (0.00)	0.08 (0.00)	0.09 (0.00)	0.08 (0.00)	0.09 (0.01)	0.09 (0.01)	0.08 (0.01)
X(HAp)	0.28	0.30	0.30	0.27	0.30	0.25	0.30	0.29	0.25	0.24

Table 3.4. Cont'd.

Rock Type	Metadiabase dyke (GRV-11-04)																			
Grain #	9		10		15		16		17		22		25		27		28		29	
Spot #	1	2	1	2	1	2	1	2	1	2	1	2	1	2	1	2	1	2	1	2
Trace Elements (ppm)																				
Mg	72	89.6	74.7	76.9	70.9	72.5	74	75.9	80.2	72.2	82.2	79.7	75.1	80.4	74.1	74.8	74.8	81.5	121	78.5
Si	444	600	420	531	575	505	468	410	674	459	449	492	436	410	435	440	385	518	750	469
V	8.71	20.1	19	22.8	35.6	23.2	22.2	12.9	35.6	14.3	14.8	15	26.8	20	27.9	31.4	13.2	11.3	18.3	17.4
Cr	7.35	5.72	5.7	5.59	4.88	5.2	5.51	4.2	10.5	8.6	6.1	6.8	5.6	7.12	6.36	6.2	6.58	7	7.4	6.8
Mn	410	404	384	393	461	454	449	455	478	476	372	385	458	450	465	477	444	438	361	343
Co	bdl	bdl	1.83	1.72	bdl	bdl	bdl	2.4	bdl	bdl	bdl	bdl	bdl	bdl	bdl	1.61	bdl	bdl	bdl	1.89
Cu	bdl	bdl	bdl	bdl	bdl	bdl	bdl	bdl	bdl	0.51	bdl	bdl	1.12	bdl	bdl	bdl	bdl	bdl	1.6	bdl
Zn	bdl	bdl	0.22	bdl	bdl	bdl	bdl	bdl	bdl	bdl	bdl	bdl	bdl	bdl	bdl	bdl	bdl	bdl	bdl	bdl
As	271	204	198	210	353	272	270	272	367	273	176	219	314	313	343	372	197	209	255	255
Sr	238	218	216	221	213	218	207	210	210	202	214	225	202	212	226	236	205	212	203	197
Y	274	341	326	318	309	299	210	167	229	235	314	355	130	177	259	252	282	331	278	296
Zr	bdl	0.042	bdl	bdl	0.076	bdl	bdl	bdl	0.042	bdl	bdl	bdl	bdl	bdl	bdl	bdl	bdl	bdl	bdl	bdl
Ba	0.54	0.57	bdl	bdl	0.36	bdl	bdl	bdl	0.92	bdl	bdl	0.45	bdl							
La	83.2	100	31.1	56.6	48.8	47.7	58.3	26.2	39.1	19.1	77.3	73.4	6.95	19	14.3	16.6	33.7	27.6	7.52	7.38
Ce	310	398	161	246	251	235	205	117	177	96.7	322	331	41.7	89.2	87.1	96.6	153	137	48.7	52.1
Pr	53.3	67.5	33	45.6	48.8	46.8	34.3	21.8	33.1	20.8	56.1	59.5	9.12	18.1	18.9	20.4	28.5	27.6	11.8	13
Nd	300	381	213	266	307	287	191	137	197	142	315	345	65.5	115	132	142	181	185	87.2	98.1
Sm	76.2	95.4	60.8	68.9	81.4	76.3	50.5	37.5	51.7	46	79.9	88.9	20	33.4	39.8	40.8	50.3	57.1	33.4	36
Eu	10.2	12.9	8.28	9.32	6.9	6.99	6.4	4.44	4.97	5.04	11.3	11.6	2.32	4.06	4.79	5.01	6.6	7.56	5.65	6.28
Gd	78.1	94.2	68.9	71.3	81.6	78.2	53.2	42.2	53.9	57	82.6	85.9	25.5	41.1	52	51.6	60.2	67.4	44.8	49.4
Tb	9.79	12.2	9.58	9.64	10.4	10.3	6.96	5.34	7.23	7.36	10.9	11.9	3.33	5.1	6.98	6.78	8.39	9.81	6.61	7.04
Dy	54.1	65.1	53.5	52	55.9	54.6	37	28.6	39.9	40.8	59.4	64.5	18.8	29.1	39.7	38.5	46.5	54.8	38.2	42
Ho	10.8	12.9	11.5	11.3	11.2	11.1	7.59	6	8.27	8.82	12.1	13.3	4.32	6.36	8.95	8.63	10	11.9	9.02	9.63
Er	25	30.9	29.6	28.1	27.1	26.4	19	14.7	20.9	21.5	28.5	30.9	11.7	16.3	23.6	22.7	25.7	30.2	25.3	26.1
Tm	2.93	3.67	3.64	3.55	3.08	3.16	2.21	1.77	2.54	2.49	3.47	3.92	1.59	2.07	2.86	2.88	3.17	3.77	3.32	3.45
Yb	16.2	19.5	20.5	20.1	17.1	16.9	12.6	9.77	14	13.9	18.8	22.7	9.75	12.9	18	17.1	18	21.1	19.9	20.6
Lu	2.19	2.44	2.85	2.75	2.4	2.28	1.9	1.55	1.99	1.98	2.45	3.01	1.87	2.14	2.98	2.73	2.46	2.96	3.09	3.18
Pb	0.229	0.627	0.368	0.474	0.713	0.57	0.407	0.201	0.893	0.418	0.47	0.538	0.388	0.287	0.553	0.478	0.374	0.344	0.147	0.099
Th	1.02	3.42	1.84	2.46	4.26	3.49	1.8	0.873	4.99	2.15	2.27	2.72	2.05	1.22	2.91	2.55	1.7	1.59	0.102	0.161
U	2.8	2.07	1.56	2.45	5.94	1.83	2.86	1.97	6.13	2.29	1.79	2.14	3.14	2.08	2.49	2.63	1.93	2.39	3.56	3.38

Table 3.4. Cont'd.

Rock Type	Metadiabase dyke (GRV-11-04)																				
Grain #	34		36		37		40		41		42		45		49		55		58		
Spot #	1	2	1	2	1	2	1	2	1	2	1	2	1	2	1	2	1	2	1	2	
Trace Elements (ppm)																					
Mg	76.6	76.4	83.8	88	83.4	81.8	82.6	84.2	86	87.7	83	79	86.3	85.7	91.1	80.3	93.7	79.9	99.9	111	
Si	363	379	663	627	462	321	550	548	422	274	414	421	311	549	471	473	684	473	450	415	
V	32.6	29.1	41	29.5	14.6	8.75	21.1	22.9	19.1	5.03	23.9	31.1	14.6	36.8	20.9	39.3	31.6	27.4	29.3	27.4	
Cr	7.26	6.65	6.6	4.9	5.7	6.36	6.61	6.8	5.2	5.75	6.4	6.1	7.26	6.4	6.77	8.8	5.45	6.38	7.3	5.3	
Mn	512	524	395	395	388	417	419	395	386	383	493	494	412	460	419	424	476	491	452	472	
Co	bdl	bdl	bdl	bdl	bdl	2.13	bdl	bdl	1.4	bdl	bdl	bdl	3.66	bdl	1.26	bdl	1.38	bdl	1.15	bdl	4.5
Cu	bdl	bdl	bdl	bdl	bdl	bdl	bdl	bdl	bdl	bdl	bdl	bdl	bdl	bdl	bdl	bdl	bdl	bdl	bdl	bdl	1.32
Zn	bdl	bdl	bdl	bdl	bdl	bdl	bdl	bdl	bdl	bdl	bdl	bdl	bdl	bdl	bdl	bdl	bdl	bdl	bdl	bdl	bdl
As	394	393	386	284	220	228	242	251	229	205	284	373	222	409	197	348	411	317	337	387	
Sr	237	237	235	239	219	222	219	216	221	227	201	226	200	225	224	232	200	202	219	220	
Y	256	265	379	385	305	247	303	370	253	198	319	290	189	276	389	201	340	320	243	213	
Zr	0.041	0.047	0.066	0.033	bdl	bdl	bdl	0.031	0.044	bdl	bdl	bdl	bdl	bdl	bdl	0.073	bdl	bdl	0.043	bdl	
Ba	bdl	0.34	0.3	0.37	bdl	bdl	0.65	bdl	0.38	0.37	bdl	bdl	bdl	bdl	0.46	0.41	bdl	bdl	bdl	0.82	
La	7.3	9.27	103	91.4	85.8	43.3	83.2	50.5	70.8	50.5	10.3	18.4	10.5	81	57.2	43.4	34.8	30.1	26.6	23.9	
Ce	51.3	60	462	428	380	206	361	279	320	230	71	103	70.5	389	319	219	191	182	171	145	
Pr	12.1	13.5	79.9	75.1	64.1	38.2	63.5	56.2	53.8	39.4	15.5	20.8	13.9	67.2	66	40.1	35.3	36.9	33	28.2	
Nd	89.5	98.2	442	419	349	222	346	346	288	207	110	143	93.9	356	385	225	215	221	202	170	
Sm	29.2	30.9	112	102	81.8	59.2	87.9	98.6	67.2	51	35.7	41.4	27.7	79	112	56.9	60.8	65.3	51.3	44.3	
Eu	3.48	3.59	15.3	14.3	11	7.88	11.6	13.6	9.49	7.01	4.24	4.54	3.66	10.3	15.4	7.2	7.78	8.03	7.44	6.31	
Gd	40.4	40.8	106	101	81.3	60.7	88.6	101	64.4	48.8	48.1	48.1	38.2	69.3	111	49.9	71.9	73.8	54.4	48.3	
Tb	5.48	5.73	13.5	13.3	10.9	8.36	11.5	13.6	8.39	6.47	6.6	6.31	5.08	9.58	14.7	6.45	10	10.2	7.01	6.14	
Dy	32.8	33.7	74.2	71.2	58.2	46.2	60.1	75.9	45.6	35.2	39.8	38.6	28.9	51.2	82	35.6	56.9	56.3	39.7	33.8	
Ho	7.94	8.15	14.5	14.4	11.6	9.13	12.2	14.7	8.82	6.89	9.68	8.65	6.69	10.2	15.8	6.95	12	11.8	8.29	7.38	
Er	22.6	23.1	33.9	34.7	27.6	22.7	27.9	35.2	21.5	16.5	27.2	24.8	17	23.8	37.9	17.2	29.4	29.5	22.1	20	
Tm	3.04	3.03	4.07	4.26	3.44	2.7	3.26	4.18	2.64	2.03	3.7	3.24	2.21	3.07	4.35	2.12	3.6	3.38	2.71	2.37	
Yb	19.6	19.9	21.9	22.9	17.7	15.4	18.1	22.9	14.7	10.9	24.1	19.6	13.6	16.3	23.9	12.3	20.7	19.5	16.2	14.5	
Lu	3.15	3.25	2.82	3.08	2.32	2.09	2.3	2.83	1.77	1.47	3.94	3.07	2.04	2.24	2.82	1.65	2.94	2.71	2.49	2.25	
Pb	0.445	0.786	1.54	1.07	0.554	0.352	0.655	0.736	0.607	0.168	0.539	0.595	0.121	1.49	0.9	0.728	1.71	1.19	0.659	0.508	
Th	1.95	3.84	7.68	5.22	2.36	1.33	3.18	3.29	2.59	0.564	2.61	2.64	0.338	7.43	4.39	3.35	8.67	6.04	3.02	2.15	
U	4.34	3.73	6.85	4.00	2.07	2.41	2.17	6.79	2.60	2.41	2.28	4.18	2.59	7.36	7.34	8.98	5.08	6.90	4.12	2.66	

CHAPTER 3 FIGURES

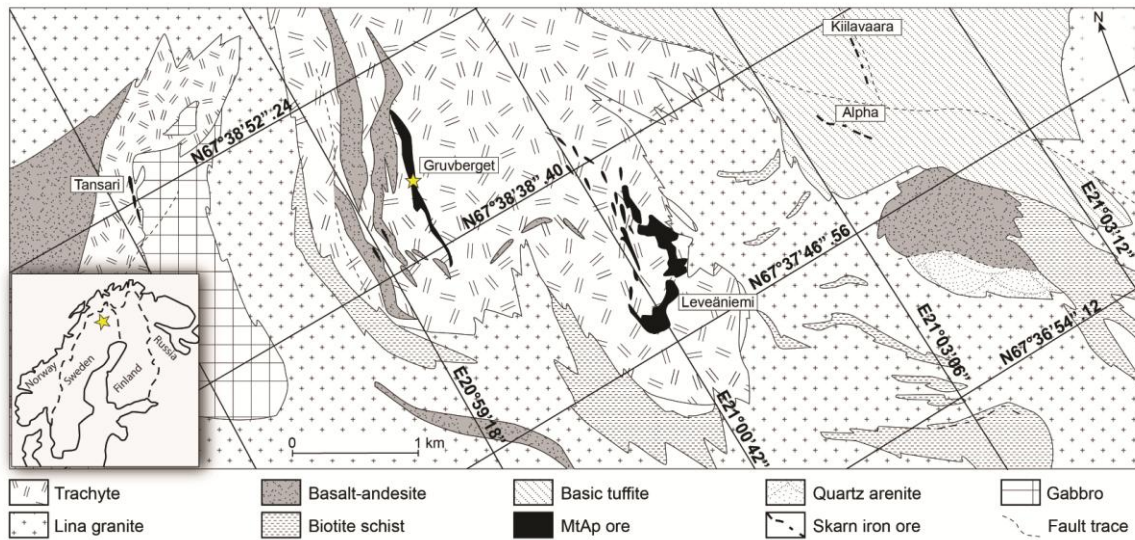


Figure 3.1 Generalized geologic map of the Svappavaara area of Northern Sweden, highlighting the spatial and geologic context of the major IOA and skarn type iron ore deposits. The star indicates the study area of the Gruvberget IOA deposit. Modified from Frietsch (1980).

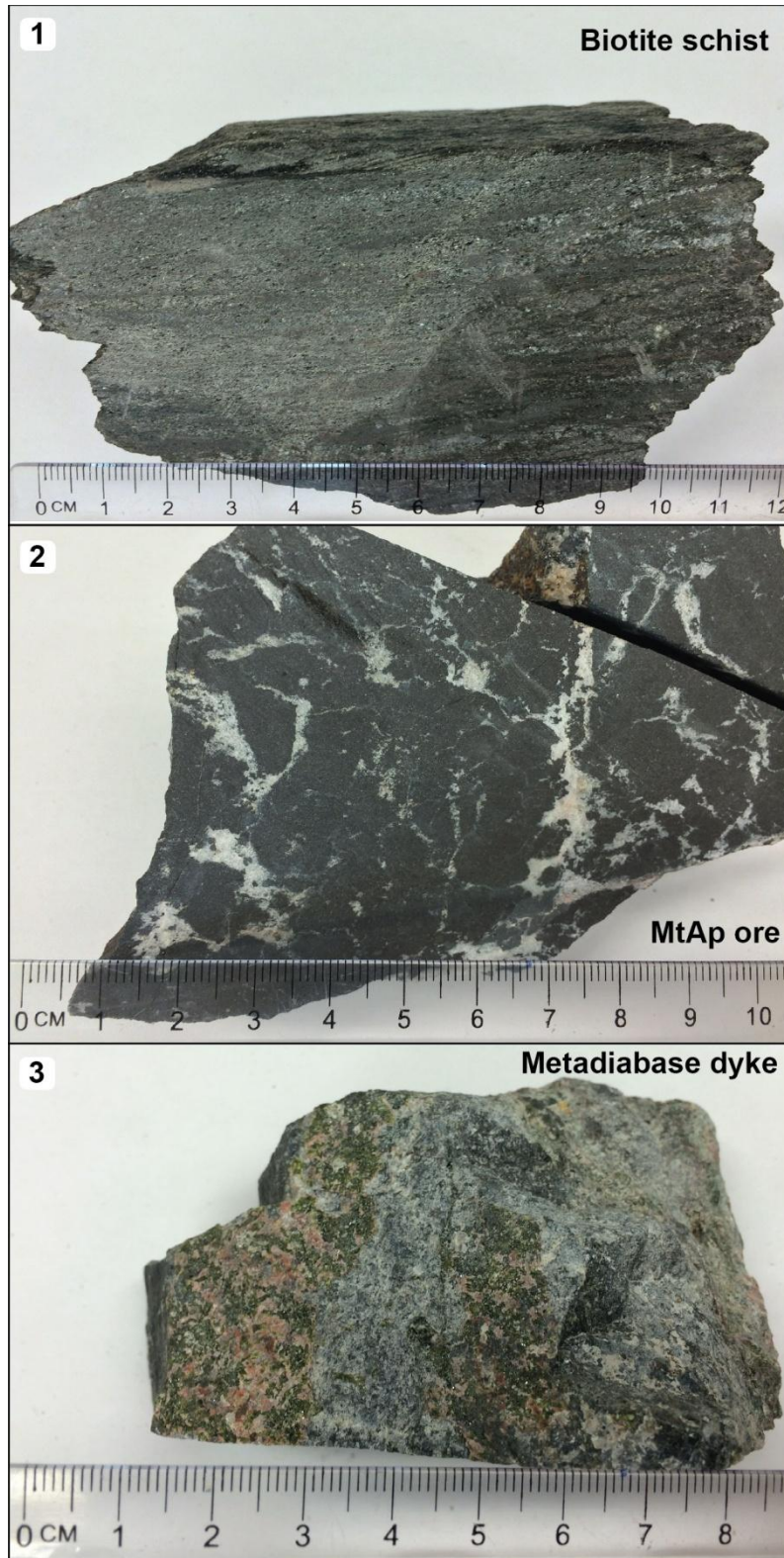


Figure 3.2 The respective samples illustrated here are as follows: **1** GRV-11-01 is a biotite schist from the footwall; **2** GRV-11-02 is a MtAp ore sample ore; and **3** GRV_11-04 is a crosscutting metadiabase dyke.

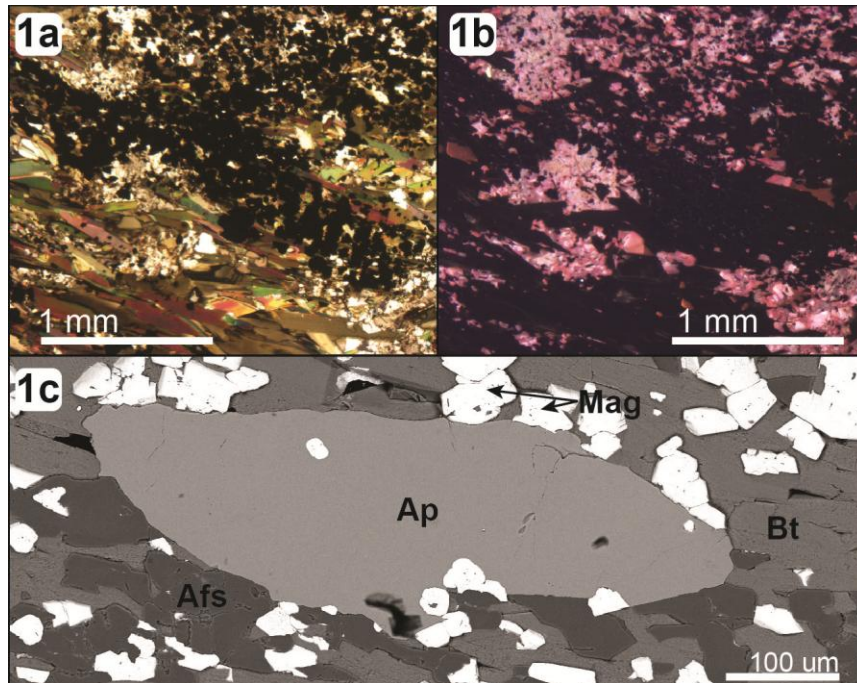


Figure 3.3 Cathodoluminescence (1b; 2b and 2d; and 3b), transmitted light microscopy in cross-polarized light (1a; 2a and 2c; and 3a) and back-scattered electron (BSE) images (1c and 3c) of the three Gruvberget samples. Note that in the biotite schist all minerals, including apatite, form along the distinct foliation (aligned from left to right in image 1c). The habit of apatite in the ore sample was well-defined by transmitted light and CL imaging (2a-d): revealing clusters of subhedral apatites (purple-green in CL—2c) intergrown with calcite. The metadiabase sample shows apatite coexisting with actinolite and Fe-Ti-oxide (3c; likely an alteration assemblage), surrounded by scapolite. Ap = apatite, Act = actinolite, Afs = Alkali feldspar Bt = Biotite, Mag = Magnetite, Ilm = Ilmenite, and Scp = Scapolite.

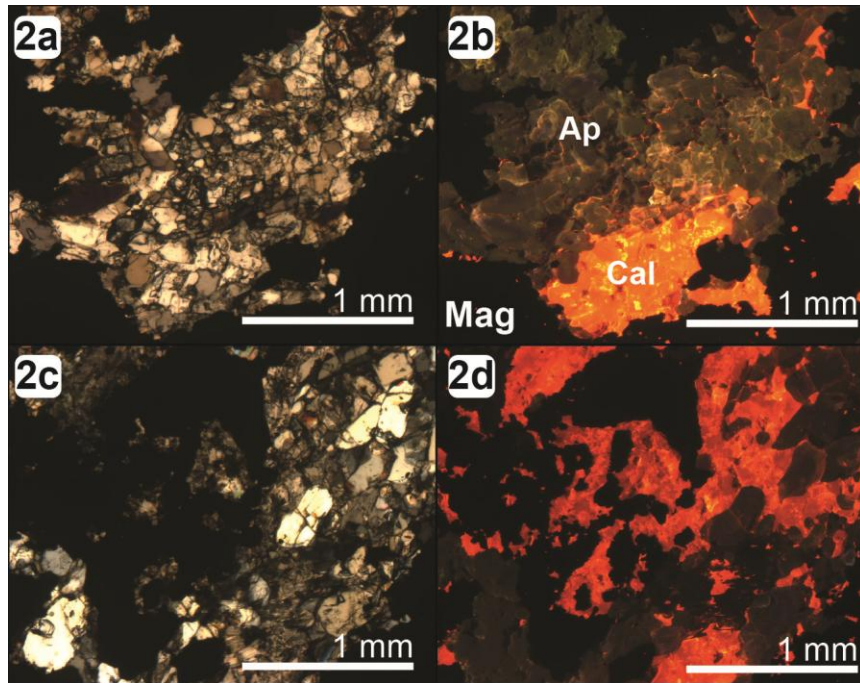


Figure 3.3 Cont'd.

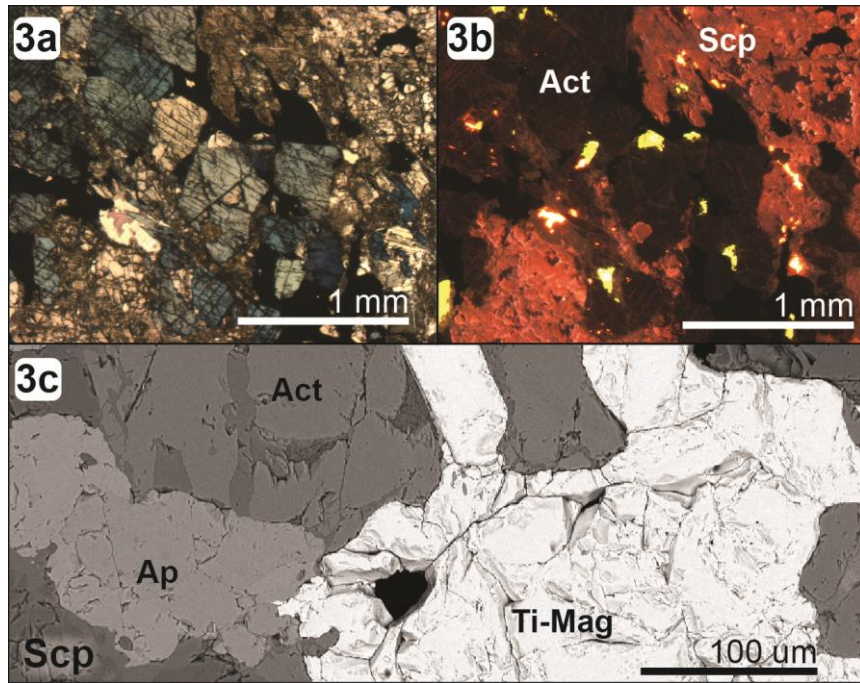


Figure 3.3 Cont'd.

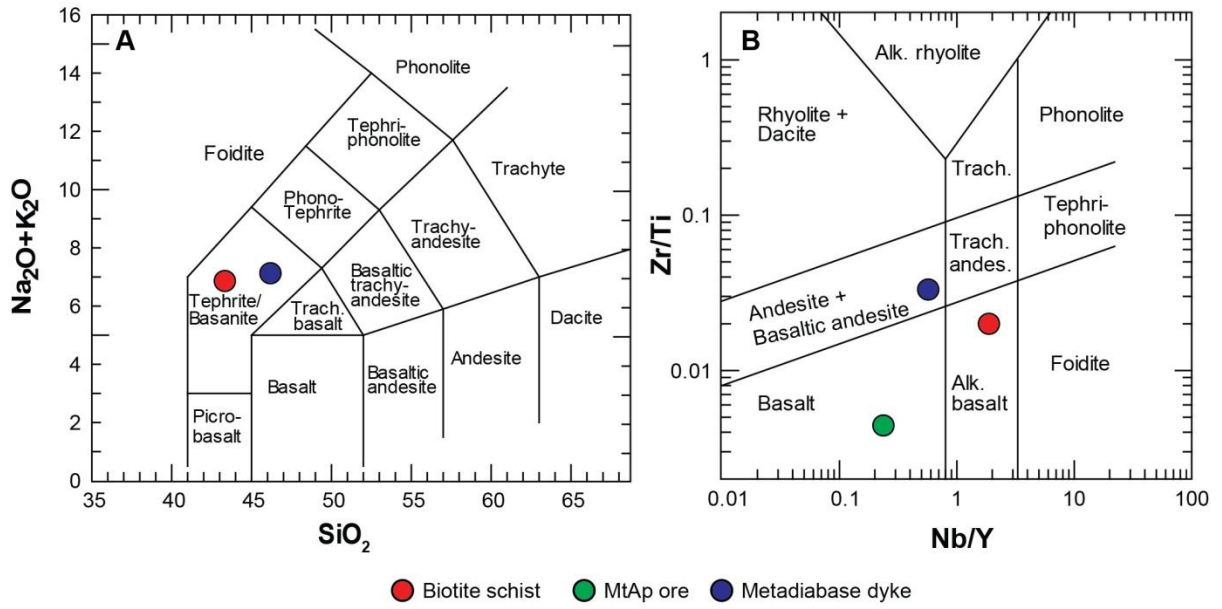


Figure 3.4 Whole-rock total alkali versus silica content rock type discriminant plot in **A**, and immobile/incompatible element discriminant plot in **B** for the three Gruvberget samples.

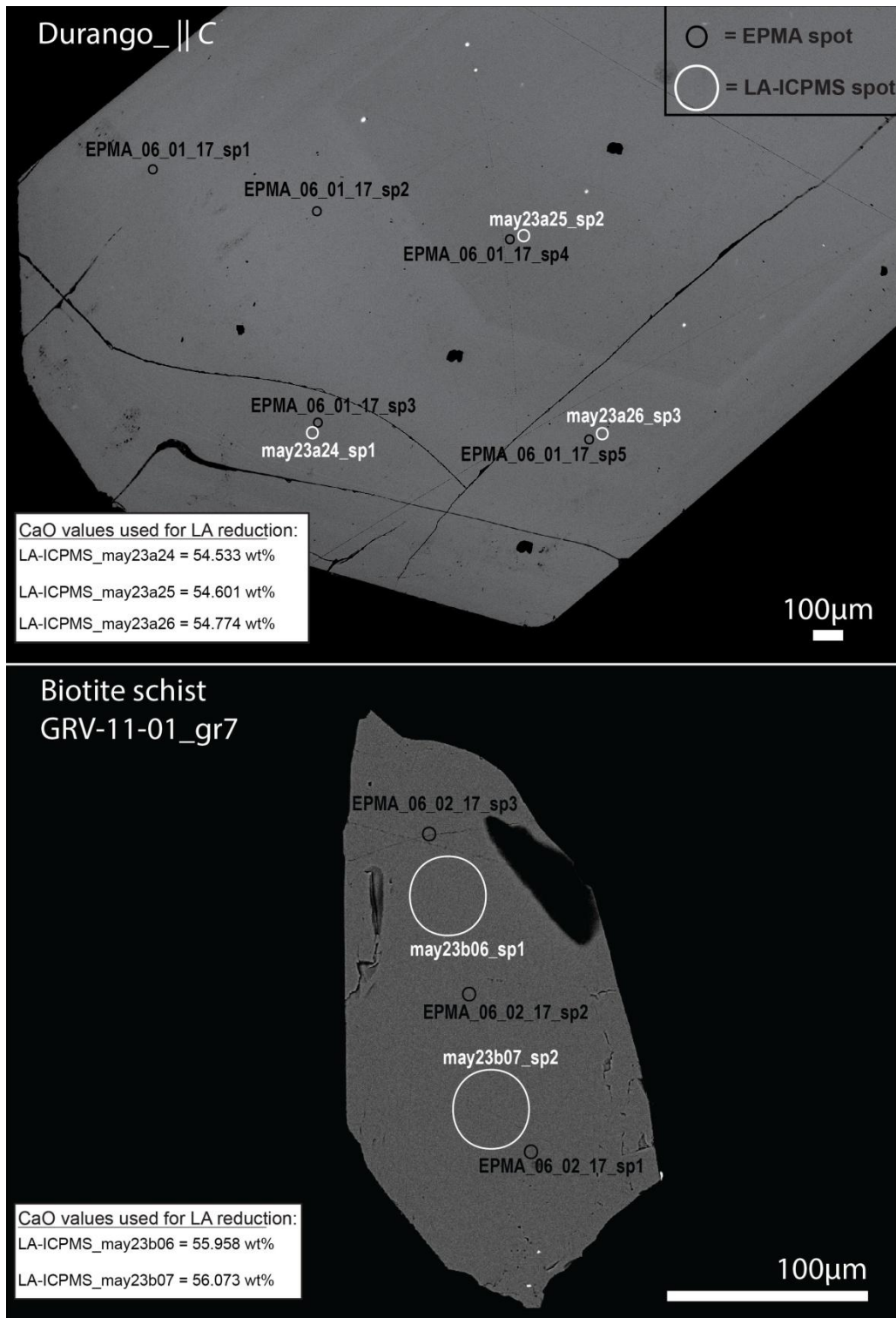


Figure 3.5 Representative BSE images with locations of analyses performed on the reference apatites and Gruvberget apatites. The reference apatite shown here is the Durango apatite mounted parallel to the *c*-axis. Note that the elemental Ca values calculated from the CaO values shown here were used to reduce the LA-ICPMS data

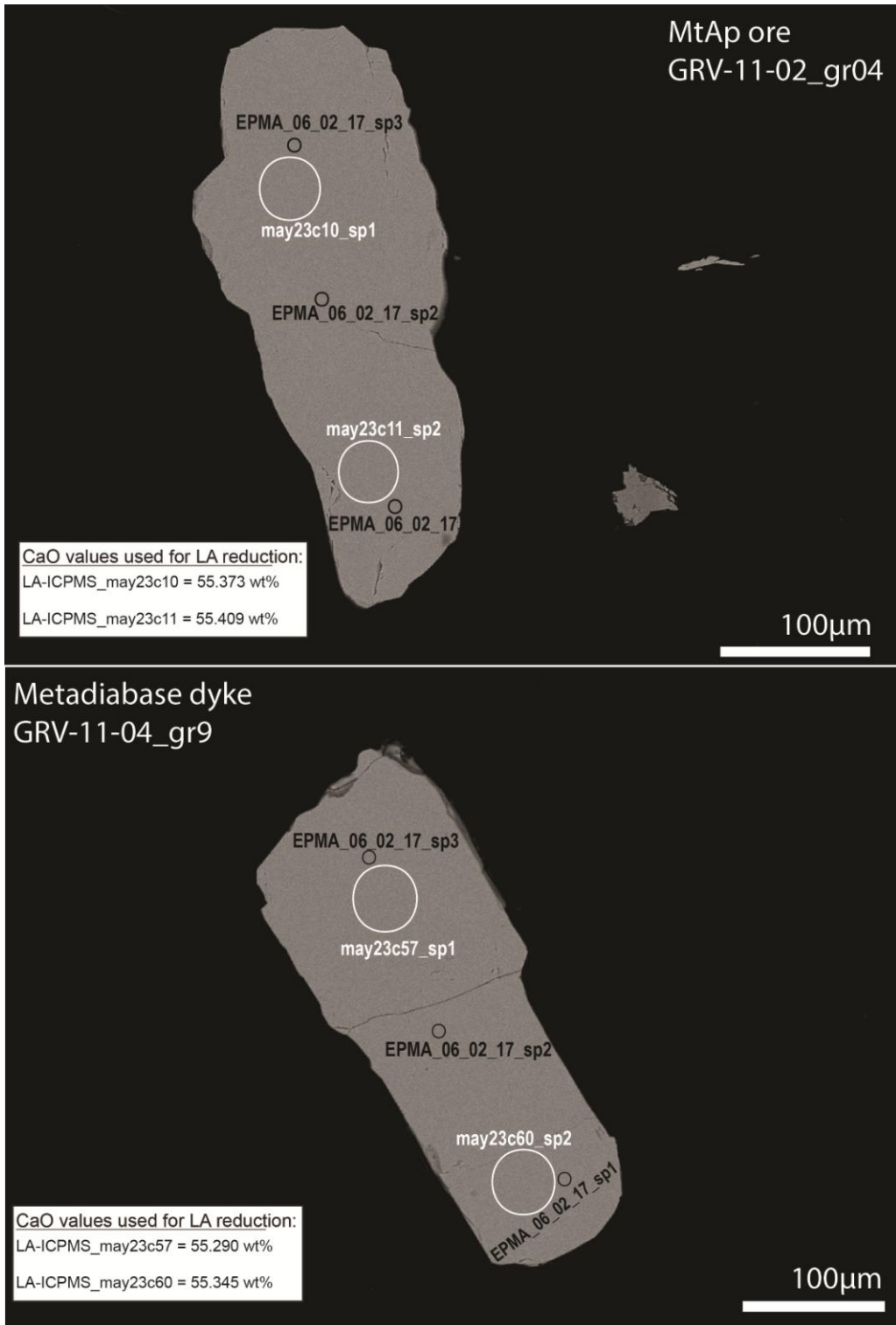


Figure 3.5 Cont'd.

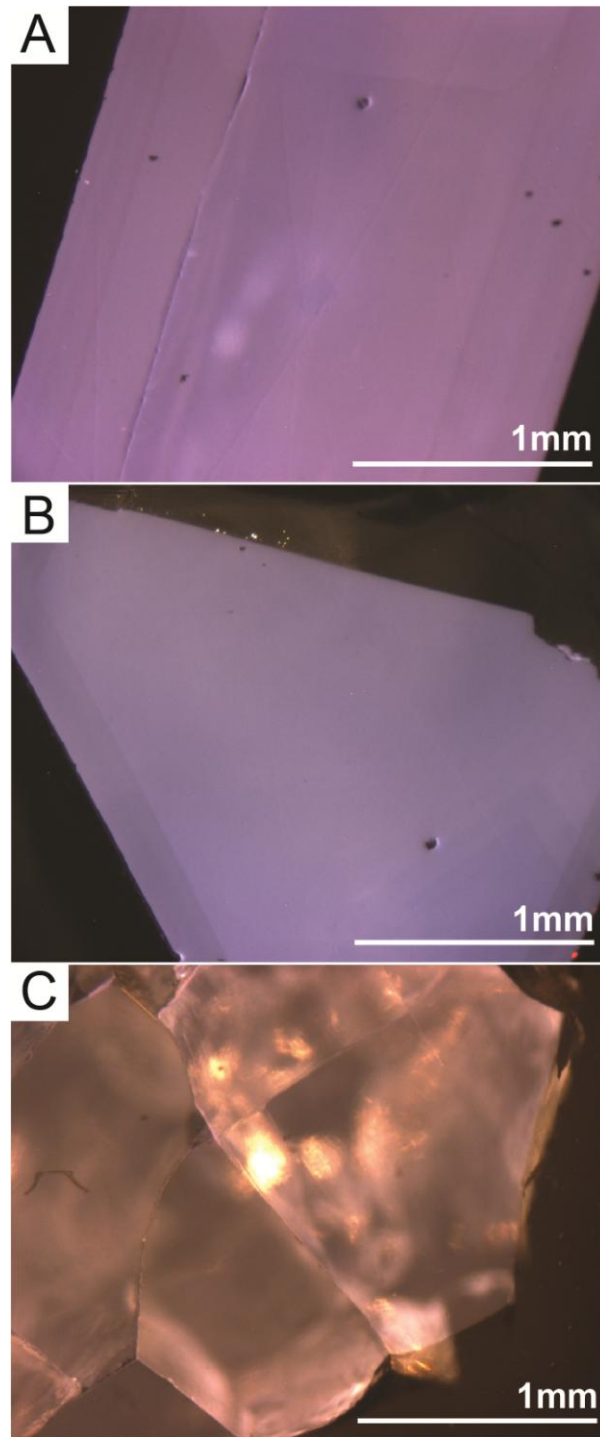


Figure 3.6 Cathodoluminescence (CL) images of the reference apatites used in this study. Note the variation in luminescence colour due to variability in REE^{3+} and Mn^{2+} activation. Each image was taken at 5x magnification using a cold-cathode CL, with a Cu-cathode used as the electron source. The corresponding samples for each CL image are: A- Durango \parallel c -axis; B- Durango \perp c -axis; C- Kola Kovdor-A; D- Kola Kovdor-C; E- Mineville; F- Mud Tank; G- MUN Sludyanka; H- JMH Sludyanka; and I-Otter Lake.

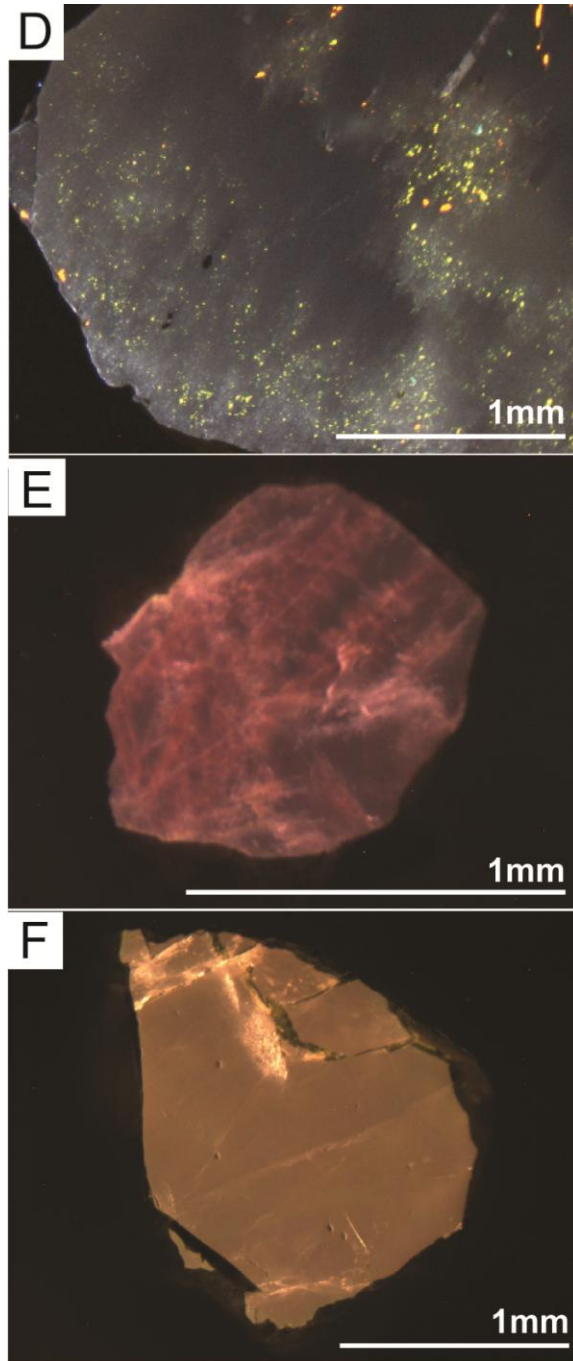


Figure 3.6 Cont'd.

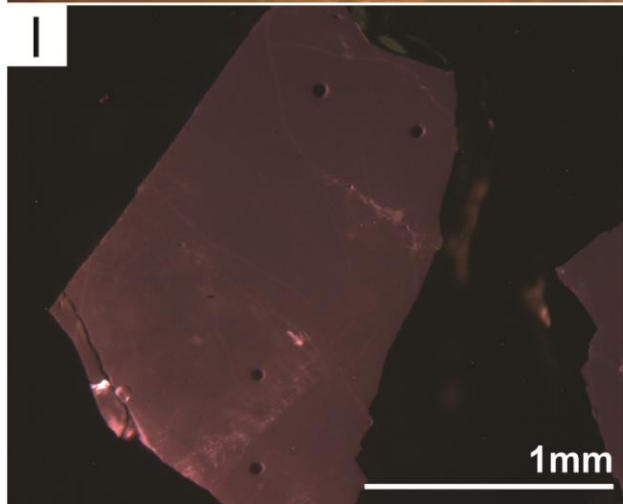
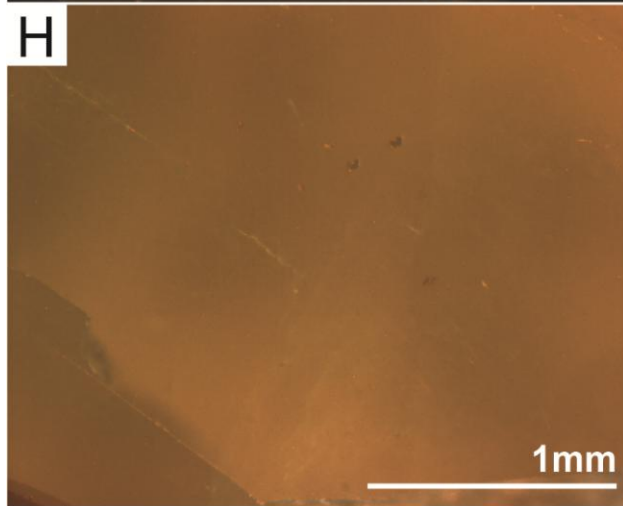
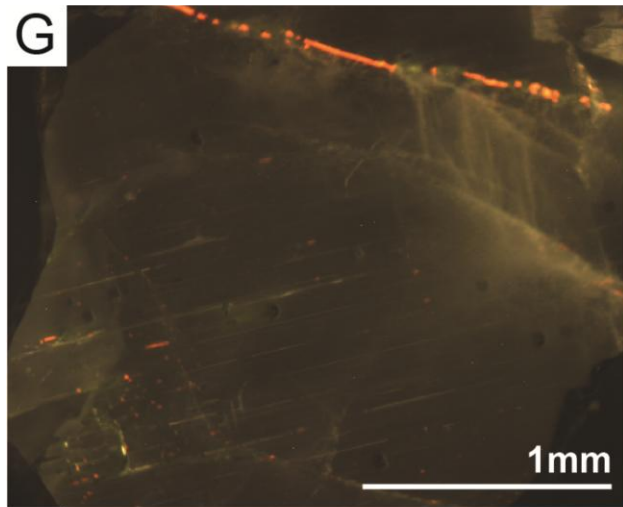


Figure 3.6 Cont'd.

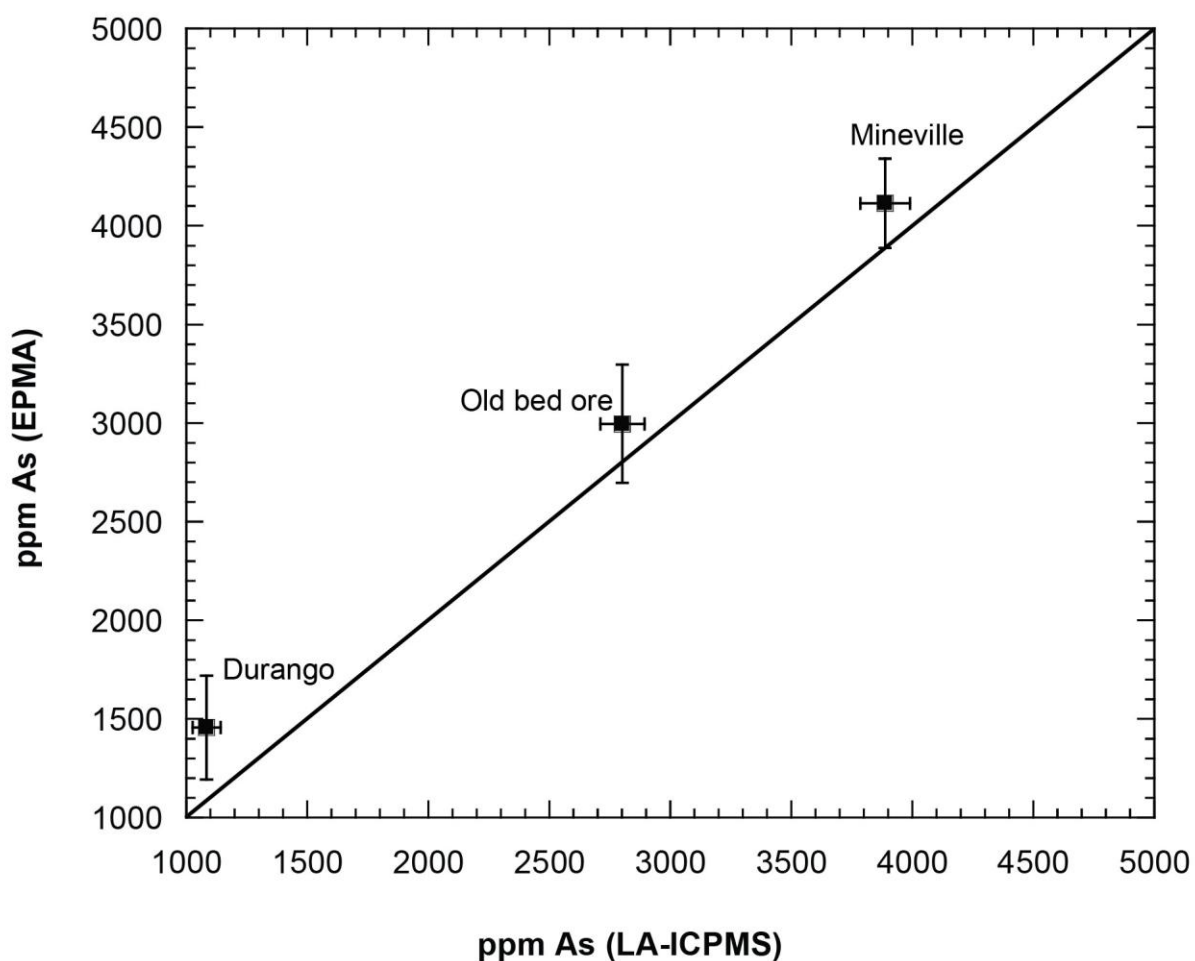


Figure 3.7 Comparison between LA-ICPMS and EPMA measurements for As. Note the similarity in As values between both techniques, which indicates minor interference effects on As measurements via LA-ICPMS. The data used for the "Old bed ore" apatite sample is from unpublished LA-ICPMS and EPMA data from JM Hanchar, pers. comm. samples from the Old bed ore at Mineville, NY; which provided an excellent intermediate As content to constrain the variation between techniques. The EPMA measurements for Durango, Old bed ore and Mineville represent 5, 30, and 5 measurements respectively, and the LA-ICPMS measurements, in the same order, represent 3, 23 and 3 respectively. Error bars represent $\pm 1\sigma$ for all data points.

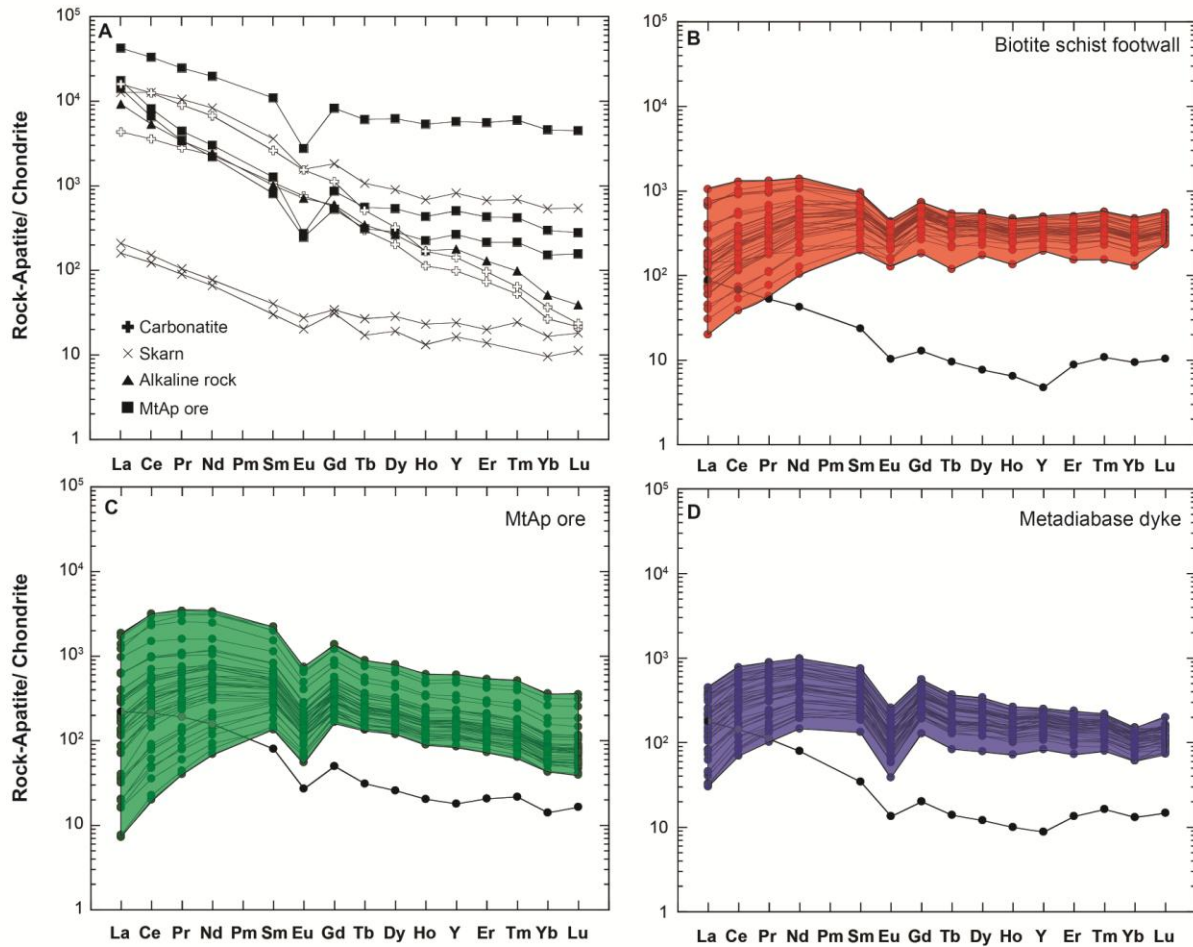


Figure 3.8 Rare earth element chondrite normalized diagrams showing variation REE chemistry. Chondrite normalization values from Anders and Greve (1989) of all reference (A) and Gruberget apatite (B - D) samples. Note, in A, the general LREE enrichment relative to HREE, and deepest Eu anomalies in apatites associated with silicate rocks such as Durango and Mineville ($\text{Eu}/\text{Eu}^* < 0.5$), whereas the carbonatites and peralkaline apatites show a gentle to flat Eu anomaly ($\text{Eu}/\text{Eu}^* \approx 1$). See text for further discussion. All Gruberget samples show a similar REE pattern; with $(\text{Ce}/\text{Yb})_{\text{cn}}$ values ranging from 1 to 6 and Eu/Eu^* values of 0.4 to 0.6.

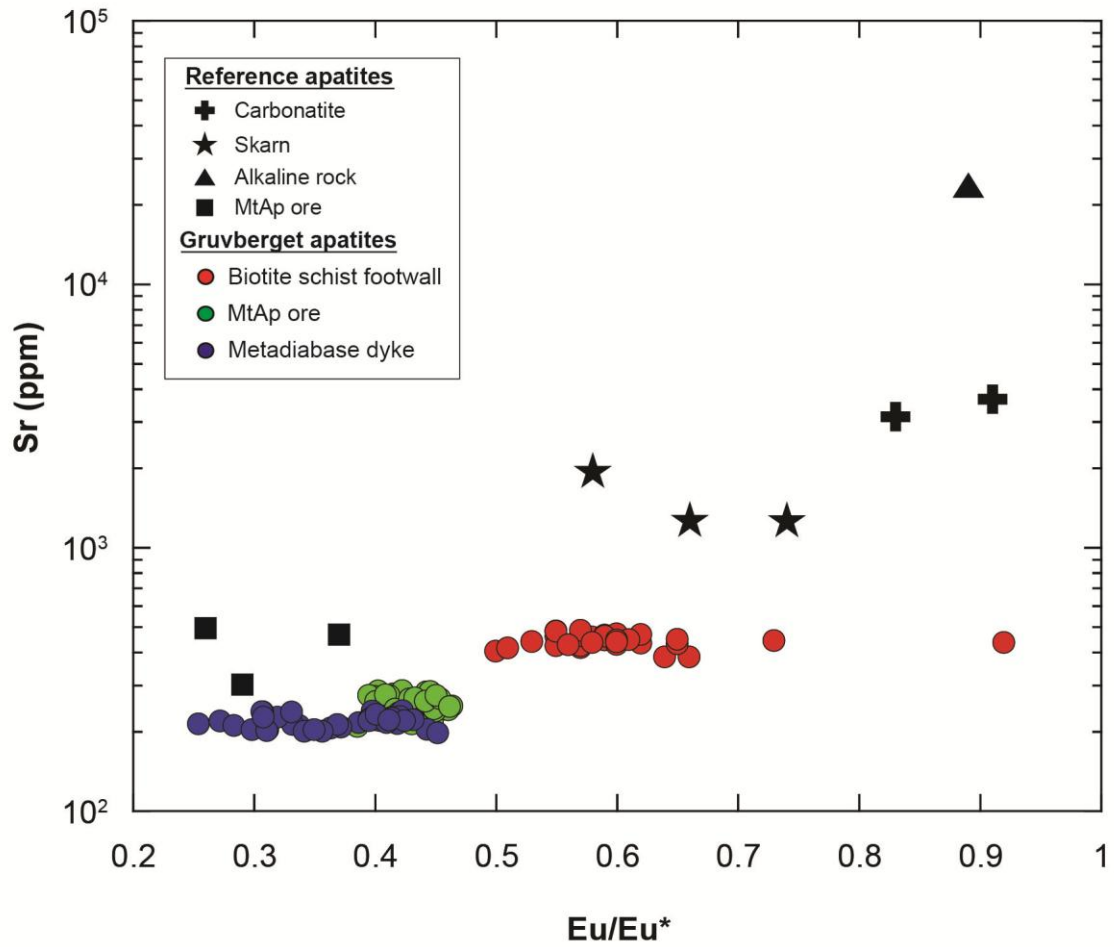


Figure 3.9 Variation in europium anomalies (Eu/Eu^*) with respect to the Sr content of apatite.

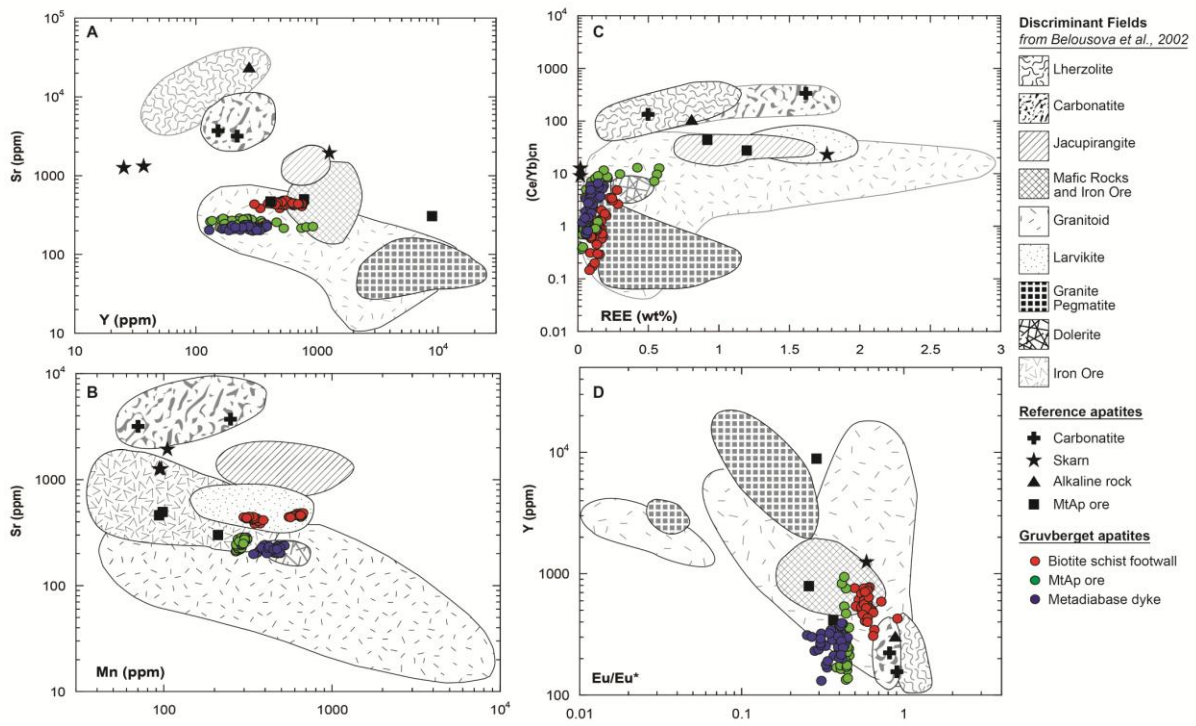


Figure 3.10 Plot of reference and Gruverberget apatite compositions superimposed onto the composition fields proposed by Belousova et al. (2002). Note that most samples lie within, or near, the defined compositional fields with the exception of some anomalously REE enriched samples (e.g., Mineville); see text for discussion.

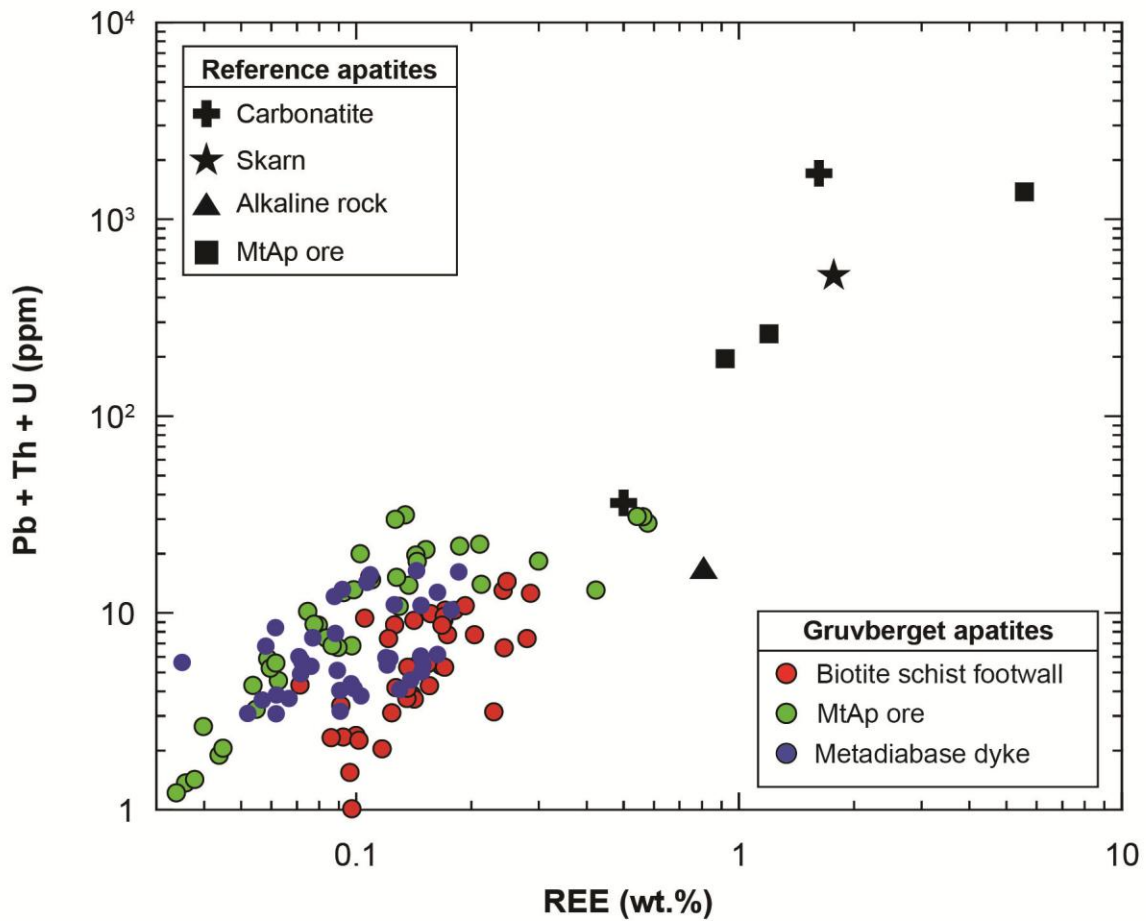


Figure 3.11 Plot of total Pb + Th + U (ppm) against REE wt. % of all reference apatite and three Gruvberget apatite samples. The positive correlation between Pb + Th + U and total REE content in apatite suggests a source mutually enriched in HFSE and REE.

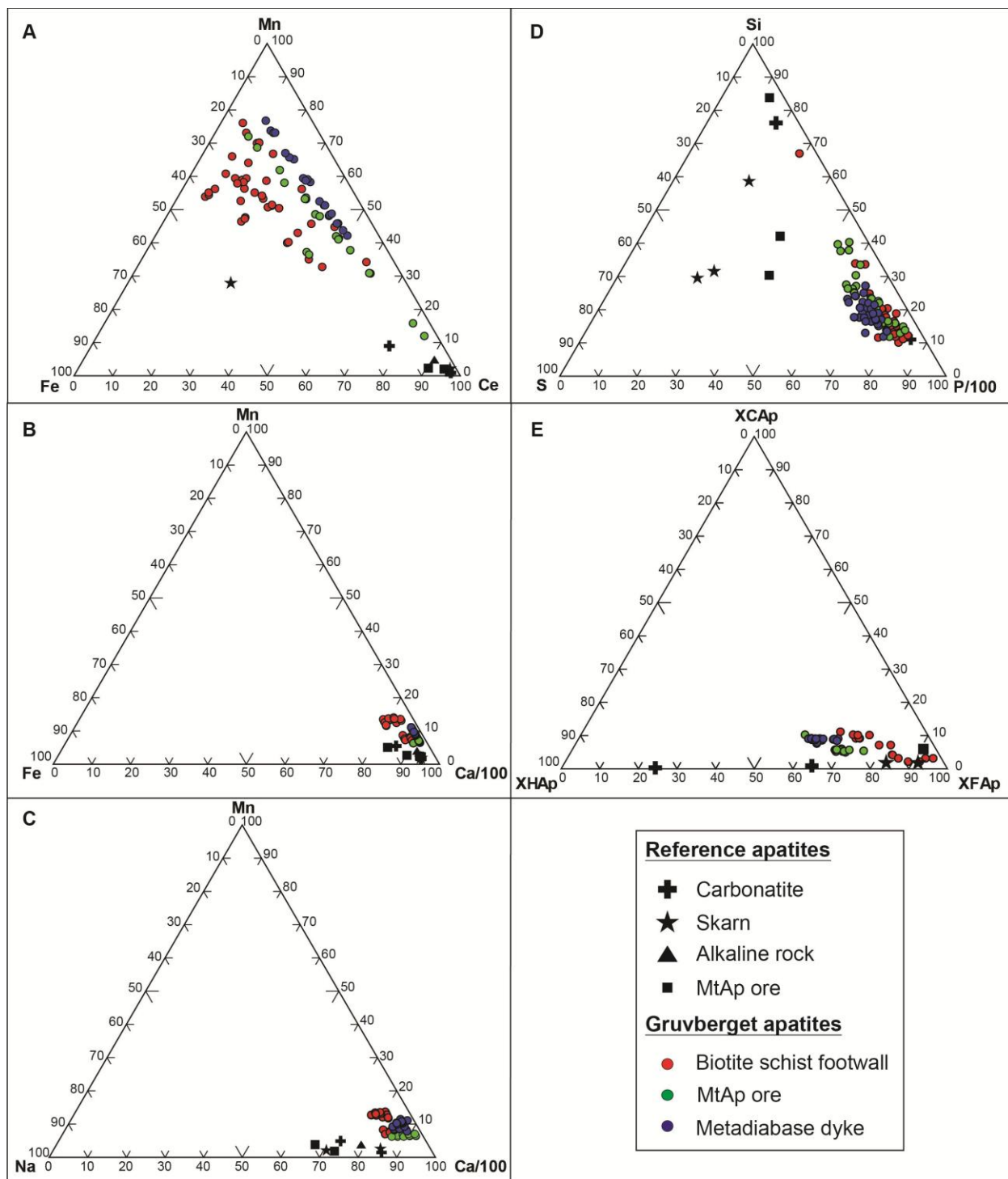


Figure 3.12 Ternary diagrams defined by Piccoli and Candela (2002) showing major compositional trends of reference and Gruvberget apatites.

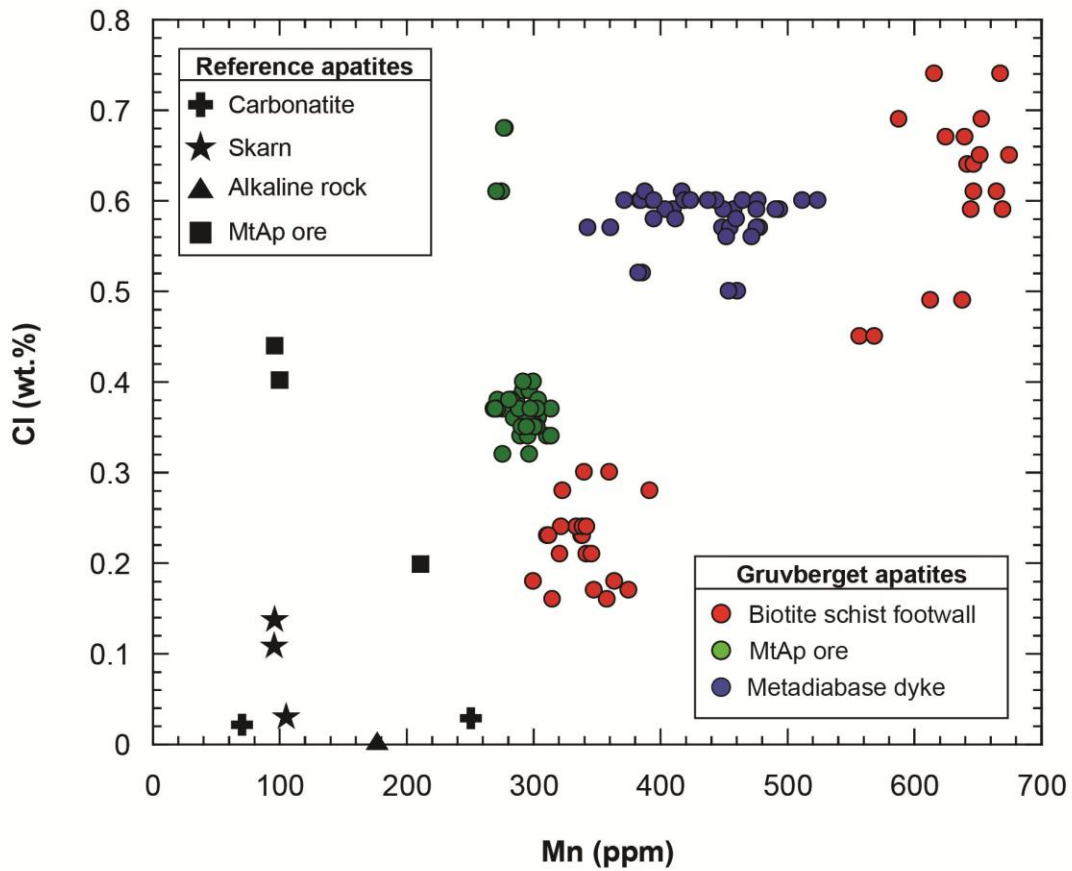


Figure 3.13 Plot of Cl (wt. %) and Mn (ppm) for the reference apatite and three Gruvberget apatite samples. Note that the metadiabase dyke and MtAp ore form respective clusters, whereas the biotite schist exhibits two distinct clusters.

Chapter 4: Conclusions

A study on synthetic apatite is presented in Chapter 2 and a comparative study of natural apatite is presented in Chapter 3.

The experimental component of this study (Chapter 2) investigated the effectiveness of Na^+ and Si^{4+} charge balancing REE^{3+} substitution for Ca^{2+} in apatite. The results have implications for melt composition and crystal structure controls on the REE composition of apatite. The positive correlation between Si and REE contents show that coupled substitution takes place. The high concentrations of Si and REE, compared with Na and REE, suggests that Si is the more effective than Na in charge balancing REE substitution under the experimental conditions used in this study. Once the maximum amount of REEs and Si in the melt is achieved and, and saturation is reached, a REE_2O_3 phase precipitates.

The relatively low Na contents in the Na and REE-doped apatites indicate that the incorporation of Na is inhibited; hence it was considered an ineffective mechanism for charge balancing REEs at the experimental conditions presented here.

The experimental configuration used may have allowed for volatilization of Na from the melt, or Na is less compatible in the apatite structure and thus less effective in charge balancing the REEs. Results from evacuated silica tube syntheses do not conclusively rule out the former, so the inability to incorporate Na in apatite may be a result of both factors.

Also, the un-geologic (i.e., very different from a silicate melt) composition and structure of the fluorite flux that was used may also have influenced the ability for the synthetic apatites to incorporate Na into their structure

The melt REE contents are directly reflected in the synthetic apatite REE compositions. Syntheses were done with REE and Si doping with the addition of REE, in molar proportions, as

LREE=HREE, LREE>HREE, and LREE<HREE. The heightened LREE enrichment and suppressed HREE enrichment for LREE>HREE and LREE<HREE, respectively, indicates that the larger M1 and M2 sites occupied by Ca in apatite impose a crystal structure control preferentially concentrating LREEs that share a similar ionic radii to the host Ca1 and Ca2 cations. This suggests that the crystal chemistry of apatite resulting from these syntheses is controlled by melt composition and the selectivity of the apatite crystal structure.

Natural REE and Si enriched apatites derived from several localities yield similarities to synthetic apatite doped with Si at equal proportions of REEs, and LREEs in excess of HREEs. Comparison between synthetic apatites to natural apatites from selected apatite localities supports the substitution mechanism in equation (1).

Chapter 3), presents analytical results for the major, minor, and trace element composition of reference apatites from well-studied geological environments and apatite from of the Gruvberget MtAp deposit, in northern Sweden. The reference apatites provided insights into the geological environments/processes responsible for a given apatite composition, which was used as a tool to assess the case study Gruvberget apatites.

The presence of the alteration assemblage scapolite and actinolite coexisting with apatite in the Gruvberget ore and host rocks is a result of pervasive sodic-calcic alteration. Hence, it is postulated that the primary composition of the Gruvberget apatites was overprinted through metasomatism by hydrothermal fluid(s) composed of a sodic-calcic Cl-brine.

All three Gruvberget apatite samples are relatively depleted in REE (especially LREE) compared to other MtAp deposits (e.g., Mineville), and are enriched Cl, OH and Mn relative to all of the reference apatites analyzed. Enrichment in Cl and OH in the Gruvberget apatites was inferred to be a result of metasomatic alteration by hydrothermal fluids that affected all three of

the rock units at Gruvberget from which apatite was sampled. This is attributed to the susceptibility of apatite to metasomatism causing overprinting of the primary halogen composition (e.g., fluorapatite altered to chlorapatite). Reaction between the Gruvberget apatites and a Cl-rich brine may have removed the LREEs during the metasomatism. In some cases, however, relict primary signatures (e.g., a mantle signature yields a weaker REE enrichment) in apatite may be retained providing insight into the evolution of rock- and ore-forming processes based on petrographic and geochemical evidence.

Further research regarding apatite will yield more insights into the utility of this chemically robust mineral. In the case of the study presented here there is great potential for additional work to resolve some unanswered questions. More experimental work is needed to explain the low concentration of Na in the synthetic apatites. This would involve changes to the run conditions, and the experimental method to ensure Na retention in apatite. The isotopic evolution of the natural apatites and their host rocks may be explored through various isotopic systems such as Rb-Sr, Sm-Nd, and Lu-Hf. Fluid inclusion studies would have implications for the composition of ore-forming and/or hydrothermal fluids. Precise apatite ages (e.g., U-Pb, Nd-Sm, or Lu-Hf, or fission track) may also provide a deeper understanding of the temporal evolution of each sample, documenting the time of crystallization as well as any subsequent alteration.

APPENDIX

APPENDIX TABLES

Table A.1a. External reference standard (Sludyanka apatite) composition.

	¹³⁹ La	¹⁴⁰ Ce	¹⁴¹ Pr	¹⁴⁵ Nd	¹⁴⁷ Sm	¹⁵¹ Eu	¹⁵⁷ Gd	¹⁵⁹ Tb	¹⁶³ Dy	¹⁶⁵ Ho	¹⁶⁷ Er	¹⁶⁹ Tm	¹⁷³ Yb	¹⁷⁵ Lu
	ppm													
Hanchar, 2002 (MUN Slud)														
Analysis ID														
se24a03	31.45	66.21	7.46	26.74	5.19	1.09		0.70	4.89	0.93	2.19	0.35	1.98	0.23
se24a04	30.66	61.36	7.00	24.84	5.03	0.91		0.66	4.50	0.83	2.34	0.31	1.92	0.24
se24b03	34.58	71.39	7.99	31.07	5.67	1.17		0.81	5.32	0.90	2.83	0.35	2.09	0.27
se24b14	33.86	67.78	8.20	29.98	5.54	1.20		0.73	5.07	0.85	2.46	0.40	2.01	0.30
se24c03	33.89	69.02	8.58	28.96	6.22	0.98	5.42	0.65	3.82	1.01	2.27	0.42	1.70	0.30
se24c18	34.28	71.25	8.00	26.85	5.75	1.04	5.00	0.67	4.33	0.86	2.26	0.45	1.95	0.26
se25a03	35.86	72.44	7.91	27.48	4.75	1.21	6.07	0.76	4.74	1.04	2.32	0.25	1.62	0.20
se25a10	32.77	75.37	8.29	28.11	4.75	1.28	6.58	0.98	5.28	1.20	1.78	0.40	2.52	0.33
se25a11	32.16	110.54	9.34	22.48	3.62	1.29	3.30	0.57	3.43	0.60	2.14		1.26	
se25a18	28.92	125.89	8.27	21.36	3.85	0.99	2.99	0.54	2.52	0.45	1.82	0.17	0.82	0.24
se25c03	28.41	116.69	8.86	22.19	3.54	1.02	3.26	0.46	2.69	0.64	1.36	0.24	1.03	0.26
se25c11	27.18	119.56	8.49	26.16	4.23	0.89	3.68	0.59	3.32	0.49	1.65		1.69	0.20
se27a05	34.24	67.65	8.02	28.17	5.29	1.17	5.97	0.76	4.56	0.88	2.82	0.38	1.98	0.26
se27a06	32.40	65.81	7.64	26.05	5.14	1.17	4.95	0.69	4.49	0.93	2.59	0.36	1.74	
se27a07	37.29	74.60	9.19	30.51	7.80	1.11	7.14	0.93	6.07	1.04	2.73		2.55	
se27c03	34.44	82.38	8.74	29.35	5.40	1.18	5.20	0.74	4.53	1.06	2.55	0.29	1.59	0.36
se27c04	33.81	79.23	7.52	26.27	5.22	1.68	5.34	0.82	5.25		2.28			
se27c11	34.95	79.25	8.13	32.26	6.93		6.35		5.12		3.91			0.45
se27c12	33.79	77.69	8.20	26.52	5.21	1.14	5.85	0.71	4.16	0.91				
se27c13	34.84	74.90	8.40	27.73	4.96	1.21	5.79	0.88	5.24	0.94	2.82	0.36	2.11	0.28
se27c14	34.31	65.22	7.72	27.52	5.20	1.02	5.66	0.78	4.70	1.13	3.13	0.37	2.64	0.45
se27d03	32.22	66.11	7.76	29.78	5.86	1.17	5.02	0.85	6.01	1.00	2.20			
se27d04	32.85	76.86	8.48	28.05	5.69	1.10	5.54	0.86	4.87	0.92	2.51	0.31	2.16	0.33
se27d05	32.18	92.33	7.76	25.67	4.56	0.93	4.70	0.88	4.64	0.71	2.06		2.78	0.37
se27d11	26.34	64.16	6.15	24.12	4.11	0.93	4.79	0.47	3.53	0.93	1.52	0.30		
se27d12	34.98	70.09	8.44	30.85	5.61	1.21	6.13	0.84	5.28	1.10	2.66	0.39	1.95	0.29
se27d13	34.29	93.55	7.21	25.44	9.18	1.44	5.67			0.83			2.32	
oc01a03	33.66	85.77	7.43	25.00	4.46	1.09	5.25	0.69	4.49	1.02	2.35	0.51		
oc01a04	32.69	71.11	7.80	35.34	6.65	1.41	5.59	0.66	4.47	1.16	2.86	0.38	3.39	0.36
oc01a16	30.65	94.63	8.15	23.02	3.94	1.34			4.21	0.76	2.87			
oc01a17	39.74	74.52	6.61	31.34	6.16			0.70		1.87		0.56		
oc01a18	37.66	71.07	8.51	29.39	6.20	1.22	6.39	0.92	5.39	1.16	3.29	0.45	2.51	0.30
Average	33.17	79.83	8.01	27.46	5.37	1.15	5.29	0.73	4.56	0.94	2.43	0.36	2.01	0.30
Stdev	2.84	16.99	0.68	3.13	1.19	0.17	1.04	0.13	0.85	0.26	0.54	0.09	0.57	0.07

Table A.1a. Cont'd.

	¹³⁹ La	¹⁴⁰ Ce	¹⁴¹ Pr	¹⁴⁵ Nd	¹⁴⁷ Sm	¹⁵¹ Eu	¹⁵⁷ Gd	¹⁵⁹ Tb	¹⁶³ Dy	¹⁶⁵ Ho	¹⁶⁷ Er	¹⁶⁹ Tm	¹⁷³ Yb	¹⁷⁵ Lu
	ppm													
Dempster, 2003 (MUN Slud)														
LA-ICP-MS	33.20	79.90	8.00	27.50	5.40	1.10	5.00	0.70	4.30	0.90	2.20	0.40	2.00	0.20
Standard deviation (ppm)	2.90	17.50	0.70	3.20	1.20	0.30	0.50	0.30	1.40	0.30	0.90	0.10	0.60	0.20
Dempster, 2003 (MUN Slud)														
Solution ICP-MS	38.20	76.20	8.30	30.20	5.70	1.20	4.90	0.80	4.50	0.90	2.50	0.40	1.90	0.20
Canali, 2015 (MUN Slud)														
Analysis ID														
jn06b04	38.73	73.90	8.06	31.47	6.08	1.29	5.64	0.87	4.82	0.97	2.53	0.36	2.04	0.25
jn06b25	36.94	70.40	7.94	30.50	6.10	1.37	5.44	0.86	5.04	0.96	2.37	0.32	1.93	0.26
oc21c22	38.22	71.10	7.84	29.50	5.82	1.26	5.29	0.72	4.61	0.95	2.35	0.33	1.79	0.25
my23a18	37.56	74.30	8.07	29.40	4.48	1.26	6.47	0.74	4.80	0.83	2.23	0.44	1.89	0.19
my23a19	36.05	74.60	8.19	31.50	4.30	1.16	6.46	0.60	4.68	0.88	2.04	0.22	1.31	0.19
my23a20	36.62	73.00	7.99	28.40	4.75	1.25	5.72	0.70	4.24	0.67	2.36	0.42	1.39	0.30
Average	37.35	72.88	8.02	30.13	5.26	1.27	5.84	0.75	4.70	0.88	2.31	0.35	1.73	0.24
Stdev	1.01	1.75	0.12	1.24	0.83	0.07	0.51	0.10	0.27	0.12	0.16	0.08	0.30	0.04
Chafe, 2013 (MUN Slud)														
Analysis ID														
mr01a07	37.32			29.38	5.52				4.50		2.22			
mr01a28	34.94			29.39	5.52				4.51		2.33			
mr01a43	36.20			29.48	5.58				4.37		2.21			
mr01a54	36.00			29.25	5.55				4.45		2.39			
Average	36.12			29.38	5.54				4.46		2.29			
Stdev	0.98			0.09	0.03				0.06		0.09			
Canali, 2015 (JMH Slud)														
Analysis ID														
my23a06	47.00	85.60	9.33	32.80	6.30	1.78	6.00	1.02	5.78	1.08	2.55	0.43	2.42	0.35
my23a29	49.60	93.60	9.41	34.40	6.14	1.59	6.35	1.02	7.09	1.41	3.05	0.46	2.75	0.34
my23a30	46.60	89.70	9.30	32.90	6.20	1.78	7.16	1.09	6.79	1.42	3.08	0.53	2.36	0.38
my23a31	47.20	89.80	9.44	36.00	5.69	1.56	6.92	1.11	6.57	1.33	3.43	0.47	2.83	0.36
my23b05	44.50	84.20	9.04	33.30	6.57	1.34	7.33	1.13	6.30	1.20	3.14	0.36	2.57	0.38
my23b27	43.74	85.00	9.29	36.90	6.74	1.37	6.65	1.14	6.09	1.30	2.98	0.48	2.53	0.29
my23c03	43.81	85.20	9.40	35.20	6.20	1.53	7.19	1.01	6.11	1.35	3.54	0.43	1.88	0.33
my23c26	45.72	87.50	9.59	34.90	7.92	1.59	7.17	1.28	6.53	1.37	2.99	0.57	2.32	0.34
my23c49	42.47	81.80	8.93	34.00	6.51	1.21	6.67	1.12	6.34	1.23	3.52	0.36	1.76	0.36
my23c70	42.47	83.40	8.95	33.80	6.07	1.54	6.23	1.08	5.88	1.37	3.29	0.48	2.40	0.49
my23c92	44.70	86.70	9.43	35.30	6.93	1.63	6.61	1.17	6.30	1.38	3.27	0.52	2.18	0.38
jn06a04	43.17	84.80	9.08	34.30	6.69	1.62	6.85	1.05	6.49	1.29	3.50	0.48	3.02	0.40
jn06a27	44.58	83.50	8.90	34.30	6.29	1.58	6.81	1.05	6.48	1.30	3.31	0.47	2.80	0.37
jn06a60	44.03	83.70	9.17	36.50	6.76	1.61	7.17	1.09	6.89	1.45	3.40	0.49	3.11	0.37
oc21c05	41.62	81.50	8.49	34.00	6.67	1.52	6.78	1.02	6.32	1.31	3.22	0.42	2.58	0.38
Average	44.75	85.73	9.18	34.57	6.51	1.55	6.79	1.09	6.40	1.32	3.22	0.46	2.50	0.37
Stdev	2.14	3.28	0.29	1.23	0.51	0.15	0.39	0.07	0.36	0.10	0.26	0.06	0.38	0.04

Table A.2a. EPMA analyses of calcium phosphate starting material.

Analysis #	P₂O₅ (wt%)	SiO₂ (wt%)	CaO (wt%)	Total (wt%)	
1	47.357	0.093	51.283	98.733	
2	46.163	0.012	48.677	94.852	
3	45.567	0.089	51.916	97.572	
4	56.827	0.006	44.661	101.494	
5	54.821	0.003	45.861	100.685	
6	50.873	0.005	45.486	96.347	
7	50.234	0.011	45.697	95.905	
8	55.851	0.007	44.755	100.581	
9	48.098	0.052	50.755	98.885	
10	55.384	0.010	42.614	97.992	
11	48.014	0.093	51.086	99.171	
12	52.493	0.010	44.752	97.264	
13	56.272	0.010	44.452	100.677	
14	46.210	0.069	51.697	97.969	
15	52.285	0.007	47.722	99.976	
16	53.819	0.004	44.972	98.753	
17	55.069	0.006	43.923	98.964	
18	51.742	0.015	45.288	97.004	
19	43.511	0.006	37.987	81.482	
20	55.258	0.005	44.703	99.901	
21	47.784	0.026	44.153	91.918	

Table A.2b. Analytical conditions used for EPMA analyses of calcium phosphate starting material

Element	Calibrant	Peak time (s)	Background time (s)	Beam Current (nA)	Beam diameter (µm)
Ca	Synthetic fluorapatite	10	5	30	10
P	Synthetic fluorapatite	10	5	30	10
Si	Albite	120	60	30	10

Table A.3. LA-ICPMS detection limits.

Element	Isotopic mass	Average detection limit (ppm) n=120
Mg	24	2.36
Si	29	86.69
V	51	0.18
Cr	52	2.42
Mn	55	0.73
Co	59	3.52
Cu	63	0.79
Zn	66	1.38
As	75	0.24
Sr	88	5.63
Y	89	0.37
Zr	90	0.13
Ba	137	0.70
La	139	2.26
Ce	140	4.52
Pr	141	0.58
Nd	145	3.31
Sm	147	1.14
Eu	151	0.30
Gd	157	0.91
Tb	159	0.11
Dy	163	0.39
Ho	165	0.09
Er	167	0.35
Tm	169	0.12
Yb	173	0.51
Lu	175	0.10
Pb	208	0.17
Th	232	1.32
U	238	0.06

Table A.4. EPMA analytical conditions for synthetic apatite analyses.

Element	X-ray line	Crystal	Standard	Average detection limit (ppm-1s) n = 289	Peak time (sec)	Background time (sec)
F	Ka	LDE1	Fluortopaz	74.39	40	20
P	Ka	PETL	Apatite	23.35	120	60
Na	Ka	TAP	Albite	28.81	40	20
Si	Ka	TAP	Albite	21.01	120	60
Ca	Ka	PETH	Apatite	13.47	120	60

Table A.4. EPMA analytical conditions for Gruvberget and reference apatite analyses.

Element	X-ray line	Crystal	Standard	Average detection limit (ppm-1s) n = 253	Peak time (sec)	Background time (sec)
F	Ka	LDE1	JMH_fluorapatite_319	228.26	20	10
Fe	Ka	LIFL	Arsenopyrite	79.25	40	20
Mn	Ka	LIFL	Rhodenite	131.66	40	20
As	Ka	LIFL	Arsenopyrite	550.64	40	20
Ca	Ka	PETL	JMH_fluorapatite_319	65.70	20	10
Sr	La	PETL	Celestite	147.85	40	20
S	Ka	PETL	Sphalerite	68.21	40	20
Na	Ka	TAP	Albite	77.07	20	10
Si	Ka	TAP	Albite	103.18	20	10
Mg	Ka	TAP	Diopside	60.02	40	20
Cl	Ka	PETH	JMH_chlorapatite_346	49.36	20	10
Y	La	PETH	YP5O14	143.49	40	20
P	Ka	PETH	Apatite	108.05	20	10

APPENDIX FIGURES

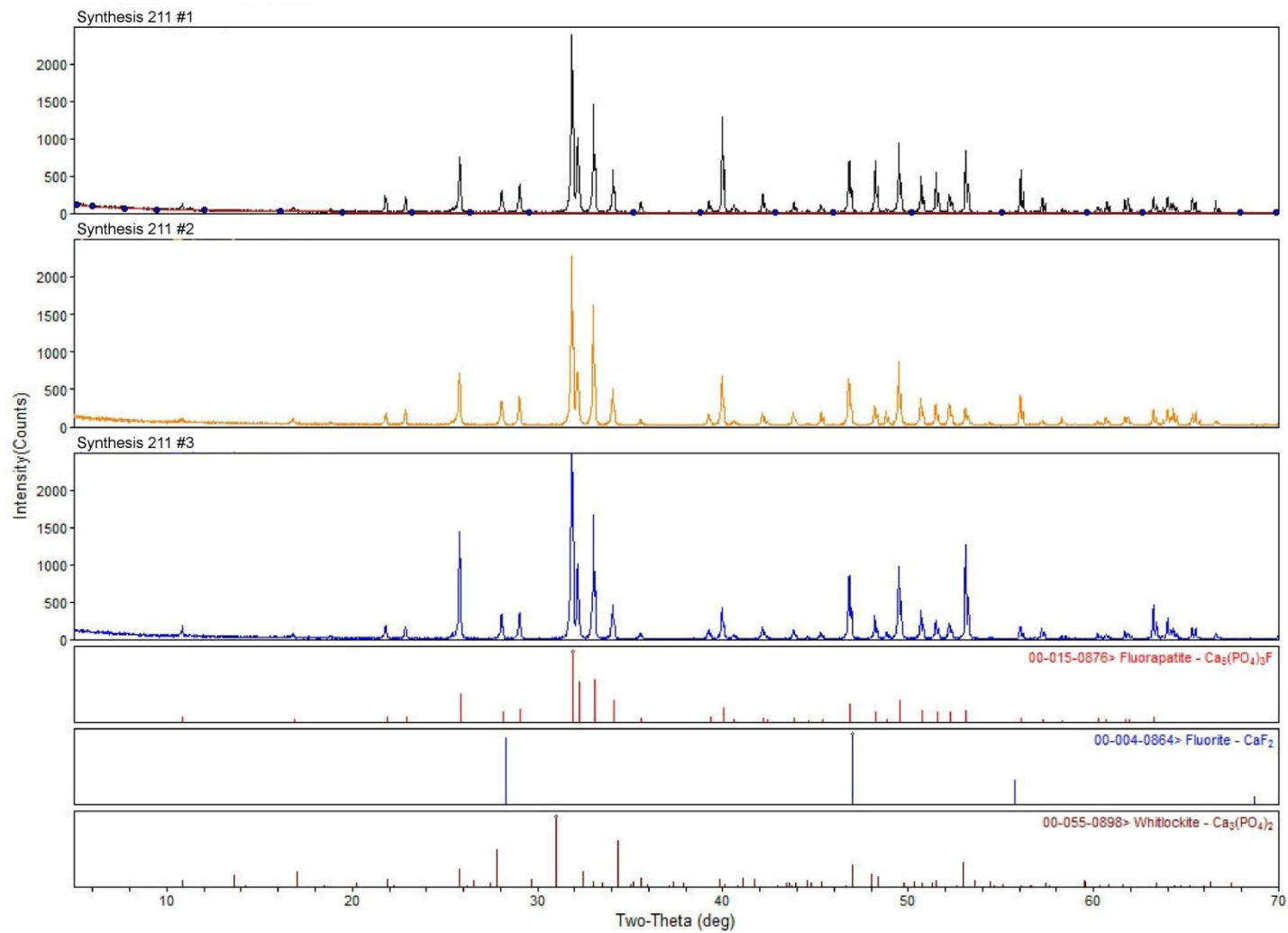


Figure A.1. X-ray diffractograms from batch 211 undoped synthetic apatite.

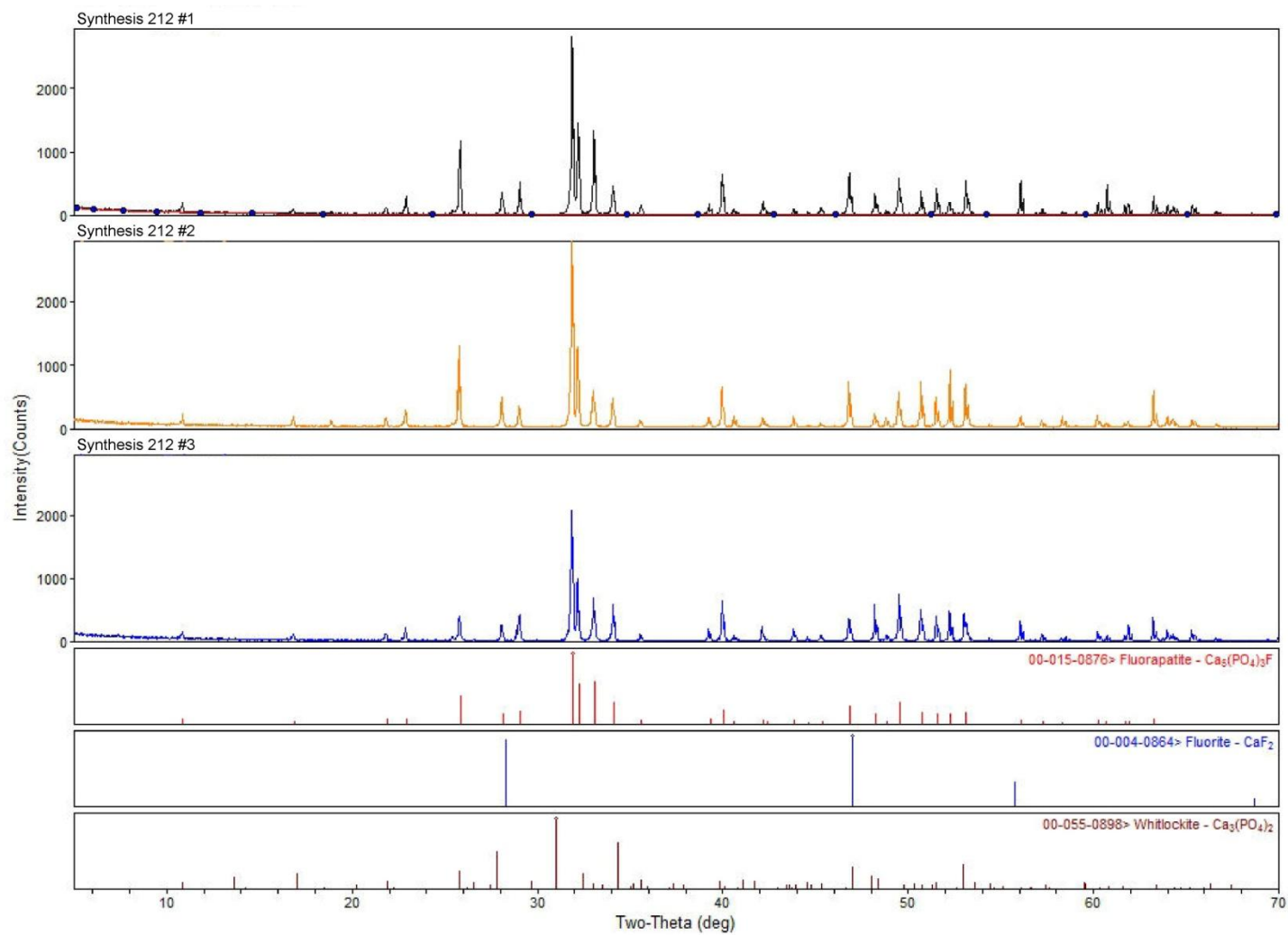


Figure A.2. X-ray diffractograms for apatite from synthesis 212: REE-doped with Si at 1x.

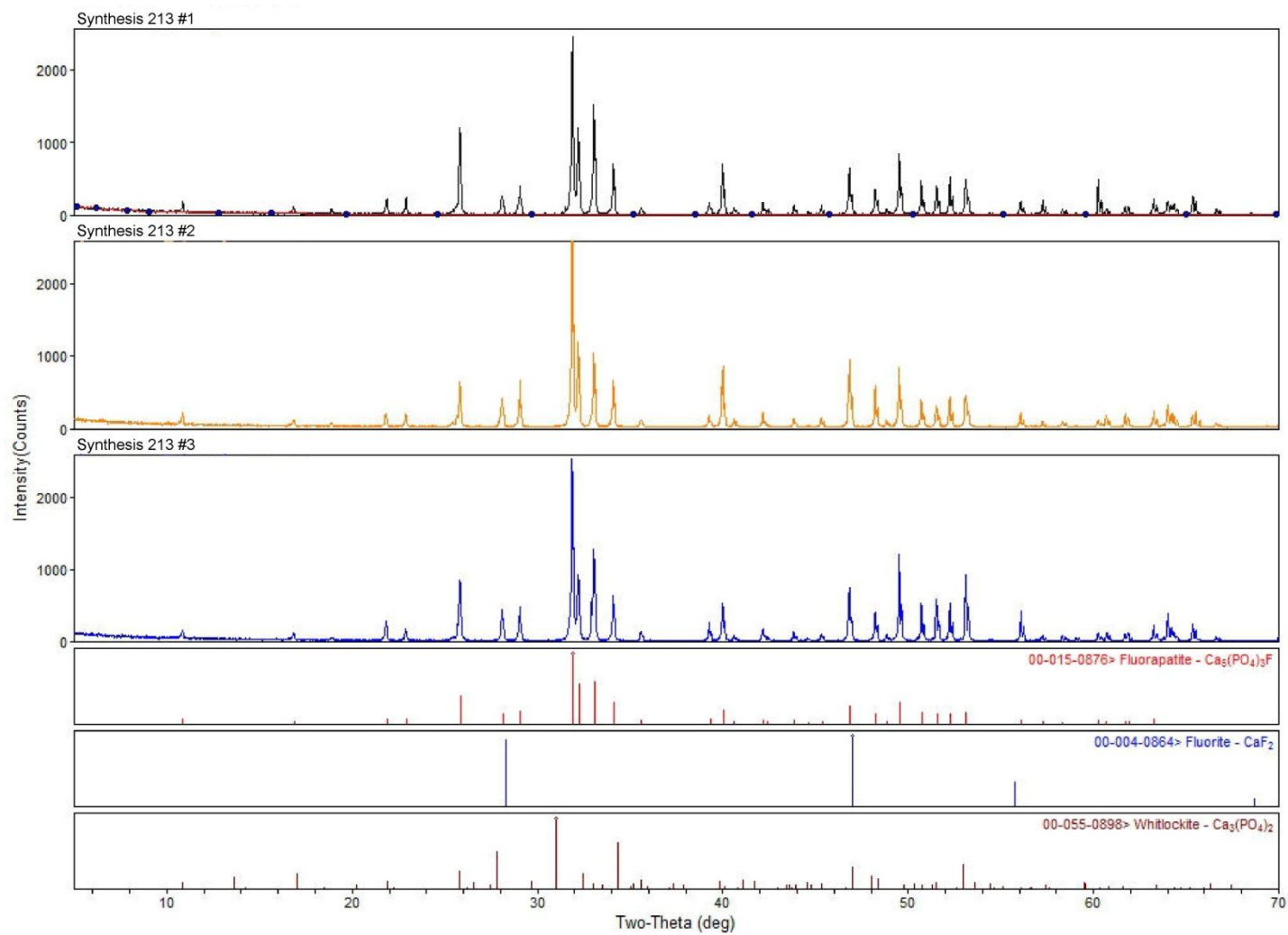


Figure A.3. X-ray diffractograms for apatite from synthesis 213: REE-doped with Si at 10x.

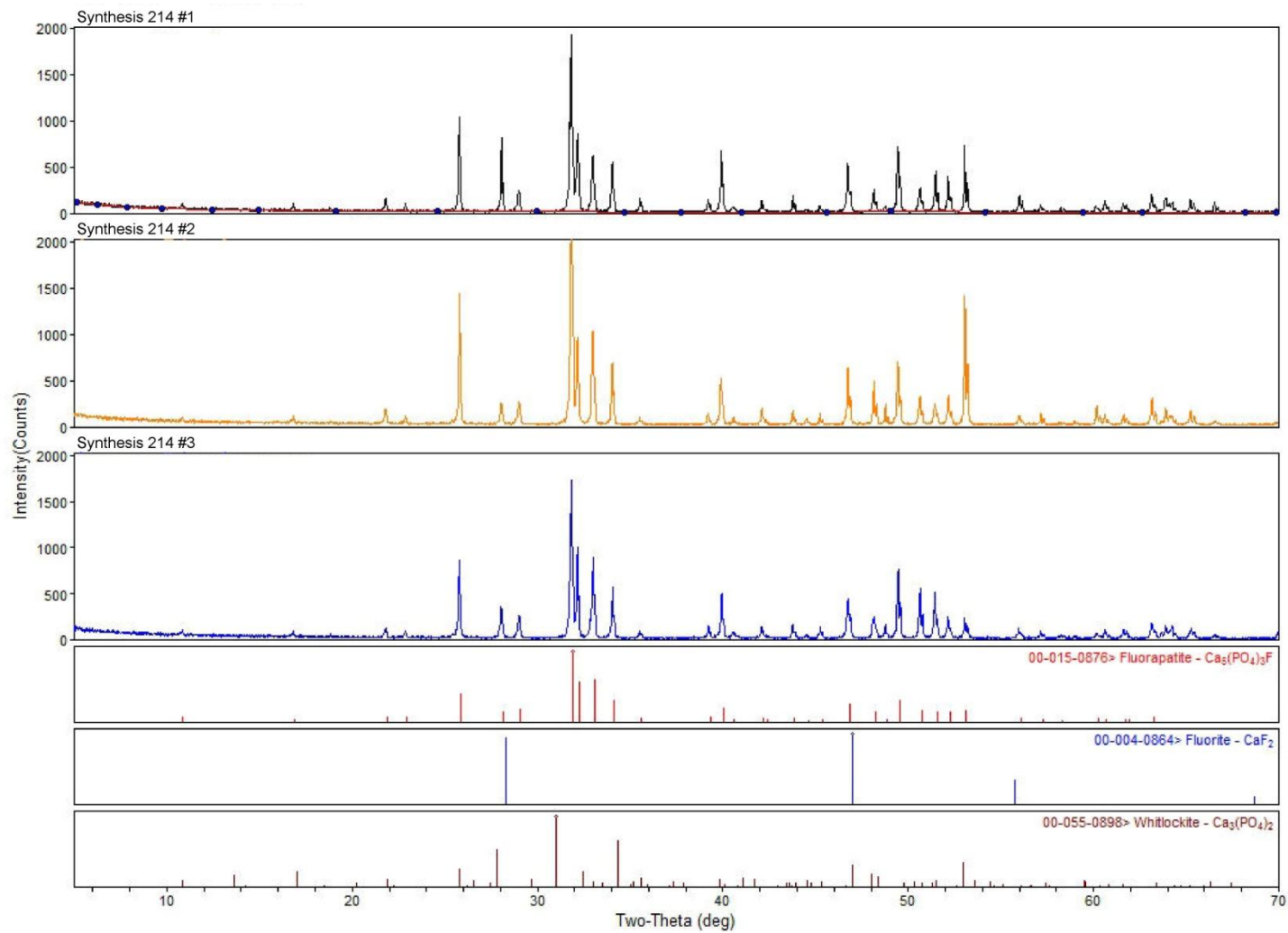


Figure A.4. X-ray diffractograms for apatite from synthesis 214: REE-doped with Si at 100x.

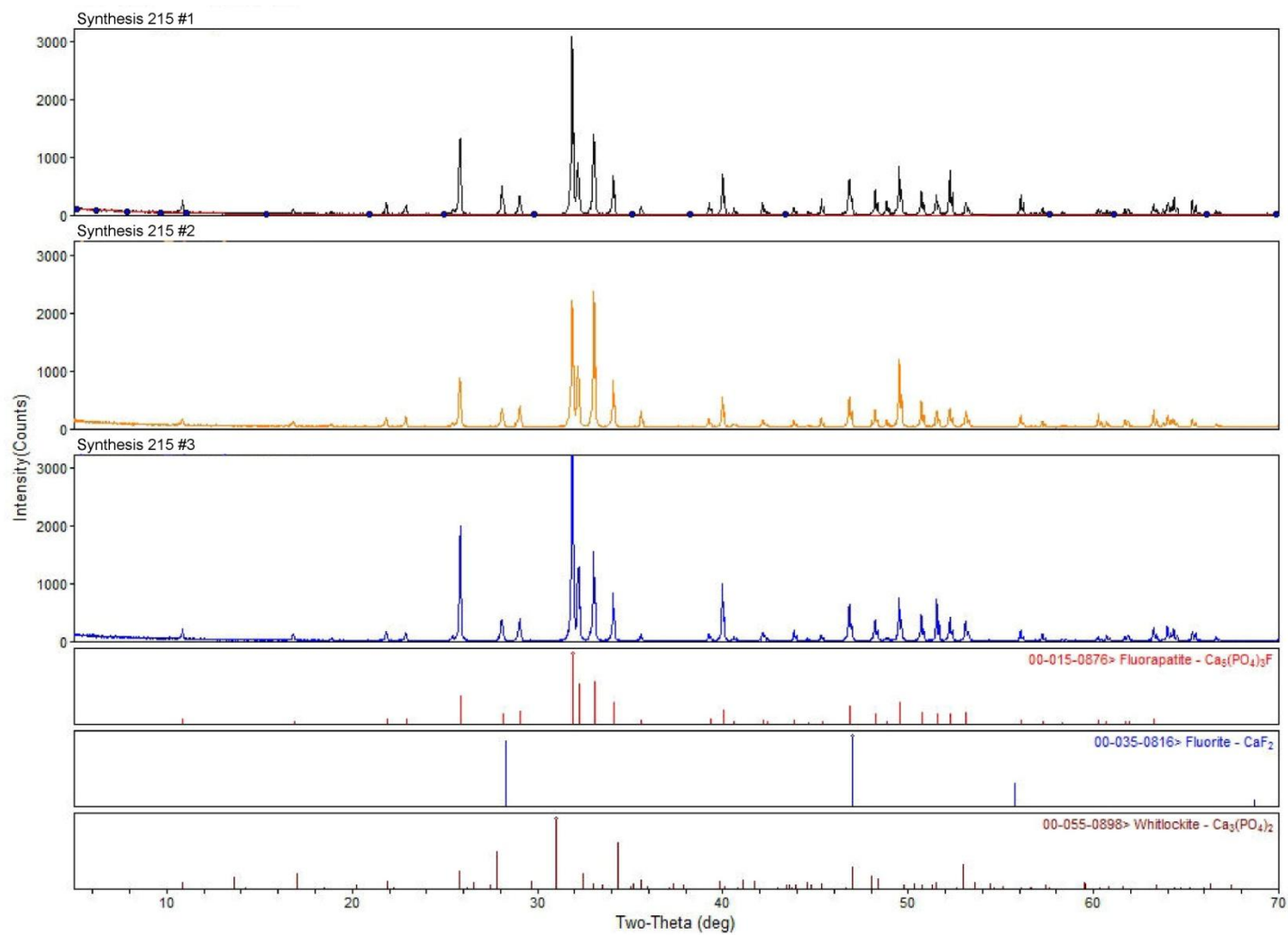


Figure A.5. X-ray diffractograms for apatite from synthesis 215: REE-doped with Na at 1x.

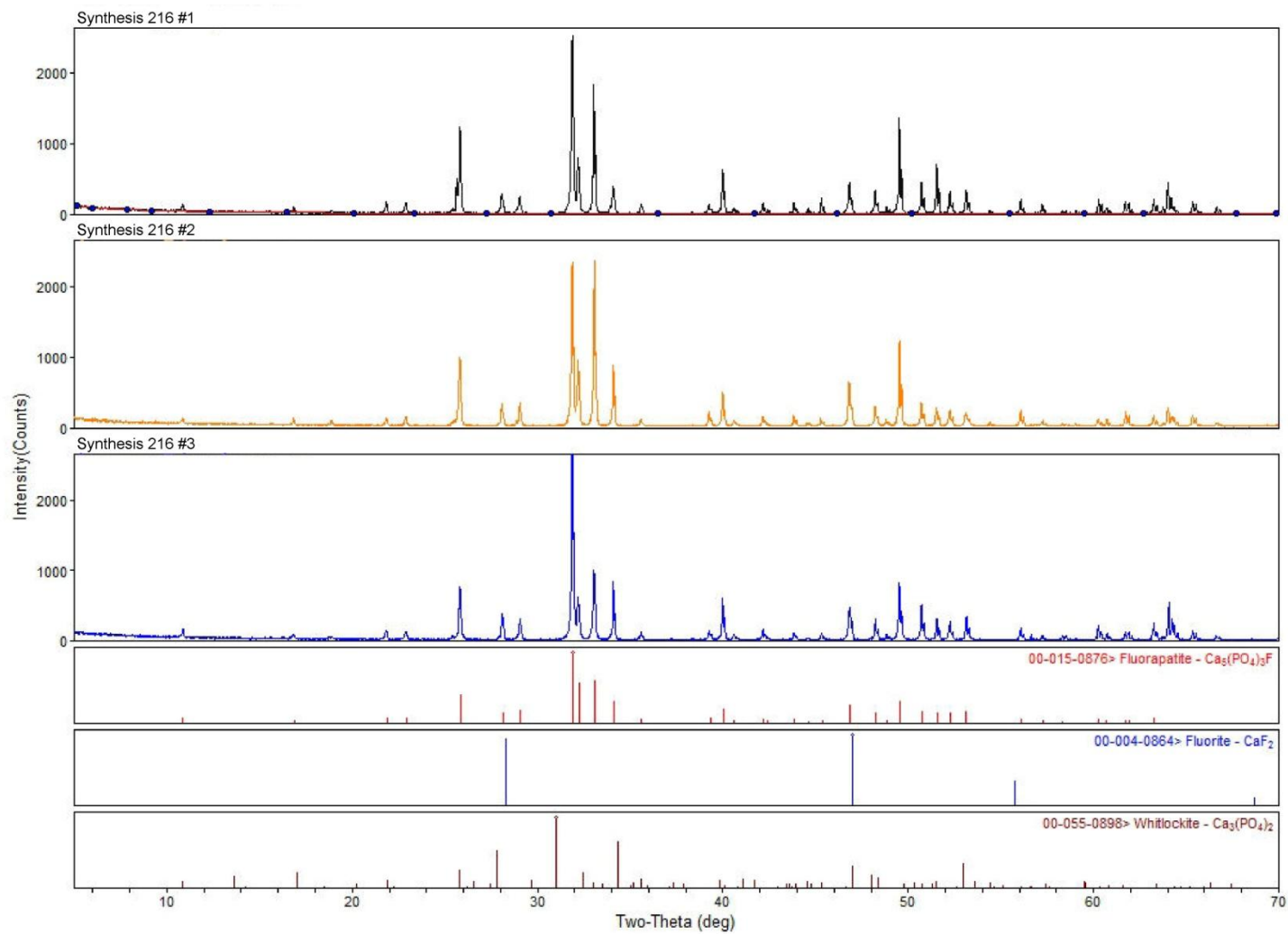


Figure A.6. X-ray diffractograms for apatite from synthesis 216: REE-doped with Na at 10x.

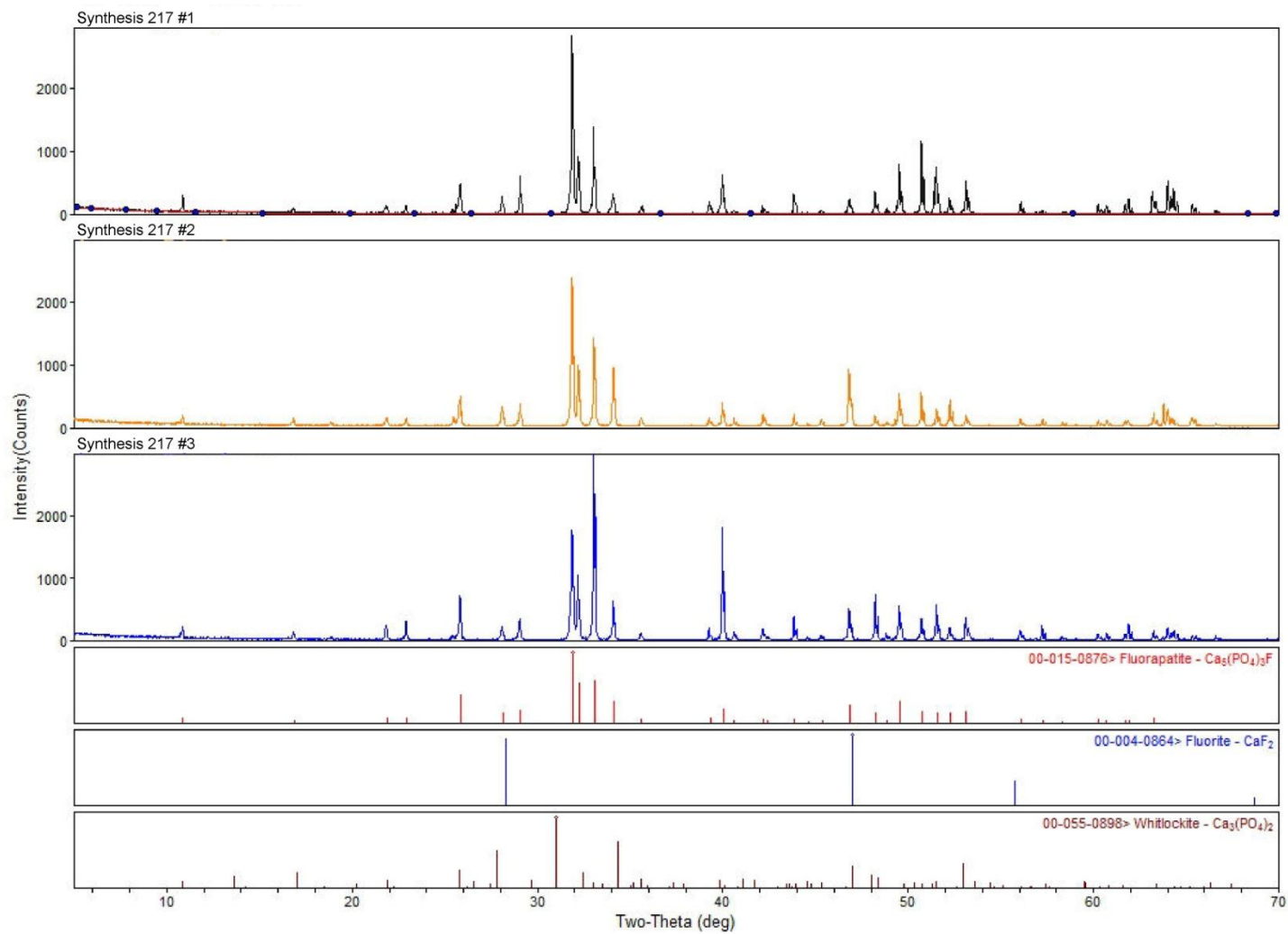


Figure A.7 X-ray diffractograms for apatite from synthesis 217: REE-doped with Na at 100x.

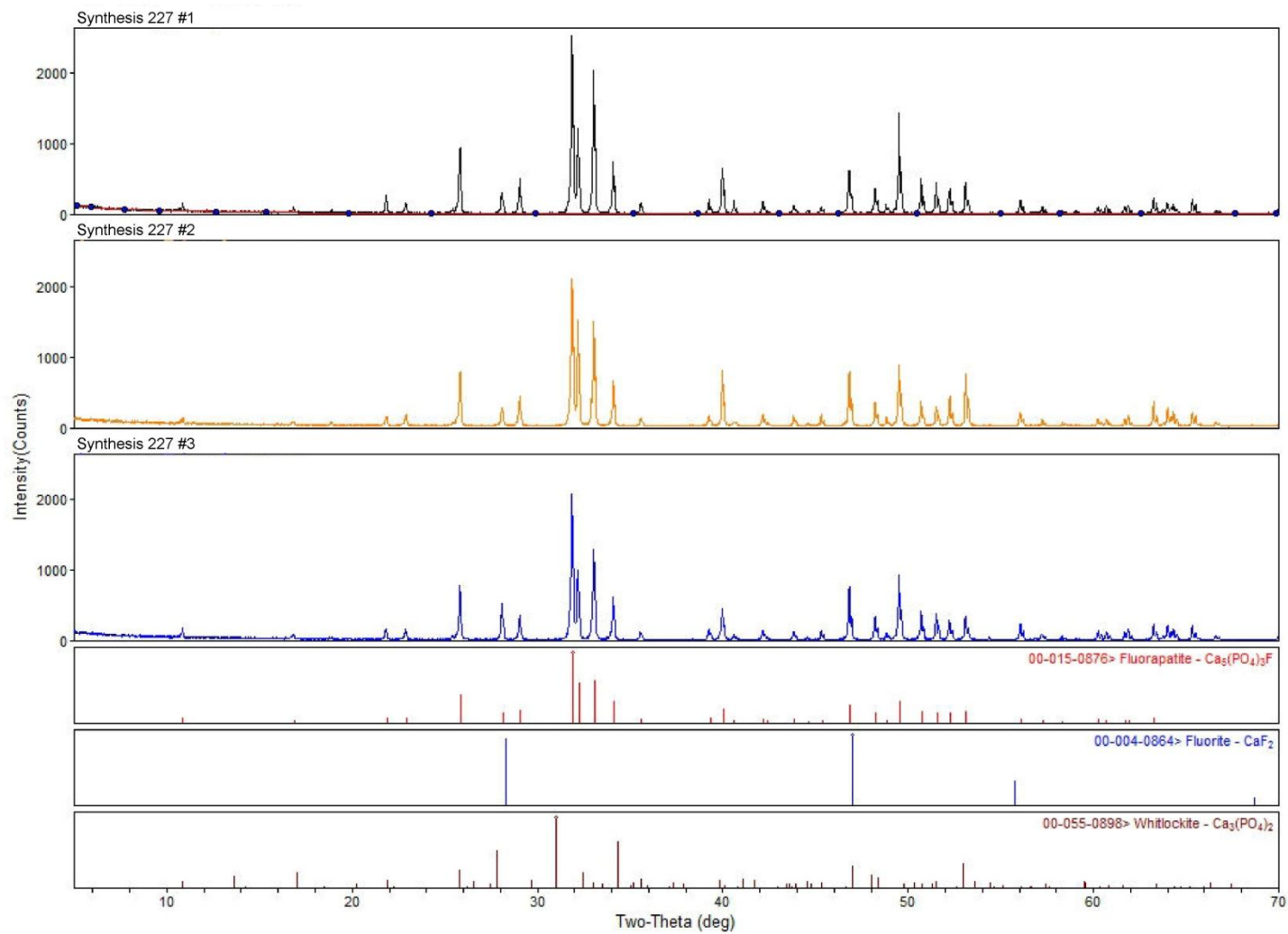


Figure A.8 X-ray diffractograms for apatite from synthesis 227: REE-doped with Si at 20x; LREE > HREE.

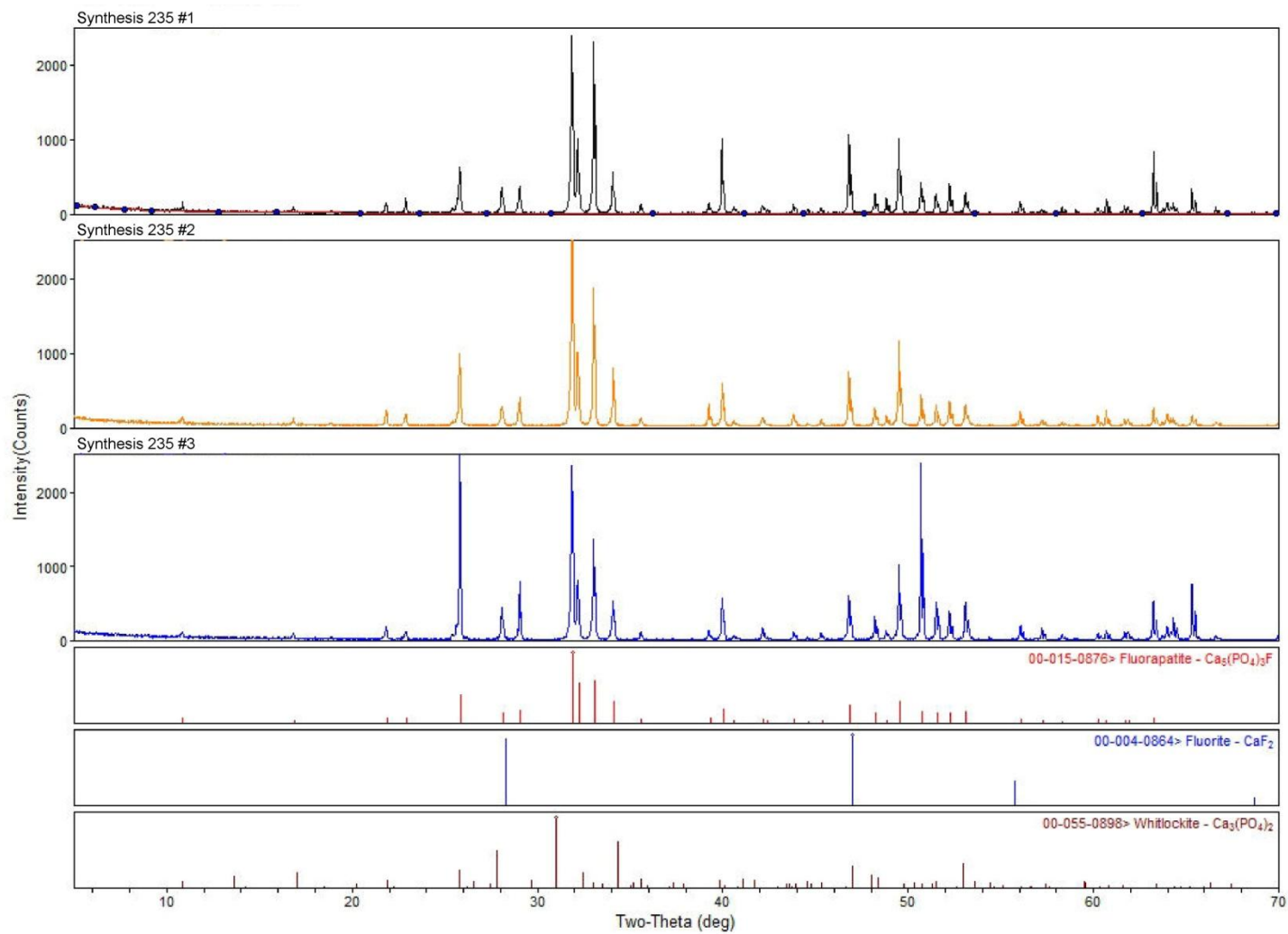


Figure A.9 X-ray diffractograms for apatite from synthesis 235: REE-doped with Si at 20x; LREE = HREE.

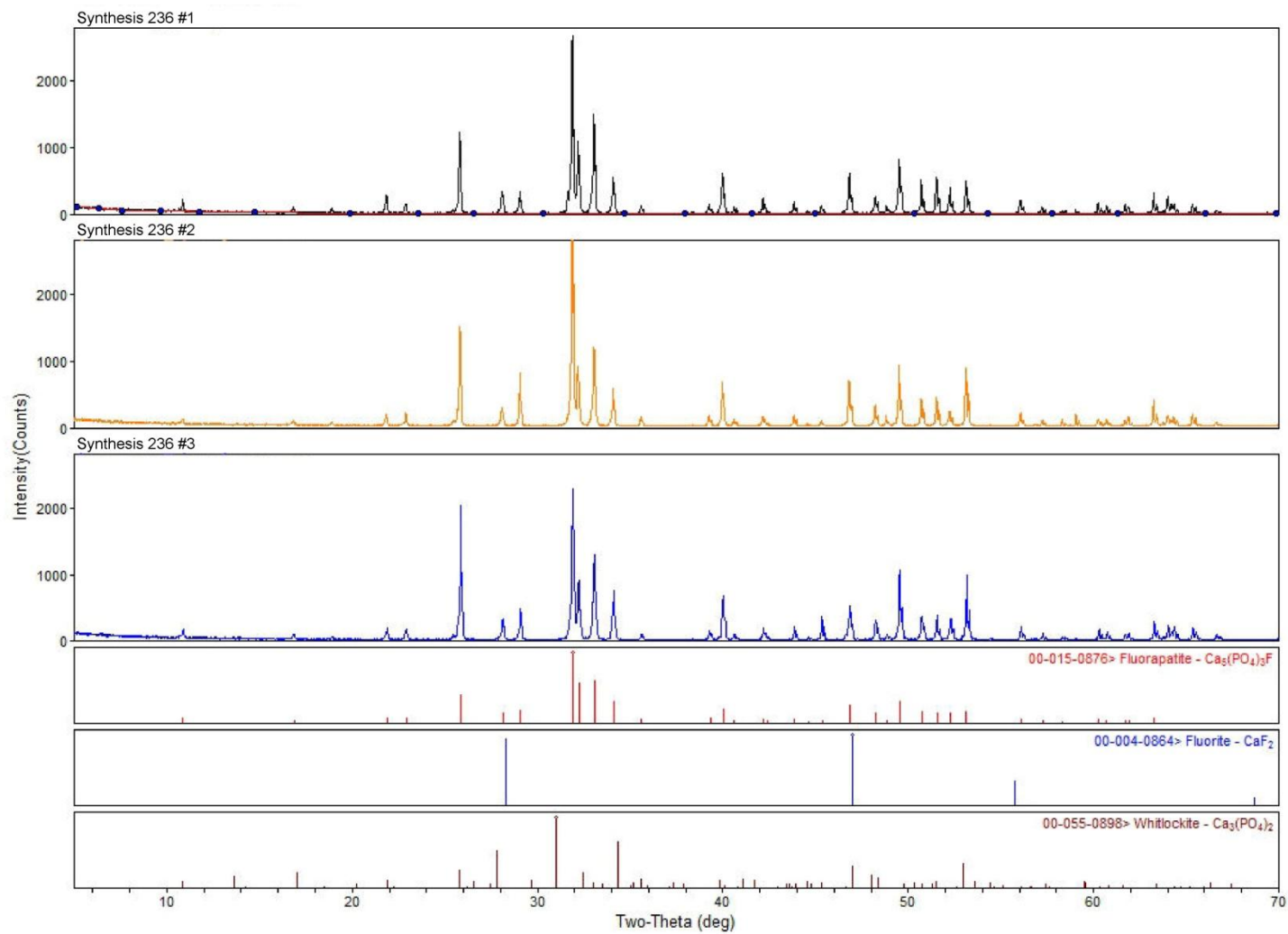
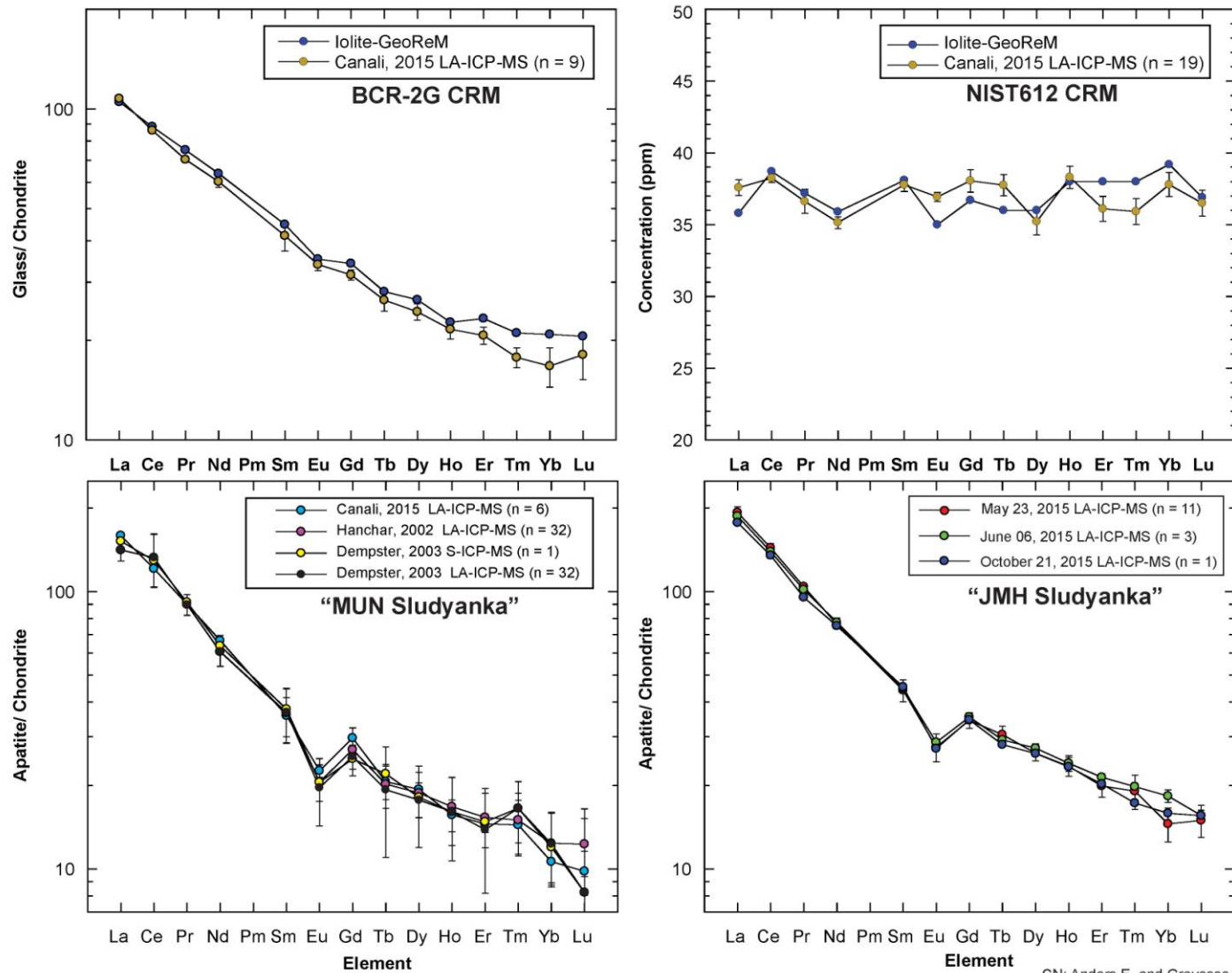


Figure A.10 X-ray diffractograms for apatite from synthesis 236: REE-doped with Si at 20x; LREE < HREE.



CN: Anders E. and Grevesse N. (1989)

Figure A.11. Rare earth element spider diagrams for BCR-2G and NIST612 certified reference materials (CRM), and "MUN Sludyanka" and "JMH Sludyanka" natural apatite external reference standards. Note that the y-axis denotes samples that have been normalized to chondrite.

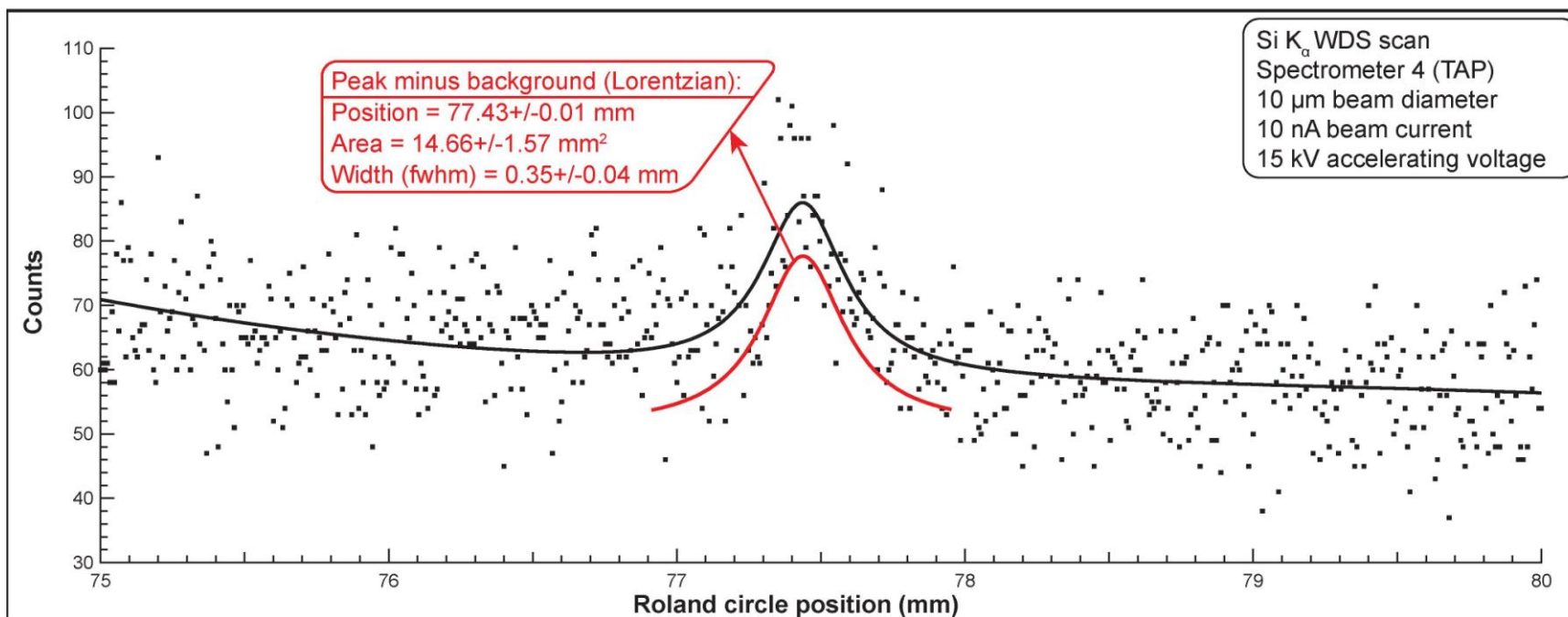


Figure A.12. Wave scan for Si K α peak (at ~77 mm) on Ca₃(PO₄)₂ starting material used for apatite syntheses. The peak at 77.43 +/- 0.01 mm corresponds to the Si K α peak, and subsequent quantitative analyses confirmed the presence of Si in the starting material; hence, this was confirmed as the source of Si contamination.